

Geologic controls on seismic velocity from well logs and
seismic tomography at the Rotokawa and Ngatamariki
Geothermal Fields, New Zealand

By Steven Sewell

A thesis

submitted to Victoria University of Wellington

in fulfilment of the requirements for the degree of

Doctor of Philosophy in Geophysics.

Victoria University Wellington

2022

Abstract

In this thesis, the factors controlling seismic velocity at the log scale (less than a metre) were explored and this knowledge used to interpret seismic velocity images at the field scale (greater than 200 m) obtained via seismic tomography at two geothermal fields in the Taupō Volcanic Zone in New Zealand; the Ngatamariki and Rotokawa fields. Seismic velocity imaging has the potential to provide valuable insights into geothermal reservoirs that can be used for well targeting, resource management and conceptual and numerical models. However, the potential factors influencing seismic velocity in geothermal reservoirs are many. In this thesis, the factors controlling seismic velocity were explored by pairing geophysical logging data, which included P-wave velocity, S-wave velocity (for two wells), neutron porosity, density, gamma, resistivity and formation image logs with newly acquired geochemical (via portable XRF) and mineralogical (via quantitative XRD and automated mineral scanning) data from drill cuttings in three deep wells in the Ngatamariki field. The combined analysis of these datasets demonstrates that the largest factor controlling seismic velocity in the two fields is porosity, which in turn can be influenced by both primary lithology, alteration and ductile deformation above the magmatic intrusions that provide the heat in high-temperature, volcanic, geothermal systems. The results also show that the physical and chemical properties of the tuff-dominated Tahorakuri Formation in the north of the Ngatamariki field were dramatically altered by high-temperature ($>375^{\circ}\text{C}$) alteration and ductile-deformation processes during an intrusion event that occurred approximately 65 kya. Wide-spread quartz deposition in the Tahorakuri Formation in the north of the field due to the intrusion event appears to have decreased porosity and increased velocity relative to the same formation in the south of the field (quartz abundance of 58% in the north cf. 38% in the south, V_p of 4.34 km/s in the north cf. 3.78 km/s in the south). Ductile deformation that occurred when temperatures in the past were above the brittle-ductile transition ($>375^{\circ}\text{C}$) has resulted in closing of pore space and a zone of very low porosity (mean of 4%) and consequent high seismic velocity (mean of 4.89 km/s) that extends approximately 400 m above the intrusion in NM9. The knowledge gained from this work provided the framework for interpreting the results of the seismic tomography.

To improve the resolution and robustness of the seismic tomography, 30 seismometers were deployed across the Ngatamariki and Rotokawa fields, to complement the existing seismic network of 22 seismometers, for approximately one year. From this deployment, a sub-set of 351 of high-quality earthquakes were used to perform the tomography analysis. A 1D Monte Carlo VELEST analysis was performed using this dataset by randomly generating 1000

different 1D starting models with velocity distributions based on measured velocity data and knowledge of rock types across the two fields. This yielded an average 1D model for the two fields which was then used as the basis for 3D inversion work. VELEST also inverts for station correction terms that can be used to provide an indication of the spatial variation in velocity for V_p and V_s with negative station corrections indicating faster velocity and positive station corrections indicating slower velocity. Three areas of similar station correction terms were identified; an area of negative V_p and V_s station corrections in the northwest of Ngatamariki, an area of positive V_s station corrections to the east of Ngatamariki and positive V_p and V_s station correction terms at Rotokawa. The spatial pattern of the station correction terms agrees well with the spatial patterns of velocity observed in the 3D inversions.

3D inversion of the same earthquake dataset was performed using the program tomoDD. Inversions were performed using three different inversion grids and two different starting velocity models. Model solution robustness and uncertainty were assessed using both ray-path coverage measures and synthetic testing. In all of the inversions performed, a west to east, high (V_p up to 4.8 km/s, V_s up to 2.7 km/s) to low velocity (V_p up to 3.8 km/s, V_s up to 2.2 km/s) transition was observed in the north of the Ngatamariki field for both V_p and V_s . High velocity in the northwest of Ngatamariki was observed over the depth range of 1-3 km bsl (below sea level), corresponding mostly to the Tahorakuri Formation tuffs and volcanoclastics above the intrusion in the north of the field. As was demonstrated with the logging, geochemical and mineralogical datasets, high velocity in this area is likely associated with reduced porosity due to alteration (particularly quartz deposition) and ductile-deformation that occurred during an intrusion event. The area of high velocity in the northwest of Ngatamariki aligns well with high gravity and high resistivity at 1.5 km bsl from a 3D inversion of magnetotelluric data. The transition between high to low velocity, gravity and resistivity all occur approximately across the NM9 well in the north of the field, suggesting that drilling in the northeast of the Ngatamariki field is unlikely to encounter the low permeability that was observed in the NM4 and NM8 wells.

The findings of this thesis highlight that alteration and deformation above magmatic intrusions in geothermal fields can cause pronounced changes in the physical, chemical and mineralogical properties of the rock and that these changes may be imaged by seismic tomography methods. This has potential implications for well targeting in geothermal fields and wider implications for seismic imaging of magmatic systems.

Acknowledgements

I have a great many people to thank for their support of this project and the data collection that went along with it. First and foremost, many thanks to my supervisors Martha Savage and John Townend for their guidance and patient support of my thesis. Thanks also for the many years now of supporting MSc and PhD projects on the geothermal fields in New Zealand.

I would like to thank greatly Mercury Energy and the Rotokawa Joint Venture for supporting this thesis by providing data for the Rotokawa and Ngatamariki geothermal fields and their financial support for the seismometer deployment. Many thanks in particular to former Mercury employees John Clark and Ian Richardson for supporting this project in its initial phase and to David Wootton of Mercury for assisting with access to the fields for the seismometer deployment. Kenny Graham, Stefan Mroczek and Chet Hopp are thanked greatly for their assistance in doing the fieldwork, it was a lot of fun and I owe you all a beer sometime.

The seismometers used in the fieldwork for this project were provided by ANSIR (Australian National Seismic Imaging Resource) and I thank them for providing this. In particular, Michelle Salmon is thanked for supporting the project and organising shipping of the equipment to New Zealand.

Mark Simpson and Michael Gazley are thanked greatly for their keen support and wisdom throughout the collection of the portable XRF, XRD and mineralogy data and the many discussions and emails on its interpretation. I thank also Isabelle Chambefort for the discussions on the interpretation of the geochemical and mineralogical datasets at Ngatamariki. Thankyou also to GNS Science Wairakei for providing access to drill cuttings and for hosting me during collection of the portable XRF data.

Larry Hutchings of Lawrence Berkeley National Laboratory is thanked greatly for hosting me at LBNL, providing code and assistance during the initial phases of this work. Stephen Bannister and Sandra Bourguignon at GNS Science are thanked for discussion of my tomography results and guidance on how to approach the inversions. Donna Eberhart-Phillips is thanked for discussion of my results and her great suggestions on how to approach my tomography work based on her many years of experience in the area.

Adrian Benson is thanked for his assistance during the fieldwork and for writing the code used to process the seismic data. Aleksandr Beliaev is thanked for the many times he assisted with computing and coding issues.

To Bill Cumming, I thank you greatly for the discussions on my thesis work throughout my PhD and for your mentoring, guidance and friendship throughout my career in geothermal. Thank you for always being so generous with your time and support.

To my parents, thank you for always supporting me, including throughout the duration of my PhD. To my wife Anna thank you for your support throughout the PhD and putting up with my complaining during the hard-slog of writing it! This is for you, our son Leo James Sewell and baby number two due in October this year.

Contents

Abstract	3
Acknowledgements.....	5
Figures.....	11
Tables.....	17
1 Introduction.....	21
1.1 Motivations.....	21
1.2 Aims of this study	23
1.3 Seismic Velocity in Geothermal Fields.....	24
1.4 The Rotokawa and Ngatamariki Geothermal Fields	27
1.4.1 Geologic Setting.....	33
1.4.2 Seismic Activity at Rotokawa and Ngatamariki	35
1.5 Thesis Content.....	38
2 Data and Methods	41
2.1 Data	41
2.1.1 Geophysical Logging	41
2.1.2 Rock Geochemistry and Mineralogy	43
2.1.3 Seismic Data	44
2.2 Methods.....	50
2.2.1 Combining rock geochemistry and mineralogy to interpret velocity measurements from wireline data	50
2.2.2 Seismic Tomography	54
3 Geologic factors controlling seismic velocity at the Ngatamariki Geothermal Field from comparison of wireline logging data to quantitative analysis of geochemistry and mineralogy.	
75	
Abstract	75
3.1 Introduction	76

3.2	Data and Methodology	81
3.2.1	Portable XRF (pXRF)	81
3.2.2	SEM-based Automated Mineral Mapping	85
3.2.3	Quantitative XRD	86
3.2.4	Formation Logs in NM8, NM9 and NM10.....	87
3.2.5	Depth Correction of Cuttings Based on Potassium from pXRF and Gamma Logs 88	
3.2.6	Defining Geochemical Units.....	90
3.3	Results	91
3.3.1	Geochemical units.....	104
3.3.2	Seismic Velocity	109
3.3.3	Relationships Between Seismic Velocity, Neutron Porosity and Density.....	114
3.4	Discussion	116
3.4.1	NM8.....	117
3.4.2	NM9.....	118
3.4.3	NM10.....	124
3.4.4	Comparison Between Northern (NM8 and NM9) and Southern (NM10) Tahorakuri Formation	126
3.5	Conclusions	131
4	Monte Carlo 1D Velocity Inversion of the 2017-2018 Expanded Array Data	133
	Abstract.....	133
4.1	Introduction	134
4.2	Data and Methodology	136
4.2.1	Travel-time data	136
4.2.2	VELEST Using Monte Carlo Starting Models	140
4.3	Results	141
4.3.1	Data fit	141
4.3.2	Final Velocity Models.....	143

4.3.3	Station Corrections.....	146
4.3.4	Hypocentres	150
4.4	Discussion	152
4.5	Conclusions	156
5	3D Velocity Inversion of the 2017-2018 Expanded Array Data	159
	Abstract.....	159
5.1	Introduction	160
5.2	Data and Methodology	162
5.2.1	Travel-time Data	162
5.2.2	Inversion code tomoDD.....	162
5.2.3	Synthetic testing.....	167
5.3	Results	168
5.3.1	Data Fit.....	168
5.3.2	Data Coverage.....	170
5.3.3	Final Velocity Models.....	170
5.3.4	Synthetic Testing	182
5.4	Discussion	196
5.5	Conclusions	202
6	Synthesis	205
6.1	Summary	205
6.2	Implications for the Rotokawa and Ngatamariki Geothermal Fields.....	208
6.2.1	Ngatamariki.....	208
6.2.2	Rotokawa	209
6.3	Implications for Application of Seismic Tomography in Geothermal Areas	214
6.4	Prospects for Further Research	214
6.5	Concluding Statement	218
	References.....	219

Appendices.....	239
A.1. Expanded array seismic network	239
A.2 Automatic Data Processing for Local Earthquake Seismic Tomography: Rotokawa and Ngatamariki 2012-2017 Dataset	243
A.3. Example manual and automatic picks from the tomography dataset.....	277
A.4. Original Stratigraphy of Logged Intervals	285
A.5. Station Correction Terms	287
Electronic Appendices	293

Figures

Figure 1.1. Location of the Rotokawa (R), Ngatamariki (N) and other high temperature geothermal fields in the Taupō Volcanic Zone (TVZ).	28
Figure 1.2. Location of wells at Rotokawa and Ngatamariki.	29
Figure 1.3. Natural state temperatures for selected wells in the Ngatamariki field.	30
Figure 1.4. Conceptual model cross-section of the Ngatamariki field.	31
Figure 1.5. Conceptual model cross-section for Rotokawa.	32
Figure 1.6. Location of microseismic events for Rotokawa	38
Figure 2.1. Measured velocities from NM9.....	43
Figure 2.2. Seismometer locations for the 2017-2018 expanded array.	45
Figure 2.3. Zoomed-in view of the seismometer locations for the expanded array.....	46
Figure 2.4. Data continuity over the 2017-2018 period of the expanded array.	47
Figure 2.5. Automated data processing flow chart.	49
Figure 2.6. P and S pick uncertainties for the 100 events that were manually picked.	50
Figure 2.7. Summary of alteration minerals commonly found in high temperature, volcanic geothermal systems and their temperature stability.....	52
Figure 2.8. Flow diagram of the steps involved in seismic tomography.	56
Figure 2.9. (a) The shooting method of ray-tracing.....	61
Figure 2.10. The approximate ray tracing pseudo-bending method..	62
Figure 2.11. Schematic of the trade-off curve method for selecting appropriate (a) damping and (b) smoothing parameters for an inversion.	65
Figure 2.12. Example of the checkerboard synthetic test.	70
Figure 2.13. An example of the improvement in resolution within the source region gained by using the double-difference tomography approach.....	73
Figure 3.1. Geologic cross-section showing well tracks, the main geologic units and selected natural state temperature isotherms.	80
Figure 3.2. (a) Schematic diagram showing the basic principle behind the pXRF.	82

Figure 3.3. Selected elemental analyses with time for the NIST2710a standard for the DELTA (a) and VANTA (b).....	83
Figure 3.4. Example of (a) drill cuttings in 25 mm epoxy mount (b) the mineralogy map produced by the SEM-based automated mineralogy mapping for sample NM8 1250 mRF...	86
Figure 3.5. Example of the cuttings depth correction undertaken using the gamma ray log and pXRF potassium for NM9.	90
Figure 3.6. Centred-log ratio for selected pXRF data for NM8.....	92
Figure 3.7. NM8 pXRF data.	93
Figure 3.8. Mineral abundance in NM8 from automated mineralogy (TIMA) and quantitative XRD.	94
Figure 3.9. NM8 geophysical logs.....	95
Figure 3.10. Centred-log ratio for selected pXRF data for NM9.....	96
Figure 3.11. NM9 pXRF data.	97
Figure 3.12. Mineral abundance in NM9 from automated mineralogy (TIMA) and quantitative XRD..	98
Figure 3.13. NM9 geophysical logs.....	99
Figure 3.14. Centred-log ratio for selected pXRF data for NM10.....	100
Figure 3.15. NM10 pXRF data.	101
Figure 3.16. Mineral abundance in NM10 from automated mineralogy (TIMA) and quantitative XRD.	102
Figure 3.17. NM10 geophysical logs.....	103
Figure 3.18. Box and whisker plot of Vp (km/s) for each geochemical unit.....	110
Figure 3.19. Box and whisker plot of Vs (km/s) for each geochemical unit for NM8 and NM10.	111
Figure 3.20. Box and whisker plot of Vp/Vs for each geochemical unit for NM8 and NM10.	112
Figure 3.21. Kernel Density Element (KDE) plot of Vp versus neutron porosity.....	115

Figure 3.22. Kernel Density Element (KDE) plot of Vp versus density. The dashed black line shows the density of quartz (2.65 g/cm ³).	116
Figure 3.23. FMI log data from NM9.	121
Figure 3.24. Neutron porosity versus porosity derived from the density log (using a matrix density of 2.65 g/cm ³ and fluid density of 1 g/cm ³) for the tuffs in NM10 ('Tuffs 10').	124
Figure 3.25. Vp and Vs versus clay content for chlorite, illite, kaolinite, and total clay (Chlorite* + Muscovite + Kaolinite*) from the TIMA data.	125
Figure 3.26. Schematic cross-section showing the interpreted large-scale velocity structure below -500 masl at Ngatamariki based on the well log and cuttings analysis.	129
Figure 3.27. Neutron porosity vs. Vp for NM9 and NM10 in this study.	130
Figure 4.1. Seismometers and the starting event locations used in the VELEST analysis (obtained from NonLinLoc).	137
Figure 4.2. Close-up of seismometers and the starting event locations used in the VELEST analysis (obtained from NonLinLoc) over the two geothermal fields.	138
Figure 4.3. Number of P and S picks per event.	139
Figure 4.4. Starting (a) Vp and (b) Vs models compared to checkshot and Vp and Vs logs.	141
Figure 4.5. RMS residual misfit between observed and calculated traveltimes for each iteration for all 999 final models obtained.	142
Figure 4.6. Distribution of the final RMS residual misfit for all 999 final models obtained after seven iterations.	143
Figure 4.7. Box and whisker plot of the starting and final Vp for each layer of the VELEST inversions.	144
Figure 4.8. Box and whisker plot of the starting and final Vs for each layer of the VELEST inversions.	145
Figure 4.9. Vp station corrections.	146
Figure 4.10. Vp station corrections zoomed in.	147
Figure 4.11. Vs station corrections.	148
Figure 4.12. Vs station correction zoomed in.	149

Figure 4.13. Starting (obtained from NonLinLoc) versus the final average hypocentre locations (i.e. average location from all 999 VELEST runs).	151
Figure 4.14. Distribution of hypocentre shifts in x (east-west), y (north-south) and z (depth) from the average location for all models. std = standard deviation in metres.	152
Figure 4.15. Distribution of origin time shifts for all models.....	152
Figure 4.16. Comparison between measured V_p and V_s in wells NM9 (checkshot and sonic logs) and NM10 (sonic logs) and the distribution of the final 500 models.	154
Figure 5.1. Location of nodes for the different grids used for absolute data inversion.	164
Figure 5.2. Trade-off curves for the absolute travelttime data.....	165
Figure 5.3. 1D starting model used in the 3D inversions (red line) and velocity starting values applied to NW Ngatamariki and Rotokawa in the 3D ‘geo’ starting model.....	167
Figure 5.4. Distribution of P and S residuals for the absolute arrivals for the 1D (a and b), 2D (c and d), coarse 3D (e and f), fine 3D (g and h) and 3D geo model (i and j).	169
Figure 5.5. Derivative weight sum (DWS) for V_p	171
Figure 5.6. Derivative weight sum (DWS) for V_s	172
Figure 5.7. V_p for the fine model.	173
Figure 5.8. V_s for the fine model.....	174
Figure 5.9. V_p for the geo model.....	175
Figure 5.10. V_s for the geo model.	176
Figure 5.11. Comparison between the geo and fine model with the same velocity scale for V_p	177
Figure 5.12. Comparison between the geo and fine model with the same velocity scale for V_p	178
Figure 5.13. Comparison between the geo and fine model with the same velocity scale for V_s	179
Figure 5.14. Comparison between the geo and fine model with the same velocity scale for V_s	180
Figure 5.15. Change in data percent, data fit and hypocentre shift for each iteration.	182

Figure 5.16. Spike test for Vp at 0.2 and 1 km bsl.	184
Figure 5.17. Spike test for Vp at 1.5 and 2.0 km bsl.	185
Figure 5.18. Spike test for Vp at 2.5 and 3.0 km bsl.	186
Figure 5.19. Spike test for Vs at 0.2 and 1 km bsl.	187
Figure 5.20. Spike test for Vs at 1.5-2 km bsl.	188
Figure 5.21. Spike test for Vs at 2.5 and 3.0 km bsl.	189
Figure 5.22. Synthetic recovery of the main interpreted features for Vp at 0.2 and 1 km bsl.	190
Figure 5.23. Synthetic recovery of the main interpreted features for Vp at 1.5 and 2km bsl.	191
Figure 5.24. Synthetic recovery of the main interpreted features for Vp at 2.5 and 3 km bsl.	192
Figure 5.25. Synthetic recovery of the main interpreted features for Vs at 0.2 and 1 km bsl.	193
Figure 5.26. Synthetic recovery of the main interpreted features for Vs at 1.5 and 2km bsl.	194
Figure 5.27. Synthetic recovery of the main interpreted features for Vs at 2.5 and 3 km bsl.	195
Figure 5.28. Comparison between velocity and gravity data.....	197
Figure 5.29. Comparison of resistivity at 1.5 km bsl from a 3D inversion of magnetotelluric data across the two fields and velocity from the geo model.	199
Figure 6.1. Summary of interpretation based on the work in this thesis.	211
Figure 6.2. Hypocentres for the 1209 earthquakes recorded and located during the 2017-2018 field deployment.	212
Figure 6.3. Hypocentre depths for (a) Ngatamariki North, (b) Ngatamariki South and (c) Rotokawa for the 1209 earthquakes recorded and located during the 2017-2018 field deployment.....	213

Tables

Table 1.1. Possible factors influencing seismic velocity in geothermal areas and their expected effects.....	26
Table 2.1. Common elements and, the minerals they are commonly found in, for both primary mineralogy in TVZ volcanic rocks and geothermal alteration minerals.....	53
Table 3.1. Elastic moduli, density, Vp and Vs for some of the common minerals found in this study at room pressure and temperature.	78
Table 3.2. Correction factors used on the pXRF data.....	84
Table 3.3. Petrophysical property differences for the Tahorakuri Formation between the north (NM8 and NM9) and south (NM10).....	127
Table 4.1. Number of events and picks and whether manually or automatically picked for all events and for each cluster of events.	139
Table 4.2. Hypocentre and ray length statistics for each layer for all final models.....	153

Glossary

mRF Depth in metres down a well relative to the drilling rig floor (~10-30 m above ground level)

km bsl Vertical kilometres below sea level

masl Vertical metres above sea level

injectivity A measure of a well's ability to accept a volume of fluid per unit pressure, here reported as tonnes per hour bar (t/h.bar)

alteration Change in rock mineralogical composition due to interaction with fluids

box-and-whisker Plot showing the distribution of data whereby the box contains 50% of the values (25% either side of the mean which is shown as a vertical line within the box), the whiskers show the full extent of the data excluding outliers and diamonds are outliers defined as data that is greater than 1.5 times the interquartile range above or below the upper and lower quartile.

permeability The ability of a porous or fractured material to allow fluids to pass through it.

TVZ Taupo Volcanic Zone, a zone of back-arc rifting in the central north island of New Zealand

hypoDD A program for re-locating earthquakes relative to each other with high accuracy (Waldhauser and Ellsworth, 2000).

tomoDD A program based on hypoDD that determines velocity structure and relocates earthquakes relative to each other (Zhang and Thurber, 2003).

dt A time differential, usually referring to the time difference between the calculated (from a velocity model and ray-tracing algorithm) and measured time.

VELEST A program for calculating a 1D velocity model using natural or man-made seismic sources (Kissling et al., 1994).

XRF X-ray fluorescence, a technique for determining elemental abundance

pXRF Portable XRF, a handheld device used to obtain rapid elemental abundance analysis

TIMA Tescan Integrated Mineral Analyzer, a device that uses both Energy Dispersive X-Ray (EDX) and backscattered electron (BSE) signals to map mineralogy in a sample

XRD X-ray Diffraction. A technique used to determine and quantify mineral composition in a powdered sample.

SEM Scanning Electron Microscope. A device that produces images of a sample by scanning the surface with a focused beam of electrons which can be used to determine the chemical composition of the sample.

EDS Energy Dispersive X-ray Spectroscopy. A technique used for chemical analysis of a sample using x-rays.

Regularization A method used in inversion of ill-posed problems.

Ray-path Path of shortest travelttime through a medium.

ART-PB Approximate ray-tracing using pseudo-bending. An efficient algorithm used for determining travel-times of ray-paths.

WCC Waveform Cross-correlation. A method used to compare two or more waveforms which can be used to obtain highly accurate relative arrival times between two earthquakes.

Borehole compensated sonic log A geophysical logging tool that uses two sets of monopole sources and receivers at different locations on the tool such that effects due to irregularities in the borehole wall between the sensors and/or tilt of the tool are removed.

1 Introduction

1.1 Motivations

Electricity generation from geothermal resources is a low-carbon, renewable energy source that has been in use around the world for over 100 years (e.g. Dickson & Fanelli, 2013). Currently, approximately 15% of New Zealand's electricity comes from geothermal power plants (Carey et al., 2015). Geothermal reservoirs are typically between 1 – 4 km depth and therefore expensive drilling is required to tap into these resources. Since 2010, geothermal wells drilled in New Zealand have cost on average between NZ\$10 to \$15 million per well (Hole, 2013). Drilling is also risky with well success rates during initial exploration of resources between 50 to 60%, ~70% during development phase drilling and ~85% during the operational phase of a project (International Finance Corporation, 2013). Geophysical techniques can be used at all stages of a geothermal project to maximise the chance of drilling successful wells (e.g. Cumming, 2016).

Robust resource monitoring and management during the operational phase of a geothermal project allows geothermal resources to be sustainably utilised with minimal environmental impacts. Monitoring and management also minimises the amount of additional drilling needed to maintain electricity generation throughout the operational lifetime of projects. Monitoring thermodynamic changes over time within the reservoir (e.g. temperature and steam-liquid phase changes in the reservoir over time) is one of the most important aspects of resource monitoring and management (Grant, 2013; Hernandez et al., 2015; Hunt, 2012). Geophysical techniques can be used to infer thermodynamic changes occurring within the reservoir in areas that are not directly monitored by measurements made in wells (e.g. Hunt & Bowyer, 2007; Sherburn et al., 2015). Seismic monitoring also has particular importance in understanding hazards and risks associated with induced seismicity (Sherburn and White, 2005).

Imaging of seismic velocity variations via seismic tomography within geothermal reservoirs has potential utility for both well targeting and resource monitoring and management. Seismic tomography has been a popular geophysical method for imaging the subsurface since the mid-1970s at all scales of investigation; global (>100 km), lithospheric-crustal (10 – 100 of km), local (<10 km) (e.g. Rawlinson & Sambridge, 2003; Nicholas Rawlinson et al., 2010; Thurber & Ritsema, 2007). The term 'seismic tomography' is a somewhat generic term that is often

used to describe a range of methods with the common goal of determining spatial and temporal variations in the seismic properties of the subsurface (e.g., compressional wave velocity (V_p) and shear wave velocity (V_s), attenuation, elastic properties). The seismic properties that are imaged can then be interpreted in terms of subsurface variations in rock and fluid properties (e.g. lithology, temperature, fluid content, compressibility, pressure change, fracturing, etc) (Iyer and Hirahara, 1993; Thurber and Ritsema, 2007). Both natural (e.g. earthquakes) and/or manmade (e.g. explosive charges, induced events) seismic sources can be used (Thurber and Ritsema, 2007).

Seismic velocity is known to vary with important geothermal reservoir properties such as porosity/permeability, temperature and water/steam saturation (e.g. Boitnott, 1995; Jaya et al., 2010; Siratovich et al., 2014). However, there are relatively few examples of the application of seismic velocity imaging via tomography to operating geothermal reservoirs. One possible reason for this is that spatial resolution of variations in seismic velocity derived from tomographic inversions is dependent on the distribution of earthquakes and surface seismometers (e.g. Hutchings et al., 2011; Julian & Foulger, 2012) and therefore, without dense seismometer networks, spatial resolution is on the order of several kilometres. Another major reason is that, compared to oil and gas, relatively little is known about what factors influence seismic velocity within and adjacent to geothermal reservoirs (e.g. Farina et al., 2019).

In this study, data from the high-temperature Rotokawa and Ngatamariki geothermal fields was used to provide a robust case-study of how seismic velocity imaging can be used to better understand geothermal resources. Well-logging data from three wells in the Ngatamariki field provided a unique and rich dataset with which the factors controlling seismic velocity could be explored. Seismic tomography, with an expanded seismic array of 55 seismometers across the two fields allowed the large-scale velocity structure to be determined and related back to the observations made at the well-log-scale.

Prior to undertaking this work, a number of differences in seismic velocity were anticipated based on the known differences in geology, alteration and thermodynamics between the two fields. For instance, the northern part of Ngatamariki was known to have low permeability that had been related to the presence of an old intrusion and its associated alteration halo (Chambefort et al., 2016b). (Sherburn et al., 2003) also reported a high V_p anomaly (>15% above background) in the north of Ngatamariki that they attributed to the diorite-tonalite intrusion, however this feature was not well resolved spatially as the study used a regional

seismic monitoring network with wide spacing between seismometers. Bannister et al., (2015) also observed relatively high V_p between 5 and 15 km beneath Rotokawa and Ngatamariki which they attribute to a possible solidified magma. Since the diorite-tonalite intrusion and its associated alteration were known to be low-permeability, imaging it with seismic tomography was expected to provide better constraints on the extent of this low-permeability within the Ngatamariki field.

A sharp lateral temperature gradient was also known to exist at Rotokawa in the north-northeast of the field (340°C measured in well RK24 to ~200°C in well RK19 within 1 km distance (Sewell et al., 2015). This was associated with a transition from good (injectivity >5 t/h.bar, convective heat transfer) to very low permeability (injectivity <1 t/h.bar, conductive heat transfer) and it was thought that there may be seismic velocity changes associated with this. Pressure responses to production within the Rotokawa reservoir have also had unusually high spatial variability (up to 40 bars) since the start of the Nga Awa Purua plant production in 2010, which has also increased the extent and concentration of steam at the top of the reservoir (Hernandez et al., 2015). The large pressure changes and increase in steam content were anticipated to possibly have associated changes in seismic properties at the beginning of this study. The region between the Rotokawa and Ngatamariki geothermal fields was also of interest: based on reservoir engineering considerations, the two fields are hydraulically isolated and, therefore, both temperature and permeability are inferred to decrease between the two fields. Therefore, it was anticipated that there may be velocity changes between the two fields that might be imaged with seismic tomography.

1.2 Aims of this study

The overall aims of this study were to:

- Provide a robust-case study of the utility of seismic tomography in geothermal fields for well targeting and resource management; and
- Expand the understanding of the factors that influence seismic velocity in geothermal fields

Specific research questions related to these aims were:

- What are the dominant factors influencing seismic velocity within the high temperature, volcanic-hosted, Ngatamariki and Rotokawa geothermal reservoirs?

- What effects do variations in rock properties (e.g. lithology, alteration, fracturing, matrix porosity/permeability) have on seismic velocity?
- Can large-scale changes in reservoir rock properties (e.g. permeability) be inferred from seismic tomography at spatial resolutions sufficient for reservoir management or well targeting in these two reservoirs?

1.3 Seismic Velocity in Geothermal Fields

The rock physics work done on geothermal core samples previously shows that seismic properties vary with temperature, permeability and saturation (steam content), properties that are of interest for geothermal resource development and management (Boitnott, 1995; Farina et al., 2019; Ito et al., 1979; Jaya et al., 2010; Poletto et al., 2018). For example, Jaya et al. (2010) measured seismic velocity with varying temperature in cores from Iceland. They found that seismic velocity decreases and attenuation increases with increasing temperature. However, they noted the likely contribution of either small steam bubbles and/or thermal cracking in their samples, both of which have a similar effect on seismic properties as temperature. Ito et al. (1979) measured the effect of steam-liquid content in several samples and found strong variations in V_p and P-wave attenuation at the phase transition between steam and liquid. Significant work has been done to date on measuring P and S wave velocities (V_p and V_s respectively) in core samples from Rotokawa and Ngatamariki. Siratovich et al. (2014) performed V_p and V_s measurements on cores of the Rotokawa Andesite and found a correlation between V_p and matrix porosity/permeability. The porosity/permeability variations were in turn related to microfractures within the samples. Siratovich et al. (2015) also measured V_p and V_s before and after thermal stimulation of these samples and found decreases in V_p (of as much as 15%) and V_s , which they interpreted in terms of the formation of new microfractures. Wyering et al. (2014) also found a strong correlation between V_p , V_s and porosity at the Ngatamariki field. They also attribute velocity variations to changes in hydrothermal alteration, particularly clay alteration, and lithology.

Velocity variations deduced from seismic tomography studies in geothermal areas have been interpreted in terms of both reservoir properties and geology. The largest geothermal field in the world, the Geysers field in California, has been widely studied due to its large size, long-standing seismic monitoring, widespread seismic activity and the steam-dominated nature of the reservoir. Foulger et al. (1997) and Julian et al. (1996) first identified a low- V_p/V_s anomaly (~9% lower than surrounding areas) at the field that coincided with the highly produced part

of the reservoir. This was interpreted as being due to low pore pressure and boiling in pore space resulting in increasing steam content. Subsequent studies in the area have reproduced these findings (Gunasekera et al., 2003; Lin and Wu, 2018). Theoretical considerations and laboratory experiments suggest that this low- V_p/V_s anomaly represents a zone in which the pore fluid is predominately vapor, pressure is low, and the shear modulus is increased as a result of the drying of argillaceous (illite clay) material in the reservoir rocks (Boitnott & Boyd, 1996; Boitnott & Kirkpatrick, 1997). Gritto & Jarpe (2014) and Gunasekera et al. (2003) presented evidence that velocity changes have occurred within the reservoir over time as a result of the production activities. De Matteis et al. (2008) and Vanorio et al. (2004) reported similar low V_p/V_s at the steam-dominated Larderllo-Travale field in Italy, which they argued is due to steam-bearing formations. They also found a high-velocity transition at depth within the field that they suggested is due to lithology variation or to the presence of less-fractured parts of the crystalline basement. Foulger & Toomey (1989) and Jousset et al. (2011) identified several high-velocity bodies beneath the Hengill field in Iceland that they relate to solidified magma bodies. A low-velocity body was also identified that was interpreted to possibly contain partial melt and represent the heat source for the Hengill field. A low-velocity body was also identified by Zhang & Lin, (2014) beneath the Coso geothermal field in the US that was interpreted as being due to felsic magmatic intrusions. Muksin et al. (2013) presented results of a seismic tomography study for the Tarutung basin in Indonesia that contains several high-temperature geothermal fields. They found high- V_p/V_s values near to the surface within the Sarulla graben and northeast of the Tarutung basin which were interpreted as fluid-bearing, fractured sediments.

Most of the fluid and rock property variations within geothermal reservoirs are expected to decrease seismic velocities relative to their surroundings (e.g. high temperature, fracturing, gas and steam) (Table 1.1). Clay alteration also has a similar effect on seismic properties. Although some studies have shown the effect of clay alteration on seismic velocity and attenuation in geothermal systems (e.g. Wyering et al., 2014) this not been investigated in detail. In contrast, a large amount of experimental and rock physics modelling work on the relationship between clay type and content and seismic velocity and attenuation has been carried out within the oil and gas sector. Increased use of shale reservoirs has driven a lot of recent research into the effects of clay content on the physical properties of these reservoirs (e.g. Guo et al., 2012; Khadeeva and Vernik, 2014; Liu et al., 2014; Sayers and Den Boer, 2018; Zhu et al., 2011).

Table 1.1. Possible factors influencing seismic velocity in geothermal areas and their expected effects.

	V _p	V _s	References
Higher porosity (matrix)	↓	↓	(Mavko et al., 2009a; Wyering et al., 2014)
Increased fracturing	↓	↓	(Berryman, 2007; Moos and Zoback, 1983)
Clay alteration (smectite)	↓	↓	(Mondol et al., 2007; Tosaya and Nur, 1982; Vanorio et al., 2003)
Clay alteration (illite and chlorite)	↓	↓	(Mondol et al., 2007; Tosaya and Nur, 1982; Vanorio et al., 2003)
Steam	↓	↓	(Boitnott, 1995; Gritto and Jarpe, 2014; Julian et al., 1996)
Gas	↓	↓	(Wang, 2001; Wang et al., 2020)
High Temperature	↓	↓	(Farina et al., 2019; Jaya et al., 2010)
Alteration that decreases porosity (e.g. silicification)	↑	↑	(Avseth et al., 2010; Durán et al., 2019)
Alteration that increases porosity (e.g. mineral leaching in acidic zones)	↓	↓	(Mayer et al., 2016; Wyering et al., 2014)
Magma / Partial melt	↓	↓	(Berryman, 2000; Lees, 2007)

The Rotokawa and Ngatamariki andesite reservoirs often contain abundant chlorite and illite clay alteration (Chambefort et al., 2016a; McNamara et al., 2016) which may have an influence on seismic velocity and attenuation. The presence and effect of clay may therefore represent a significant ambiguity when interpreting seismic velocity and attenuation variations in terms of reservoir properties of interest such as permeability and temperature.

1.4 The Rotokawa and Ngatamariki Geothermal Fields

The Ngatamariki and Rotokawa Geothermal fields are high-temperature geothermal fields in the Taupō Volcanic Zone (TVZ) on the North Island of New Zealand (Figure 1.1). Electricity generation on the Rotokawa field began in 1997 with a small binary power plant (~30 MWe) and in 2010 a second 140 MWe triple-flash power plant was installed bringing the total installed capacity to ~170 MWe. Fluid take from the reservoir is approximately 60 – 70 kt/day and ~70% of this fluid is injected back into the reservoir with the remaining 30% of fluid lost to the atmosphere through evaporation (Hernandez et al., 2015). Injection occurs approximately 1 km to the south-southeast of the production wells (Figure 1.2). Electricity generation at Ngatamariki began in early 2013 with the commissioning of an 82 MWe binary power plant. Fluid take from the reservoir is approximately 50 kt/day and, as the power plant is of binary design (whereby heat is extracted from the geothermal fluid by heat exchange to a secondary working fluid), ~100% of the produced fluid is injected. Injection occurs at two locations; approximately 1.5 km north and south of the production wells.

Boseley et al. (2010) and Chambefort et al. (2016) described the conceptual hydrologic model for the Ngatamariki field and a summary is provided here (Figure 1.4). The highest measured temperatures (285°C) and upflow area for the field are interpreted to occur between wells NM7 and NM2, but a lack of drilling means the high-temperature upflow could extend east and west of these wells. Fluid outflows to the south, as demonstrated by the ~30 – 40°C cooler reservoir temperatures in the southernmost wells (NM6 and NM10). The deep reservoir is predominantly liquid-dominated (i.e. temperatures were below the boiling point in the natural state), but a small zone of boiling and two-phase (steam + liquid) fluid existed in the natural state around the NM2 and NM3 wells in the north of the field. Wells NM4 and NM8 in the north of the field encountered particularly low-permeability, manifest as low injectivity (< 1 t/h.bar) and conductive temperature profiles (linear with depth) in the natural state in NM4 and NM8 (Figure 1.3).

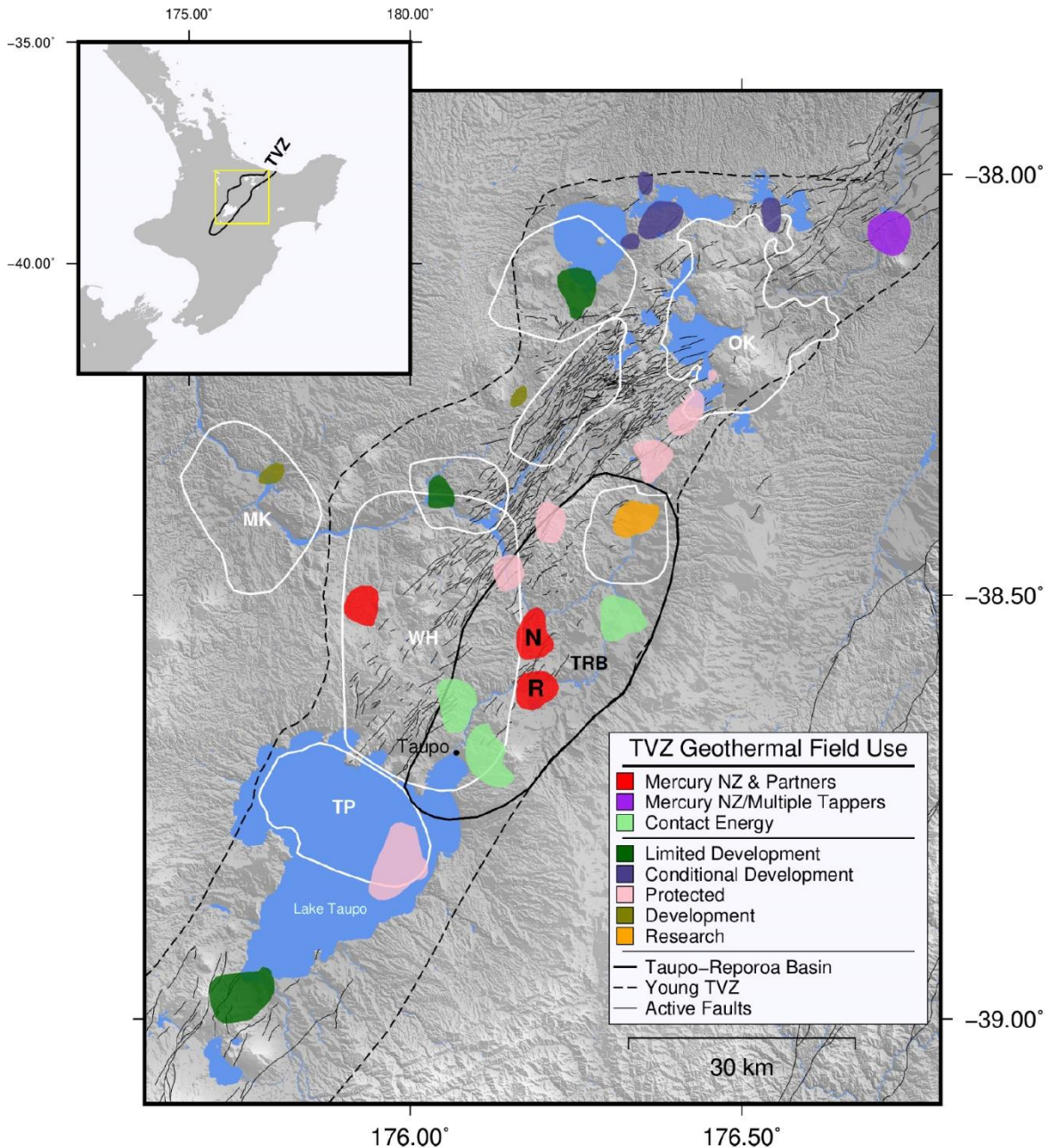


Figure 1.1. Location of the Rotokawa (R), Ngatamariki (N) and other high temperature geothermal fields in the Taupō Volcanic Zone (TVZ). The black dashed line shows the boundary of the young TVZ, as defined by Wilson et al. (1995). White outlines show the location of rhyolitic calderas as interpreted by (Wilson et al., 1995) (WH-Whakamaru Caldera, TP-Taupō Caldera, OK-Okataina, MK-Mangakino). The Taupō-Reporoa Basin (TRB), within which Ngatamariki and Rotokawa are located, is outlined in thick black after Downs et al. (2014). After Hopp (2019).

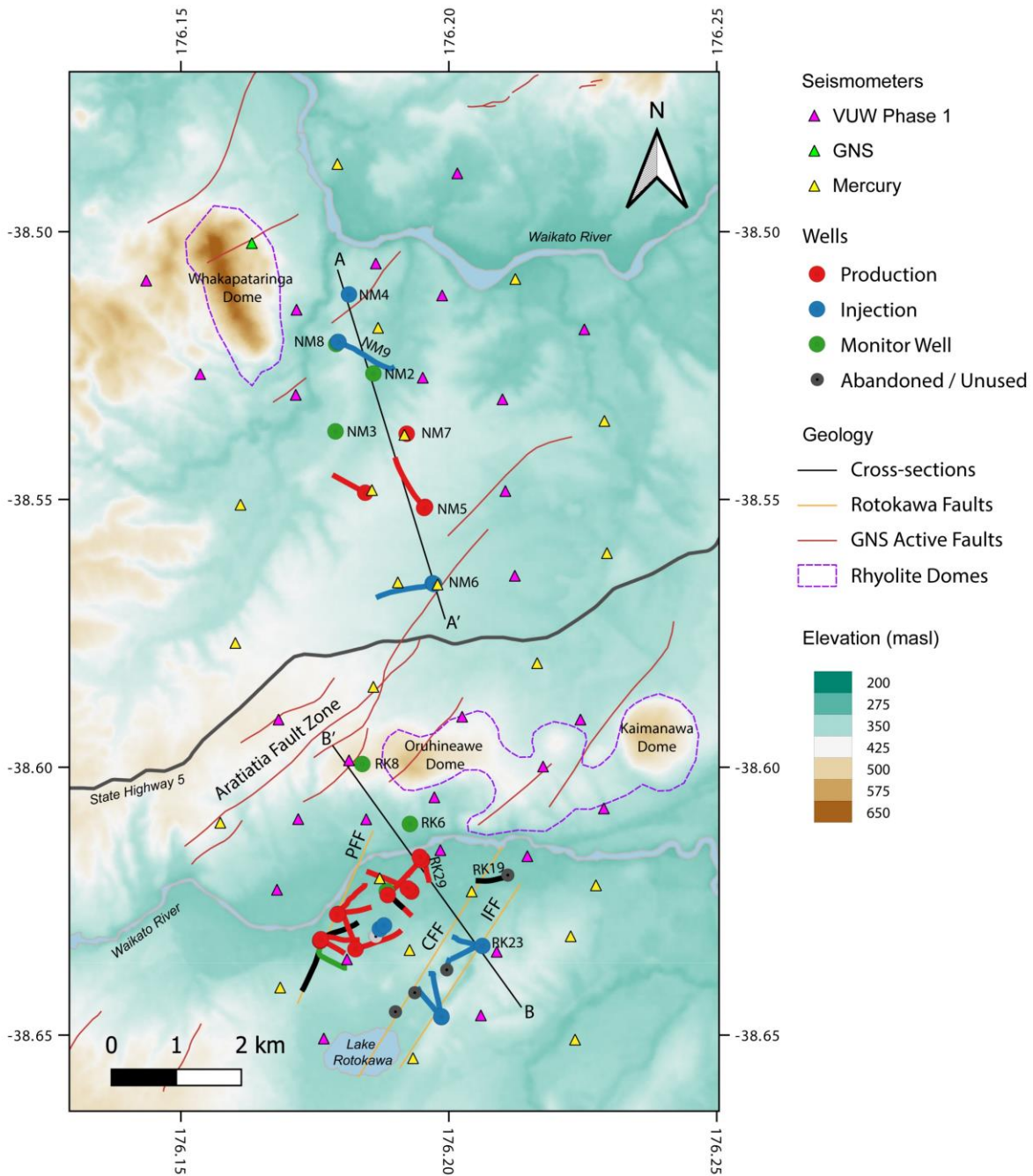


Figure 1.2. Location of wells at Rotokawa and Ngatamariki. Black lines (A – A’ and B – B’) show the location of the conceptual model cross-sections shown in Figure 1.4 for Ngatamariki and Figure 1.5 for Rotokawa respectively. Known faults from the GNS Science active faults database (Langridge et al., 2016) and from stratigraphic offset between the wells as described by McNamara et al. (2016) are also shown. Seismometers used in this study are shown as triangles —yellow = seismometers owned by Mercury Energy, green = seismometers owned by GNS Science, pink = seismometers deployed in Phase 1 of the 2017 – 18 expanded array deployment.

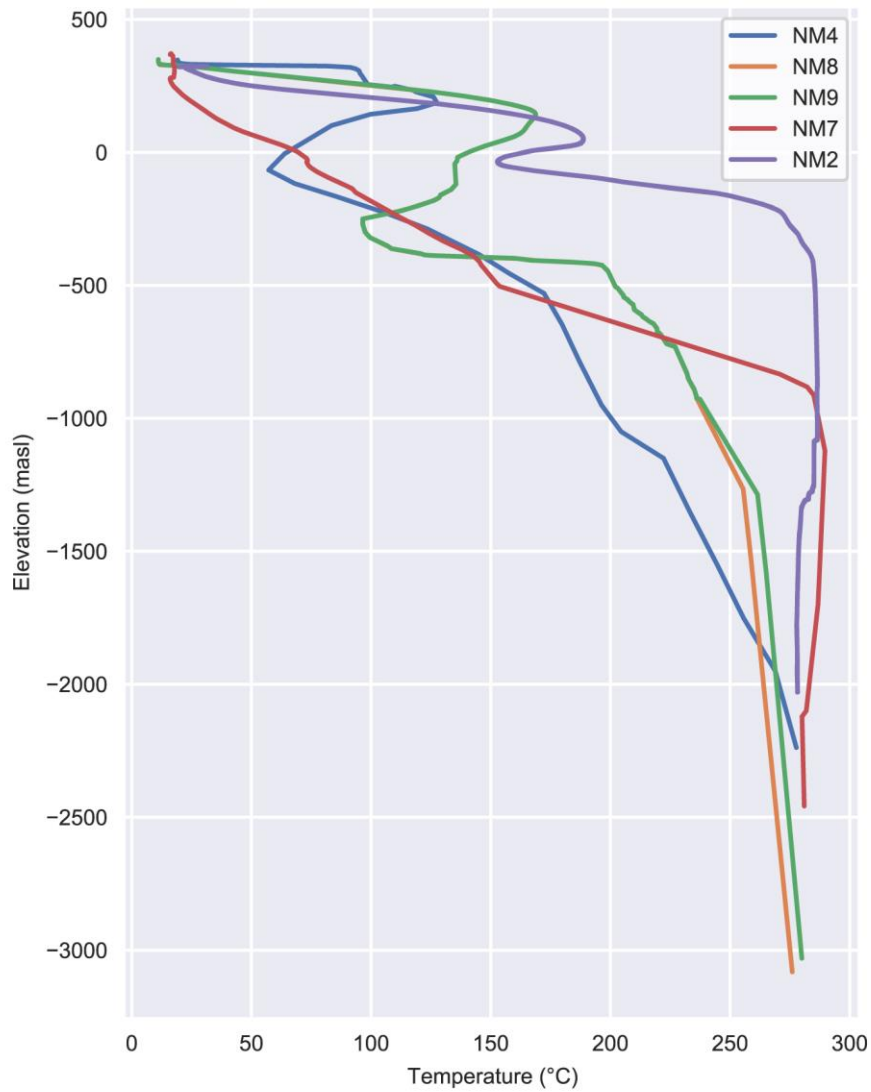


Figure 1.3. Natural state temperatures for selected wells in the Ngatamariki field. NM4, NM8 and NM9 in the north of the field have conductive temperature profiles between -500 to -2500 masl (linear increase in temperature with depth) indicating a lack of vertical permeability in this part of the field. NM2 and NM7 have convective, near-isothermal, temperature profiles over the same elevation interval, indicating sufficient vertical permeability for convection to take place.

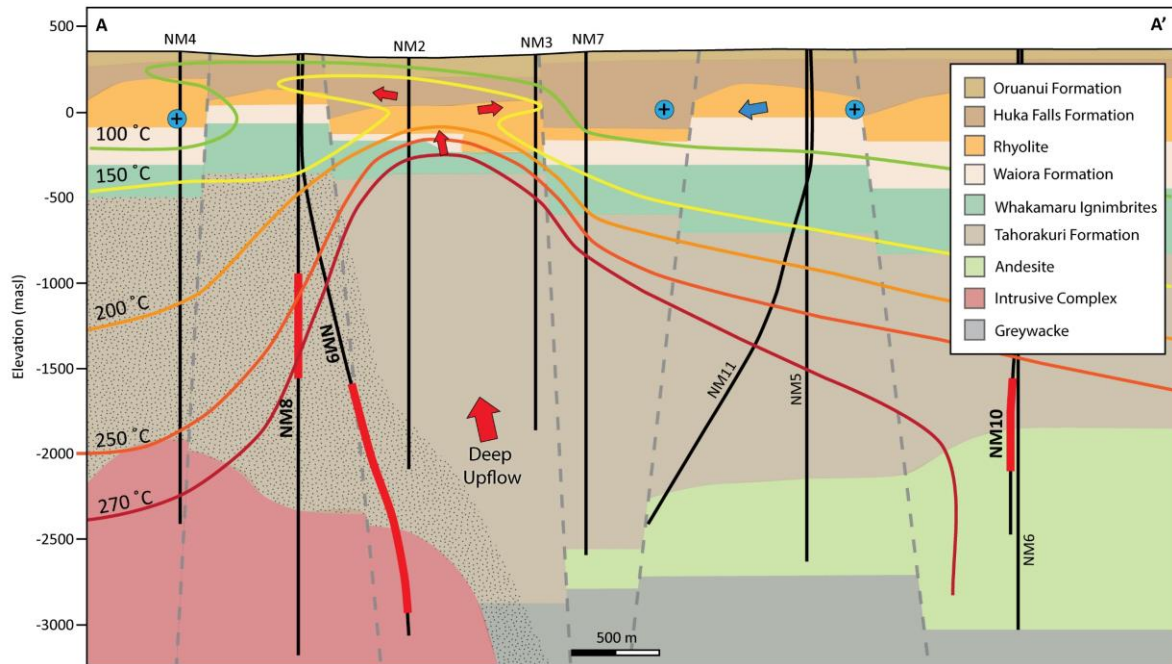


Figure 1.4. Conceptual model cross-section of the Ngatamariki field. Red arrows indicate the movement of geothermal fluids, blue arrows and circles with plus signs (indicating flow into the cross-section) indicate the movement of cold, meteoric fluids. The red lines on the well tracks (black lines) show the geophysically logged sections of NM8, NM9 and NM10. The stippled Tahorakuri Formation indicates the interpreted extent of magmatic alteration (phyllitic, advanced argillic and potassic) that was produced by the intrusion complex in the north of the field. Adapted from Boseley et al. (2010); Chambefort et al. (2016b). See Figure 1.2 for location of cross-section.

This has been interpreted as due to the presence of an intrusion and its alteration halo in the north of the field (Chambefort et al., 2016). A low vertical permeability “clay-cap” overlies the deep reservoir and is characterised by smectite and smectite-illite alteration and conductive temperature profiles, similar to that observed in most geothermal systems around the world (e.g. Cumming, 2016). Above the deep clay cap lies an intermediate aquifer system, hosted mainly in rhyolite lavas. Permeable connection between the intermediate aquifer and deep reservoir occurs between NM2 and NM3. Fluid therefore rises and boils from the reservoir into the intermediate aquifer in this area. Geothermal fluid mixes with cooler groundwaters within this zone and flows beneath a shallow clay cap discharging at thermal areas.

The conceptual hydrologic model for the Rotokawa field is described in detail in McNamara et al. (2016) and Sewell et al. (2015) and a summary is provided here (Figure 1.5). The highest measured temperatures (340°C) and upflow for the field are in the south where fluid is currently injected. Fluid outflows to the north and north-west as demonstrated by progressively cooler reservoir temperatures (~300°C) and geochemical gradients. In contrast to Ngatamariki, the Rotokawa field is a ‘2-phase’ reservoir with a thick zone at the top of the reservoir where temperatures are at the boiling point and both steam and liquid coexist (Hernandez et al., 2015). Wells RK8 in the north and RK19 in the northeast both have low permeability and conductive temperature profiles, indicating the extent of the deep reservoir in these areas. As at Ngatamariki, an intermediate aquifer of mixed groundwater and geothermal fluid overlies the deep reservoir. Both deep and shallow low permeability smectite and smectite-illite clay cap overly the deep reservoir and intermediate aquifer respectively. Fluid flows from the deep reservoir and intermediate aquifer occurs through permeable connections mostly along the Central Field Fault where boiling-point-for-depth temperatures occur between the production and injection wells in the south of the field.

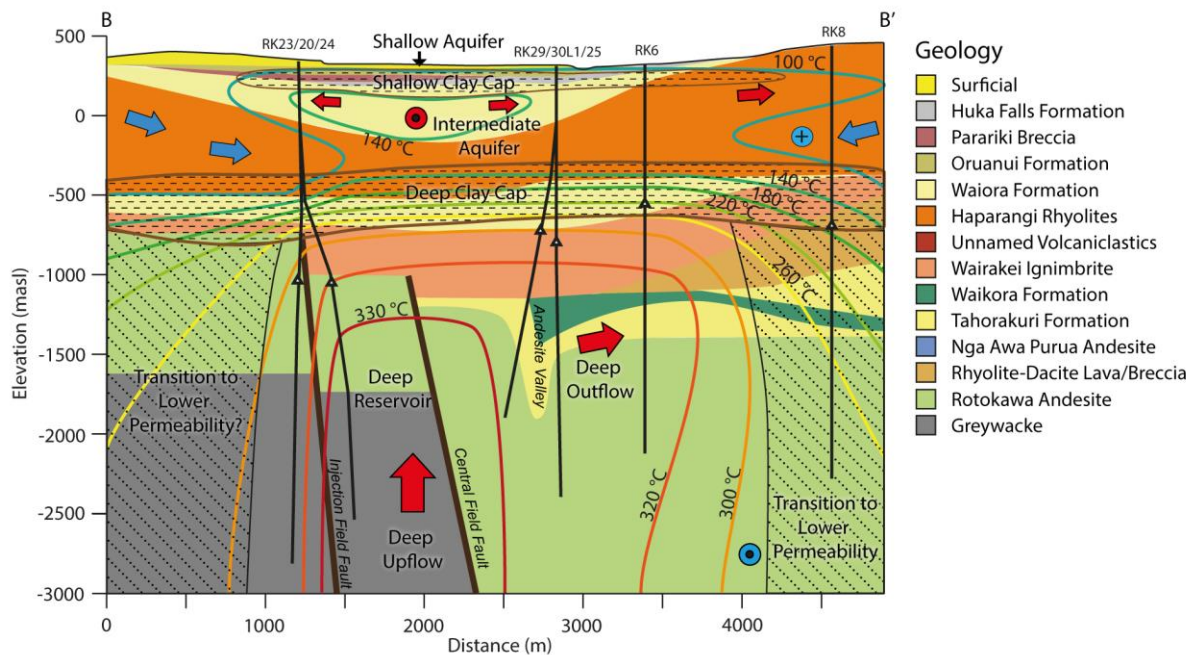


Figure 1.5. Conceptual model cross-section for Rotokawa. After Sewell et al. (2015). See Figure 1.2 for location of cross-section. Red and blue arrows and circles indicate the direction of hot and cold fluids respectively. Circles with dots indicate flow out of the cross-section whilst circles with plus signs indicate flow into the cross-section. Wairakei Ignimbrite = Whakamaru Ignimbrite.

1.4.1 Geologic Setting

The Rotokawa and Ngatamariki geothermal fields are located within the central Taupō Volcanic Zone (TVZ) on the eastern margin of the TVZ rift (Figure 1.1). The TVZ is a NNE-SSW oriented zone of active back-arc rifting and is one of the world's most productive areas of silicic volcanism (Wilson et al., 1995; Wilson & Rowland, 2016). Rifting and consequent andesitic-volcanism began around 2 Ma which later became rhyolitic-dominated from around 1.6 Ma (Wilson et al., 1995; Wilson and Rowland, 2016). Eight rhyolitic eruption centres and 34 inferred caldera-forming ignimbrite eruptions have been identified in the central TVZ (Wilson et al., 1995).

The central TVZ, within which the Rotokawa and Ngatamariki fields are located, is dominated by rhyolitic volcanism (Wilson and Rowland, 2016). The fields are also within the Taupo-Reporoa basin, a Quaternary-aged zone of particularly high extensional-tectonism and rhyolitic volcanism which is thought to be an important factor in producing the faults and fracturing within the geothermal fields (Downs et al., 2014). Faults and fractures that have been identified within the two fields via surface mapping, stratigraphic offset in boreholes, microseismic activity and borehole image logging strike predominantly NE-SW, similar to the overall structural grain of the TVZ (Chambefort et al., 2016; Hopp, 2019; McNamara et al., 2016; Mroczek et al., 2019).

The surface geology at both fields consists mostly of young pyroclastic material (unconsolidated tephra consisting of pumice and andesite, greywacke and rhyolite lithics) and reworked volcanoclastic sediments (Chambefort et al., 2016; McNamara et al., 2016). Two areas of outcropping rhyolite domes occur in north western Ngatamariki (Whakapapataringa) and between Ngatamariki and Rotokawa (Oruhineawe and Kaimanawa) which form local topographic highs (Figure 1.2). The Oruhineawe rhyolites at Rotokawa have been shown to be relatively young, forming approximately 100 ka (Milicich et al., 2020). The area around Lake Rotokawa is covered by hydrothermal eruption breccias formed from repeated hydrothermal eruptions over the past ~20,000 years extending along the NE-SW-oriented Central Field Fault (Browne & Lawless, 2001; McNamara et al., 2016; Sewell et al., 2015).

Drilling within the two fields has provided good constraints on the geology from surface to approximately 3 km bsl. The upper 1 km of the fields consists mostly of surficial deposits (loosely compacted pumice and sediments), the Huka Falls Formation (lacustrine mudstones,

siltstones and sandstones), rhyolites, the Waiora Formation (volcaniclastic sediments) and the Whakamaru group ignimbrite (also known as the Wairakei Ignimbrite) (Figure 1.4 and Figure 1.5). Below the Whakamaru Ignimbrite is the Tahorakuri Formation, which consists mostly of interlayered tuffs and volcaniclastic sediments with minor intervals of ignimbrites, rhyolites and basaltic to andesitic lavas, dykes and breccias. The Tahorakuri Formation lies between approximately 1 and 2 km bsl at Ngatamariki and is the main formation hosting the geothermal reservoir. The Tahorakuri Formation at Rotokawa is considerably thinner and is absent in many wells. Below the Tahorakuri Formation in the south of the Ngatamariki field, and throughout Rotokawa, is a sequence of andesitic lavas and breccias. Permeable zones for production wells at Rotokawa mostly occur in these andesite layers which are at least 1.5 km thick in the production area. Beneath the andesite is Mesozoic-aged greywacke which is the basement rock of the TVZ (Chambefort et al., 2014; McNamara et al., 2016; Wilson and Rowland, 2016). This has been intersected in one well in the south of the Ngatamariki field at 3 km bsl in NM6 and is the main injection formation at Rotokawa where it is intersected at ~1.5-2 km bsl. The greywacke is offset vertically by at least 500 m across the Central Field Fault in the Rotokawa field, indicating this is a major structure within the field (McNamara et al., 2016; Sewell et al., 2015).

Alteration at both fields is mostly typical of geothermal systems in New Zealand and worldwide (Browne, 1978; Stimac et al., 2015). Alteration above 1 km bsl is heterogenous but mostly consists of argillic (characterised by smectite) and advanced argillic alteration (characterised by kaolinite, alunite, dickite) (Chambefort et al., 2016; McNamara et al., 2016). The upper 1 km has zones of relatively high smectite clay, particularly within the hydrothermally altered Huka Falls formation and in the southern part of the Tahorakuri Formation of the Ngatamariki field (Boseley et al., 2010; Chambefort et al., 2016; Sewell et al., 2015). Areas of near-boiling-point-for-depth temperatures in the upper 1 km occur at both fields where high vertical permeability allows fluid to flow from the deep reservoir into overlying aquifers and to the surface (Boseley et al., 2010; Sewell et al., 2015). Consequently, the alteration mineralogy in these areas reflects the prevailing subsurface temperatures (i.e. illite-smectite, illite and chlorite clays are formed and smectite is absent). Transitional alteration (characterised by mixed layer illite-smectite) is common between approximately 500 – 1000 mbsl in both fields, directly overlying the reservoir. The transitional alteration grades into propylitic (characterised by illite, chlorite and epidote) within the reservoirs where temperatures exceed ~240°C for most of the fields.

A distinctive feature of the Ngatamariki field is the intrusion complex (diorite to tonalite in composition) and its associated magmatic-hydrothermal alteration halo that has been intersected in three of the wells in the north of the field (Arehart et al., 2002; Chambefort et al., 2017; Christenson et al., 1997). This is the only young intrusion that has been drilled within the TVZ to date. Age dating shows this intruded into the Tahorakuri Formation at ~0.65 – 0.71 Mya, before the Whakamaru Group ignimbrites, and provided a heat source for the geothermal system operating during this time (Chambefort et al., 2014). Alteration within the Tahorakuri Formation above the intrusion reflects this magmatic phase ranging from potassic (biotite + magnetite ± K-feldspar) to advanced argillic (pyrophyllite ± minor andalusite ± topaz ± anhydrite ± rare alumino-phosphates (AP) and fluorine-bearing minerals) and phyllic (quartz + muscovite + pyrite) assemblages (Chambefort et al., 2017). Phyllic alteration is the most wide-spread of the alteration types and is typified by intense silicification, white mica and pyrite (Chambefort et al., 2017). This earlier phase of alteration formed between ~0.71 and 0.33 Mya based on a lack of magmatic alteration observed in the Whakamaru Group ignimbrites in the northern Ngatamariki wells (Arehart et al., 2002; Chambefort et al., 2017).

1.4.2 Seismic Activity at Rotokawa and Ngatamariki

A microseismic monitoring array of 10 seismometers has been operating at Rotokawa since mid-2008. GNS Science maintains and services the network on an approximately three monthly-basis and performs earthquake location analysis for Mercury Energy. From 2008 to late-2012, the analysis was based on manual picking and hypoDD relocation for only the Rotokawa area (Figure 1.6). Beyond late-2012, the analysis has been based on automated picking and combines both the Ngatamariki and Rotokawa seismometers into one array. Detected event magnitudes at Rotokawa are mostly between 0.5 and magnitude 2 (Sherburn et al., 2015).

Sewell et al. (2015) and Sherburn et al. (2015) described how the seismic monitoring has been used to inform how injection fluids flow within the Rotokawa reservoir. Prior to October 2008, seismic activity recorded during injection into RK16 in the northwest of the Rotokawa field indicated the presence of a NW-SE fault that connected injection to production wells operating at the time in the centre of the field (Sewell et al., 2015). Tracer testing confirmed the fault provided a conduit for relatively rapid return of injection back to production wells (Addison et al., 2015). Therefore, in order to mitigate the risk of prematurely cooling production wells, injection was shifted to the southeast of the field (RK20) in October, 2008. A step-change in

the injection rate, and consequent increase in the seismicity rate, was observed in 2010 with the start of the NAP power plant (Sherburn et al., 2015). The majority of the seismicity since 2010 is located on the injection-side of a major fault in the field, the Central Field Fault (Sewell et al., 2015; Sherburn et al., 2015). This pattern was used to infer that the fault is acting to slow the flow of injection fluids back to the production wells, which is further supported by tracer testing (Winick et al., 2015). Swarm-like microseismic activity and the larger magnitude events are mostly along the Central Field Fault (Sewell et al., 2015).

A microseismic monitoring network has operated at Ngatamariki since 2012 that consists of nine surface seismometers (4.5 Hz 3C geophones and Nanometrics Taurus recorders with 200 Hz sampling rates) and three downhole seismometers (NS12, NS13 and NS14) installed at between 300-514m depth in groundwater monitoring wells on the NM7, NM12 and NM6 well pads (Figure 1.6). The downhole instruments on the NM7 pad (NS12) and NM12 pad are at 514 m and 350 m depth respectively and are both 15 Hz, high-temperature seismometers from IESE (Model F41-15.0). The downhole seismometer on the NM6 pad (NS14) is at 202 m depth and is a 4.5 Hz slim-hole seismometer from IESE (Model F50-4.5). The downhole instruments all use Nanometrics Taurus recorders with sampling rates of 100 Hz. GNS Science services the Ngatamariki network as well with analysis from the commencement of the network in May 2012 through to September 2014 using manually picked arrivals and hypoDD for only the Ngatamariki stations (Figure 1.6). Beyond September 2014 arrival times have been automatically picked incorporating the seismometers at both Rotokawa and Ngatamariki.

Two distinct clusters of seismicity occur at Ngatamariki located around the injection wells in the north (NM8 and NM9) and the south (NM10 and NM6) of the field. The southern area is more seismically active than the north and also has larger magnitude events (Hopp 2019). Activity in the south was observed to form a NE-SW trend between the NM10 injection well and NM5 production well, both during drilling of the NM10 well and shortly after injection in the field commenced (Figure 1.6) (Buscarlet et al., 2015; Hopp et al., 2016). Tracer testing in the field has shown that this fault provides a conduit along which injection fluids travel quickly from NM10 to the NM5 well (Buscarlet et al., 2015).

Hopp (2019) analysed the seismicity at both fields between 2012 and 2015, and found similar seismicity patterns to previous studies for both fields, but with more detailed definition of structural features. Hopp (2019) also found that the stress state is unusual (no principal stress is vertical) in the north of the Ngatamariki field using focal mechanisms from selected events

in each of the three seismicity clusters. This was thought to be related to the presence of the intrusion in the north of the field. Of the three seismicity clusters, Rotokawa has been the most active, followed by southern Ngatamariki then northern Ngatamariki both in terms of the number of events and the magnitudes of those events (Hopp, 2019).

Civilini et al. (2016) used the seismic data from a temporary array across Ngatamariki to derive shear-wave velocities in the upper 200 m at both fields using the refraction microtremor (ReMi) method. They found a spatial correlation of changing velocity structure across the Aratiatia fault zone in the south of Ngatamariki. Mroczek et al. (2019) performed a shear-wave splitting analysis using the same dataset. They found that the fast polarizations mostly align with the TVZ NE-SW structural trend with more complexity in these directions than was observed at Rotokawa. They also found changes in shear-wave anisotropy and V_p/V_s ratios as injection was shifted more to the north of the Ngatamariki field. This was related to the opening and closing of microcracks in response to the changes in pore fluid pressures.

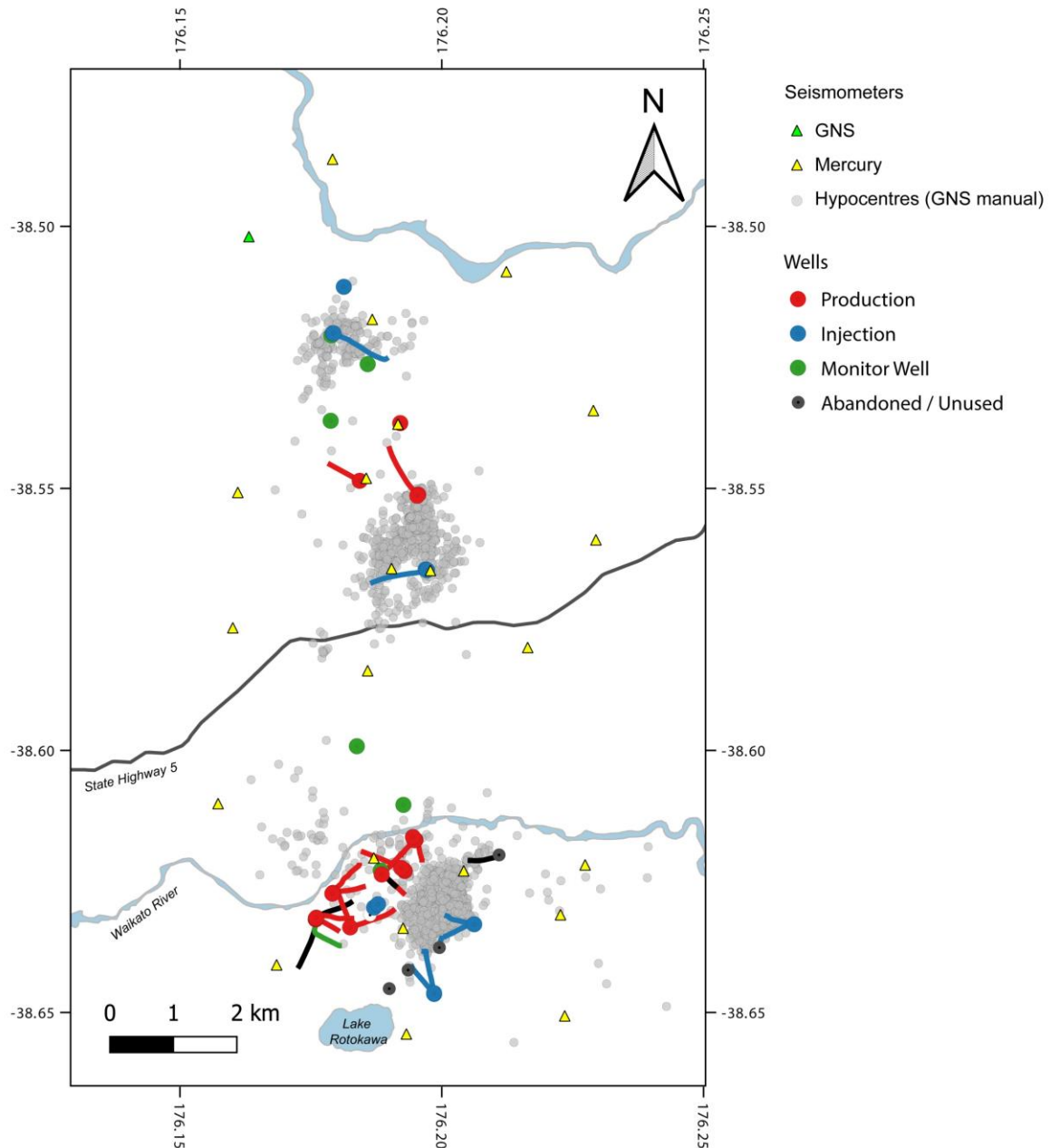


Figure 1.6. Location of microseismic events for Rotokawa (Jan, 2010 to Aug, 2012) and Ngatamariki (May, 2012 to September, 2014) from manual picking and location using hypoDD by GNS Science.

1.5 Thesis Content

Following this introductory chapter, Chapter 2 provides an overview of the data and methods used in the thesis. Chapter 3 presents the analysis of the well logging dataset facilitated by geochemical and mineralogical analysis of drill cuttings over the logged intervals. The chapter utilised the seismic velocity and other geophysical measurements from existing well logging data in three wells at Ngatamariki acquired by Schlumberger under contract to Mercury Energy

and newly acquired portable XRF, XRD and automated mineralogy scans for this PhD to develop an understanding of the rock properties influencing seismic velocity in the Ngatamariki field. Sample preparation for the portable XRF, XRD and automated mineralogy scanning was largely performed by the author with some assistance/guidance from Victoria University staff, Dr Michael Gazley and Dr Mark Simpson. The automated mineralogy scanning was performed by CSIRO in Perth and the data from the scans was processed to mineralogy images and abundances by Dr Michael Gazley. The analysis and interpretation of the pXRF, XRD and automated mineralogy scans was mostly undertaken by the author with assistance from Dr Michael Gazley and Dr Mark Simpson.

Chapters 4 and 5 present the seismic tomography analysis performed on the expanded array dataset acquired during 2017-2018. Details of the instrumentation used in the expanded array can be found in Appendix A.1. The field deployment and servicing of the 2017-18 expanded seismic array was led by the author with assistance from Adrian Benson, Chet Hopp, Kenny Graham and Stefan Mroczek. Adrian Benson wrote a code to correct for timing errors that occurred for most of the ANSIR seismic recorders. The data processing, including both automated event detection and location and manual picking, was conducted by the author. The author developed an automated event detection and location python-based processing workflow for this purpose built using the Obspy framework (Beyreuther et al., 2010), NonLinLoc (Lomax et al., 2000) and hypoDD/hypoDDpy (Krischer, 2015; Waldhauser and Ellsworth, 2000), automated P-picking of Chen and Holland (2016) and a novel automated S-wave picking approach developed by the author. The automated processing workflow is detailed in Appendix A.2. Chapter 4 covers a Monte-Carlo-style 1D inversion whereby 1000 starting 1D models were trialled to determine a 'best-fitting' 1D model using the program VELEST (Kissling, 1995). This provided a robust 1D starting model for subsequent 3D inversion, and an initial assessment of the spatial variations in velocity around the field via the station correction terms produced by the inversion. Chapter 5 details the 3D inversion of the expanded array dataset using the program tomoDD (Zhang, 2003). Solution robustness and resolution were assessed as well in this chapter via ray path coverage assessment and synthetic tests. All of the tomographic inversions and synthetic testing was performed by the author using VELEST and tomoDD. Chapter 6 provides a synthesis of the results and discusses future directions for the application of seismic tomography in geothermal fields.

Chapters 3, 4 and 5 were written with the intent of publication and are therefore written in the style of scientific journal articles. There is therefore some overlap in these chapters with Chapter 2, the data and methods section.

2 Data and Methods

2.1 Data

This thesis utilised both existing data acquired mostly by Mercury Energy for the purposes of the exploration and development of the Ngatamariki and Rotokawa fields and data acquired specifically for this thesis. Data acquired for this thesis falls into two categories; data acquired for investigating what factors control seismic velocities (as measured in 3 wells at Ngatamariki) and data acquired for seismic velocity imaging of the subsurface. Data acquired for the seismic velocity investigation included portable XRF (pXRF), XRD and automated mineralogy measurements made on drill cuttings. Data for the seismic velocity imaging were from both existing seismometers owned by Mercury Energy and GNS Science and an additional 30 seismometers obtained from ANSIR (Australian National Seismic Imaging Resource) and deployed across the two geothermal fields over 2017 and 2018 specifically for this thesis. The following chapter describes these datasets and the methodologies used.

2.1.1 Geophysical Logging

Geophysical or wireline logging data is obtained by lowering instruments down a well and taking measurements that allow the physical properties of the rocks to be determined. These commonly include measurements of rock electrical resistivity, density, gamma radiation, neutron porosity, self-potential and seismic (or sonic) velocities. Geophysical logging is commonplace in oil and gas fields and is widely used to assess reservoir properties and determine the size and extent of reservoirs. It has been much less common in geothermal fields for a number of reasons (e.g. temperature limitations of the instruments, lack of understanding of how the measurements relate to formation properties and less direct correlation to reservoir parameters than in the case of oil and gas). There is therefore a scarcity of wireline logging datasets that can be used to understand what factors in geothermal reservoirs influence geophysical properties.

Chapter 3 of this thesis makes use of one of the few published wireline logging datasets acquired in high temperature geothermal reservoirs (Wallis et al., 2012). The dataset consists of a suite of geophysical logs that generally included seismic velocity, gamma, neutron porosity, resistivity, self-potential, density and formation imaging (FMI) acquired in three

wells (NM8, NM9 and NM10) during the development drilling campaign at Ngatamariki between depths of -800 to -3000 masl (Wallis et al., 2012). These measurements were made at high depth resolution (< 1 m) throughout the logged section of each well and therefore provide dense sampling of the in-situ physical properties of the rock. Full waveform sonic logs were acquired in NM8 and NM10 and hence both compressional (V_p) and shear (V_s) seismic velocity measurements are available for these wells. A borehole compensated sonic log was acquired in NM9 and hence there are no V_s measurements for this well.

Together, the logs cover the main reservoir hosting lithologies and alteration types found at Ngatamariki (Figure 1.4). NM8 and NM9 are located in the north of the Ngatamariki field and span the Tahorakuri Formation and diorite-tonalite intrusion whilst NM10 is in the south of the field covers the Tahorakuri Formation and andesite. Previous work on the field has shown that the intrusion in the north of the field caused alteration of the rock mineralogy that is very different from that in the south of the field (Chapter 1, Chambefort et al., 2017). Hence the wireline logging dataset provides a unique opportunity to assess the rock property changes that occur above intrusions in geothermal fields.

A checkshot survey was performed in NM9 between 55 and 2045 m measured depth (-0.3 to 1.7 km bsl) within the 13 5/8" cased hole section (Dahlhaus, 2013). Two air guns in a 3m deep pit filled with water were used as the seismic source. Downhole receivers consisted of two, 3-component downhole seismometers. A hydraulic clamping arm was used to push the downhole seismometers against the casing to obtain the best possible signal-to-noise. Shot-receiver spacing was varied depending on the geology, but averaged between 20-40 m vertical depth.

High quality P wave arrivals (picking accuracy ± 1 ms) were obtained for most of the survey below 275 m depth (0.75 km bsl). Above this depth, multiple casing strings resulted in 'casing ring' and so the error in arrival time picks was consequently greater (± 5 ms) above 275 m depth.

P-wave velocities from the checkshot show a general increase with depth, but with high variability (Figure 2.1). The most prominent velocity feature is a very high velocity (up to ~ 6 km/s) layer at ~ 0.2 - 0.5 km bsl which is associated with a highly welded and weakly altered portion of the Wairakei Ignimbrite. A clear change in the waveform data was apparent within and below this layer, showing that multiple reflections occurred within this unit with consequent loss of transmitted seismic energy through the layer (Dahlhaus, 2013). High

velocities (up to ~5 km/s) were also measured between ~1.2 to 1.7 km bsl within the Tahorakuri Formation; these high velocities don't appear to be associated with a particular lithology.

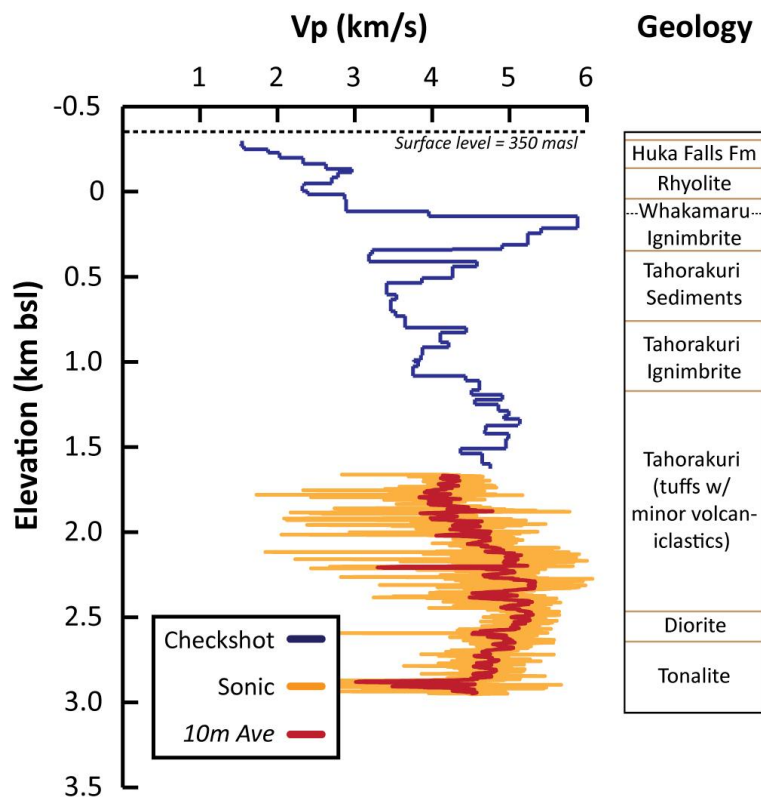


Figure 2.1. Measured velocities from NM9. The blue line shows the checkshot interval velocity (velocity between two shot-receiver depth points). The orange line shows the sonic log velocity at full 0.15 m depth resolution. The red line shows the sliding average velocity over approximately 10 m depth intervals from the sonic log. A simplified, geologic log for the well modified from Lewis et al., 2013 is shown on the right. The dashed line within the Whakamaru Ignimbrite shows the location of the transition between partially welded (above) and strongly welded (below).

2.1.2 Rock Geochemistry and Mineralogy

Rock geochemistry and mineralogy in geothermal fields is controlled both by the primary mineralogy of the rock when it was formed and the alteration of the rock by chemical reactions between the geothermal fluids and rock (e.g. Browne, 1978). Seismic velocity, and other geophysical properties such as density and resistivity, often vary with lithology and alteration, mostly due to changes in the porosity.

Rock cuttings, the small chips of rock that are excavated during drilling, are routinely collected, typically at <5 m intervals, during the drilling of a geothermal well and are the basis of the geological analysis performed (e.g. identification of rock and alteration types). In order to gain a more detailed assessment of the relative effects of lithology and alteration on seismic velocity, geochemistry and mineralogy data were acquired for the drill cuttings samples over the geophysically logged intervals of the three wells at Ngatamariki (NM8, NM9 and NM10). This included detailed geochemistry analyses via portable XRF (pXRF) for every sample available (every 5m depth interval) and selected automated mineralogy (TIMA) and quantitative XRD analyses. Together the wireline logging data and cuttings geochemistry and mineralogy data allow a more detailed and quantitative assessment of the factors controlling seismic velocity than would normally be obtained via routine geological analysis of the cuttings or by making measurements on sparse rock cores that typically span only a very small interval (<2 m).

2.1.3 Seismic Data

As described in Section 1.4.2, a seismic monitoring network consisting of 20, mostly 4.5 Hz, surface seismometers has been operating across the Rotokawa and Ngatamariki area since 2012 (Figure 2.2). This network is owned by Mercury Energy and is operated for them by GNS Science. To improve the spatial resolution of velocity variations across the fields for the tomography work in this thesis, a further 30 instruments were deployed across the two fields from April, 2017 to May, 2018 (Figure 2.2 and Figure 2.3). The instruments were provided by the Australian National Seismic Imaging Resource (ANSIR) with funding for the field work and data collection provided by Mercury Energy. Appendix A.1 provides full details of the instrument types and recorders for the entire seismic network used in this thesis.

The 30 additional instruments were spread evenly across the two fields within the area of the existing Mercury array for the first 7 months of recording (Figure 2.2 and Figure 2.3). Eight of the instruments were relocated to stations approximately 2-5 km around the initial deployment area for the final ~5 months of recording. This was done to improve ray path coverage outside the two geothermal fields.

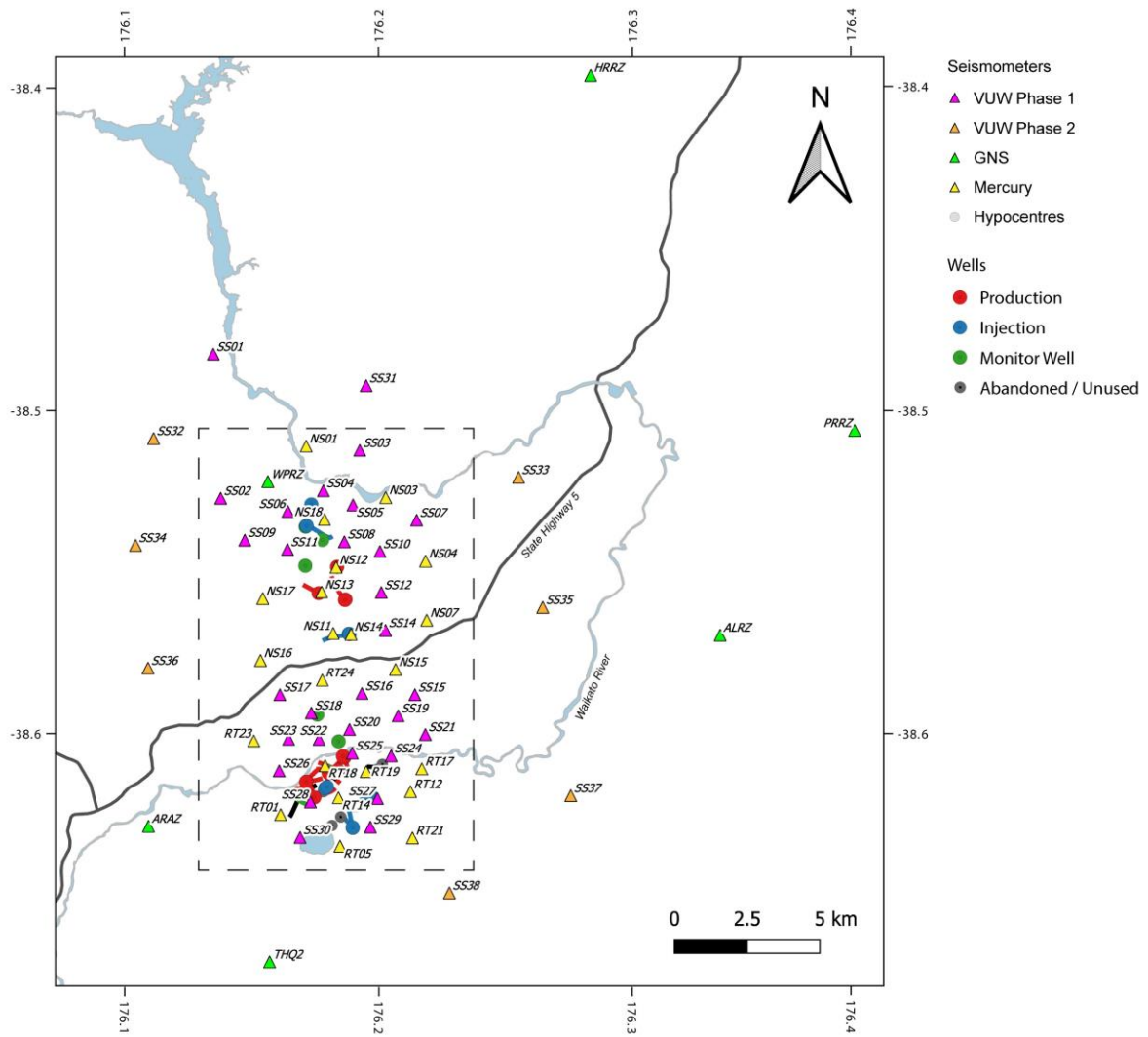


Figure 2.2. Seismometer locations for the 2017-2018 expanded array. The dashed box shows the location of the map in Figure 2.3.

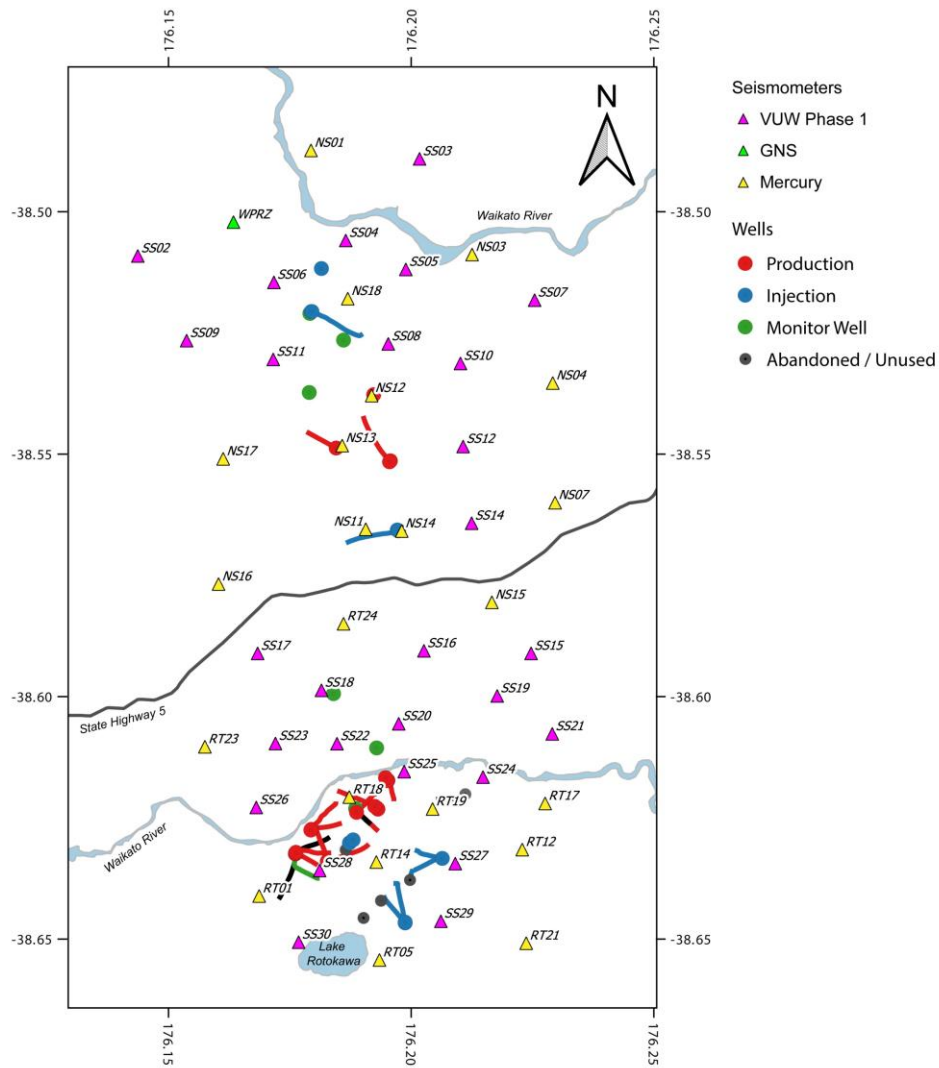


Figure 2.3. Zoomed-in view of the seismometer locations for the expanded array.

Data recovery for the expanded array stations was hampered by a number of issues including timing issues and recorder malfunctions that caused them to switch off in-between servicing trips (Figure 2.4). The timing issues were mostly resolved in post-processing using a python program developed by Adrian Benson at VUW, however data beyond 2018 was lost due to a timing problem that could not be resolved using the program. Due to this, and a number of stations shutting down not long after commencement of recording, there was little useable data for the stations that were moved in late-2017 to positions outside the geothermal fields.



Figure 2.4. Data continuity over the 2017-2018 period of the expanded array.

An automated processing method was developed based around the Obspy framework (Beyreuther et al., 2010) to detect and locate seismic events that occurred during the deployment (Figure 2.5, Appendix A.2). This method utilises the network detection algorithm of Obspy (Beyreuther et al., 2010) to detect events using the entire array, with events detected when 10 or more seismometers are triggered by STA/LTA automatic picks. Three different automatic P-wave picking algorithms were combined to obtain a P-wave pick. Two novel S-wave picking algorithms developed for this work by the author were combined to obtain an S-wave pick. Uncertainties of the automatic pickers were based on signal-to-noise ratio of the picking characteristic functions with the magnitude of uncertainty (time uncertainty before and after the pick) calibrated by comparison of the signal-to-noise of the characteristic functions to manually picked uncertainties. NonLinLoc was used to obtain locations at both the P-pick only

stage and using both the P and S picks. Several iterations of filtering events and picks (e.g. those with high residuals, events with azimuthal gap $> 180^\circ$, etc) were performed after each run of NonLinLoc. Differential catalog and cross-correlation data were obtained using hypoDDpy (Krischer, 2015), which utilises an Obspy function for cross-correlation derived differential times. The absolute locations from NonLinLoc were used as the starting hypocentres for running hypoDD and tomoDD. The program hypoDD was used to relocate hypocentres relative to each other.

In total, 1209 events were detected and located for the 2017-2018 expanded array deployment. These initial locations were then used to select 100 well-recorded events for manual picking of arrival times. Emphasis was placed on identifying and using particularly on well recorded events that occurred outside of the three main clusters of activity around the injection wells to maximise ray-path coverage (Figure 2.2). The manual picking procedure followed that of Diehl & Kissling (2009) and included picking of uncertainties (Figure 2.6). Of the 100 events manually reviewed, 87 were included in the final tomography dataset (as 23 were omitted as they were not well recorded and had high picking uncertainties). An additional 215 high-quality automatically picked events were added to the manually picked catalog. A more detailed description of the automated event location workflow and the catalog used for tomography can be found in Appendix A.2 and in Chapter 3 respectively.

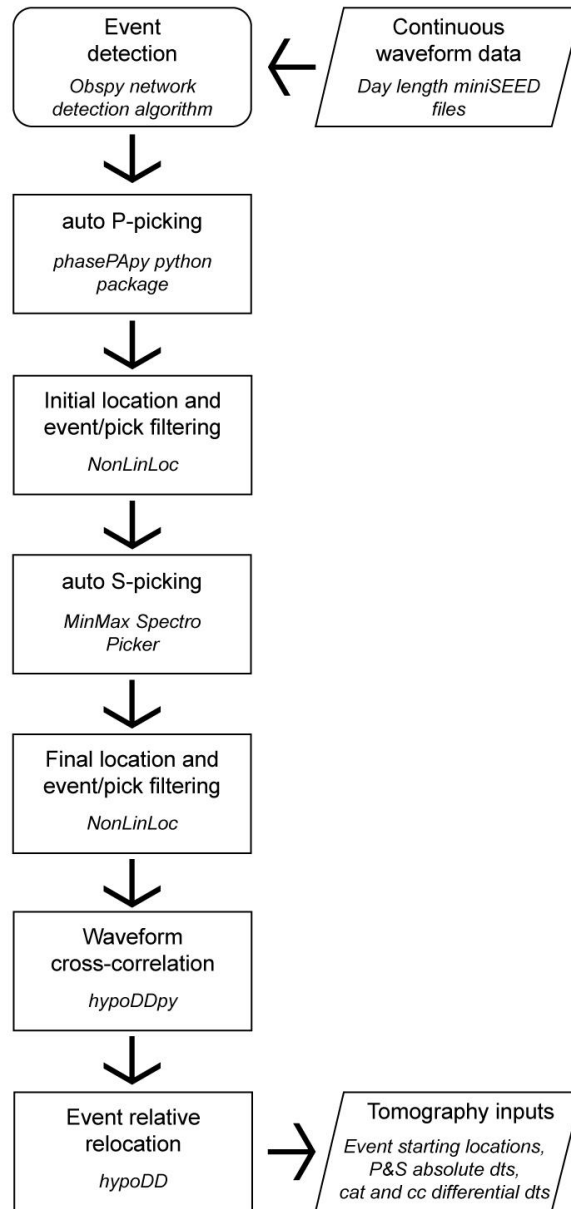


Figure 2.5. Automated data processing flow chart. Detail of the automated processing workflow is provided in Appendix A.2.

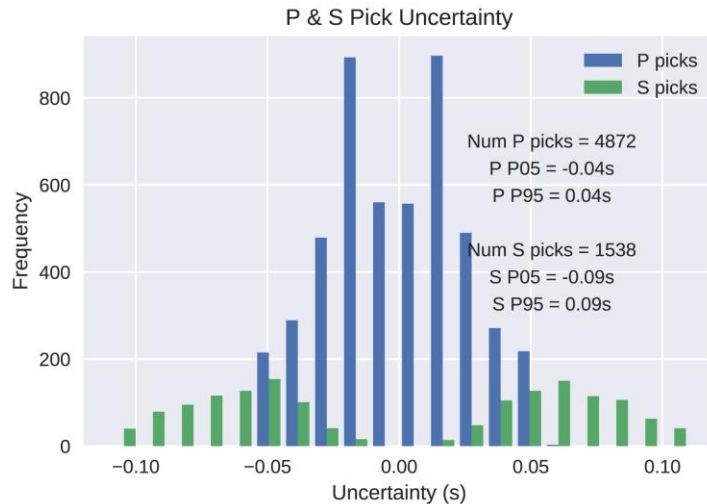


Figure 2.6. P and S pick uncertainties for the 100 events that were manually picked. Pick uncertainties were estimated manually following the procedure of Diehl and Kissling (2009). P05 and P95 are the 5th and 95th percentile for the uncertainty distributions (i.e. 90% of picks had uncertainty between P05 and P95).

The catalog of manually picked events resulted in more events at Rotokawa than in the other clusters of activity and therefore, in order to even out the event distribution and to provide better statistical sampling of arrival times from the three areas, 202 high quality (>10 P picks and >1 S pick with high SNR picks) automatically picked events were added to the manually picked events. The combined final catalog of events that was used for the tomography consisted of 302 events with 6778 P arrivals and 2436 S arrivals. Some examples of the automated and manual picks and their uncertainties are included in Appendix A.3. Starting locations for the 1D VELEST analysis were obtained using the NonLinLoc program (Lomax et al., 2000).

2.2 Methods

2.2.1 Combining rock geochemistry and mineralogy to interpret velocity measurements from wireline data

The interaction of geothermal fluids and gas cause changes in both geochemistry and mineralogy. The changes that occur are controlled by a number of factors including; temperature, fluid pH, fluid chemistry, geochemistry/mineralogy of the original rock and boiling (Browne, 1978). Due to the general increase in temperature with depth, different alteration minerals are formed with increasing depth, particularly clay minerals. Stimac et al. (2015) discuss the common alteration minerals and describe the common alteration zones that

typically form in geothermal systems (Figure 2.7). The shallowest alteration zone is termed the argillic zone, characterised by abundant smectite clay. The smectite clay zone forms a low-vertical-permeability seal over the geothermal reservoir that prevents overlying cooler waters from downflowing. The smectite clay in this zone has high cation exchange capacity and therefore has low electrical resistivity (Ussher et al., 2000). Magnetotelluric (MT) surveys, the main geophysical technique applied in the characterization of geothermal resources, images this clay zone and its geometry is used to interpret the hydrology and thermodynamics of the geothermal system (Cumming, 2016). A transitional zone is typically observed below the argillic zone that has mixed layer clays (illite-smectite) (Stimac et al., 2015). The reservoir zone of most volcanic geothermal systems is termed the propylitic zone, most commonly characterised by illite and/or chlorite clays and epidote (Browne, 1978). Advanced argillic alteration zones also commonly occur in geothermal systems wherever fluids are acidic (Reyes, 1990). This frequently occurs in the near-surface where H₂S gas can be oxidised to form acidic sulphate fluids. Low-pH fluids directly above magmatic intrusions can also form advanced argillic alteration (e.g. Heřmanská et al., 2019). The higher temperatures here form different minerals than near-surface advanced argillic alteration including dickite, pyrophyllite and andalusite (Chambefort et al., 2017). Potassic alteration, characterised by biotite, actinolite and garnet, can occur immediately adjacent magmatic intrusions (e.g. Muraoka et al., 1998).

Alteration processes cause changes in rock geochemistry as elements are added or removed from the primary minerals to secondary minerals. Table 2.1 provides a summary of the elements that are typically exchanged during geothermal alteration processes.

Certain rock elements are often considered to be immobile, that is they are not typically involved in fluid-rock chemical exchange (Mauriohooho et al., 2016; Simpson and Mauk, 2000). Elements that are usually considered immobile include zircon, titanium, yttrium and aluminium (Simpson et al., 2003). As these elements are not typically involved in fluid-rock interactions, they can be used to identify lithological changes. However, if fluid pH is very low, these elements may become mobile, as documented by Chambefort et al. (2017) for the Ngatamariki field.

In this study, geochemical data were obtained via portable XRF (pXRF) and mineralogical data obtained by quantitative XRD and automated mineralogy scanning (TIMA). Portable XRF operate via emitting x-rays which cause the electrons in elements to move to different energy states. As this occurs, electromagnetic energy is released. Each element has a characteristic

wavelength and the intensity of this characteristic wavelength is proportional to the abundance of that particular element within the sample. Further detail on pXRF is provided in Chapter 3.

APPROXIMATE TEMPERATURE STABILITY OF COMMON HYDROTHERMAL MINERALS													
T° C	100	120	140	160	180	200	220	240	260	280	300	320	340
	Smectite-Kaolinite				MLC-Chlorite			Propylitic			Propylitic ± Potassic		
	Argillic Zone				Transition Zone			Reservoir Zone			Intrusive Contact Zone		
Smectite	<-----	-----	-----	-----	-----	-----	-----	-----	-----	-----	-----	-----	-----
Illite-Smectite				-----	-----	-----	-----	-----	-----	-----	-----	-----	-----
Illite/Sericite						-sericite	-----	-----	-----	-----	-----	-----	-----
Mordenite	<-----	-----	-----	-----	-----	-----	-----	-----	-----	-----	-----	-----	-----
Laumontite		-----	-----	-----	-----	-----	-----	-----	-----	-----	-----	-----	-----
Wairakite											-----	-----	-----
Chlorite-Smectite			-----	-----	-----	-----	-----	-----	-----	-----	-----	-----	-----
Chlorite			-----	-----	-----	-----	-----	-----	-----	-----	-----	-----	-----
Titanite (Sphene)													>-----
Epidote													>-----
Prehnite													>-----
Adularia													>-----
Dolomite	<-----	-----	-----	-----	-----	-----	-----	-----	-----	-----	-----	-----	-----
Anhydrite													>-----
Calcite	<-----	-----	-----	-----	-----	-----	-----	-----	-----	-----	-----	-----	>-----
Chalcedony		-----	-----	-----	-----	-----	-----	-----	-----	-----	-----	-----	-----
Quartz													>-----
Cristobalite		-----	-----	-----	-----	-----	-----	-----	-----	-----	-----	-----	-----
Pyrite	<-----	-----	-----	-----	-----	-----	-----	-----	-----	-----	-----	-----	>-----
Biotite													>-----
Garnet													>-----
Actinolite													>-----
Advanced Argillic Zone Key Minerals													
Kaolinite	<-----	-----	-----	-----	-----	-----	-----	-----	-----	-----	-----	-----	-----
Dickite													>-----
Pyrophyllite													>-----
Illite/Sericite													>-----
Diaspore		-----	-----	-----	-----	-----	-----	-----	-----	-----	-----	-----	>-----
Alunite	<-----	-----	-----	-----	-----	-----	-----	-----	-----	-----	-----	-----	>-----
Plagioclase	Sm/Kao				MLC-Chl-Cal-Z-W-(Ser)			Ep-Chl-Ab-Il-W-Cal-Preh			Ep-Chl-Ab-Il-Cal-Ser		
Olivine	FeOx- Py				FeOx-Qtz-Cal			Chl-Qtz			Chl-Qtz		
Pyroxene	Sm/Kao- FeOx				MLC-Chl-Tit			Chl-Ep-Qtz-Cal-Preh			Chl-Ep-Qtz-Cal		
Magnetite-Ilmenite	FeOx- Py				Tit-FeOx-Py			Py-Tit			Py-Tit		
Biotite	Stable/Clays- FeOx				Chl-Tit-FeOx			Chl-Tit			Stable		
Amphibole	Stable/Clays- FeOx				Chl-Tit-FeOx			Chl-Tit			Stable (actinolite)		
Quartz	Stable				Stable			Stable			Stable		

Sm, smectite; Kao, kaolinite; MLC, mixed layer Ill-Sm; Ill, illite; Chl, chlorite; Cal, calcite; Z, zeolites; W, wairakite; FeOx, oxides and hydrated iron oxides; Py, pyrite; Ep, epidote; Tit, titanite; Ab, albite; Ser, sericite; Preh, prehnite.

Figure 2.7. Summary of alteration minerals commonly found in high temperature, volcanic geothermal systems and their temperature stability. The bottom panel shows the typical alteration minerals that form from the given primary mineral for each zone. After Stimac et al. (2015).

Table 2.1. Common elements and, the minerals they are commonly found in, for both primary mineralogy in TVZ volcanic rocks and geothermal alteration minerals from experience in geothermal fields and epithermal deposits (Mauk and Simpson, 2007; Mauriohoo et al., 2016; Simpson et al., 2019; Simpson and Mauk, 2000). Elements in brackets are often, but not always, substitutes for the element in that row. N.b. there are many other possible elemental changes and these are provided only as a guide.

Element	Primary minerals	Alteration minerals	Common observed abundance change relative to host rock geochemistry during hydrothermal alteration
K (Rb)	K-feldspar	Illite, adularia	Increase
Ca (Ba)	Plagioclase	Calcite, Epidote	Generally decrease but can be offset by calcite and epidote formation
Na (Sr)	Plagioclase	Albite	Generally decrease
Si	Quartz	Quartz, amorphous silica, aluminosilicates (e.g. kaolinite, pyrophyllite)	Minor gains or losses
Fe	Pyroxene	Pyrite, chlorite, epidote	Minor change
S		Pyrite, arsenopyrite	Increase

Both X-ray diffraction (XRD) and automated mineralogy scanning were used in this study to obtain quantitative mineralogy data. XRD is a widely-used method to determine the mineralogical composition of rock samples. An x-ray beam incident upon the sample being measured is diffracted at specific angles due to the crystalline structure of the minerals within the sample. The intensity of the diffracted energy is proportional to the amount of that specific mineral within the sample. Automated mineralogy scanning techniques use a Scanning Electron Microscope (SEM) and Energy Dispersive x-ray Spectrography (EDS) to map minerals in a sample (e.g. Schulz et al., 2020). Each pixel analysed (pixel size is typically 1-40 micron) uses the SEM and EDS measurements to obtain geochemistry. Analysis software matches the geochemistry to a mineral based on a user-defined library of the chemical composition of minerals. The result is a map of and quantification of the minerals within a sample. Further detail on XRD and automated-mineralogy is provided in Chapter 3.

The general method used in this study was to define geochemical units within which the geochemistry was relatively constant. Changes in immobile elements were also used to identify changes that were likely due to changes in lithology rather than alteration. Both the XRD and automated mineralogy were used together to identify minerals present and quantify them. Chapter 3 provides more detail on how each technique works and how the data were used to interpret the processes driving the observed changes in seismic velocity in the well logging data.

2.2.2 Seismic Tomography

Seismic travel-time tomography utilises P and S wave arrival times recorded at seismometers from either natural seismic events and/or manmade seismic sources to derive images of seismic properties (e.g. velocity and attenuation) in the subsurface. If we represent some physical property of the subsurface as a set of model parameters m , a source and receiver ‘observed’ dataset d then the relationship between the two,

$$d = g(m) \tag{2.1}$$

is the basis of the tomography problem. For the ‘forward problem’, the source-receiver dataset d is calculated given a set of model parameters. For the inverse problem, the model parameters m are calculated from the dataset d . In the case of seismic tomography, the relationship between the observed data and the model parameters is highly non-linear and most widely-used local

earthquake tomography inversion codes (including tomoDD used here) typically linearise the problem and iteratively adjusting the model parameters to obtain a satisfactory fit between observed and forward calculated data, subject to any regularization conditions that are imposed. For such an inversion, the accuracy of the model parameters (how close they are to the actual values) is dependent on (Rawlinson & Sambridge, 2003):

- How closely the observed data match the calculated data from the model;
- Parameterisation assumptions (e.g. starting model used, inversion grid used);
- Errors in the observed data (e.g. noise);
- Accuracy of the method used to calculate data from the model
- Extent to which the data constrain the model parameters (e.g. source-receiver distribution)

Fully non-linear inversion methods (e.g. stochastic, simulated annealing and global search methods) have been in use for some time and are now also widely used for seismic tomography (Pullammanappallil and Louie, 1993; Ruan et al., 2019; Thurber and Ritsema, 2007). The general steps required to produce a tomographic image via iterative non-linear inversion (commonly used in seismic tomography) are; model parameterisation, forward calculation, inversion, solution robustness/resolution (Figure 2.8).

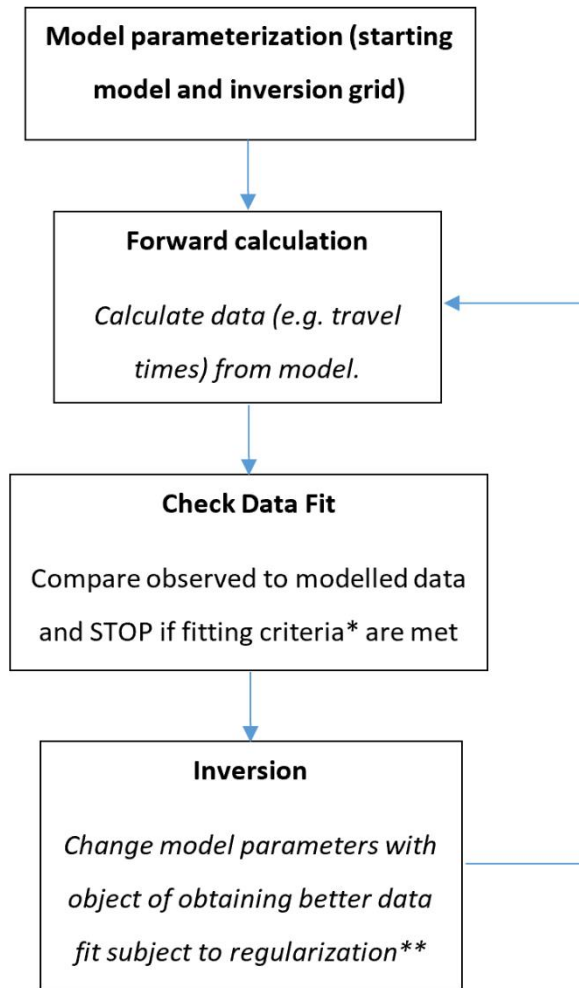


Figure 2.8. Flow diagram of the steps involved in seismic tomography. *Fitting criteria – usually involves checking whether a specified observed to modelled data fit is achieved OR improvement in data fit per iteration is below a certain threshold. **Regularization - required as observed data has uncertainty and the inverse problem is usually underdetermined. Often this involves ‘damping’ which encourages model solutions close to the starting model and smoothing which encourages model solutions with minimal variation

Parameterisation

There have been many varied approaches to parameterising the subsurface for seismic tomography, each approach having its own pros and cons (Zhao, 2015). The choice of how to parameterise a model ideally should be based on; a priori information about the region being modelled (e.g. existing velocity data, geologic information), whether or not the traveltimes data indicates the presence of interfaces (sharp changes in velocity), data quality and ray path coverage and the capabilities of the inversion method used (Rawlinson & Sambridge, 2003).

Choice of parameterisation is a crucial factor as it imposes restrictions on what can be resolved and it can also result in artefacts that may not be required by the actual data.

Three main approaches to discretizing the earth have been used in seismic tomography; constant velocity blocks, regular and irregular grids of velocity nodes (with a specified interpolation function between nodes) and interfaces whose geometry is varied. The simplest approach is the constant velocity block which was the basis of early seismic tomography work (Aki and Lee, 1976). The main drawback of this approach is its inability to effectively model the varying levels of heterogeneity of seismic properties observed within the earth, unless very small block sizes are used (which dramatically increases computational burden) (Thurber & Ritsema, 2007). To overcome these issues, Thurber (1983) proposed the use of rectangular grids of velocity nodes with trilinear interpolation between the nodes. This results in the velocity field being continuous throughout the model volume whilst the velocity gradient is discontinuous between cells (the boundaries formed by joining adjacent nodes). This approach is implemented in the SIMULPS family of tomography codes which has been the workhorse of local earthquake tomography applications since its introduction by Thurber (1983). It is also the parameterisation method utilised in the double-difference tomography code (tomoDD) of Zhang and Thurber, 2003 which is used in this work.

Interface parameterisation has often found use in reflection and refraction tomography where determining sub-horizontal geological layering is the primary objective (Rawlinson & Sambridge, 2003). In this approach, the subsurface is represented by sub-horizontal layers which either span the entire model space or pinch out (Rawlinson et al., 2010). The main advantage of this approach is the ability to more accurately represent layered strata. This approach has not commonly been used in local earthquake tomography which is likely related to differences in source-receiver geometry (local earthquake tomography source-receiver geometry often results in sub-vertical ray paths, reflection and refraction tomography results in sub-horizontal paths). However, hybrid approaches, such as that developed by Rawlinson (2012) in their FMTOMO code, that allow for both interface and grid parameterisation by specifying sub-horizontal layered interfaces within which a grid of velocity nodes can be defined could potentially be utilised for local earthquake tomography.

Station correction terms

Inevitably most parameterisation schemes fail to adequately discretise some aspect of the subsurface (Thurber and Ritsema, 2007). In earthquake tomography, this is often the case for

the shallow subsurface (upper 100's of metre's in local earthquake tomography) where seismic properties may be highly variable. In this case, static or station correction terms may be introduced into the parameterisation to account for variations local to each station. These terms can be either included as part of the inversion or constrained a priori (e.g. from refraction surveys). The goal of including these corrections is to prevent local velocity anomalies (that result in traveltimes anomalies) from inducing apparent deeper anomalies when the inversions are performed (Thurber and Ritsema, 2007). The effectiveness of this approach in achieving this goal however ultimately depends on the ability of the data used to resolve the local, shallow velocity field. Due to the mostly sub-vertical source-receiver geometry for local earthquake tomography, shallow velocity structure (above the source depths) is generally not well determined. Therefore, for most local earthquake tomography datasets the shallow velocity structure is a source of significant uncertainty (i.e. whether a traveltimes anomaly is due to shallow, local velocity variation or deeper velocity variation).

Initial (starting) models

Because the inverse problem of seismic tomography is highly non-linear, and the most widely used tomography codes historically (e.g. tomoDD) are linearised in such a way that they may find a local minimum of an objective function rather than the global minimum. Solutions obtained can therefore be highly dependent on the initial model used in the inversion (Kissling et al., 1994). If a-priori knowledge of the velocity is available (e.g. sonic logs, VSP/checkshot surveys, geology), this can be used to narrow the range of possible starting models. However, in many cases this information is limited and the range of possible initial models is large. The problem of uncertainty in initial models is exacerbated by the fact that many of the metrics used to assess model robustness and uncertainty (e.g. resolution and co-variance matrices and ray coverage measures such as derivative weight sum and ray density tensors) are insensitive to the uncertainty in the initial model (Thurber and Ritsema, 2007).

To address this, Kissling et al. (1994) proposed the use of the code VELEST (Kissling, 1995) to obtain a 'minimum 1D model' by performing multiple inversions for 1D velocity. In their approach they use a similar inversion procedure to that of standard 3D tomography (i.e. similar to the SIMULPS code of Thurber, 1983), but invert only for hypocentres, 1D velocity and station corrections. The resultant 1D velocity model is thus approximately equal to the average velocity for the particular layer depth range. VELEST also solves for 'station correction' terms for each seismometer used in the inversion. These terms account for velocity variation from

the 1D average velocity model (which includes local, shallow velocity structure and larger scale 3D velocity variation). The station correction terms can therefore provide an indication of relative 3D velocity variation within an area (i.e. which areas are on average higher velocity and which areas slower velocity) (e.g. Clarke et al., 2009).

Using VELEST, Kissling et al. (1994) proposed a ‘recipe’ to obtain an initial model or models for use in subsequent 3D inversions. They advocate a ‘trial and error’ approach whereby a range of different layer geometries and velocities are trialled with the goal of minimising the RMS misfit between observed and calculated traveltimes. Clarke et al. (2009) take a more systematic approach of determining the velocities for each layer by trialling 1000 different starting velocity models generated from randomised normal distributions of velocity values for each layer based on the expected range of subsurface velocities for their study area. Regardless of how many starting models are trialled, Kissling et al. (1994) note that their approach does not necessarily result in obtaining a single optimal solution. The procedure may still indicate a large range of possible 3D inversion starting models, particularly for layers that are not well constrained by the traveltimes data (e.g. shallowest layers). Therefore, uncertainty in initial models may still result in uncertainty in the final model solution obtained and this uncertainty may not be readily apparent in the standard tests of solution robustness and uncertainty (Rawlinson et al., 2014).

Forward Calculation – determining traveltimes

Calculating traveltimes between a source and receiver is often referred to as the forward problem or forward calculation. Because most tomography uses the first-arrivals of P and S wave energy this usually involves finding the minimum traveltimes between the source and receiver. The traveltimes t between a source S and receiver R is given by the path integral:

$$t = \int_S^R \frac{1}{v(x)} dl \quad (2.2)$$

where dl is differential path length, x is the position vector and v is velocity. Propagation of the seismic wavefront in all directions can be described by the eikonal equation;

$$(\nabla_x T)^2 = \frac{1}{[v(x)]^2} \quad (2.3)$$

where T is the traveltimes of the wavefront and $v(x)$ the velocity field.

For a ray, which is by definition perpendicular to the wavefront, the eikonal equation becomes the ray equation

$$\frac{d}{dl} \left(\frac{1}{v(x)} \frac{dx}{dl} \right) = \nabla \left(\frac{1}{v(x)} \right) \quad (2.4)$$

which forms the basis for most traveltimes determinations used in tomography via ray tracing techniques (Rawlinson and Sambridge, 2003). Wavefront tracking techniques, which usually use finite difference approaches to solving the eikonal equation, have also been used (Rawlinson, 2012).

Ray tracing techniques generally fall into two sub-categories; shooting and bending (Figure 2.9). Shooting methods determine the traveltimes by iteratively adjusting the initial ray projection angle from the source until the ray passes sufficiently close to the receiver. Bending methods iteratively adjust the geometry of an arbitrary ray that passes from the source to the receiver until the path of least travel-time is found (i.e. Fermat's Principle is satisfied). Bending methods have traditionally been the most commonly employed method to solve the forward problem in local earthquake tomography (e.g. Thurber, 1983; Zhang and Thurber, 2003). The main difference between shooting and bending methods are computational speed, bending being faster by a factor of ~10, whilst shooting methods are generally more robust in highly complex velocity media or where sharp velocity contrasts are apparent (Julian and Gubbins, 1977; Rawlinson and Sambridge, 2003).

Um and Thurber (1987) developed a 'pseudo-bending' ray-tracing technique. In this variation of the bending approach, an initial guess ray consisting of three points (source-receiver and one other point) is defined and the geometry perturbed until the minimum traveltimes is found within a specified limit). The number of line segments is then doubled (by adding two additional points along the path) and the geometry perturbed to again find the minimum traveltimes. This process is repeated until the change in traveltimes between iterations satisfies some criteria.

Thurber (1983) implements another variation of the bending method in which initial traveltimes are calculated by a set of circular arcs that connect the source and receiver. The dip of the plane of the arcs is then varied to fully sample the 3D velocity volume and the arc that yields the smallest traveltimes is selected as the ray-path. This 'approximate ray tracing pseudo-bending' (ART-PB) technique is the basis for the forward calculations in the widely used

seismic tomography codes SIMULPS (Thurber, 1983) and the tomoDD code of Zhang and Thurber (2003) which is used in this work.

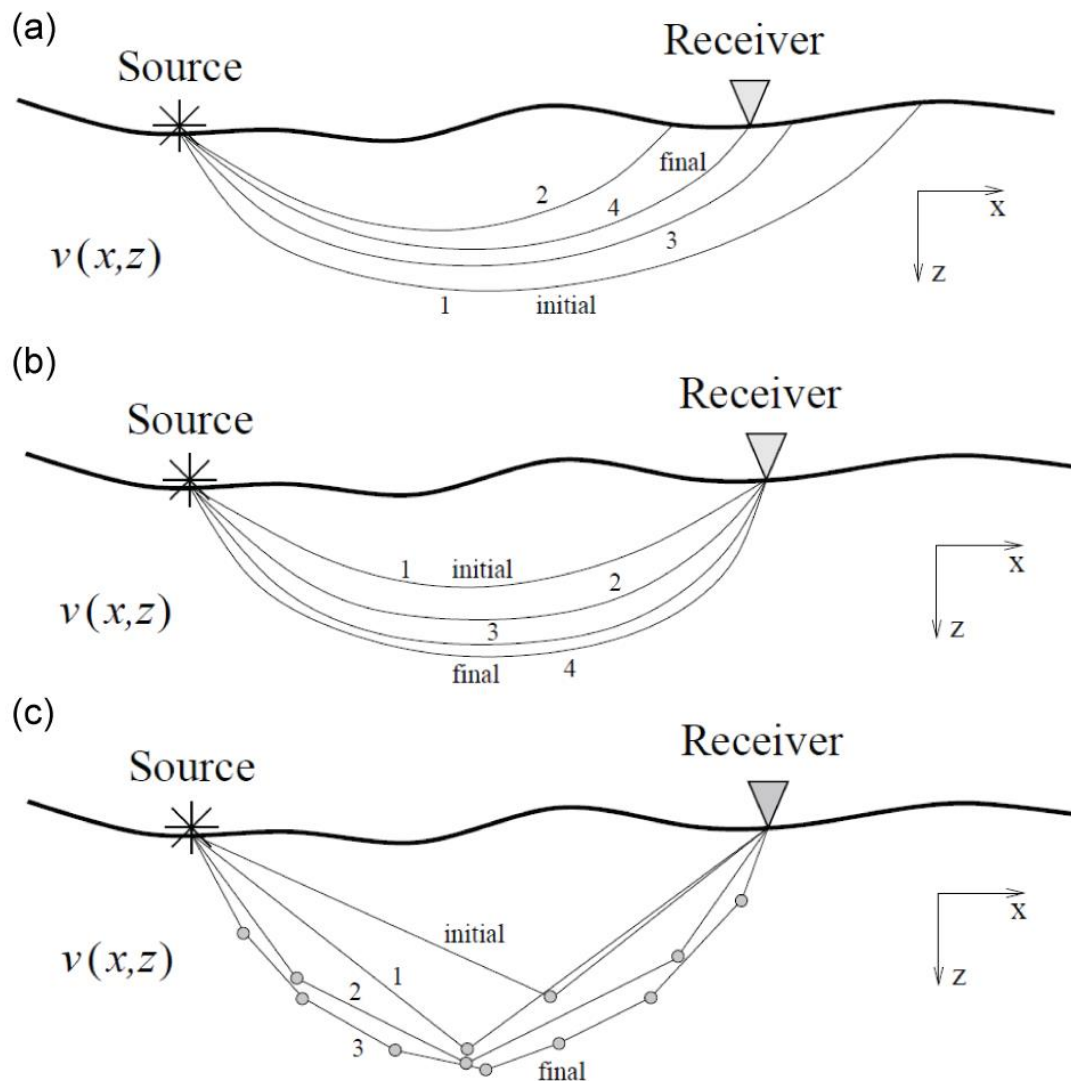


Figure 2.9. (a) The shooting method of ray-tracing. The initial, take-off angle of the ray is iteratively adjusted (ray-paths 1-4) until the ray path from the source intersects the receiver. (b) the bending method whereby the geometry of the ray is adjusted until the minimum traveltime path is found, (c) the pseudo-bending method whereby the line segments of an initial three point guess ray are iteratively halved and adjusted until the traveltime converges. After Rawlinson and Sambridge (2003).

Thurber (1983) test their ART-PB technique against the ray-tracer of Pereyra et al. (1980) which utilises the bending method in a finite difference scheme on a dataset from Bear Valley, California. Their testing showed that the standard deviation of traveltimes between the two methods was within 0.01s and therefore conclude that the ART-PB method robustly determines

ray-paths whilst reducing computational burden substantially. Haslinger and Kissling (2001) further test the robustness of the ART-PB method by comparing to a shooting method using both synthetic tests and real data. They find that both methods are precise to within 10 ms for ray lengths less than 60 km and that the two methods yield very similar ray-paths. They do however note differences in the resolution matrices derived using the two different approaches. Although ray-tracing algorithms are computationally quicker than wavefront tracking approaches, they can be unstable in highly-contrasting, heterogenous velocity media (Rawlinson et al., 2006).

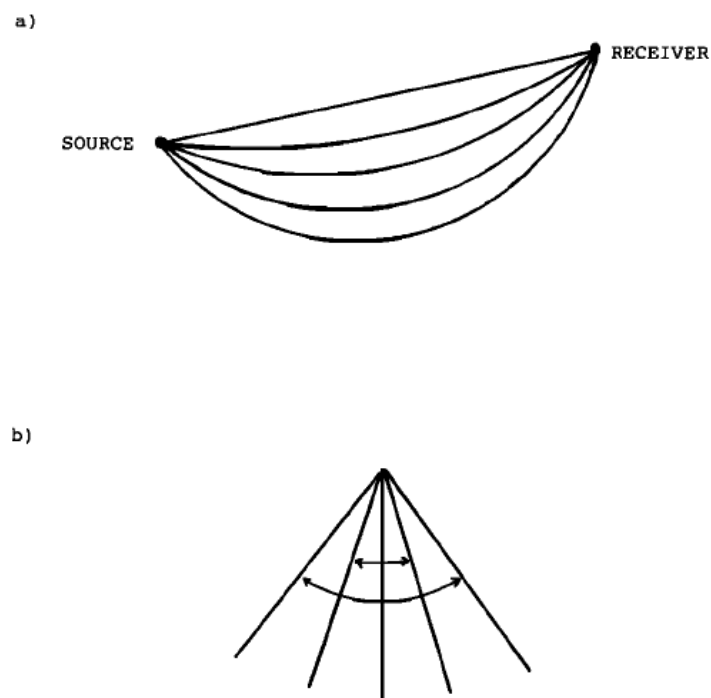


Figure 2.10. The approximate ray tracing pseudo-bending method. (a) A number of circular arcs are constructed between the source and receiver. (b) The dip of the plane of the arcs is then varied to sample the 3D velocity field. The arc with the smallest traveltime is selected as the ray-path. After Thurber (1983).

Inversion

The inverse step of adjusting the model parameters to better match the observed data can be performed in a variety of ways. Most inversion in seismic tomography is accomplished by linearising the highly non-linear tomography problem and iteratively improving the match between model predictions and data. By far the most common method of inversion in local

earthquake tomography is the conjugate least-squares method, in particular the LSQR algorithm of Paige and Saunders, (1982). To address model non-uniqueness most inversion schemes include some form of regularization such as damping and smoothing which allow a unique model solution to be obtained. The following focuses on the conjugate gradient method of inversion that is commonly used in local earthquake tomography studies.

The most common form of inversion used in tomography is that which seeks to minimise an objective function that contains a data residual term (difference between observed and calculated traveltimes as determined by the forward calculation method used) and one or more regularization terms. The objective function $S(m)$ generally consists of a term which measures the difference between observed and calculated data $\Psi(m)$, a damping term $\Phi(m)$ which encourages model solutions that are close to the initial model and a minimum structure (or smoothing) term $\Omega(m)$ which encourages model solutions which vary smoothly.

$$S(m) = \frac{1}{2} [\Psi(m) + \varepsilon\Phi(m) + \eta\Omega(m)] \quad (2.5)$$

Where ε is the damping factor and η is the smoothing factor. The regularization terms are required to reduce the non-uniqueness of the solution, enabling the inversion to find a local solution in the model solution space. If it is assumed that observed data errors are Gaussian, then

$$\Psi(m) = \|g(m) - d_{obs}\|^2 \quad (2.6)$$

where $g(m)$ is the calculated data, d_{obs} the observed data. Since each residual is squared, a major weakness in this definition of data fit is its sensitivity to outliers in observed data (e.g. incorrect picking of first arrivals). Common practice is to remove data outliers (those with anomalously high residuals calculated from preliminary inversions) from the dataset, but the method of defining outliers is often arbitrary (e.g. remove data if the residual is greater than a few standard deviations from the mean) (Rawlinson et al., 2014). An alternative method of reducing the influence of data outliers is the uniform reduction scheme of Jeffreys (1932) whereby outliers are assigned small weights rather than completely eliminating them. Sambridge (1990) demonstrates the benefits of implementing this approach in the context of local earthquake tomography.

Alternatively, if uncertainty estimates have been made for the observed data (based on picking error via either automated or manual approaches), then more accurate data can be given a greater weight in the objective function via

$$\Psi(m) = (g(m) - d_{obs})^T C_d^{-1} (g(m) - d_{obs}) \quad (2.7)$$

where C_d is the data covariance matrix. If errors are uncorrelated and true representations of the observed data error, then the covariance matrix consists of the uncertainty for each observed traveltime $C_d = [\delta_{ij}(\sigma_d^j)^2]$ where δ_{ij} is the Kronecker delta function, σ_d^j is the uncertainty of the j^{th} traveltime. However, this description of uncertainty implies that uncertainty is Gaussian, which may not necessarily be the case for arrival time data (Rawlinson et al., 2014). Unless the uncertainty truly represents the uncertainty in the data, the covariance matrix is more akin to a data weighting matrix, whereby more accurate data are given more weight in determining the objective function (Rawlinson and Sambridge, 2003).

Regularization terms are usually included in the objective function to reduce the non-uniqueness of the solution (i.e. to enable the inversion to find a local solution in the model solution space). This usually involves inclusion of a damping term, $\Phi(m)$, which encourages model solutions that are close to the initial model and a minimum structure (or smoothing) term $\Omega(m)$ which encourages model solutions which vary smoothly. The choice of the damping and smoothing terms therefore determines how well the model solution matches the observed data, how close the model is to the starting model and how smoothly the model varies. Hence, correct choice of these terms is a critical one in obtaining a model that obtains a good fit to the observed data whilst avoiding introducing model variations that are not necessarily required to obtain a good fit to the data. The most commonly employed approach to determining appropriate smoothing and damping values to use is to construct ‘trade-off’ curves for the particular dataset being inverted (Figure 2.11). In this approach, a number of separate inversions are performed each using different combinations of damping and smoothing. The data misfit and model perturbation are then plotted for each damping value and misfit and model roughness (or model variance). Appropriate values for damping and smoothing will be those which have a high data fit whilst minimising the model perturbation in the case of damping and high data fit with minimal model roughness in the case of smoothing.

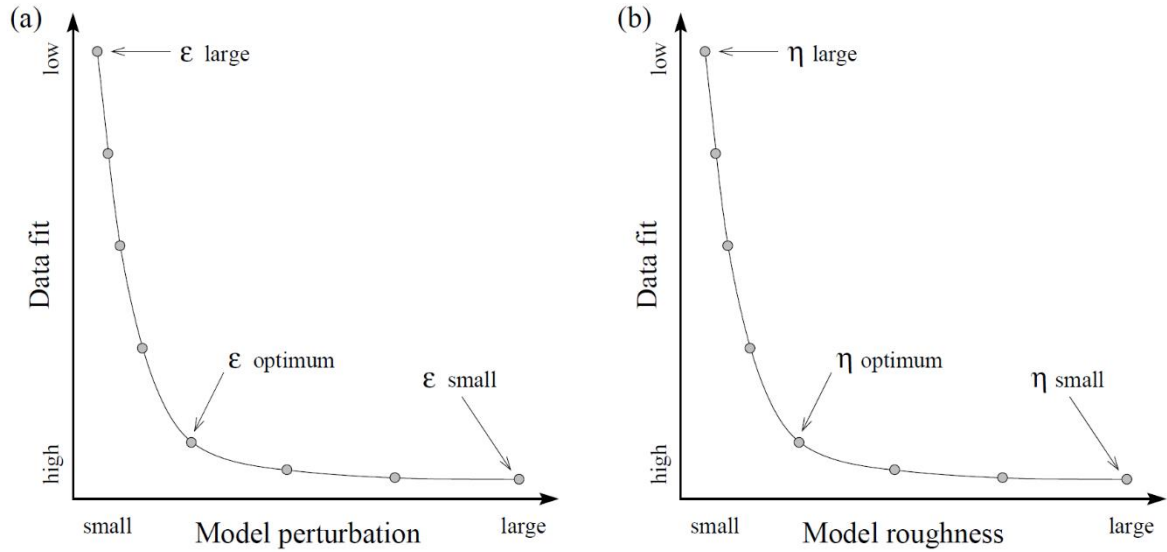


Figure 2.11. Schematic of the trade-off curve method for selecting appropriate (a) damping and (b) smoothing parameters for an inversion. A number of separate inversions are performed with varying values of damping and smoothing and plots of data fit versus model perturbation (variation from the initial model) and model roughness (spatial variation in the final model) respectively are constructed. The optimal values of damping and smoothing will be those which have high data fit whilst minimising the model perturbation (from the initial model) or roughness (model variance). After Rawlinson and Sambridge (2003).

The objective function in Equation (2.5) incorporates two different regularization frameworks; Bayesian and Occam's. In the Bayesian approach, smoothing is not applied and only damping is used to regularise the inversion (i.e. $\eta = 0$ and $\varepsilon = 1$ in Equation (2.5)). The regularization term in the objective function for this case can be written as

$$\Phi(m) = (m - m_0)^T C_m^{-1} (m - m_0) \quad (2.8)$$

where $m - m_0$ is the 'perturbation' or change from the initial model m_0 and C_m is the a priori model covariance matrix. If uncertainties in the initial model are uncorrelated, then $C_m = [\delta_{ij}(\sigma_m^j)^2]$ where δ_{ij} is the Kronecker delta function, σ_m^j is the uncertainty associated with the j^{th} initial model parameter. As with the data covariance matrix, the model covariance is more akin to an initial model weighting matrix unless the values truly represent the uncertainties in the initial model.

Minimising the objective function utilising only damping regularization results in a model solution that minimises data misfit whilst being as close as possible to the initial model (i.e. the

Bayesian approach prioritises the *a priori* information contained in the initial model). The main problem with a Bayesian approach in the context of geophysical inversion is that a priori information that meaningfully constrains the inversion is often unavailable (e.g. for the seismic tomography problem, independent measurements of seismic velocity, such as those obtained through logging or refraction surveys, are often non-existent or provide limited coverage of the area being modelled) (Rawlinson and Sambridge, 2003). The other regularization framework is Occam's approach, which seeks to find a model solution that minimises the amount of model structure (i.e. the smoothest possible model) necessary to fit the data (i.e. $\eta = 1$ and $\epsilon = 0$ in Equation (2.5)). The Bayesian approach has traditionally been the most widely used approach in seismic tomography and is used in the SIMULPS family of tomography codes (i.e. damped least squares) (Evans et al., 1994; Thurber and Eberhart-Phillips, 1999). The tomoDD code used in this work utilises both damping and smoothing regularization.

There are numerous numerical methods available for finding a minimum or minima in the objective function. Probably the most popular approaches, are the gradient based methods, particularly the conjugate gradient method, which make use of the derivatives of $S(m)$ at a specified point in the model solution space. A local minimum is then found when the derivative is zero. The LSQR algorithm of Paige and Saunders (1982), a variant of the conjugate gradient method, has historically been the most widely used algorithm for solving the local earthquake tomography problem. (Rawlinson & Sambridge, 2003; Thurber & Ritsema, 2007).

Obtaining a final solution

As depicted in Figure 2.8, obtaining a final seismic tomography model solution that adequately matches the observed and calculated data requires multiple iterations of inversion and forward calculation. There are a number of criteria that can be used to decide when to stop this cycle of inverse and forward calculation. In the SIMULPS family of tomography codes, iterations are ceased when either (1) the F-test fails, a test to see if the data misfit variance between the previous and current iterations is sufficiently different (i.e. the overall fit between the observed and calculated traveltimes has improved sufficiently); (2) the solution norm falls below a user defined value (when the model is both satisfactorily close to the initial model and the spatial complexity/roughness of the model falls below a user defined cut-off); (3) the number of iterations (velocity inversion-hypocentre relocation loops) exceeds some arbitrary number of iterations (ultimately designed to limit the computational time); or (4) the weighted RMS data

misfit falls below a user defined value (which usually won't happen if this is set to be less than the picking uncertainty).

Resolution, solution robustness and uncertainty

The seismic tomography problem is 'ill-posed' in that there is no single unique solution and there are many possible models that satisfy the observed data equally well. Resolution, solution robustness and model uncertainty in seismic tomography arises from a number of different sources

- Ray-path coverage, how well the traveltimes dataset constrain the problem
- Simplifying assumptions made in the inverse (e.g. regularization imposed) and forward calculation (e.g. assumptions of ray tracing)
- Resolution limitations imposed by the parameterisation used
- Uncertainty in the observed data (and ability to accurately measure data uncertainty)

Unfortunately, there are no perfect measures of solution resolution, robustness or uncertainty for the seismic tomography problem (Rawlinson et al., 2014). Hence, best practice is to utilise a range of methods for assessing model robustness and uncertainty. The most widely used methods are those which assess the ray path coverage through the model which aims to provide a measure of how well the data constrain different parts of the model, synthetic testing which aims to measure the ability of the dataset to recover different synthetic models (therefore providing a measure of spatial resolution throughout the model) and model resolution and covariance analysis which aims to provide direct measures of resolution and uncertainty for each node/cell throughout a model. Each method has its pros and cons in terms of evaluating model robustness and uncertainty which are discussed below.

Ray coverage or ray density measures are often used to provide insight into the ability of a particular dataset to resolve the spatial variations in a model. Increasing the number of ray paths in a tomographic inversion, by adding sources or receivers will, in general, result in an improved final model, providing greater data redundancy (e.g. chances of detecting and accurately determining arrival times and their uncertainties is increased by having more receivers) and in general higher possible spatial resolution.

The simplest measure of ray path density is the hit count, which is simply the total number of times a block or node cell is traversed by the available ray paths. The main issue with this is that rays passing closer to the centre of the block or cell provide more constraint than those passing further from the centre. To account for this, Thurber and Eberhart-Phillips (1999) proposed the use of the derivative weight sum (DWS) which measures the total weighted ray length through the block or cell. The DWS therefore reflects how closely rays pass to the centre of blocks or the actual node of the cell and is hence a better representation of how well constrained the nodes or blocks are by the data.

However, more rays traversing through or close to nodes does not necessarily result in better constraints on the nodes (Rawlinson et al., 2014). For example, if many rays traverse the same nodes in the same direction, despite the high ray density, the nodes will not be uniquely constrained by the data (i.e. there are many possible node values that will satisfy the data). This is a common problem in local earthquake tomography as often sources (earthquakes) tend to form clusters around seismogenic zones (e.g. along a fault). If this is the case, adding sources from a similar location (with no additional receivers) to the observed dataset does not provide additional constraint and may make the inverse problem less well constrained if there are large differences in uncertainty in the data. Ideally, ray paths would be both dense and traverse blocks/cells in multiple directions to provide the best possible constraint on each node.

For an objective function with $\eta = 0$ (i.e. a damped least squares inversion or Bayesian inversion), and ignoring observational and model representation errors, a resolution matrix R can be written as

$$R = [G^T C_d^{-1} G + \epsilon C_m^{-1}]^{-1} G^T C_d^{-1} G \quad (2.9)$$

where $G = \partial g / \partial m$, is the model partial derivatives that are calculated during the solution of the forward problem. The diagonal elements range between 0 and 1 and if $R = I$ (the identity matrix, i.e. all diagonal elements are 1) then the solution model is perfectly resolved (Rawlinson and Sambridge, 2003). The a priori covariance matrix C_m has diagonal entries whose square-root represents the uncertainty associated with the initial model parameter values.

The process of iterative inversion provides data constraints to the initial model uncertainties and results in final model uncertainties given by the a posteriori covariance matrix, which is related to the resolution and a priori covariance matrix and can be written as

$$C_M = \epsilon[G^T C_d^{-1} + \epsilon C_m^{-1}]^{-1} \quad (2.10)$$

The diagonal elements of C_M indicate the uncertainty in the final model solution parameters if the data and model covariance matrices truly reflect the uncertainty in the data and initial model respectively. As this is not usually the case, and when the damping factor is used as a ‘tuning’ parameter and selected empirically by examining trade-off curves, the diagonal elements of C_M no longer truly reflect the final model solution uncertainty, but rather the relative uncertainty between model parameter values (i.e. the diagonal elements of the *a posteriori* covariance matrix that are large are more certain and better constrained by the data than diagonal elements with small values) (Rawlinson and Sambridge, 2003).

The model resolution and covariance matrices require the solution of a much larger matrix than that required for the inverse step itself. For that reason, the computational time required when a large amount of parameters are inverted for (e.g. >10 000 parameters) has historically meant that resolution and covariance matrices have generally not been widely utilised (Rawlinson et al., 2014). A number of methods have been proposed that derive approximations of the model resolution and covariance matrices. For example, Zhang and Thurber (2007) show that use of the Lanczos bidiagonalization method implemented in the `tomoDD` code is able to provide a sufficiently accurate estimate of the model resolution matrix for a large tomographic inversion involving ~600000 observations and 5633 model parameters.

Synthetic reconstruction tests have been, by far, the most widely used method for assessing solution robustness in seismic tomography (Rawlinson et al., 2014). These tests involve generating a synthetic model/s (a wide variety of possible synthetic models can be tested) that is used to calculate data via the same forward calculation method used in the iterative inversion scheme and using the same sources and receivers as the actual dataset. This creates a synthetic dataset which is as accurate as possible from the forward calculation with ray-path coverage that reflects the distribution of source-receivers. This synthetic dataset is then inverted and the difference between the initial synthetic model and the inversion model can then be interpreted in terms of the resolution limits of the particular dataset (i.e. resolution will be better in areas where the inverted model matches the original synthetic model). A widely used synthetic test

is the so-called ‘checkerboard’ test. This test consists of a synthetic model of alternating positive and negative anomalies both laterally and with depth (Figure 2.12).

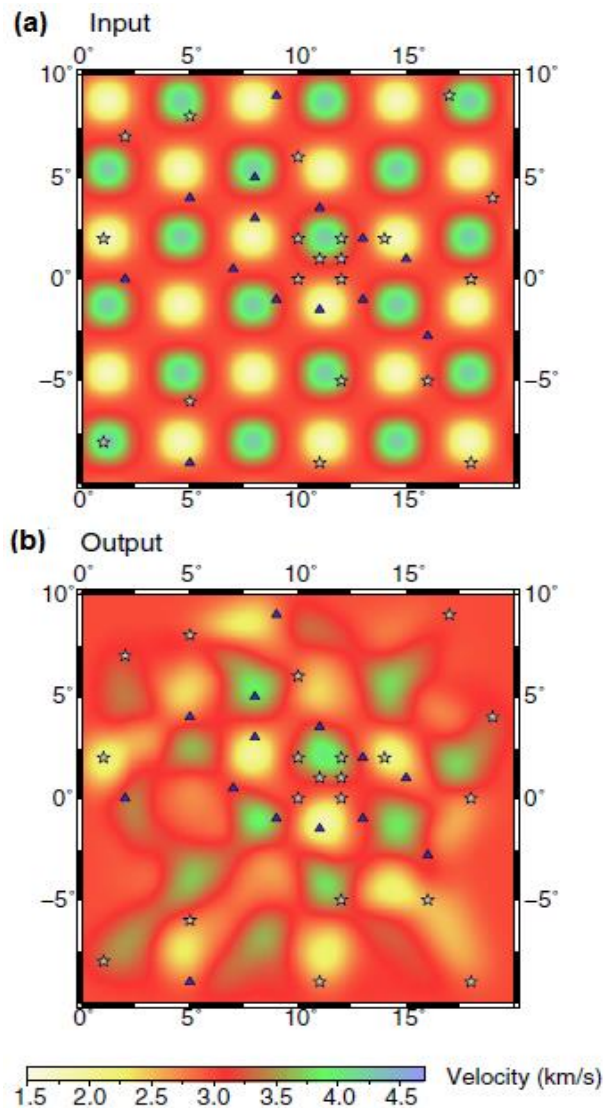


Figure 2.12. Example of the checkerboard synthetic test. (a) A synthetic model is created using alternating high and low velocity nodes. A synthetic traveltimes dataset is created from this model (via a forward calculation) and using the same sources and receivers to be used in the actual inversion. This traveltimes data is then used in the inversion process to obtain an (b) output model that can be compared to the original input model to qualitatively assess resolution of different areas of the model region (i.e. where the input and output models are very similar resolution is good). Sources are stars and receivers are triangles. Modified after Rawlinson et al. (2014).

Other common synthetic tests include the spike test, whereby a synthetic model containing one or more relatively small spatially but high amplitude anomalies are tested, and the recovery of

various geologically based features that are known or suspected to occur within the region (e.g. a subducting oceanic plate or a fault that offsets formations that have different velocities, etc). Rawlinson & Spakman (2016) provide a thorough review of the theory and use of synthetic models in tomography including common pitfalls and recommendations on how they should be carried out.

Double Difference Tomography

Absolute arrival time accuracy for both P waves, and particularly S waves (since they are superimposed on P-wave coda), can vary for both manual and automatic picking techniques. Accuracy can depend on signal-to-noise and the nature of, and correct identification of the arrivals (for example, whether arrivals are emergent), instrument response and GPS timing errors (e.g. Diehl and Kissling, 2009). Partly to address this issue, Waldhauser and Ellsworth, (2000) developed an algorithm (hypoDD) which takes advantage of the relative arrival times between events, which can be determined with higher precision and accuracy. The difference in traveltimes between two events (i and j) and station k is given by

$$r_k^i - r_k^j = \sum_{l=1}^3 \frac{\partial T_k^i}{\partial x_l^i} \Delta x_l^i + \Delta \tau^i + \int_i^k \delta u ds - \sum_{l=1}^3 \frac{\partial T_k^j}{\partial x_l^j} \Delta x_l^j + \Delta \tau^j + \int_j^k \delta u ds \quad (2.11)$$

where r_k^i r_k^j are the residuals between observed and calculated origin times such that $r_k^i - r_k^j = (T_k^i - T_k^j)^{obs} - (T_k^i - T_k^j)^{cal}$, T is the traveltimes, x_1, x_2, x_3 are the source co-ordinates, τ is the origin time, u is the slowness field, and ds is an element of the ray path length. The observed differential arrival times $(T_k^i - T_k^j)^{obs}$ can be calculated using both the difference between catalog arrival times (either automatically or manually picked arrivals) for each pair of events and/or by using waveform cross-correlation (WCC) techniques, which provide high accuracy relative times. The WCC approach is based on the assumption that waves generated by two similar sources, that have propagated along similar paths, will generate similar waveforms.

Waldhauser and Ellsworth, (2000) in their algorithm also make the simplifying assumption that the differences in velocity for each pair of events used for the relative arrival times are negligible, which is generally only valid for closely spaced events with very similar ray-paths ($\int_i^k \delta u ds$ and $\int_j^k \delta u ds$ in Equation (2.11) will be very similar and will effectively cancel). They therefore use a distance-weighting scheme to reduce or exclude data from events that are spaced far apart. However, this approach still allows event pairs to be ‘linked’ by intermediate events and therefore earthquakes that are distant can still alter each other (Wolfe, 2002).

Zhang and Thurber (2003) developed an algorithm (tomoDD) that combines both the absolute and relative arrival time data to determine both absolute and relative locations and velocity structure, solving Equation (2.11) directly. As tomoDD utilises the relative arrival times as well as absolute, it has higher spatial resolution of location and velocity within the source (earthquake) region. This results in higher resolution within the source region and thereby provides a sharper image of any velocity contrasts (Figure 2.13).

Three data types can be used in tomoDD – absolute arrivals, differential arrival times and cross-correlation data. A hierarchical weighting scheme is used to place greater emphasis on each data type at different stages throughout the inversion. The scheme starts by applying higher weighting to the catalog data (absolute and differential arrival times) to establish the ‘large-scale’ velocity structure and locate events in their correct, general region (weights 1 for absolute, 0.1 for differential and 0.01 for cross-correlation). Then the catalog differential data are weighted more to refine the event locations and velocity structure in the source region (1 for differential, 0.1 for absolute, 0.01 for cc). Finally, the waveform cc data are heavily weighted to further refine the locations and velocity structure in the source region (1 for cc, 0.01 for differential and 0.001 for absolute). The final stage of inversion places an order of magnitude more weight on waveform cross-correlation (WCC) data as these are at least an order of magnitude more precise than manual picks (Zhang & Thurber, 2006). Both damping and smoothing regularization is used to obtain a model solution that is both close to the initial input model and has minimal structure.

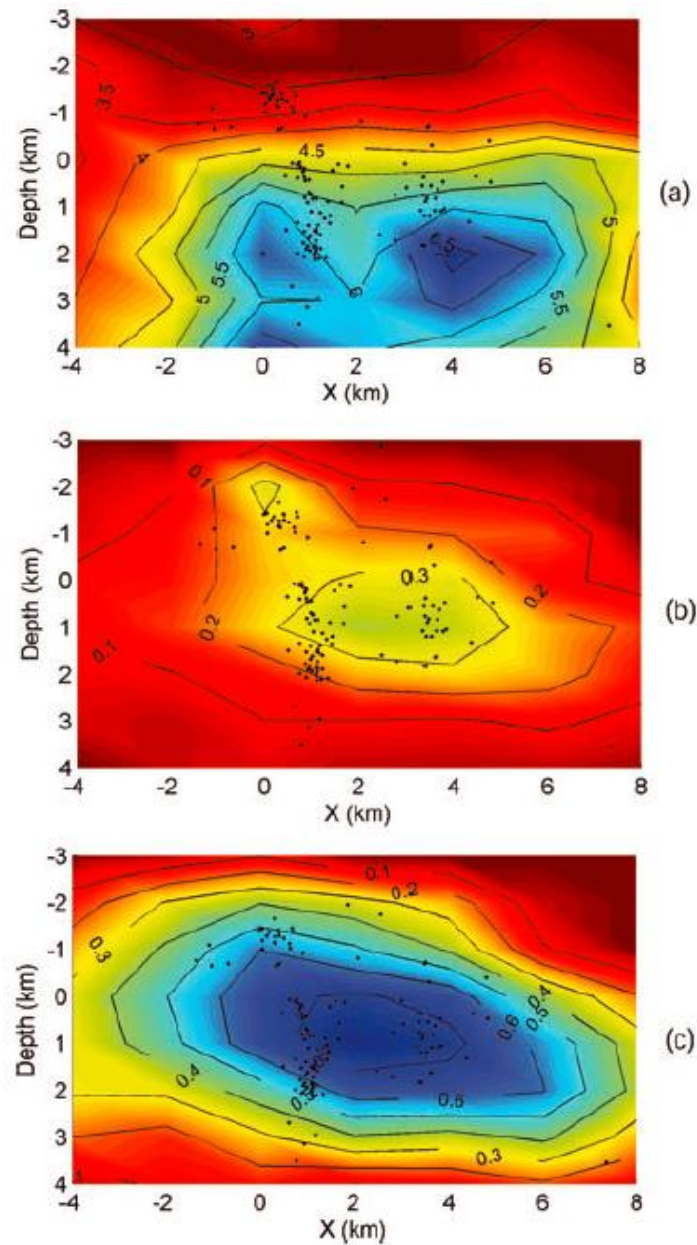


Figure 2.13. An example of the improvement in resolution within the source region gained by using the double-difference tomography approach. (a) the P-wave velocity along an E-W cross-section from the Mt Etna dataset of Zhang and Thurber (2006), (b) the model resolution values using a system with 10 times the weighting on absolute traveltimes compared to relative traveltimes (c) model resolution values for a system with 20 times higher weighting on differential times than absolute. Dramatic improvement in resolution is observed within the source region for the system with higher weighting on the relative traveltimes. The resolution is also observed to improve on the edges of the source region, which can be attributed to the additive value of better constraining one part of the model indirectly improving other regions of the model. After Zhang and Thurber, 2007.

3 Geologic factors controlling seismic velocity at the Ngatamariki Geothermal Field from comparison of wireline logging data to quantitative analysis of geochemistry and mineralogy.

Abstract

To investigate the role of lithology and alteration in controlling seismic properties at the Ngatamariki geothermal field, an analysis of petrophysical logs that included seismic velocity measurements from three wells (V_p in all wells, V_s in two wells) was conducted. The logged interval in the south of the field (NM10 well) spans the propylitic altered, tuff-dominated, Tahorakuri Formation volcanoclastics and andesite whereas the logged intervals in the north of the field (NM8 and NM9 wells) span the Tahorakuri Formation that experienced both propylitic and an earlier phase of potassic, advanced argillic and phyllic alteration that formed during intrusion of a tonalite-diorite magma body approximately 600 kya. Geochemical analyses of drill cuttings using portable X-ray fluorescence (pXRF) were conducted at a 5m depth interval spanning the geophysically logged intervals in each of the three wells. These were coupled with automated mineralogy using a Tescan Integrated Mineral Analyzer (TIMA) and quantitative X-ray diffraction (XRD) data on selected samples to inform the interpretation of the petrophysical logs. The pXRF data were used to define geochemical units and to refine major formation contacts whereas the automated mineralogy and XRD analyses of drill cuttings selected from these units were used to quantify mineralogy, particularly alteration minerals. The pXRF measurement of potassium content was also used to correct the cuttings depths to match gamma rays logs, resulting in depth corrections of up to 40 m in zones of partial lost circulation. The geochemical units and mineralogy data were then combined with the petrophysical logging dataset to interpret the dominant processes that drive seismic velocity changes in the geothermal field. The major formation types at Ngatamariki were found to have large differences in seismic velocity with the propylitic-altered Tahorakuri Formation in the south of the field having average V_p of 3.78 km/s, and V_s of 1.94 km/s, the andesite having V_p of 4.79 km/s and V_s of 2.15 km/s and the diorite-tonalite intrusion having average V_p of 4.72 km/s. The Tahorakuri Formation was found to have markedly different geochemistry, mineralogy and petrophysical properties in the north of the field compared to that in the south of the field. For the Tahorakuri Formation in the north of the field, the average quartz content

was 54%, the average neutron log porosity was 7% and the average Vp was 4.35 km/s whereas for the south the average quartz content was 36%, the average neutron porosity was 18% and the average Vp was 3.78 km/s. This is likely due to both quartz deposition infilling pore spaces and ductile deformation processes above the diorite-tonalite intrusion complex. An interval of particularly low porosity and high seismic velocity (average neutron porosity of 4%, average Vp of 4.91 km/s) occurs approximately 400m above the intrusion within the Tahorakuri Formation. Abundant andalusite at the top of this interval provides evidence that the rock in this zone was $>375^{\circ}\text{C}$ during the intrusion event. The inferred temperature, as well as deformation textures observed in an FMI log over this interval, suggest that the very low porosity is the result of ductile deformation. The interval between the andalusite altered tuff and the intrusion appears to be relatively unaltered with abundant plagioclase (average of 30%) and only subtle potassic alteration (biotite, actinolite). Abundant small aperture (<0.1 mm), low-angle ($<20^{\circ}$ dip) fractures identified in an FMI log occur within this interval which are interpreted as being due to either hydraulic fracturing due to pressure-transients that occurred within the lithostatic-pressured zone above the magma and/or from high differential stress due to the very high temperature gradient around the intrusion. The lack of alteration within this interval is interpreted as being due to the fluid within this zone being supercritical when the intrusion was emplaced with the low porosity/permeability that resulted from ductile deformation preventing further alteration as the magma cooled and during the present-day geothermal activity. There is some evidence that clay-bound porosity, dominantly within illite clay alteration in the south of the field (NM10), may play an important role in reducing seismic velocities; however, the dataset in this study spans only a small variation in clay type and abundance. The reduction of velocity by fracturing is also apparent, which has a locally (up to 20 m depth interval) large effect on velocity.

3.1 Introduction

Seismic velocity (P-wave, Vp and S-wave, Vs) has been shown to vary with important geothermal resource parameters such as fracturing (Siratovich et al., 2014), temperature (Jaya et al., 2010) and steam content (DeVilbiss, 1980; Ito et al., 1979). Seismic velocity in geothermal fields has also been shown to vary with geological formation (e.g. Hochstein and Hunt, 1970; Millett et al., 2018) and clay alteration (Wyering et al., 2014). However, the relative importance of the various factors influencing seismic velocity in geothermal resources is not well understood and there are relatively few published datasets examining the factors that control seismic velocity in geothermal resources.

Seismic velocity in a linearly elastic isotropic medium is determined by the elastic moduli and densities of the materials through which they pass (e.g. Keary et al., 1992; Mavko et al., 2009; Schön, 2015). In general,

$$velocity = \left[\frac{\text{elastic moduli}}{\text{density}} \right]^{1/2} \quad (3.1)$$

For compressional waves where the strain is in the direction of wave propagation, the velocity (V_p) is given by

$$V_p = \left[\frac{K + \frac{4}{3}\mu}{\rho} \right]^{1/2} \quad (3.2)$$

Where K is the bulk modulus, μ is the shear modulus and ρ is the density. For shear waves where the strain is perpendicular to the direction of wave propagation, the velocity (V_s) is given by

$$V_s = \left[\frac{\mu}{\rho} \right]^{1/2} \quad (3.3)$$

The elastic moduli and density, and hence V_p and V_s , of rocks vary due to many factors including the mineralogy of the rock grains, the nature of the boundaries between grains, grain shape and size, porosity, connectivity between pores, pore shape and size and pore fluid type (Mavko et al., 2009a; Saxena et al., 2018; Schön, 2015). Elastic moduli of some of the main minerals in this study are listed in Table 3.1.

Rock type is a first-order control on both mineralogy and porosity, which are usually the main factors influencing the elastic moduli and density of rocks and hence their seismic velocity. The velocity of low-porosity igneous and metamorphic rocks is generally higher than sedimentary rocks, with velocities in sedimentary rocks typically controlled by variation in quartz content (Mavko et al., 2009a; Schön, 2015; Wyllie et al., 1956). Sedimentary rocks, including volcanoclastics, have a wider range of velocities due to their generally more porous nature and more diverse mineralogy. Due to the dominance of seismic surveying techniques in imaging oil and gas reservoirs, a vast amount of research, both theoretical and empirical, has been conducted on the controls of seismic velocity in sedimentary rocks.

Table 3.1. Elastic moduli, density, Vp and Vs for some of the common minerals found in this study at room pressure and temperature. Data taken from Mavko et al., (2009a) and references therein.

<i>Mineral</i>	<i>Bulk Modulus (GPa)</i>	<i>Shear Modulus (GPa)</i>	<i>Density (g/cm³)</i>	<i>Vp (km/s)</i>	<i>Vs (km/s)</i>
<i>Quartz</i>	36.5-37.9	44-45.6	2.65	6-6.06	4.09-4.15
<i>Muscovite</i>	52-61.5	30.9-41.1	2.79	5.10-6.46	2.82-3.84
<i>Kaolinite</i>	1.5	1.4	1.58	1.44	0.93
<i>Plagioclase/Albite</i>	75.6	25.6	2.63	6.46	3.12
<i>Pyrite</i>	138.6-147.4	109.8-132.5	4.81-4.93	8.1	5.18
<i>Calcite</i>	63.7-76.8	28.4-32.0	2.71	6.26-6.96	3.24-3.59

These studies have shown that seismic velocity in sedimentary rocks mostly varies due to the mineralogy of the rock matrix, porosity, pore shape and pore fluid types (Schön, 2015). Porosity in sedimentary rocks varies widely and is typically the dominant factor in seismic velocity variation within high-porosity (10 – 30%) formations (Han et al., 1986; Wyllie et al., 1956). Although their elastic properties have been hard to directly measure (Mondol et al., 2008), clays have been shown to have lower seismic velocity through empirical measurements (Eberhart-Phillips et al., 1989; Han et al., 1986; Klimentos, 1991; Tosaya and Nur, 1982) and years of experience in geophysical logging in sedimentary basins (e.g. Brevik, 2005). This is due mostly to their ability to absorb and retain water within their crystal structure which is often referred to as ‘clay-bound porosity’ (e.g. Hurst and Nadeau, 1995). Published studies of seismic velocity in volcanic terranes are few, however some work has been done in oil and gas reservoirs hosted in volcanic formations (e.g. GuoXin et al., 2007; Watton et al., 2014; Xinmin et al., 2010).

Publications on seismic velocity variation in geothermal fields, particularly from logging datasets, are rare. Using logging data, zero-offset VSP data and analysis of drill cuttings, Millett et al. (2018) published a comprehensive analysis for one well in the Krafla geothermal field, Iceland. They found that the large-scale variations in velocity related mostly to rock type, in particular the transition between mixed lava and sheet intrusions into a dense diorite intrusion.

Their general approach to the interpretation of the wireline logging data was similar to that employed in this study, i.e. through comparing detailed cuttings analysis to wireline log responses. However, their study focused mostly on comparing log properties to rock type with little detail on alteration.

Some work has been done on measuring P and S wave velocities (V_p and V_s respectively) in core samples from the Rotokawa and Ngatamariki geothermal fields at room temperature and pressure. Siratovich et al. (2014) performed V_p and V_s measurements on cores of the Rotokawa Andesite and found a correlation between V_p and porosity/permeability. The porosity/permeability variations were in turn related to microfractures within the samples. Siratovich et al. (2015) also measured V_p and V_s before and after thermal stimulation of the samples and found decreases in V_p (up to 15%) and V_s , which they related to the formation of new microfractures. Wyering et al. (2014) and Cant (2015) also found correlations between V_p , V_s and porosity for core samples from the Ngatamariki and Rotokawa geothermal fields that they related mostly to differences in lithology. Furthermore, Wyering et al. (2014) attributed velocity variations to changes in hydrothermal alteration, particularly clay alteration type (increasing velocity as clay alteration transitioned from smectite to illite to chlorite) as well as rock type / lithology. These previous studies at Rotokawa and Ngatamariki have suggested lithological and alteration control seismic velocity, but the number of core measurements are too few to obtain statistically representative datasets and there has been no quantitative analysis relating mineralogy to V_p and V_s .

The goal of this study was to further investigate the impact that primary lithology and alteration processes have on seismic velocity in geothermal fields using a petrophysical logging dataset from three wells (NM8, NM9 and NM10) in the Ngatamariki Geothermal Field (Figure 3.1). To do this, geochemistry measurements using portable XRF (pXRF) on drill cuttings at 5 m depth intervals were combined with quantitative mineralogical data by automated mineralogy (TIMA) and quantitative XRD at selected depths on drill cuttings from the sections of the three wells over which petrophysical logging data were available. The logged sections of the wells are within the deep Ngatamariki geothermal reservoir with NM8 and NM9 in the north of the field and NM10 in the south. Wellsite geological logging and post-drilling geological analyses by GNS Science were completed for the three wells; the analyses are summarised for the logged sections of each well in Appendix A.4.

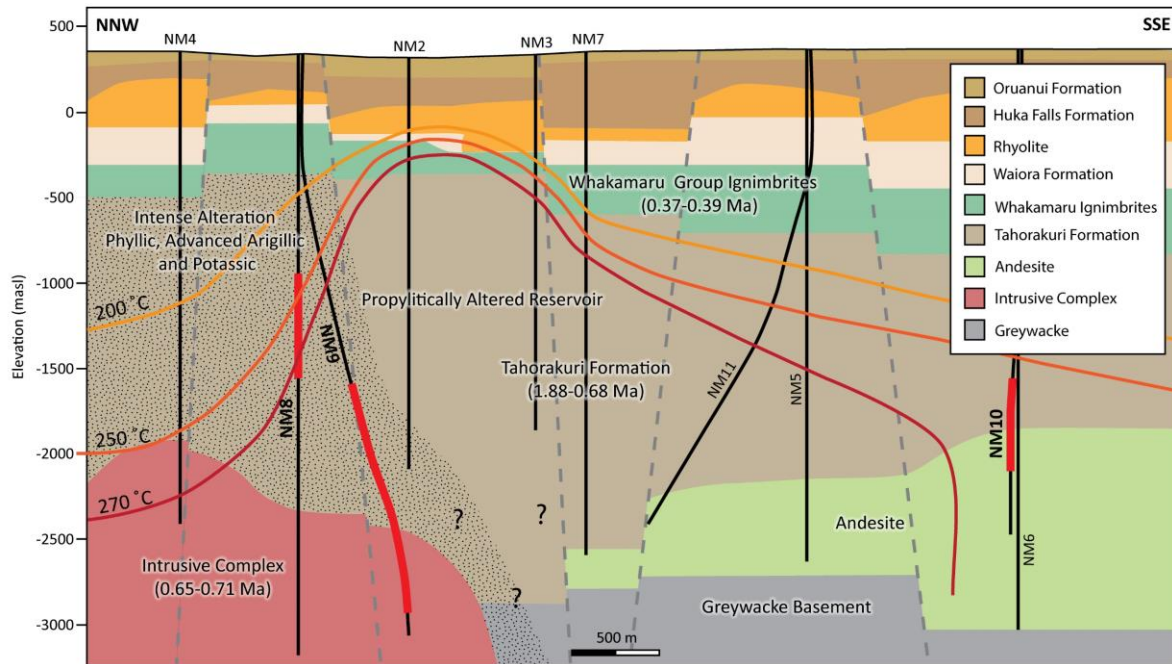


Figure 3.1. Geologic cross-section showing well tracks, the main geologic units and selected natural state temperature isotherms. The thick red lines on well tracks show the depth intervals of the petrophysical logs examined in this study. Modified after Boseley et al. (2010) and Chambefort et al. (2014).

The logged section of NM10 passes through tuffs of the Tahorakuri Formation into andesite, both of which are propylitically altered. Wells NM8 and NM9 also pass through the Tahorakuri Formation but pass into a Quartz-diorite to tonalite intrusion formed between 0.6 – 0.7 Ma (Chambefort et al. 2014). The intrusion episode resulted in potassic (biotite + magnetite ± K-feldspar), widespread phyllic (quartz + muscovite + pyrite) and advanced argillic (pyrophyllite ± andalusite ± topaz ± anhydrite ± rare aluminophosphates and fluorine-bearing minerals) alteration within the Tahorakuri Formation in the north of the field, similar to that observed for porphyry Cu systems / deposits (Chambefort et al., 2017; Hedenquist and Lowenstern, 1994). This alteration is overprinted by more recent propylitic alteration (chlorite + calcite + epidote ± wairakite ± actinolite ± albite and ± illite) similar to that seen in other high-temperature geothermal reservoirs in New Zealand and around the world (Browne, 1978; Chambefort et al., 2017). The intrusion and its alteration halo are associated with lower permeability in the north of the field, as reflected by the dominantly conductive temperature profiles and lower injectivities in NM4 and NM8 (Figure 1.3, Chambefort et al., 2017). The alteration style associated with the intrusion at Ngatamariki has not been documented in other geothermal systems in New Zealand and is relatively rare in geothermal systems worldwide. However it is

a potential analogue for the alteration processes and physical property changes that occur close to the magmatic heat sources of geothermal systems, which are currently being investigated for their potential use (e.g. Reinsch et al., 2017; Watanabe et al., 2017).

3.2 Data and Methodology

The general approach to this study was to first identify geochemical units within the wells with similar geochemistry as determined from the closely spaced (5 m sampling) portable XRF analyses. Representative samples from these units were then selected for quantitative mineralogy analysis using an automated mineralogy scanning technique (TIMA) and quantitative XRD. These were then used in conjunction with the petrophysical logs to better understand the factors influencing the seismic velocity response. The following sections provide detail on each of the datasets and methods used.

3.2.1 Portable XRF (pXRF)

Portable XRF operates on the same physics principles as laboratory-based XRF (Figure 3.2). Portable XRF instruments emit X-rays which cause inner-shell electrons of the atom being analysed to be displaced. Outer-shell electrons then fall in to fill this space and fluoresce (i.e. emit electromagnetic energy). The wavelength of the energy emitted is largely characteristic of the element and the intensity of energy emitted for a particular element is proportional to its concentration. Therefore, like laboratory XRF, pXRF provides an analysis of elemental abundance. The main difference between lab-based XRF and pXRF is the energy and power of the X-ray source used, which is lower for pXRF. As a consequence, atomically-light elements (i.e., those lighter than Mg) that can be robustly analysed by laboratory XRF cannot be determined using pXRF.

The pXRF analyses in this study were made on drill cuttings at 5 m intervals that previously had been washed and dried. Samples were directly analysed in their plastic cuttings trays as shown in Figure 3.2. Samples were packed against the side of cuttings trays so as to minimise separation between the X-ray source and sample. Most of the samples from NM9 and NM10 had average cuttings size of <1 mm whereas samples from NM8 were mostly >1 mm with some large cuttings of >10 mm. Larger cuttings from NM8 were hand-crushed to obtain samples that were mostly <2 mm in size, consistent with the recommendations for analysing drill chips in Gazley et al. (2017).

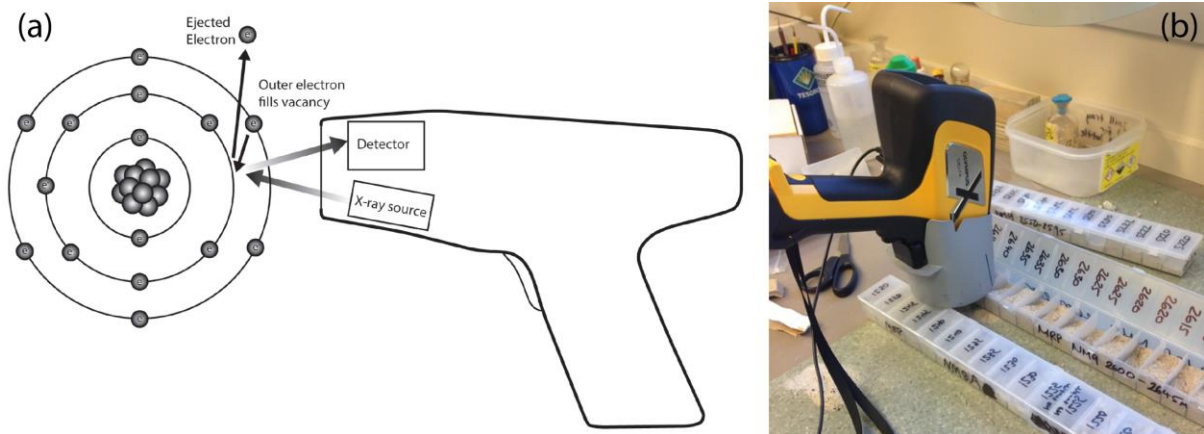


Figure 3.2. (a) Schematic diagram showing the basic principle behind the pXRF. Modified after Gazley and Fisher, 2014. (b) photo showing how the pXRF instrument was used to measure drill cuttings in plastic trays in this study.

Two different pXRF instruments were used in this study - an Olympus Delta (Delta Premium, 50 kV, 4 W Ag X-ray tube, 200 μ A current (max)), which was used to analyse samples from NM9 and NM10 and an Olympus Vanta (50 kV, 4 W Rh X-ray tube, 200 μ A current (max)) which was used for samples from NM8. Data were acquired using both a ‘geochem’ mode (which has two beam energy changes each 30 s long) and ‘soil’ mode (which has three beam energy changes each 20s long) for each instrument, however most of the elemental data used was from the ‘geochem’ mode except for K from the Delta and Ba from the Vanta which were only analysed and reported in ‘soil’ mode for the instruments used in this study. In total, each analysis took approximately 1.5 minutes to collect with beam times for the geochem and soil modes 30s and 60s respectively. Accordingly, a 1000 m section of cuttings (200 samples @ 5 m sample spacing) could be analysed in approximately one 8-hour day. Because pXRF instruments can be prone to instrumental drift (Gazley and Fisher, 2014) a NIST standard (NIST2710a) and an SiO₂ blank were analysed at the beginning and end of each day’s data acquisition and every 20 samples to monitor for instrumental drift. No substantial instrumental drift occurred for either instrument during the sample analysis (Figure 3.3).

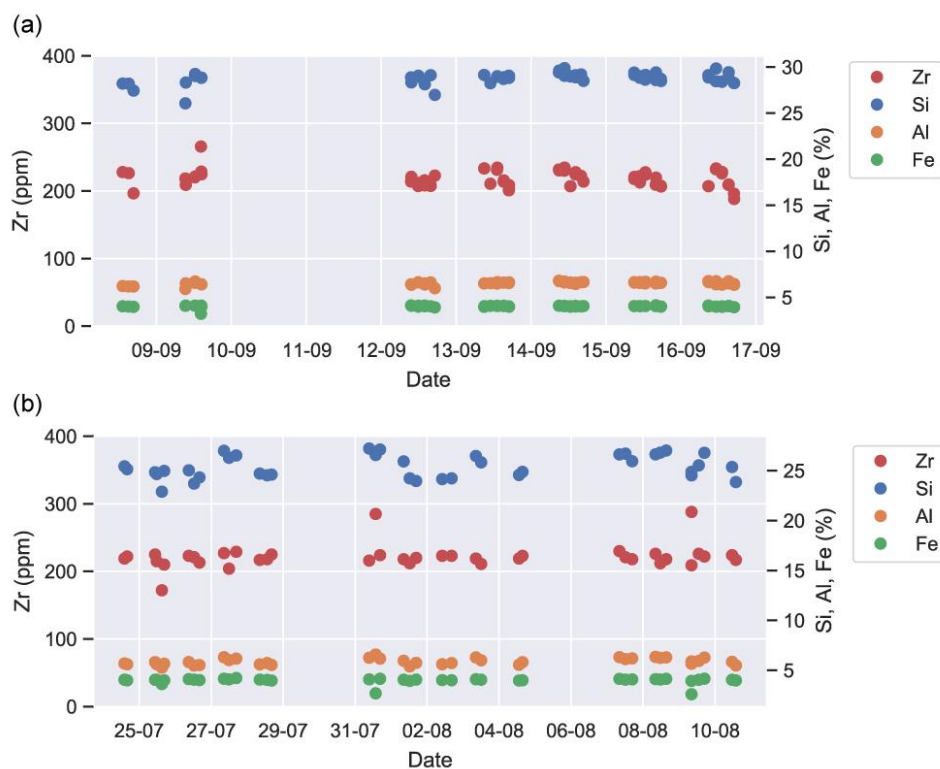


Figure 3.3. Selected elemental analyses with time for the NIST2710a standard for the DELTA (a) and VANTA (b). No significant instrumental drift was observed for either instrument.

The elemental data from the Vanta were corrected using six standards from USGS (COQ-1, SGR-1, AGV-2, BHVO-1, SCO-1, W-2) and two standards from the Geological Survey of Japan (JR-2 and JG-2) (Table 3.2) using an approach consistent with Gazley and Fisher, (2014). As the standards used did not have S in detectable concentrations, S concentrations are uncorrected and were used as reported from the VANTA. In order to make the datasets from the two different instruments comparable, the elemental data from the DELTA were normalised to the corrected VANTA data by analysing 117 samples from the three wells with both instruments (Table 3.2). The eight standards were also measured using the DELTA and were used to check the normalisation. In most cases the correction factors calculated from the standard analyses were similar to that derived from the DELTA vs. corrected VANTA data (Table 3.2). The poor correlation for Al in the DELTA compared to the VANTA results is likely due to the poorer sensitivity of the DELTA to atomically lighter elements like Al. Hence, the standards were used for correcting Al concentrations in the DELTA data. Based on the analysis of the standards, the analysis of the common samples analysed in this study using both instruments and the abundance of some elements being mostly below or close to detection

limits, seven elements (Mg, Bi, Sb, Se, Ta, V, and W) were considered unreliable and therefore were not used.

Table 3.2. Correction factors used on the pXRF data (a) Slope (correction factors), offset and square of the correlation co-efficient (R^2) for linear regressions between the VANTA measured elemental abundances and actual elemental abundances of eight standards. (b) Slope (correction factors), offset and square of the correlation co-efficient (R^2) for linear regressions between the VANTA corrected elemental abundances and DELTA measured abundances.

(a)	VANTA			(b)	DELTA		
	Slope	Offset	R^2		Slope	Offset	R^2
Al	1.0668	-845.28	0.9842	Al	0.9884	0	0.9679
As	0.9154	0	0.9743	As	0.9054	0	-0.313
Ba	1.0657	0	0.9972	Ba	0.9156	0	0.8058
Ca	1.0317	0	0.9988	Ca	1.0011	0	0.5155
Cu	1.0292	0	0.9769	Cu	1.4304	0	0.8314
Fe	0.9705	0	0.9921	Fe	0.9539	0	0.8289
K	0.9088	0	0.9786	K	0.7352	0	0.7401
Mn	0.9073	0	0.9871	Mn	1.1526	0	0.5578
Nb	0.9414	0	0.9053	Nb	0.7653	0	-0.13
Ni	1.2332	0	0.951	Ni	1.5048	0	0.5258
P	0.6069	0	0.9295	P	0.2037	0	-1.407
Pb	0.9704	0	0.9707	Pb	1.3875	0	0.8962
Rb	1.0181	0	0.9997	Rb	0.9554	0	0.7174
S	NA	NA	NA	S	0.4853	0	0.7907
Si	0.9485	0	0.9801	Si	0.991	0	-1.307
Sr	1.0325	0	0.9878	Sr	0.9948	0	0.6986

Th	0.9588	0	0.9963
Ti	0.9588	0	0.9963
U	0.7817	0	0.9611
V	0.583	0	-0.714
Y	0.9819	0	0.992
Zn	1.0492	0	0.9991
Zr	0.9927	0	0.9756

Th	1.7051	0	-0.213
Ti	1.327	0	0.2256
U	NA	NA	NA
V	1.4564	0	0.2286
Y	1.1113	0	0.6685
Zn	0.9264	0	0.2026
Zr	1.0681	0	0.8111

3.2.2 SEM-based Automated Mineral Mapping

Automated mineralogy approaches have been in use in the minerals and oil and gas sectors since the early 2000s (e.g. Pirrie & Rollinson, 2011). Although there are now several manufacturers of automated mineralogy instruments available (e.g. QEMSCAN, roqSCAN) their principle of operation is essentially the same. The instruments consist of a scanning electron microscope (SEM), equipped with multiple Energy Dispersive Spectrometers (EDS) that are used to perform EDS measurements at high-spatial-resolution (typically 10 µm or less). A high-energy electron beam is focused at each measurement point or pixel and, similar to XRF methods, the emitted electromagnetic radiation is analysed to determine the elemental concentration of each sample point. Mineralogy is then ‘mapped’ by matching the energy spectra of each pixel to a library of spectra ranges for different minerals.

The samples in this study were analysed using the Tescan Integrated Mineral Analyzer (TIMA) at the Australian Resources Research Centre, CSIRO, Perth, Australia. The instrument consists of a TESCAN MIRA3 field emission gun scanning electron microscope (FEG-SEM) operated at 25 kV and 6 nA, coupled with three Maxim PulseTor energy-dispersive X-ray detectors. The cuttings samples before measurement were mounted in 25 mm epoxy mounts and polished. The TIMA analysis was conducted over an area of approximately 3 cm² at a pixel spacing of 10 µm. Each sample took approximately 2 hours to analyse. An example of a prepared sample and its corresponding false-colour mineralogy map from the TIMA analysis is shown in Figure 3.4.

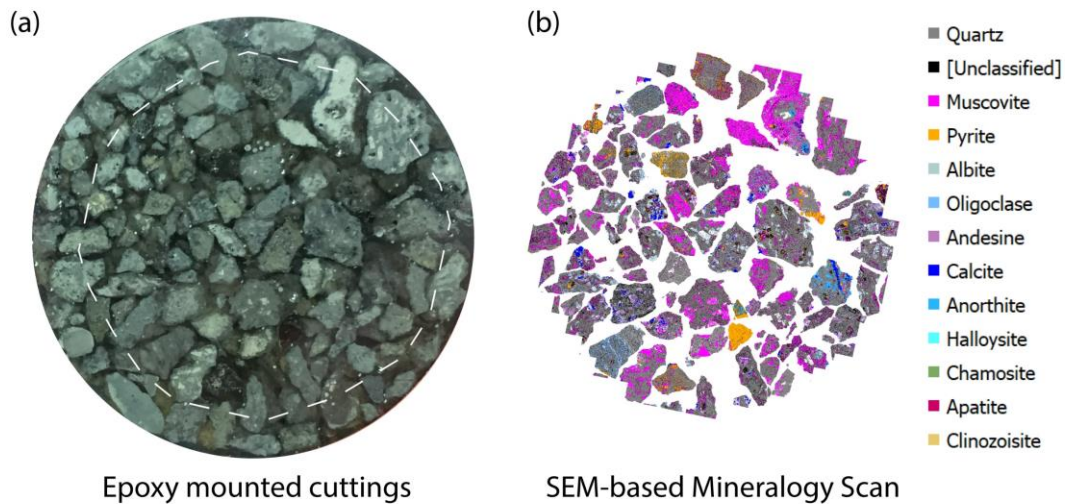


Figure 3.4. Example of (a) drill cuttings in 25 mm epoxy mount (b) the mineralogy map produced by the SEM-based automated mineralogy mapping for sample NM8 1250 mRF. Minerals in the key are listed in order of abundance. The white dashed outline in (a) shows the approximate extent of the sample that was scanned. N.B. – Muscovite \approx Illite, Chamosite \approx Chlorite, Clinozoisite \approx Epidote. Anorthite is chemically very similar to Wairakite.

Mineral maps that show the abundance and distribution of minerals were created by matching EDS analyses to the EDS profiles of reference minerals via a spectra-matching library. The reference minerals included in the library were constrained using the XRD mineral identification from this study and from previous XRD, petrography and SEM studies on the Ngatamariki field (e.g. Chambeft et al., 2017). Where it was not possible to match an EDS spectra to a reference spectra, the pixel was marked as ‘unclassified’. Most of the unclassified spectra are due to the analyses of more than one mineral grain resulting in a hybrid composition and occurred for fine-grained minerals in the groundmass, fine-grained feldspars that have been variably altered, and clay minerals that did not polish well. By converting the EDS analyses into minerals, the abundance of each mineral could be quantified. The percentage of unclassified sample varied between 8 to 33% with an average of 18%.

3.2.3 Quantitative XRD

Quantitative XRD on bulk rock samples was performed on the same samples as the automated mineralogy (TIMA) as a check on the abundance of the main minerals present (i.e. minerals with abundance $>1\%$ of the sample). X-ray diffraction scans were made on powdered samples using a PANalytical XPertPro diffractometer (40 mA, 45 kV, Cu anode). Mineral phases present were identified using HighScore software which automatically generates a list of likely

mineral phases within the sample (Degen et al., 2014). The mineral phases within the sample were manually selected from this list (based on previous XRD studies at Ngatamariki) until most of the significant peaks in the XRD scan had been matched. Mineral percentages were calculated using SIROQUANT software by comparing reference mineral profiles with that of the scanned rock using the Rietveld method (Taylor and Clapp, 1991; Wiles et al., 1981) and refined to correct for variable peak shape and preferred orientation. All samples had 10% weight zinc oxide added prior to XRD analyses with this known amount used to refine mineral percentages. In most cases, the calculated amount of zinc oxide was within $\pm 5\%$, which was considered adequate for the purposes of this study.

XRD and automated mineralogy techniques have different strengths and weaknesses and hence the two methods can often disagree on mineral quantities (Simpson et al., 2019). Automated mineralogy can detect minerals at much smaller abundances, with detection limits better than 0.1% whereas XRD generally only detects minerals that are $>1\%$ abundance (Simpson et al., 2019). Automated mineralogy on the other hand can under-report some minerals due to fine-grained minerals in the groundmass that are smaller than the pixel size (e.g. quartz, chlorite, albite, etc) (Simpson et al., 2019). In addition to the differences in the methods, there is also potential variation due to differences in the sampling (although the samples come from the same depth in the well, they are not the exact same sample). Because of the differences in the techniques and potential differences in sampling, the XRD and automated mineralogy in this study can be significantly different in places (generally $<10\%$, but up to 20-30% in some analyses).

3.2.4 Formation Logs in NM8, NM9 and NM10

Sonic logs were obtained in NM8, NM9 and NM10 as part of a suite of logs that generally included gamma, neutron porosity, resistivity, self-potential, density and formation imaging (FMI) (Wallis et al., 2012). Full waveform sonic logs were acquired in NM8 and NM10 and hence V_s measurements are available for these wells. The full waveform data were acquired using the Dipole Shear Sonic Imager (DSI) from Schlumberger which, for measurements of V_p and V_s , consists of a monopole source and eight receivers separated six inches apart with the first receiver located nine feet from the monopole source (Schlumberger, 2014). Schlumberger (2014) states that the DSI tool has a depth of investigation of nine inches. A borehole compensated sonic log was acquired in NM9 and thus there are no V_s measurements available for this well. All of the sonic logs provided seismic velocity at depth intervals of

~0.15 m. All logs were acquired by Schlumberger as part of the post-drilling completion logging and testing (i.e. after completion of drilling but prior to installing perforated casing in the reservoir section). Most of the borehole sections logged had washout of less than eight inches and hence good seismic arrivals were recorded for the majority of the logged sections. Notable exceptions to this are several zones within NM10 where severe borehole washouts (>8 inches) resulted in complete loss of seismic signal which are discussed further in the following sections. Manual review of the arrival picks in all wells provided an important quality check on the velocity data and minimised the number of incorrect picks due to cycle skipping and incorrect phase identification.

Standard petrophysical logging tools typically have maximum temperature ratings of ~175°C, so cold (~25°C) water was injected during the acquisition of the logs which meant that typical logging temperatures were in the range of ~50 – 150 °C (Wallis et al., 2012). Since natural state temperatures (estimated formation temperature prior to drilling) in the logged sections of these wells range between 260 – 280°C (Section 1, Figure 1.3) it is possible that the cooling of the rocks during drilling and during injection while logging has resulted in significant changes in the velocities. For example, it was shown by Jaya et al., (2010) that changes in temperature on the order of 100 – 200 °C can result in changes in seismic velocity of up to 0.5 km/s. However, since the borehole temperatures during the acquisition of the petrophysical logs varied less than 50 °C for most of the logged intervals, relative velocities should be maintained, including between wells. The log velocities may, however, be higher than their true, natural state values due to the cooling of the rocks by the injection.

3.2.5 Depth Correction of Cuttings Based on Potassium from pXRF and Gamma Logs

The depth from which drill cuttings originate is calculated rather than directly measured. The calculation is based on pumping rates, and losses or gains of fluid from the wellbore to the formation. A key assumption is that cuttings travel with uniform, constant velocity during their ascent to surface with little or no mixing. These assumptions mean that cuttings depth calculations can have large uncertainties (\pm 10s of metres) compared to typical sampling intervals (<5 m) (Naganawa et al., 2018). The cuttings depth calculations are particularly uncertain where partial losses (loss of fluid and cuttings to the surrounding formation) occur due to incomplete knowledge of the amount of fluid and cuttings lost to the formation. This presents a challenge when trying to compare cuttings-based measurements with *in-situ* measurements (Millett et al., 2018).

To address this issue, the cuttings depths were corrected using the K concentrations provided by the pXRF by matching to the gamma ray logs. Gamma ray logs measure the gamma ray emissions that are produced by naturally occurring radioactive isotopes U, Th and K in the formation with sub-metre depth resolution. Since most samples in this study had either undetectable or very low U and Th concentrations (below 20 ppm), the bulk of the gamma emissions from the formation are from K. Accordingly, the original calculated cutting depths can be adjusted to obtain an optimal match between the gamma and pXRF K concentration (Figure 3.5). To do this, marker horizons (prominent, and abrupt variations in the gamma response and pXRF K concentration) were identified and the depth of the cuttings were corrected to match that implied by the gamma ray log for these horizons. The cuttings depths between markers were corrected by assuming that samples between the marker horizons are equally spaced. The maximum shift in cuttings depth using this method was a shift of 40 m in NM9 at 2490 mRF. Correcting the cutting depths was an important step in being able to compare the pXRF, TIMA and XRD data to logging data obtained in the wells. This method of correcting cuttings depths may also have wider use in geological evaluation, for example obtaining more accurate stratigraphic offset data between wells which can be used to infer faults.

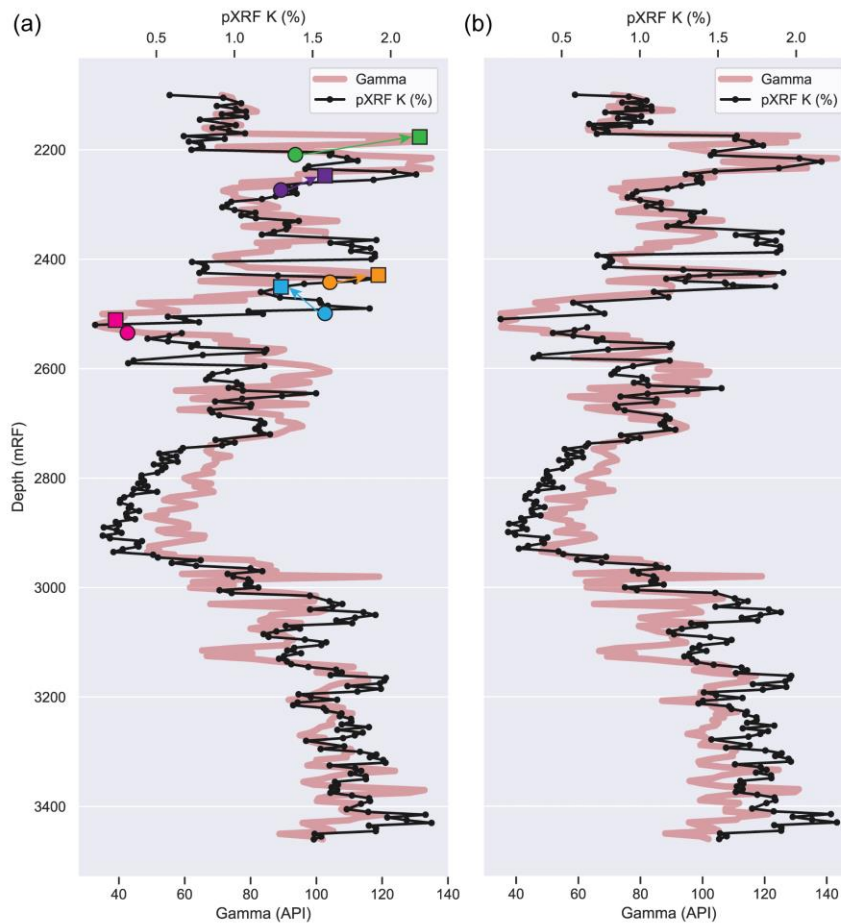


Figure 3.5. Example of the cuttings depth correction undertaken using the gamma ray log and pXRF potassium for NM9. (a) Marker horizons (orange squares and green triangles) where the pXRF K log and gamma log should align were visually identified. (b) The marker horizon cuttings depths were then assigned to be the same as the gamma log depths of the markers and the cuttings sample depths were recalculated so that samples between markers were equally spaced. This resulted in a significantly improved linear fit between the gamma and K (from $R^2 = 0.4248$ to $R^2 = 0.6576$ for this example). The maximum depth shift between the original and corrected cuttings depth was 40 m at 2490 m for this example. Partial loss of circulation (between 20 and 500 bbl/hr) occurred throughout the drilling of this particular hole section which is the most likely reason for the cuttings depths being deeper than their true depths.

3.2.6 Defining Geochemical Units

The pXRF data were primarily used to identify distinct geochemical units and the boundaries between them in all three wells. The geochemical units were defined based on either a clear change in immobile elements or a clear, step change in two or more mobile elements or both. Changes in immobile elements (Zr, Y, Ti and Al) likely represent changes in primary lithology

or formation as they are not usually involved in alteration reactions (Ahmed et al., 2019). Changes in mobile elements may be due to either changes in lithology and/or changes in alteration.

As geochemical data nearly always sum to 100%, they suffer from a constant sum or closure issue (e.g. Gazley et al., 2020; McKinley et al., 2016). When chemical data are closed, the value of each element is dependent on the others, i.e. an increase in the concentration of one element must result in the decrease in concentration of one, or more, elements. For example, alteration processes such as addition of quartz, can result in reduction of immobile element concentrations which may be incorrectly interpreted as due to a change in primary lithology. Therefore, to better identify lithology units based on immobile element changes, a centred log-ratio (CLR) transform was used in conjunction with the corrected pXRF data (Aitchison, 1982; McKinley et al., 2016). Chambeft et al. (2017) note however that their lab XRF data indicates that normally immobile elements (aluminium and titanium) are ‘partly mobile’ for their samples from Ngatamariki, likely due to the highly acidic fluids. Hence it is possible that changes in immobile elements are related to acid alteration in NM8 and NM9.

The existing geological logging interpretations (Appendix A.4) and the automated mineralogy (TIMA) and XRD data were used as cross-checks on the geochemical unit interpretations.

3.3 Results

Results are presented as well logs for all datasets in Figure 3.6 (pXRF CLR), Figure 3.7 (pXRF), Figure 3.8 (automated mineralogy/XRD) and Figure 3.9 (petrophysical logs) for NM8, Figure 3.10 (pXRF CLR), Figure 3.11 (pXRF), Figure 3.12 (automated mineralogy/XRD) and Figure 3.13 (petrophysical logs) for NM9 and Figure 3.14 (pXRF CLR), Figure 3.15 (pXRF), Figure 3.16 (automated mineralogy/XRD) and Figure 3.17 (petrophysical logs) for NM10.

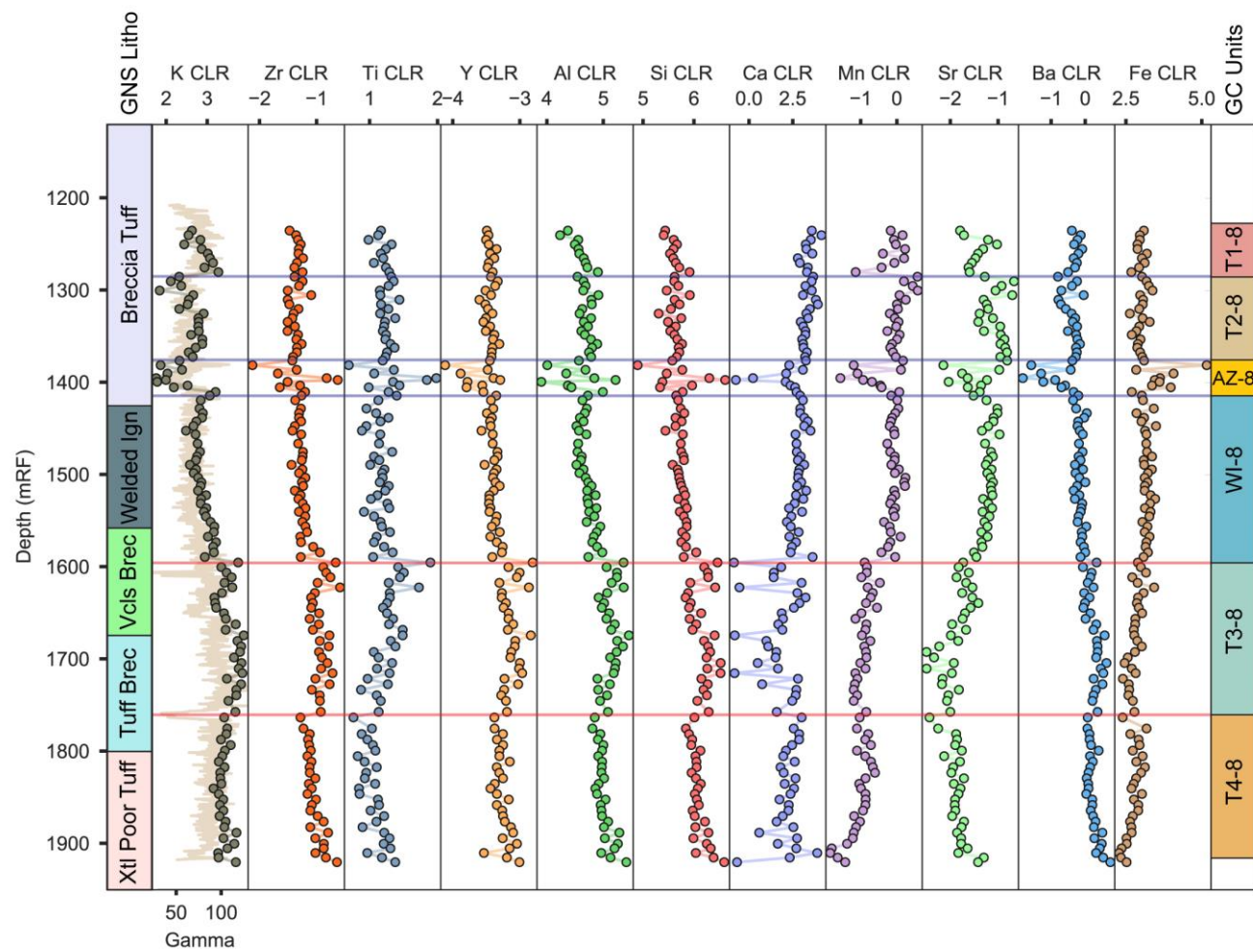


Figure 3.6. Centred-log ratio for selected pXRF data for NM8. The leftmost column is the original lithology is from Lewis et al. (2012a). Xtl = crystals, Bre = breccia, Vcls = volcanoclastic, Ign = ignimbrite. The rightmost column shows the geochemical units defined in this study. Red lines across the log indicate horizons defined by immobile elements, blue lines by mobile elements.

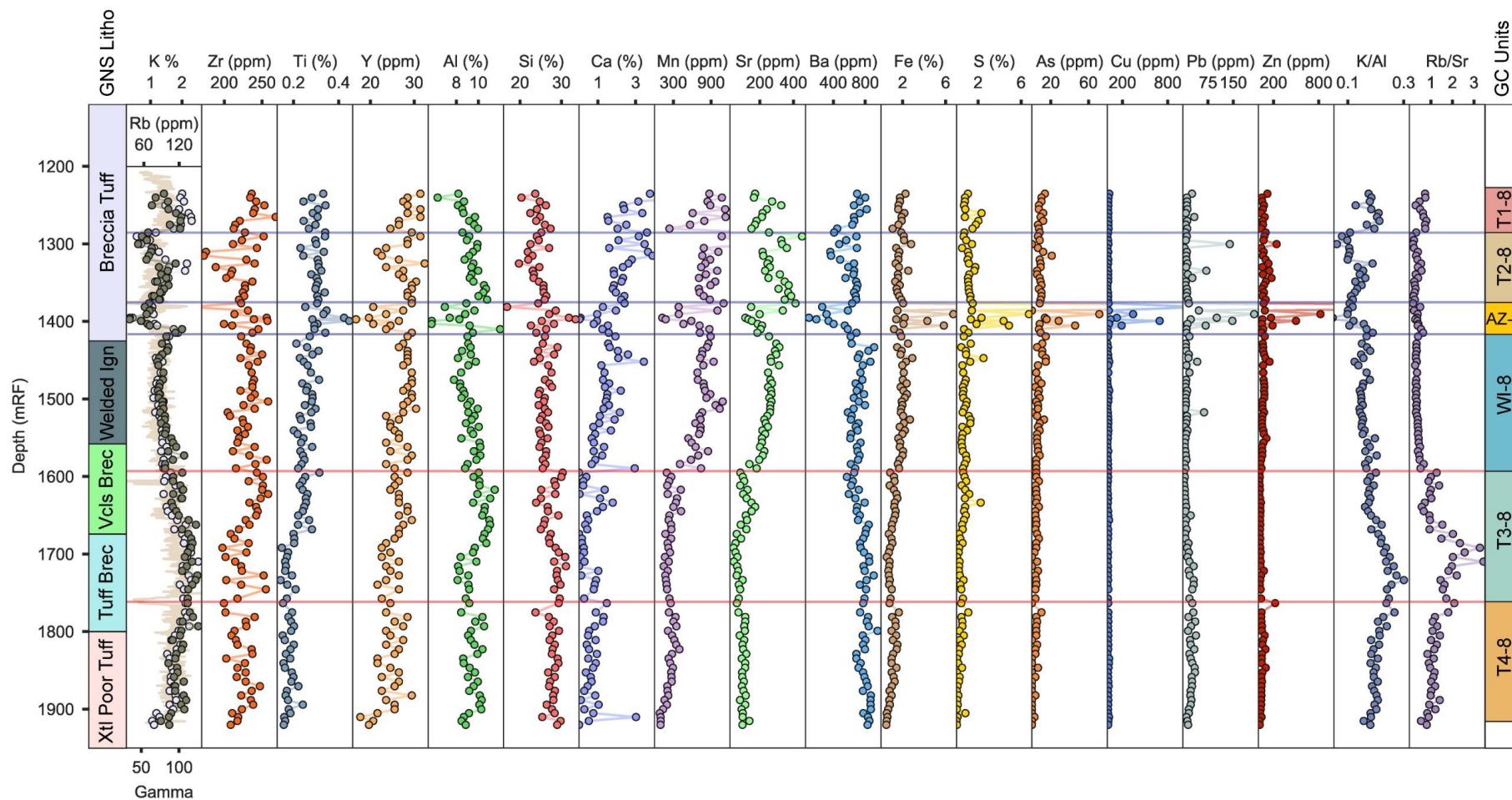


Figure 3.7. NM8 pXRF data. The leftmost column is the original lithology is from Lewis et al. (2012a). Xtl = crystals, Brec = breccia, Vcls = volcaniclastic, Ign = ignimbrite. The rightmost column shows the geochemical units defined in this study. Red lines across the log indicate horizons defined by immobile elements, blue lines by mobile elements.

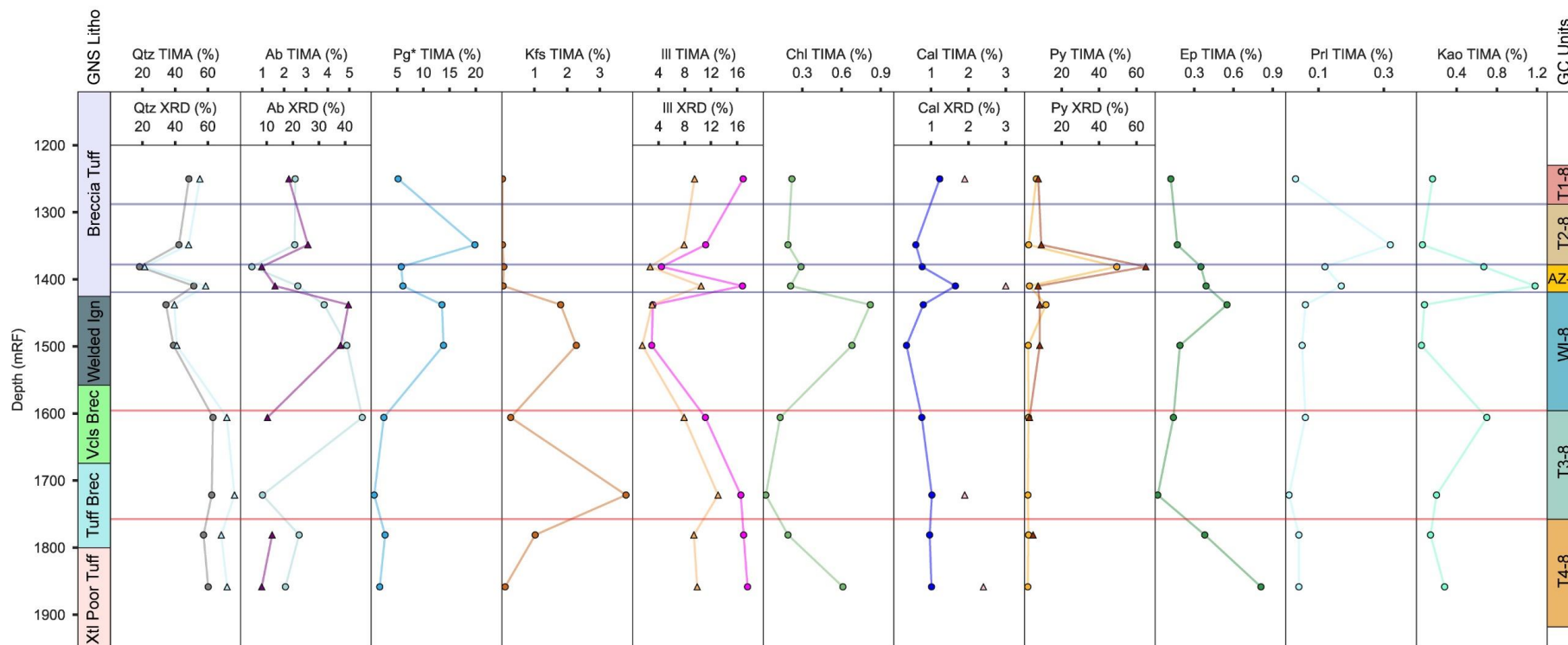


Figure 3.8. Mineral abundance in NM8 from automated mineralogy (TIMA) and quantitative XRD. The leftmost column is the original lithology is from Lewis et al. (2012a). Xtl = crystals, Brec = breccia, Vcls = volcanoclastic, Ign = ignimbrite. The rightmost column shows the geochemical units defined in this study. Red lines across the log indicate horizons defined by immobile elements, blue lines by mobile elements. TIMA data points are shown as circles and XRD data are shown as triangles. Qtz = quartz, Ab = albite, Pg* = plagioclase + , K-Felds = potassium feldspar, Ill = illite, Chl = chlorite, Cal = calcite, Py = pyrite, Ep = epidote, Prl = pyrophyllite, Kao = kaolinite.

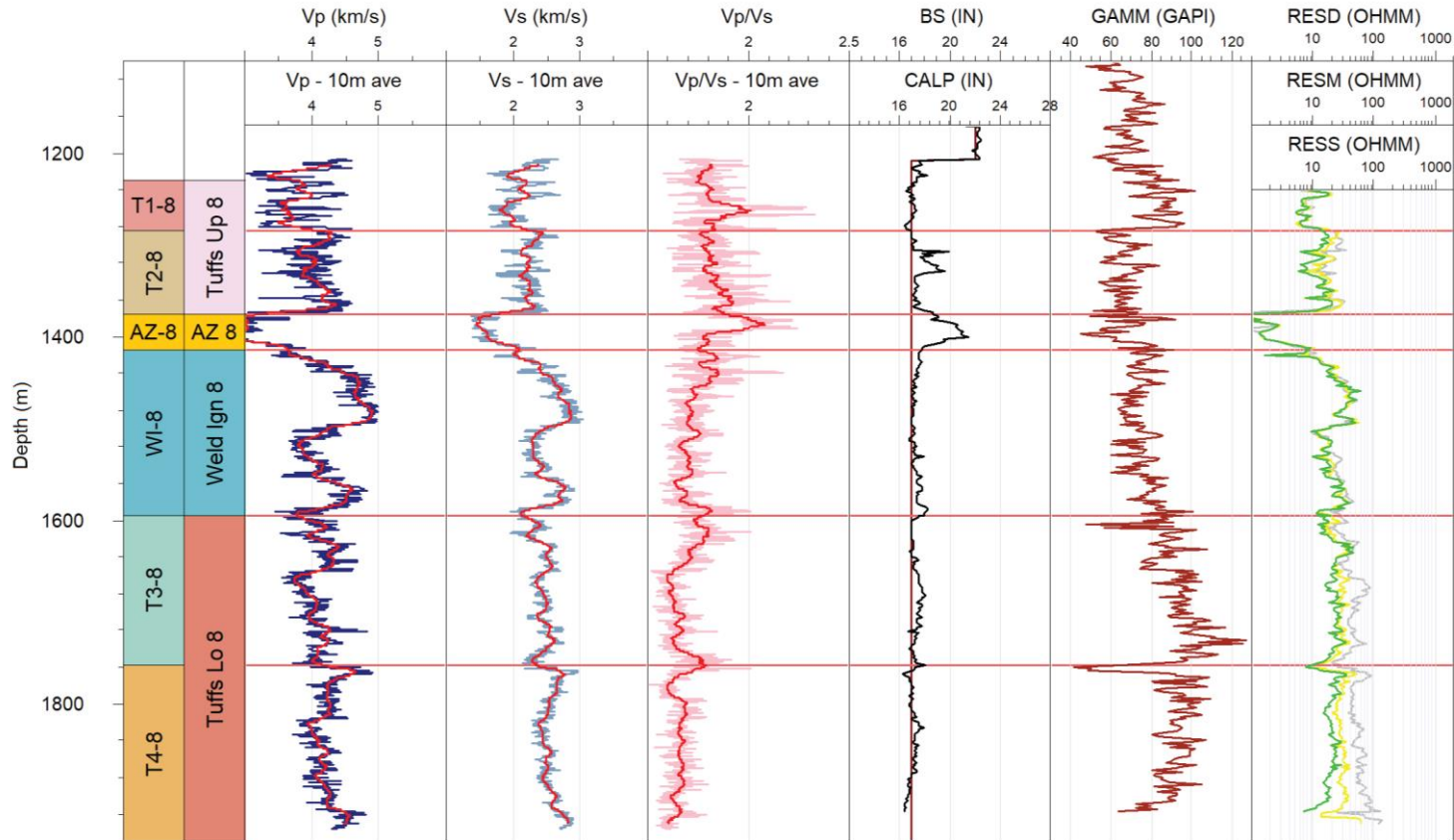


Figure 3.9. NM8 geophysical logs. The leftmost column is the geochemical units and second from the left is the geochemical groups. Vp = P-wave velocity, Vs = S-wave velocity, BS = drilling bit size (inches), CALP = caliper log (inches), GAMM = gamma log, RESD = deep resistivity (green), RESM = medium resistivity (yellow), RESS = shallow resistivity (grey). Red lines on the Vp, Vs and Vp/Vs logs show the 10 m moving average.

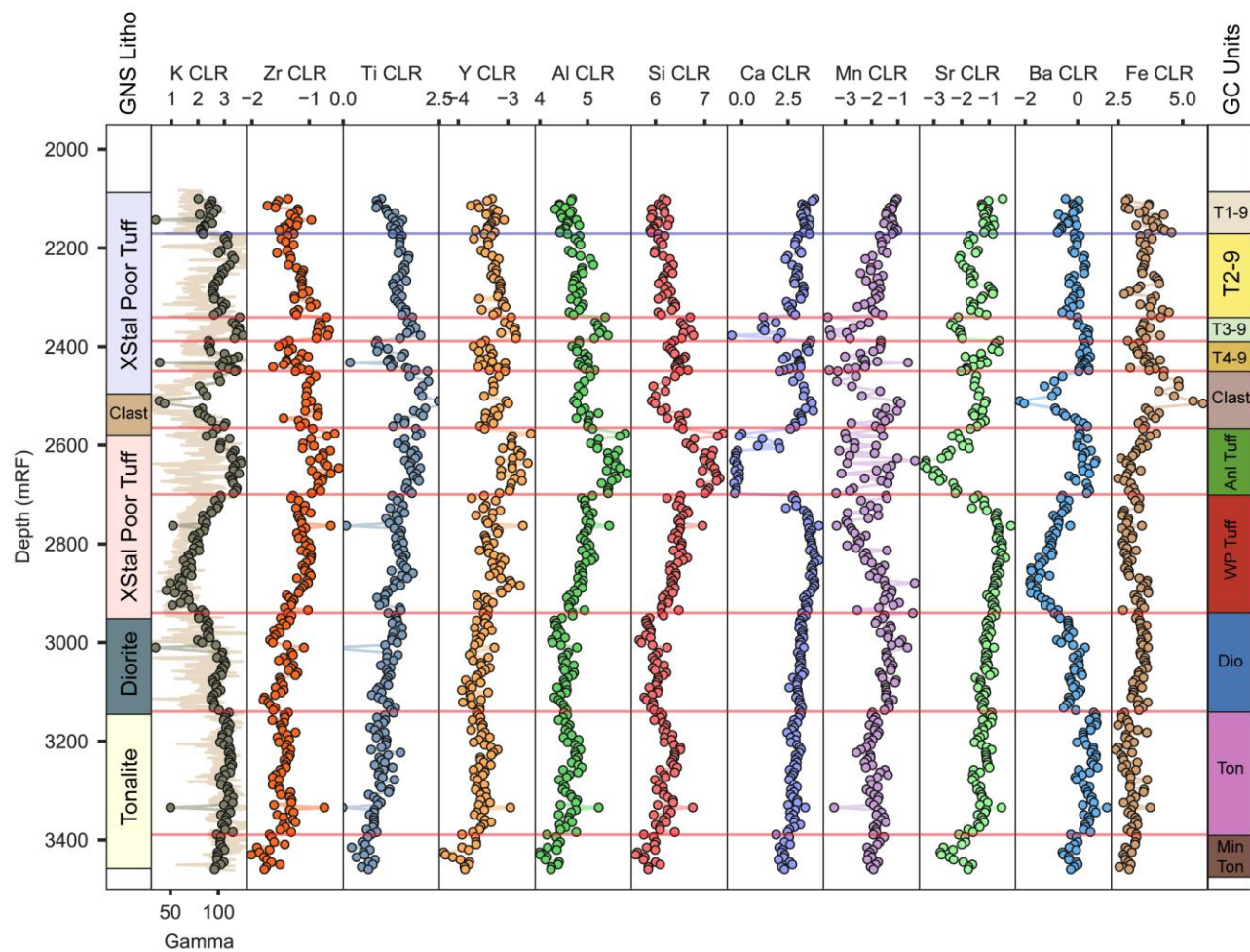


Figure 3.10. Centred-log ratio for selected pXRF data for NM9. The leftmost column is the original lithology is from Lewis et al. (2012a). XStal = crystal. The rightmost column shows the geochemical units defined in this study. Red lines across the log indicate horizons defined by immobile elements, blue lines by mobile elements.

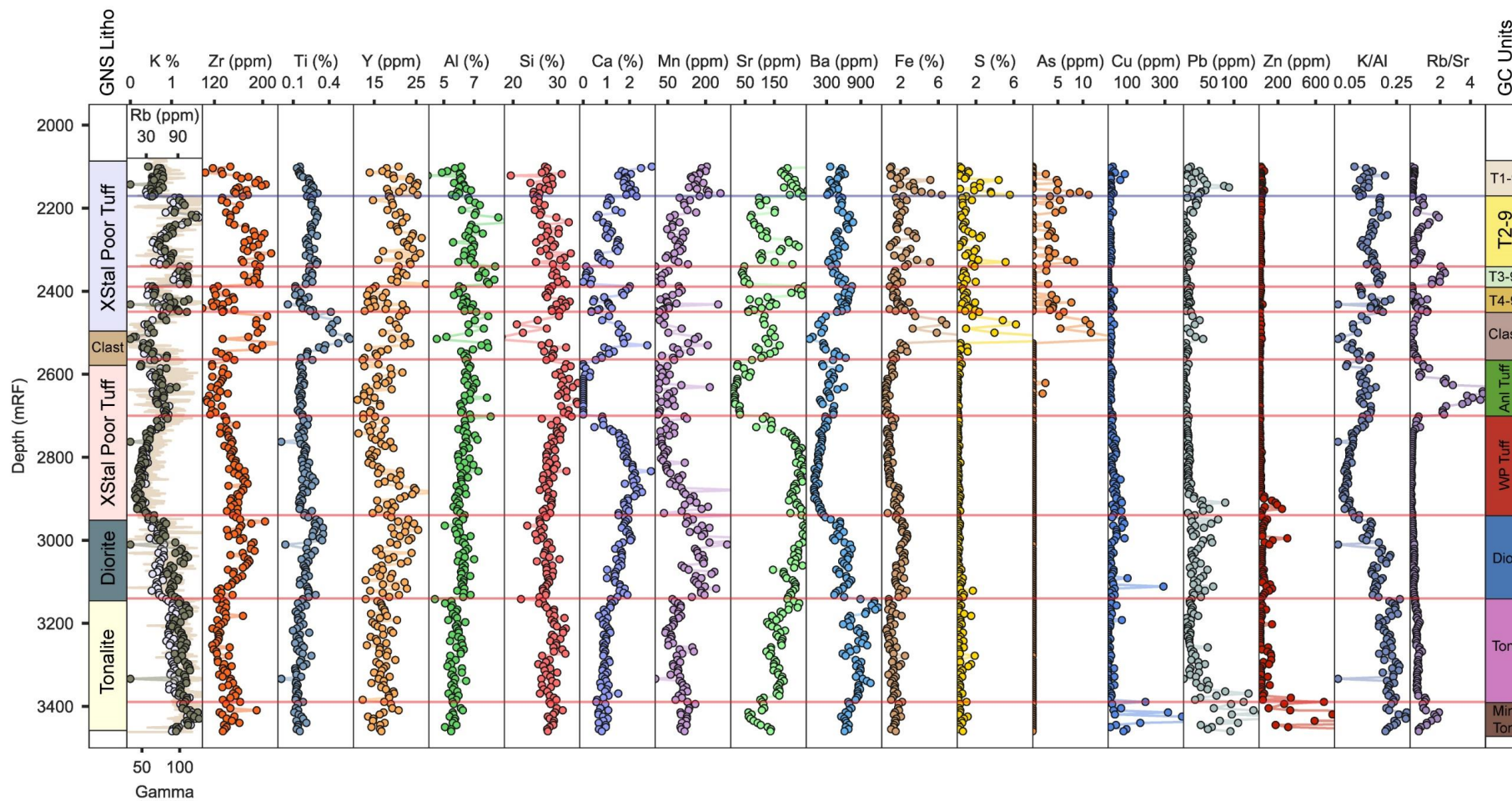


Figure 3.11. NM9 pXRF data. The leftmost column is the original lithology is from Lewis et al. (2012a). Xstal = crystal. The rightmost column shows the geochemical units defined in this study. Red lines across the log indicate horizons defined by immobile elements, blue lines by mobile elements.

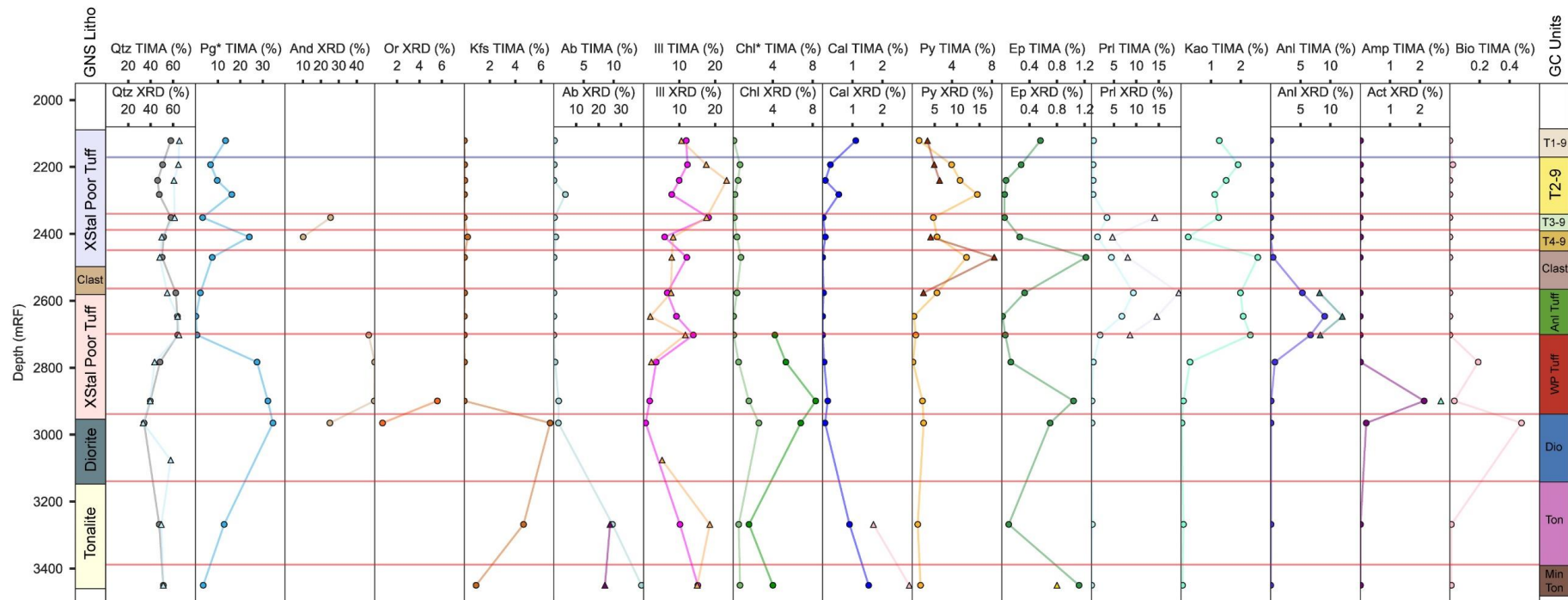


Figure 3.12. Mineral abundance in NM9 from automated mineralogy (TIMA) and quantitative XRD. The leftmost lithological column is the original lithology from Lewis et al. (2013). Geochemical units identified in this study are in the last column on the right. TIMA data points are shown as circles and XRD data are shown as triangles. Qtz = quartz, Pg* = plagioclase, And = Andesine, Or = Orthoclase, Kfs = potassium feldspar, Ab = Albite, Ill = illite, Chl* = chlorite, Cal = calcite, Py = pyrite, Prl = pyrophyllite, Kao = kaolinite, Anl = andalusite, Amp = amphibole, Act = actinolite, Bio = biotite.

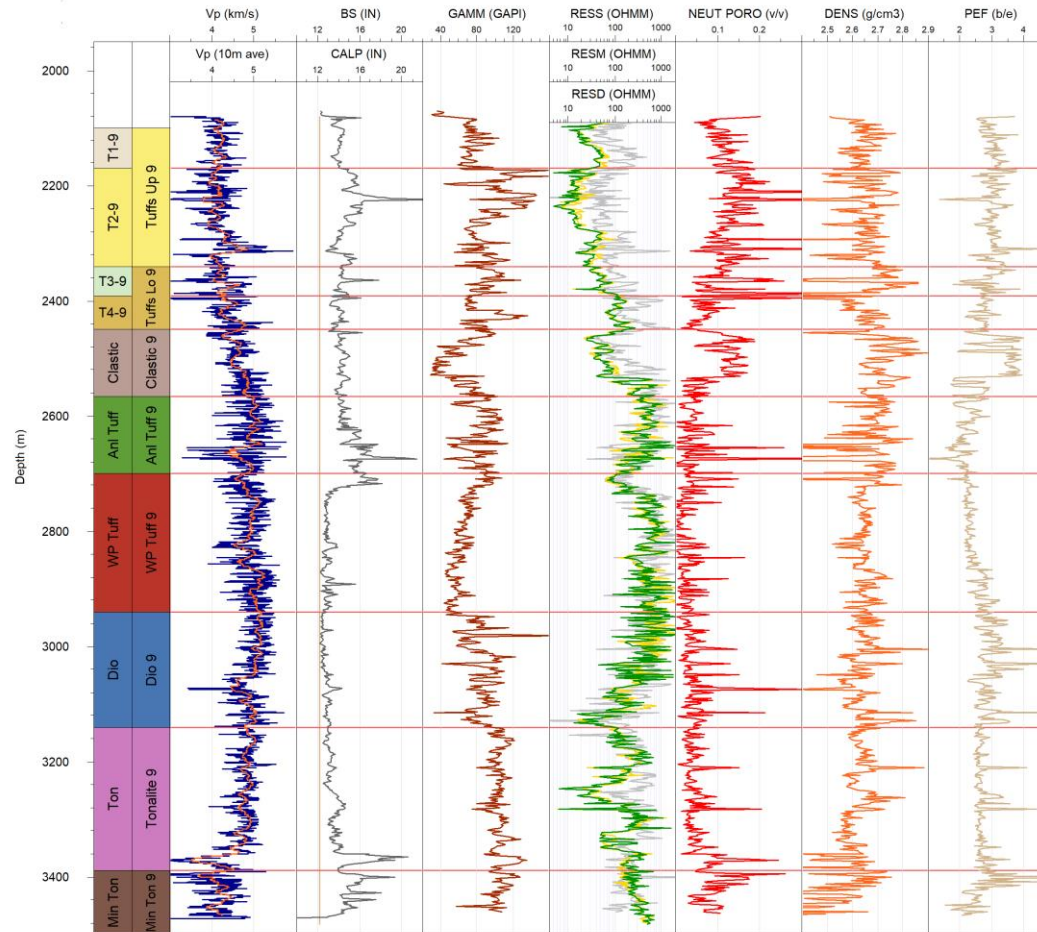


Figure 3.13. NM9 geophysical logs. The leftmost column is the geochemical units and second from the left is the geochemical groups identified in this study. V_p = P-wave velocity, V_s = S-wave velocity, BS = drilling bit size (inches), CALP = caliper log (inches), GAMM = gamma log, RESD = deep resistivity (green), RESM = medium resistivity (yellow), RESS = shallow resistivity (grey), NEUT PORO = neutron porosity, DENS = density, PEF = photoelectric factor. The red line on the V_p log shows the 10 m moving average.

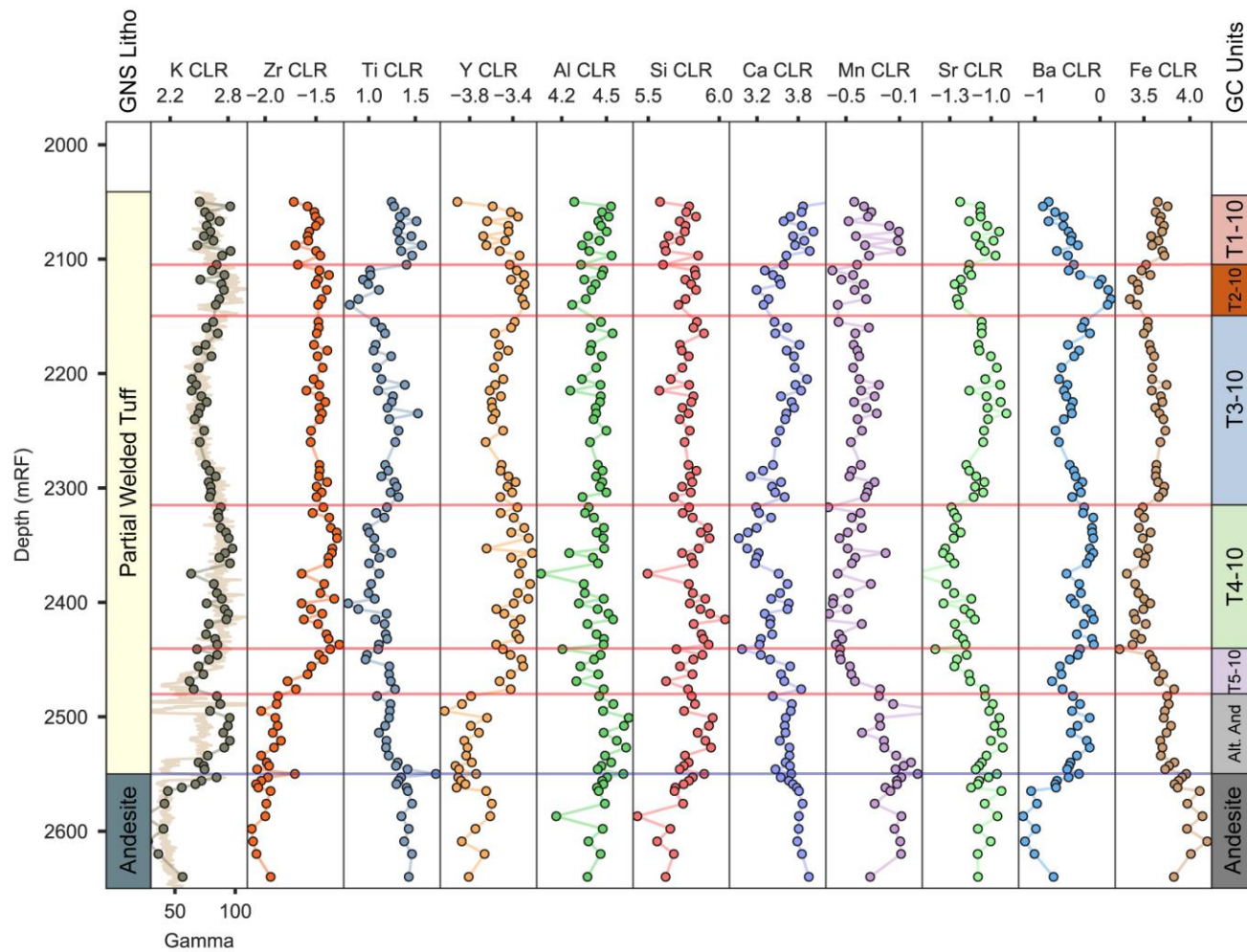


Figure 3.14. Centred-log ratio for selected pXRF data for NM10. The leftmost column is the original lithology is from Lewis et al. (2012a). The rightmost column shows the geochemical units defined in this study. Red lines across the log indicate horizons defined by immobile elements, blue lines by mobile elements.

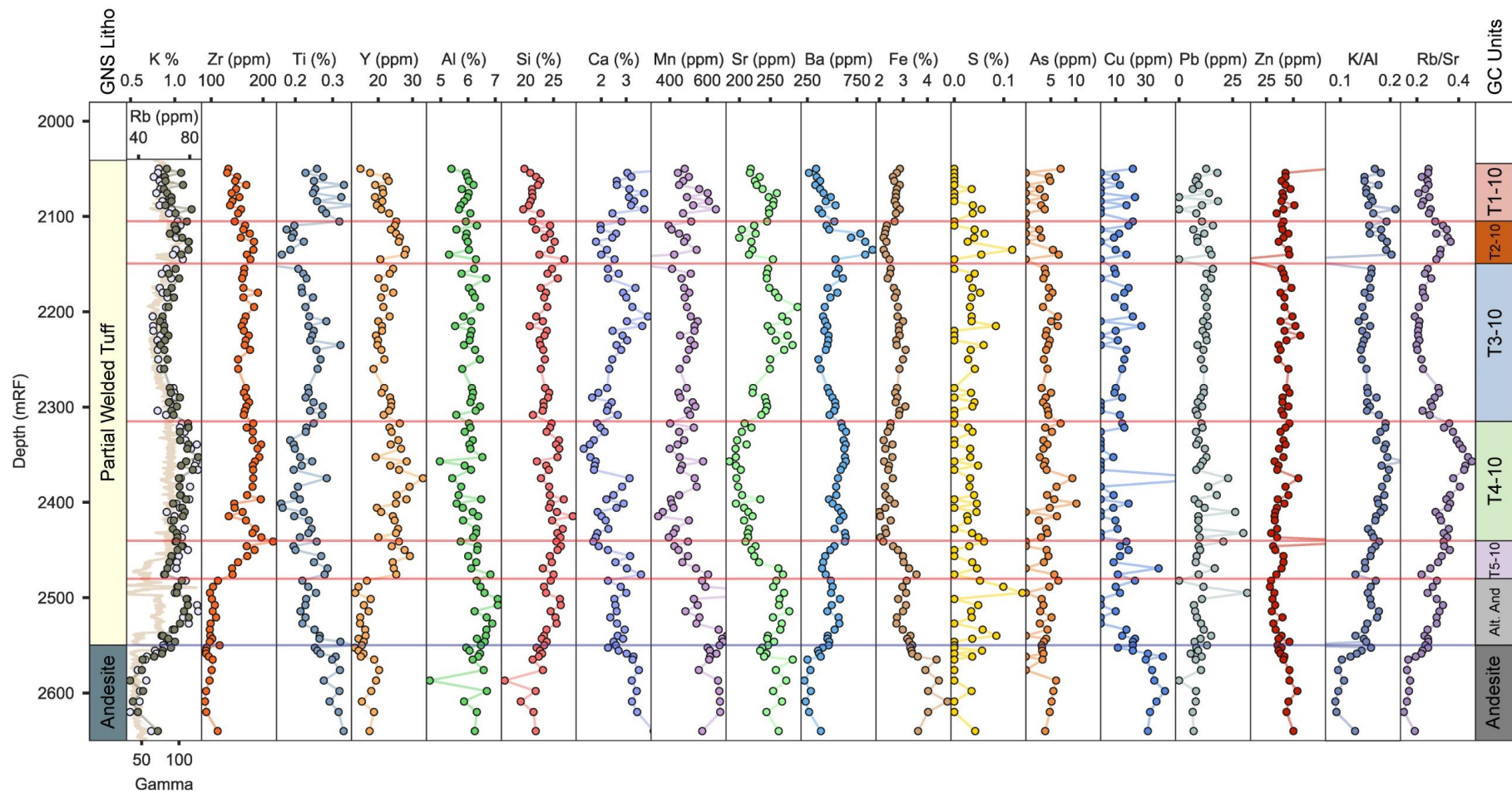


Figure 3.15. NM10 pXRF data. The leftmost column is the original lithology is from Lewis et al. (2012a). The rightmost column shows the geochemical units defined in this study. Red lines across the log indicate horizons defined by immobile elements, blue lines by mobile elements.

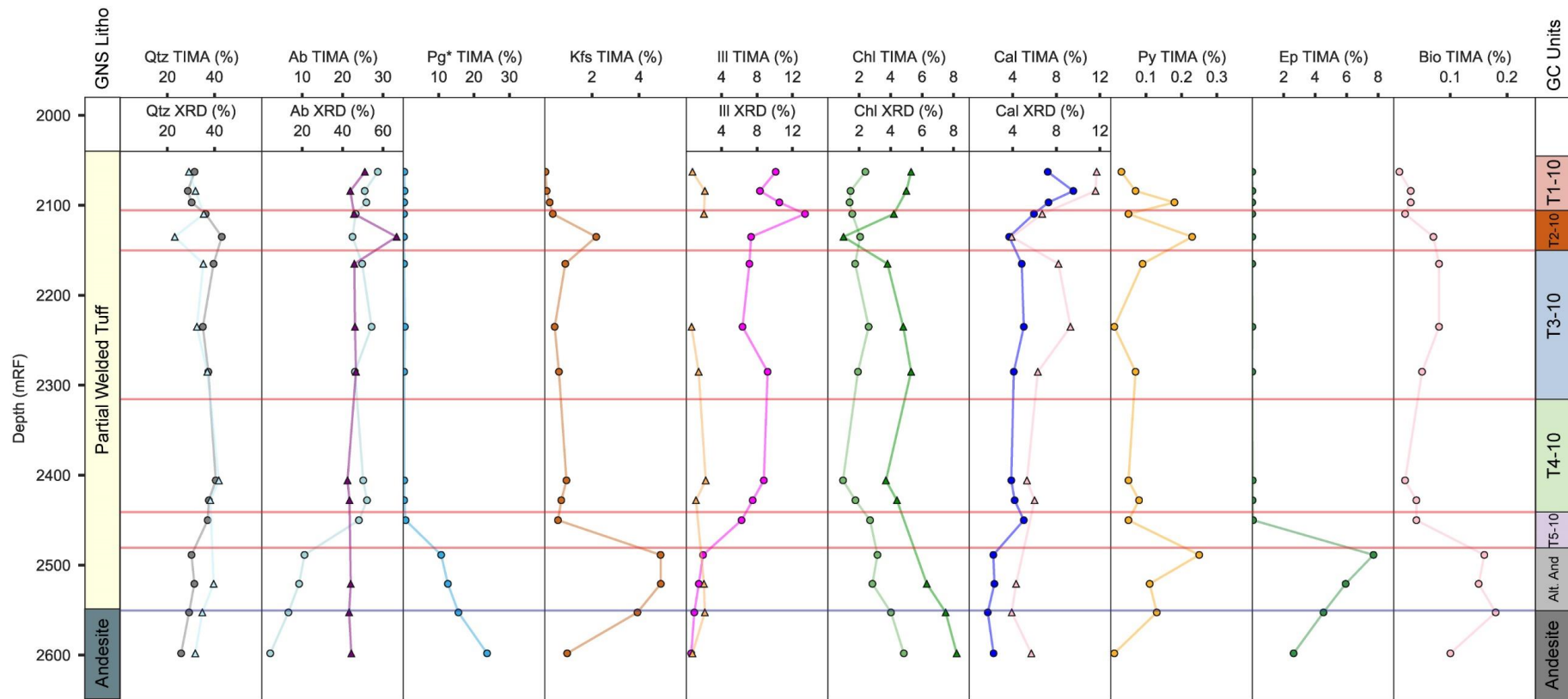


Figure 3.16. Mineral abundance in NM10 from automated mineralogy (TIMA) and quantitative XRD. The leftmost lithological column is the original lithology from Lewis et al. (2012b). Geochemical units identified in this study are in the last column on the right. TIMA data points are shown as circles and XRD data are shown as triangles. Qtz = quartz, Pg* = plagioclase, Ab = albite, Kfs = potassium feldspar, Ill = illite, Chl = chlorite, Cal = calcite, Py = pyrite, Ep = epidote, Bio = biotite.

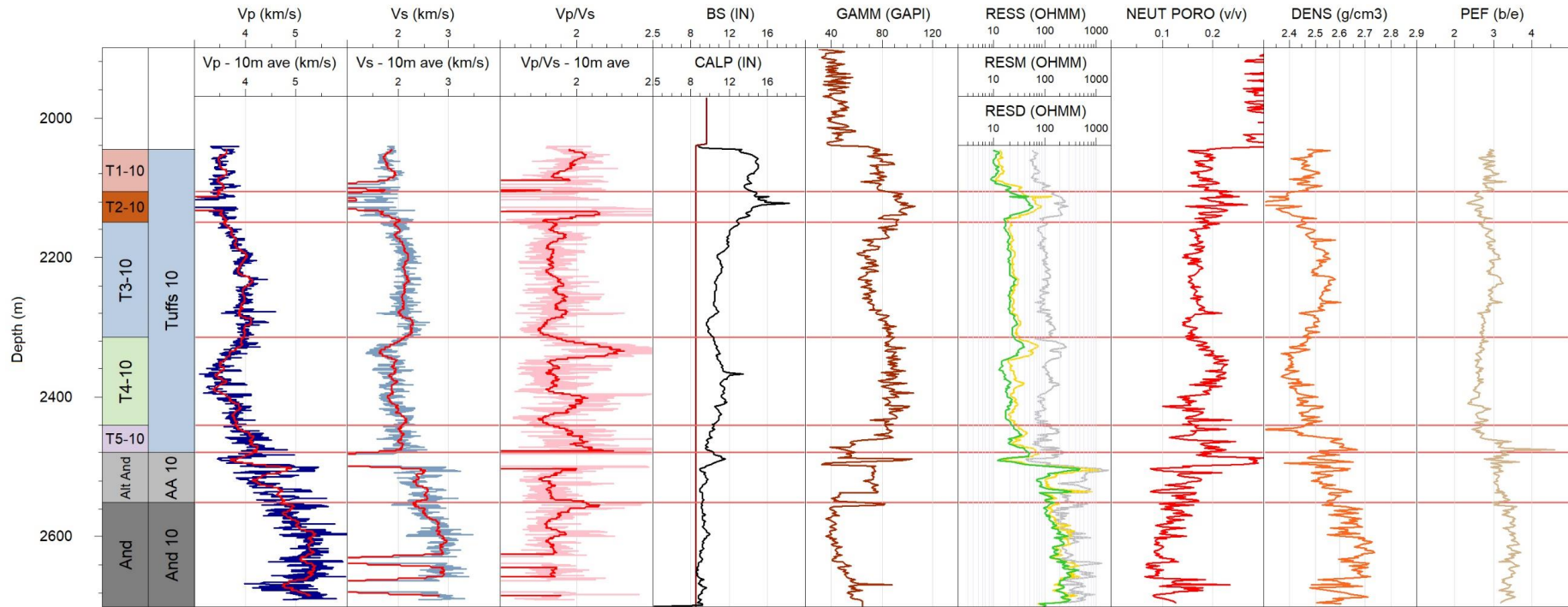


Figure 3.17. NM10 geophysical logs. The leftmost column is the geochemical units and second from the left is the geochemical groups identified in this study. Vp = P-wave velocity, Vs = S-wave velocity, BS = drilling bit size (inches), CALP = caliper log (inches), GAMM = gamma log, RESD = deep resistivity (green), RESM = medium resistivity (yellow), RESS = shallow resistivity (grey), NEUT PORO = neutron porosity, DENS = density, PEF = photoelectric factor Red lines on the Vp, Vs and Vp/Vs logs show the 10 m sliding average.

3.3.1 Geochemical units

The original lithologic units that were identified in the post-drilling geological analysis were readily apparent in the pXRF data in all cases (e.g. change from Tahorakuri Formation to intrusion in NM9 and to andesite in NM10). Relatively small but significant depth refinements of approximately ± 20 m to the contacts for the major formation contacts were suggested by the pXRF data for NM8 and NM9 (Figure 3.7 and Figure 3.11). By contrast, the contact between the Tahorakuri Formation and underlying andesite in NM10 from the pXRF data is ~75 m higher than the original interpretation of Lewis et al. (2012b) based on visual logging of the drill cuttings (Figure 3.15). The andesite contact suggested by the pXRF data is also consistent with the TIMA and XRD mineralogy (Figure 3.16) and the petrophysical logs (Figure 3.17). A possible explanation for the difference is the very fine-grained nature of the cuttings (<1 mm) over this depth range and the highly altered nature of the top part of the andesite (it is apparent from the automated mineralogy and XRD data that the uppermost andesite is highly-altered to chlorite, epidote and K-feldspar) which, together with the small size of the drill cuttings, may have made visual identification of a change to andesite difficult. Another possibility is the uppermost andesite unit ('Altered Andesite') may be an andesitic breccia.

NM8

The logged section of NM8 passes through tuffs and a welded ignimbrite of the Tahorakuri Formation (Appendix A.4). Hydrothermal alteration throughout the logged section was strong too intense to quartz, pyrite and illite (phyllic alteration) with minor overprinting of calcite, epidote and chlorite (propylitic alteration) (Lewis et al., 2012a).

The first two units in NM8 (T1-8 and T2-8) between the start of the logged section at 1230 mRF to 1375 mRF depth are tuffs, separated mainly on the basis of changes in K (and Rb) and Ca (and Sr). Plagioclase increases and illite/muscovite decreases between Tuff Units T1-8 and T2-8 in the automated mineralogy, which suggests that the gain in K and loss of Ca between the units is driven mainly by variable alteration of plagioclase to illite/muscovite (Figure 3.7 and Figure 3.8).

The most geochemically prominent zone in NM8 occurs between 1375 – 1415 mRF ('Altered Zone' or 'AZ'). The pXRF data shows clearly the abundance of Fe and S is highly elevated over this zone as is As, Cu, Pb and Zn. The cuttings sample at 1385 mRF had the highest concentration of Fe (22%), S (22%), As (456 ppm), Cu (1222 ppm), Pb (627 ppm) and Zn

(4744 ppm) (Figure 3.7). The XRD and automated mineralogy data from the same depth confirms that the pyrite content is highly elevated at this depth (50% in automated mineralogy, 65% in XRD) (Figure 3.8). There is evidence of mass gain/geochemical dilution by quartz and sulphides (predominantly pyrite) throughout the zone as shown by the loss of K, Rb, Y, Mn, Ca, Sr, Ba and relative gain in Si, Fe, S, As, Cu, Pb, Zn relative to the overlying tuffs (Figure 3.6 and Figure 3.7). The marked increase in Si and accompanying decreases in Y, Mn, Al, Sr, Ba around 1400 mRF depth is most likely due to addition of quartz causing geochemical dilution. Kaolinite (1.2%) and pyrophyllite (0.1%) are also present at detectable levels in the automated mineralogy identification (Figure 3.8). This zone with abundant pyrite was recognised during drilling but was not logged as a discrete sub-unit (Lewis et al., 2012a).

The welded ignimbrite unit in NM8 has similar geochemistry to the overlying tuffs unit (T1-8 and T2-8) despite having different mineralogy in the automated mineralogy and XRD (higher chlorite, higher potassium-feldspar, higher albite and lower illite) (Figure 3.7 and Figure 3.8). Two further tuff units below the welded ignimbrite (T3-8 and T4-8) were defined based on mostly on changes in immobile elements (Zr, Y, Ti) in the CLR log (Figure 3.6). Silicon content from the pXRF is elevated for both of these units (average of 27.8%) relative to the overlying tuff units and welded ignimbrite (average of 23.7%). This appears to be driven by higher quartz content for the lower tuffs (averages of 60% from automated mineralogy and 72% from XRD for the lower two tuff units versus 40% from automated mineralogy and 44% from XRD for the overlying units) (Figure 3.8). Calcium content is also the lowest for this interval (<1%) which can be related to lower plagioclase content. Illite/Muscovite content increases over these final two intervals with a corresponding increase in K (and Rb) content. Together these observations suggest plagioclase replacement by illite/muscovite is stronger over the lowermost two units (T3-8 and T4-8) than in the uppermost (T1-8 and T2-8).

NM9

NM9 passes through a sequence of Tahorakuri Formation tuffs and volcanoclastics and into a diorite and tonalite intrusion (Figure 3.10, Figure 3.11 and Figure 3.12). Phyllic (quartz-pyrite-illite), high temperature advanced argillic (kaolinite/dickite, pyrophyllite, andalusite) and potassic (biotite, actinolite) alteration assemblages are present resulting from proximity to the diorite-tonalite intrusion (Lewis et al., 2013). Minor overprinting of propylitic (calcite, epidote and chlorite) alteration is also observed.

NM9 shows considerably more geochemical and mineralogical variation compared to the other wells. Four tuff units were defined from the start of the logged interval between 2105 and 2450 mRF based on the pXRF data. The boundary between T1-9 and T2-9 was defined based on sharp changes in Ca and K (Figure 3.11). Units T3-9 and T4-9 are defined by changes in immobile elements (Zr, Y, Al, Ti) content and sharp changes in K (and Rb) and Ca (and Sr) (Figure 3.10 and Figure 3.11). Fe, S and As contents for the seven tuffs are elevated relative to the tuff units below the clastic unit (Fe average 2.2% for upper tuffs versus 0.9% for lower, S 1.3% versus 0.1%, As 2.2% versus 0.1%). This corresponds well with higher pyrite content shown in the XRD/TIMA data for these tuffs (3.4% versus 0.8%) (Figure 3.12). Kaolinite (or dickite) is present in the four upper tuff units (T1-9 to T4-9) at ~1-2% and pyrophyllite becomes significant (~2-15%) in tuff units T3-9 and T4-9 indicating low pH alteration has occurred within these units (Figure 3.12).

A volcanoclastic ('Clastic') unit from 2450-2565 mRF appears to have been variably diluted by addition of pyrite (addition of Fe and S) (Figure 3.12). Maximum Fe and S values occur at 2515 mRF (Fe 12.5% and S 18.2%) corresponding with the lowest values for Si (15%) (Figure 3.11). Unlike the 'Altered Zone' in NM8 which is also abundant in pyrite, this zone does not appear to have had the same degree of Cu-Pb-Zn mineralisation nor much addition of As to the rock (NM8 - Figure 3.7, NM9 - Figure 3.11). A single automated mineralogy/XRD sample within this unit shows pyrite abundance to be 5.5% from automated mineralogy and 18.3% from XRD. Acidic minerals become more abundant in this unit with kaolinite increasing to 2.6% from automated mineralogy and pyrophyllite 4.5% from automated mineralogy and 8.1% from XRD (Figure 3.12). The first significant detection of andalusite (~1%) also occurs in this unit.

Directly below the clastic unit is an andalusite-pyrophyllite altered tuff unit ('Anl Tuff') from 2565-2700 mRF (Figure 3.12). Both the pXRF data and automated mineralogy/XRD data indicate very strong, acidic alteration of this unit. Silicon concentration is higher than all units above and below (average 32% versus 28%) and the automated mineralogy/XRD data from this zone shows that quartz is higher over this interval (average 63% versus 50% from automated mineralogy, average 61% versus 52% from XRD, Figure 3.12). Calcium and Sr are both strongly depleted over this interval with Ca mostly below detection levels (<0.1%) and Sr less than 50 ppm (Figure 3.11). This corresponds with very low plagioclase content (average of 1% from automated mineralogy) and very low calcite content (average of 0.01% from automated mineralogy) throughout the interval (Figure 3.12). Sulphur is also lower relative to

the overlying units, corresponding well with a marked decrease in pyrite abundance (<2%) from the TIMA/XRD. The unit has the highest abundances of acidic minerals (average of 7% from automated mineralogy and 9.5% from XRD for andalusite, 6% from automated mineralogy and 14% from XRD for pyrophyllite and 2% from automated mineralogy for kaolinite/dickite) (Figure 3.12). Together, these acidic alteration minerals make up approximately ~5-35% of the total scanned area of the TIMA samples in this section.

The tuff unit below the andalusite-pyrophyllite altered tuff (weak potassic altered tuff - 'WP Tuff') differs markedly in mineralogy and shows gradational changes in most elements with depth (Figure 3.11). Zr, Y and Ca (and Sr) all increase gradually with depth and relative to the overlying tuff unit. Conversely, Si, Ba, K (and Rb) and Al all decrease with depth. The trends suggest possible geochemical dilution by Si which is greatest at the top of the unit and is progressively reduced with depth. The TIMA-XRD data show that quartz abundance is lower and that the amount of feldspar (classified as plagioclase in TIMA and andesine in XRD) is substantially higher than the overlying andalusite-pyrophyllite altered unit (30% in automated mineralogy, 48% in XRD) (Figure 3.12). Acidic minerals are less abundant than the overlying unit, but are still present in measurable amounts for the TIMA analyses (andalusite 0.6%, pyrophyllite 0.4%, kaolinite 0.3%). There is a marked decrease in illite/muscovite relative to all overlying tuff units and an increase in chlorite content is indicated in the XRD data (~4%) (although this is not as apparent in the automated mineralogy data which gave chlorite abundance of ~0.5%) (Figure 3.12). The first measurable occurrences of biotite (0.2% in the automated mineralogy data) and amphiboles (2% automated mineralogy, 2.5% XRD, detected as actinolite in XRD and classified mostly as actinolite in the automated mineralogy data, but with 0.2% hornblende) occur within this unit. There is also a significant increase in Pb (10-90 ppm) and Zn (10-250 ppm) content at the base of this unit relative to all overlying units (Figure 3.11).

Below the 'WP tuff' unit lies the quartz-diorite intrusion, evident in the pXRF data as a step change in immobile elements Zr, Ti and Y and in mobile elements Ba and K (Figure 3.11). Deeper step changes in Ba, Mn, K, Si, Zr and Y correlate well with the change from diorite to tonalite intrusion (Figure 3.11). The interpreted diorite and tonalite contacts from the pXRF data agree well with the original interpreted contacts (Figure 3.11). The final geochemical unit in NM9 is mineralised tonalite ('Min Ton') with high abundances of Cu, Pb and Zn which peak at 3425 mRF (Cu ~700 ppm, Pb ~200 ppm and Zn ~5265 ppm) (Figure 3.11).

The transition to intrusion diorite and tonalite is marked by an increase in K-feldspar (up to 7%), which declines with depth (Figure 3.12). Plagioclase is the dominant feldspar within the quartz diorite (up to 35%) which declines in abundance with depth. Albite abundance shows an opposite trend, increasing from <1% within the quartz diorite to 7-15% within the lowermost mineralised tonalite unit. Illite/muscovite content also appears to increase with depth, whereas chlorite decreases with depth within the intrusions. Biotite and amphiboles are present in the uppermost quartz diorite unit. Calcite content increases (1-3%) in the last two automated mineralogy/XRD samples and epidote is relatively high (~1%) for the last sample within the mineralised tonalite (Figure 3.12).

NM10

The logged section of NM10 passes through Tahorakuri Formation tuffs and into andesite, typical of other wells in the southern part of the Ngatamariki field (Figure 3.1). Both the Tahorakuri Formation tuffs and andesite are propylitically altered with an alteration assemblage more typical of geothermal reservoirs elsewhere within the TVZ and around the world (illite, chlorite, epidote, K-feldspar, albite, calcite) (Lewis et al., 2012b).

In contrast to NM9, the tuffs of the Tahorakuri Formation within NM10 show considerably less variation in geochemistry and mineralogy (Figure 3.15 and Figure 3.16). Five geochemical units were however identified within the Tahorakuri Formation based on immobile elements (Ti and Y) and changes in mobile elements (Sr, Ba, K and Fe). The T2-10 unit shows the most marked changes in geochemistry and mineralogy relative to the other tuffs. This unit is marked by an increase in K and Si, decrease in Ca and Fe and a step change in Ba content which doubles from ~400 to 800 ppm (Figure 3.15). The automated mineralogy and XRD data show some disagreement for a number of minerals for this unit (e.g. automated mineralogy shows a peak in quartz content where XRD shows a minimum), but based on the changes in the geochemistry, it is likely that the zone is higher in quartz (as shown by the automated mineralogy data, but not the XRD data, and corresponding with an increase in Si in the pXRF data) and higher in K-feldspar and/or illite (as shown by the automated mineralogy data corresponding with an increase in K) (Figure 3.15 and Figure 3.16).

The T3-10 unit shows gradual changes in K, Ca, Sr and Ba within the unit (Figure 3.15). These changes appear to be driven by variation in illite (controlling K content) and calcite (controlling Ca, Sr and Ba) seen in the XRD and automated mineralogy data (higher calcite at the top of the unit is apparent in the XRD data and increasing illite is apparent in the automated

mineralogy data). However, there is disagreement between the XRD and automated mineralogy data for illite and calcite abundance (Figure 3.16).

The T5-10 tuff unit shows a gradual decrease in Zr without a change in Y content. The unit also shows gradational changes in Fe, Sr and Ba (Figure 3.15). Although the unit shows gradational changes in Zr, Fe, Sr and Ba to values similar to the underlying andesite, it appears more likely that it is part of the Tahorakuri Formation tuff units, rather than part of the andesite based on the mineralogy being more similar to the tuffs than the andesite (high albite, low K-feldspar, low epidote) (Figure 3.16).

The transition to andesite is marked by a sharp decrease in Y and consistently low Zr content (Figure 3.15). This is accompanied by an increase in Mn, decrease in Si, increase in Ca and Sr, decrease in Ba and an increase in Fe. Two sub-units of the andesite were identified based on step changes in Y, Ca, Ba and Fe (Figure 3.15). There is a clear change in mineralogy between the Tahorakuri Formation and andesite from the automated mineralogy and XRD data with the andesite having lower quartz, higher plagioclase, lower albite (automated mineralogy data only), higher K-feldspar, higher epidote and higher biotite. Both the XRD and automated mineralogy show chlorite content increasing within the andesite and the automated mineralogy data furthermore shows a decrease in illite abundance (Figure 3.16).

3.3.2 Seismic Velocity

Seismic velocity logs are presented in Figure 3.9, Figure 3.13 and Figure 3.17, and the distribution of seismic velocity values for each geochemical unit is shown in box-whisker plots in Figure 3.18, Figure 3.19 and Figure 3.20 for V_p, V_s and V_p/V_s respectively. As most of the V_p and V_s datasets for each unit are generally not normally distributed, the variation of velocity is described by the 5th and 95th percentiles ('P5-P95') in the proceeding sections so as to exclude outliers.

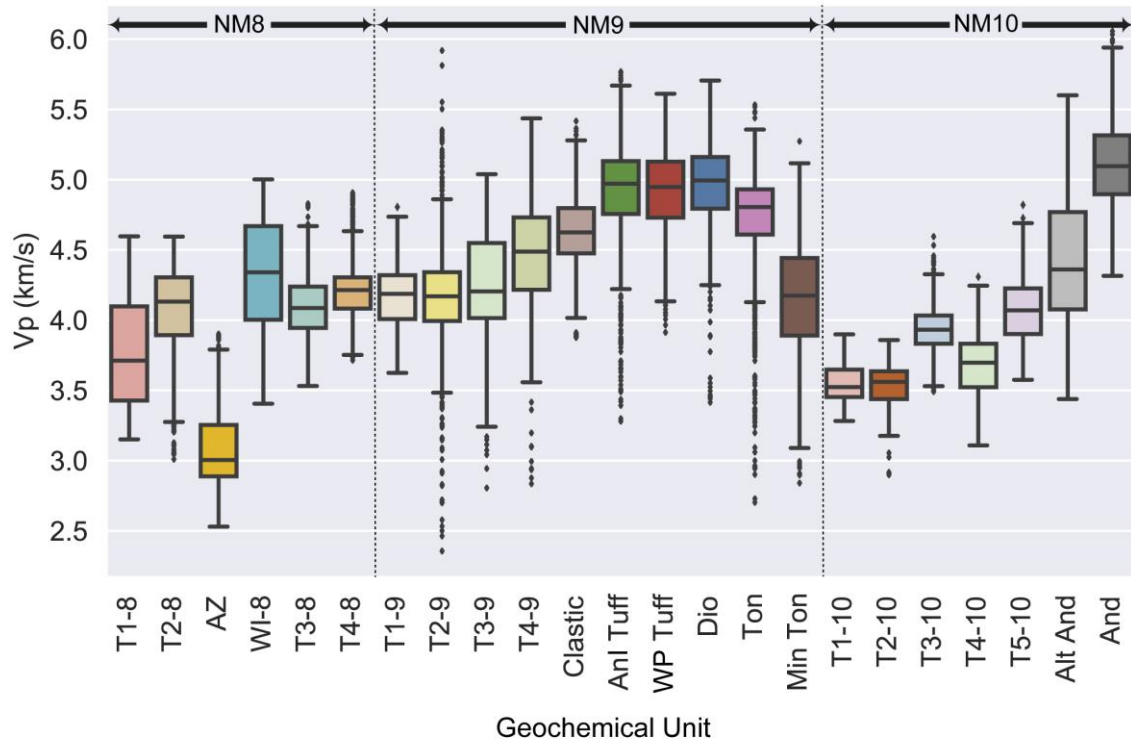


Figure 3.18. Box and whisker plot of Vp (km/s) for each geochemical unit. The ends of the box are the upper and lower quartile (i.e. 50% of values are within the box) with the black line in the box the median value. The black lines with ticks at the end indicate the maximum and minimum values (excluding outliers that are defined as values that are outside 1.5 times the interquartile range). Outliers are the black dots outside of the ticks.

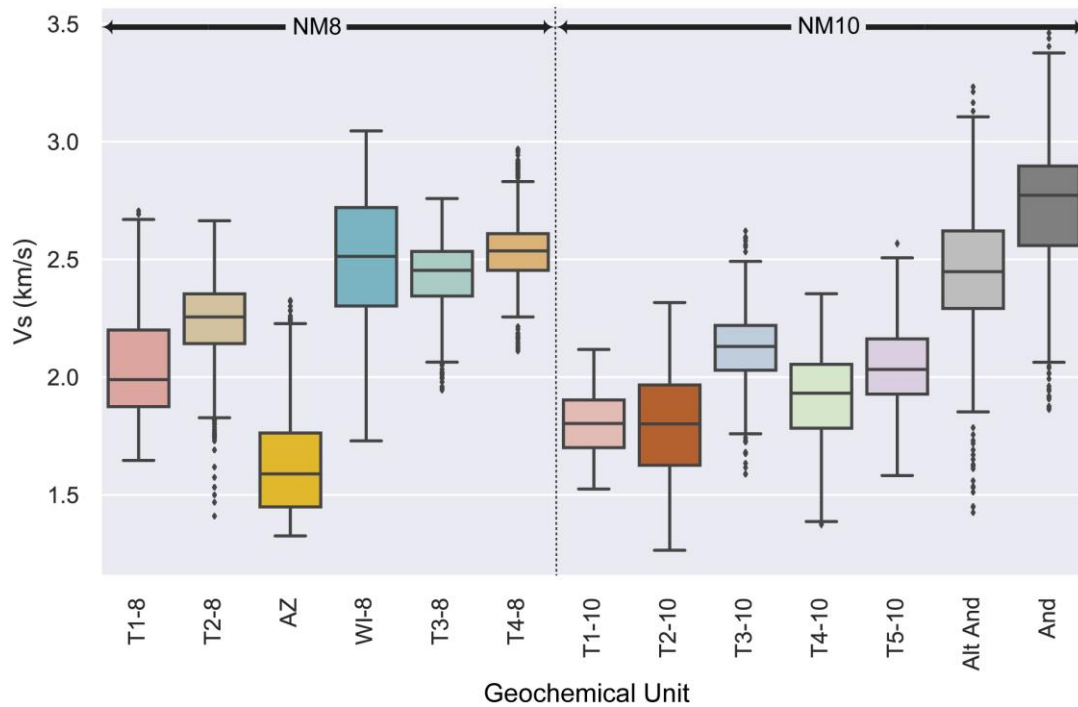


Figure 3.19. Box and whisker plot of Vs (km/s) for each geochemical unit for NM8 and NM10. The ends of the box are the upper and lower quartile (i.e. 50% of values are within the box) with the black line in the box the median value. The black lines with ticks at the end indicate the maximum and minimum values (excluding outliers that are defined as values that are outside 1.5 times the interquartile range). Outliers are the black dots outside of the ticks.

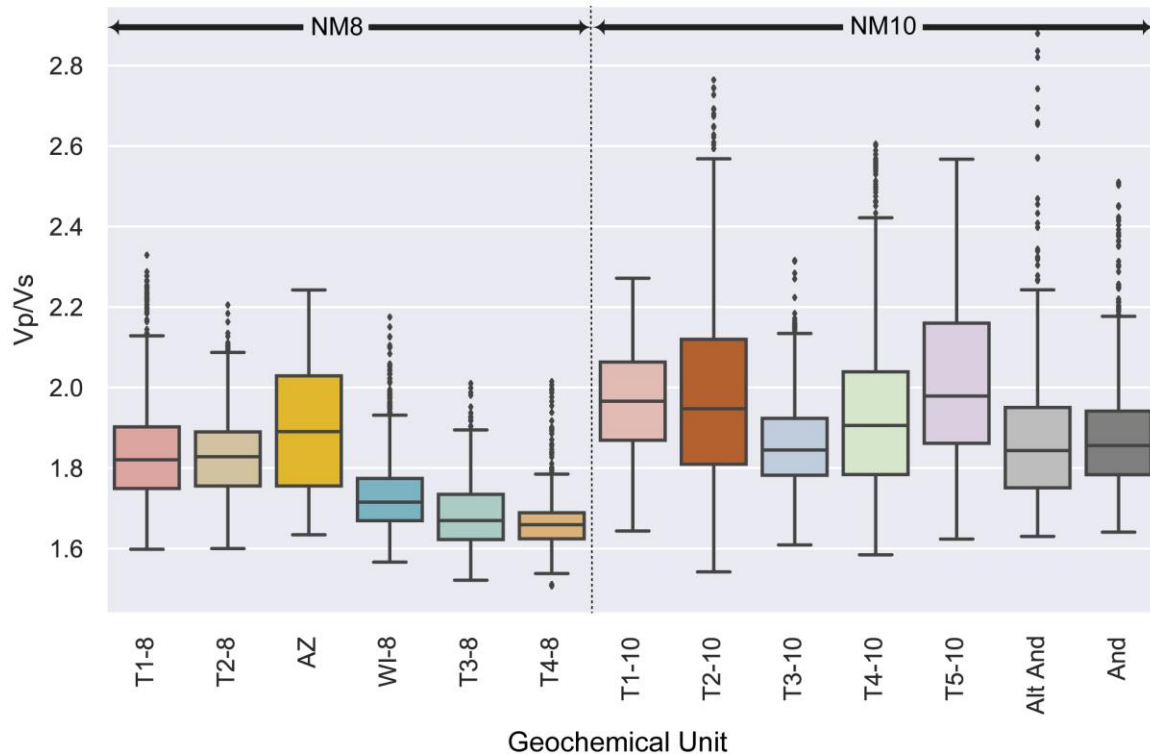


Figure 3.20. Box and whisker plot of V_p/V_s for each geochemical unit for NM8 and NM10. The ends of the box are the upper and lower quartile (i.e. 50% of values are within the box) with the black line in the box the median value. The black lines with ticks at the end indicate the maximum and minimum values (excluding outliers that are defined as values that are outside 1.5 times the interquartile range). Outliers are the black dots outside of the ticks.

NM8

Three of the four tuff units (T2-8 – T4-8) for NM8 have similar V_p with a mean of 4.13 km/s and P5-P95 of 3.51-4.46 km/s. The exception is the uppermost T1-8 unit, which has a generally lower but wider range of V_p (P5-P95 of 3.26-4.40 km/s; mean of ~3.74 km/s). There is a marked difference between the upper (T1-8, T2-8) and lower (T3-8, T4-8) tuffs for V_s (upper tuffs P5-P95 of 1.77-2.48 km/s; mean of 2.17 km/s and the lower tuffs P5-P95 of 2.24-2.69 km/s; mean of 2.48 km/s). Again, the T1-8 unit is an exception and has the lowest V_s values of the tuffs (P5-P95 of 1.68-2.47 km/s; mean of 2.03 km/s). The differences in V_s for the tuffs are also reflected in the V_p/V_s values with lower V_p/V_s for the lower tuffs (upper tuffs P5-P95 of 1.66-2.06; mean of 1.83 and lower tuffs P5-P95 of 1.58-1.80; mean of 1.67).

The altered zone (AZ unit) has by far the lowest Vp and Vs of all the units (P5-P95 of 2.64-3.63 km/s; mean of 3.04 km/s for Vp and P5-P95 of 1.38-2.02 km/s; mean of 1.60 km/s for Vs). The welded ignimbrite unit (WI-8) has variable but generally higher Vp and Vs than the tuff units in the well (P5-P95 of 3.70-4.90 km/s; mean of 4.32 km/s for Vp; and P5-P95 of 2.08-2.87 km/s; mean of 2.50 km/s for Vs).

NM9

Tuffs T1-9 and T2-9 have similar Vp with P5-P95 of 3.61-4.65 km/s and a mean of 4.16 km/s (Figure 3.13). Below this, Vp gradually increases from T3-9 through to T4-9 and into the elastic unit below the tuffs, which have an average Vp of 4.57 km/s. Vp is consistently high throughout the andalusite altered tuff ('Anl Tuff') and weak potassic altered tuff ('WP Tuff'), which together have a mean Vp of 4.89 km/s and P5-P95 of 3.28-5.37 km/s. However, there are several zones of lower Vp within these two units where the 10 m sliding average Vp lowers to around 4.5 km/s (Figure 3.13). The quartz diorite ('Dio') has similarly high Vp with an average of 4.95 km/s and P5-P95 of 4.49-5.35 km/s. About half way through the diorite, Vp values drop slightly to approximately 4.8 km/s which continues through the tonalite unit ('Ton'). Vp is substantially lower and more variable within the mineralised tonalite ('Min Ton') unit which has an average of 4.17 km/s and P5-P95 of 3.37-4.74 km/s.

NM10

The tuffs for NM10 (T1-10 to T5-10) have less variation in velocity than in NM9 and NM8 (P5-P95 of 3.38-4.17 km/s; mean of 3.78 km/s for Vp and P5-P95 of 1.58-2.31 km/s; mean of 1.94 km/s for Vs (Figure 3.17). Vp and Vs data for the T2-10 unit are limited presumably due to the borehole being washed out over this interval (average caliper shows this section of the borehole to be >8 inches wider than the bit size for most of the unit) (Figure 3.17). As expected, the Vs log appears to be more severely affected than the Vp log by the oversized borehole in this section of the well. The Vp log shows gradual changes through the T3-10 and T4-10 tuffs that to some extent appear to mirror the caliper log with lower Vp correlating with larger hole size and vice versa (Figure 3.17). However, the Vs log for these units does not appear to mirror the caliper log, showing a more abrupt change from P5-P95 of 2-2.3 km/s for T3-10 to P5-P95 of 1.7-2.1 km/s for T4-10. As the Vs log does not appear to be affected by the borehole condition, it appears that the Vp log over this section is reflecting changes in the formation. The transition from Tahorakuri Formation tuffs to andesite is associated with a gradual increase in Vp (from ~4 to 5 km/s) and Vs (from ~2 to 2.5 km/s) through the altered andesite unit ('Alt

And’). The Vs log has no measurements for an approximately 25 m zone at the top of the altered andesite (‘Alt And’), the same zone showing lower Vp (~3.5 km/s). Vp and Vs values are consistently high for the andesite (‘And’) unit with average Vp of 5.14 km/s and P5-P95 of 4.65-5.60 km/s and average Vs of 2.79 km/s and P5-P95 of 2.41-3.13 km/s. These are the highest velocities measured out of all the wells. There are two zones within the andesite where there are no Vs measurements and Vp also drops over these intervals (Vp ~4.7 km/s at 2630 mRF and ~4.2 km/s at 2670 mRF).

3.3.3 Relationships Between Seismic Velocity, Neutron Porosity and Density

Porosity

Figure 3.21 shows kernel density element (KDE) plots of Vp versus porosity (from the neutron porosity log which is available for NM9 and NM10) for each geochemical group. Shown on the plots is the Wyllie time average Vp-porosity relationship for pure quartz (6 km/s) and water (1.5 km/s) (Wyllie et al., 1956). The tuffs of NM10 and the uppermost tuffs of NM9 (T1-9 to T2-9) plot reasonably well along the Wyllie time average line whereas all others show some deviation from the line. Most data are below the line, suggesting that either the elastic moduli of the mineral constituents are on average lower than that of quartz and/or that the elastic moduli of the rock and pore space is not well described by a simple homogenous mixture of quartz and water in spherical pore spaces as is assumed for the Wyllie equation (e.g. fracturing). The exceptions are the clastic unit in NM9 (above ~10% porosity) and the two andesite units in NM10 which plot above the line, suggesting that the elastic moduli of the matrix minerals are on average higher than quartz. The tuffs of NM9 have lower porosity and higher Vp than those of NM10 (P5-P95 of 0-17%; mean of 7.5% porosity and P5-P95 of 3.83-5.29 km/s; mean of 4.59 km/s Vp for NM9 and P5-P95 of 14-22%; mean of 18% porosity and P5-P95 of 3.38-4.17 km/s; mean of 3.78 km/s Vp for NM10). There is a particularly marked decrease in porosity from the top of the andalusite tuff (‘Anl Tuff’) in NM9 with P5-P95 porosity of 4-20% and mean of 12% above the unit and P5-P95 of 0-9% and mean of 4% below (Figure 3.13).

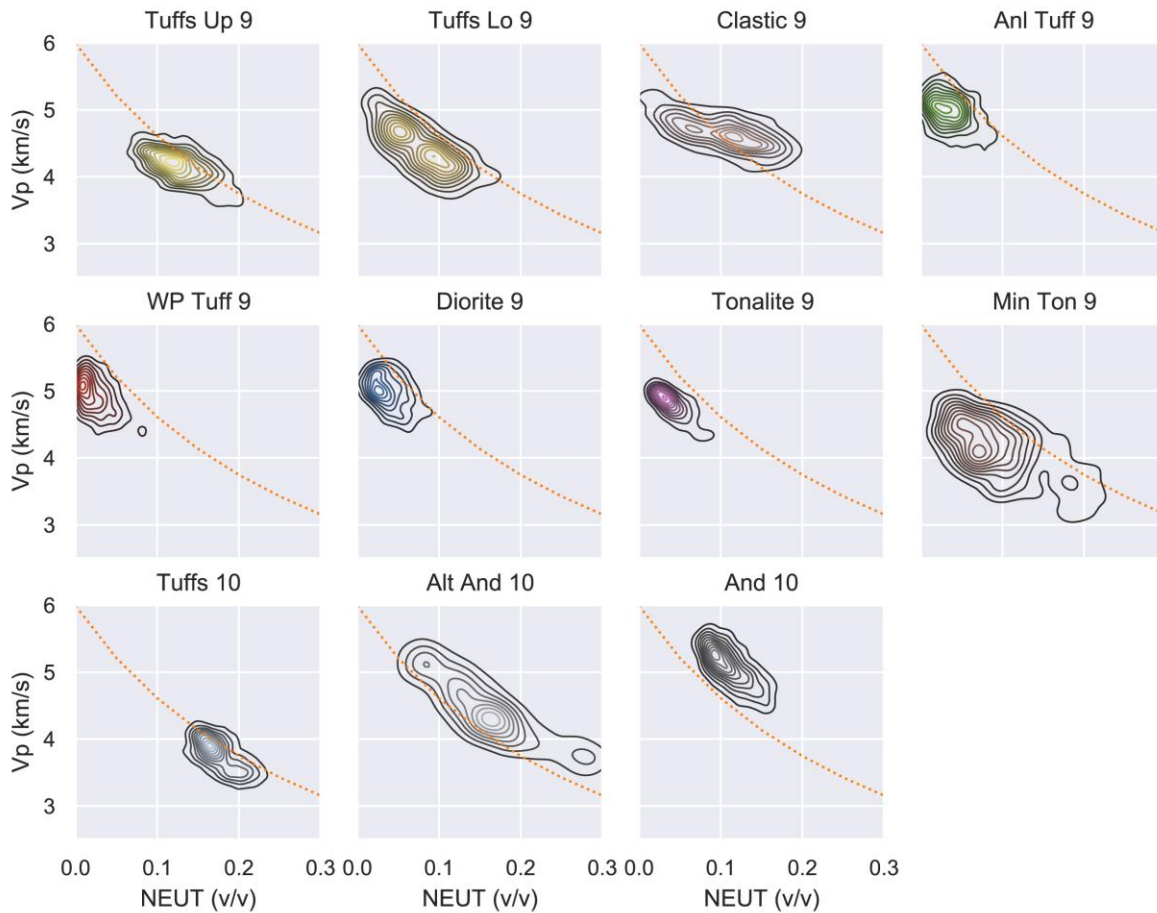


Figure 3.21. Kernel Density Element (KDE) plot of V_p versus neutron porosity for the geochemical groups (as shown in Figure 3.9, Figure 3.13 & Figure 3.17). The orange line shows the Wyllie Time Average V_p -Porosity relationship assuming quartz velocity of 6 km/s and water velocity of 1.5 km/s.

Density

Figure 3.22 shows kernel density element (KDE) plots of V_p versus density for each geochemical group. Shown on the plots is a line for pure quartz density (2.65 g/cm^3). A number of the units have densities that range above that of quartz density; the tuffs in NM9 ($2.50\text{-}2.76 \text{ g/cm}^3$), the clastic unit in NM9 ($2.59\text{-}2.85 \text{ g/cm}^3$), the andalusite tuff in NM9 ($2.32\text{-}2.77 \text{ g/cm}^3$) and the andesite in NM10 ($2.58\text{-}2.72 \text{ g/cm}^3$). The tuffs in NM9 are considerably denser than those in NM10 ($2.38\text{-}2.57 \text{ g/cm}^3$ with a mean of 2.47 g/cm^3 for the NM10 tuffs). All units in NM10 appear to have a linear relationship between V_p and density, whereas there are no clear relationships for units in NM9.

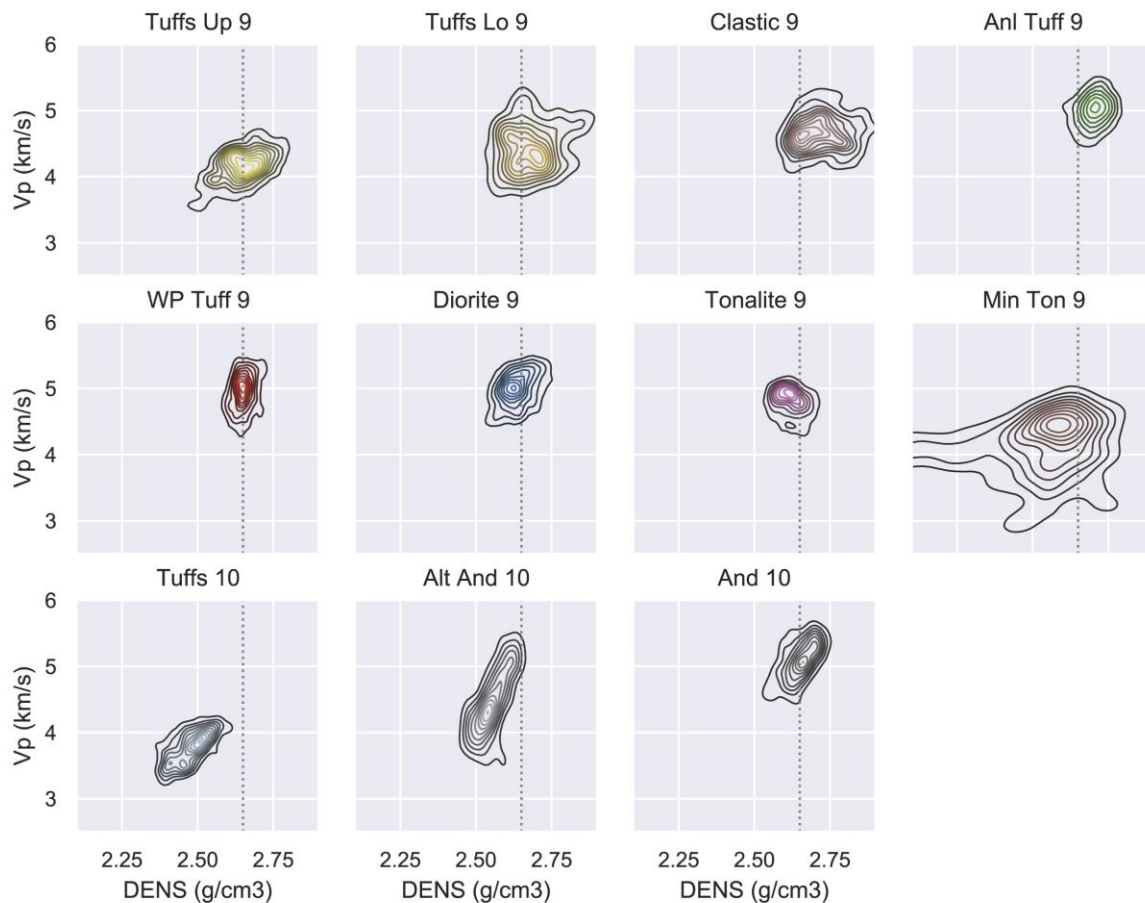


Figure 3.22. Kernel Density Element (KDE) plot of V_p versus density for the geochemical groups (as shown in Figure 3.9, Figure 3.13 & Figure 3.17). The dashed black line shows the density of quartz (2.65 g/cm^3).

3.4 Discussion

Overall, the petrophysical logging dataset demonstrates that matrix porosity is the dominant control of velocity, however closer examination of the log responses, geochemistry and mineralogy reveals that other factors, such as the elastic moduli of mineral constituents and fracturing are also important. The influence of magmatic alteration (advanced argillic, phyllic, potassic) above the Ngatamariki tonalite/quartz-diorite intrusion is also apparent in the geochemistry, mineralogy and petrophysical datasets. Ductile deformation extending approximately 400m directly above the intrusive body has caused very low porosity (<5%) and consequently high seismic velocity ($\sim 5 \text{ km/s}$).

3.4.1 NM8

The uppermost tuff in NM8 (T1-8) has lower and more variable velocity than the other tuffs in NM8 for both V_p and V_s (Figure 3.9, Figure 3.18 and Figure 3.19). There is no clear explanation for the relative lower velocity of this unit, however the variability of the velocity and some mineralogical evidence points to more abundant open fractures as a possible factor (higher calcite content than the other tuff units and calcite-wairakite veins in the TIMA scans, both suggesting stronger alteration by near neutral pH fluids (Browne, 1978) associated with the more recent hydrothermal system).

The altered zone ('AZ' unit) is distinct in its geochemistry, mineralogy and geophysical character. The zone appears to be highly altered with signs of geochemical dilution by the addition of quartz and pyrite as well as Cu-Pb-Zn mineralization (Figure 3.7). The very high abundance of sulphides, Cu-Pb-Zn mineralization and the elevated kaolinite and pyrophyllite abundance suggests this is a permeable zone that experienced high sulphidation and acidic alteration during emplacement of the Ngatamariki intrusion. Overprinting of calcite and wairakite in the TIMA analysis demonstrates that neutral pH fluids, similar to those in the currently active system, have resulted in more recent alteration. Therefore, the most likely explanation for the dramatically lower V_p and V_s for this zone is that it has abundant open fractures. Partial circulation losses that began to occur during drilling around this depth further indicates this zone is permeable.

The welded ignimbrite (WI-8) has a zone of particularly high velocity from 1440 to 1495 mRF where V_p is mostly between 4.49-4.94 km/s and V_s is mostly between 2.51-2.94 km/s (Figure 3.9, Figure 3.18 and Figure 3.19). There is also a gradual increase in velocity with depth from the top of the unit. As the geochemistry and mineralogy remains relatively unchanged within the unit (Figure 3.7 and Figure 3.8), a possible explanation for this is a gradual increase in welding with depth at the top of the unit, which is a commonly observed feature of welded ignimbrites (Streck and Grunder, 1995). V_s is notably higher for the welded ignimbrite than the overlying tuffs and V_p/V_s correspondingly lower (Figure 3.19 and Figure 3.20). These variations can again be explained by the welding resulting in very low matrix porosity and permeability.

The lower tuffs in NM8 (T3-8 and T4-8) have higher V_s than the tuffs above the mineralised zone (T1-8 and T2-8), which is also apparent as lower V_p/V_s (Figure 3.19 and Figure 3.20). Higher quartz (and Si), higher illite and lower plagioclase for the lower tuffs, suggests that

stronger phyllic alteration during the Ngatamariki intrusion event has resulted in quartz deposition in pore spaces which elevated velocities, although no porosity log data is available to verify this interpretation (Figure 3.7 and Figure 3.8).

3.4.2 NM9

The upper (T1-9 and T2-9) and lower tuffs in NM9 (T3-9 and T4-9 units) appear to show the competing effects of fracturing and quartz deposition acting to lower and raise V_p respectively (Figure 3.11, Figure 3.12 and Figure 3.13). The tuffs appear to plot parallel to the Wyllie time-average velocity-porosity relationship with a shift to lower velocities (Figure 3.21). Since the bulk mineralogy of these tuffs is dominated by quartz (~50-60%) and plagioclase (~5-20%) (Figure 3.12), a possible explanation for this is fracturing. The highly variable neutron porosity, with porosity spikes exceeding 20%, as well as high variation in the velocity and density logs provide evidence for open fracturing (Figure 3.13). A gradual decrease in average porosity for the lower tuffs (T3-9 and T4-9 units, Figure 3.13) and a corresponding gradual increase in Si content (Figure 3.11) suggests stronger phyllic alteration with depth with loss of porosity due to quartz deposition.

The upper and lower tuff units have average densities close to quartz but with significant variation above and below (Figure 3.22). Higher Fe and S (Figure 3.11) due to pyrite (up to 12% in automated mineralogy for T2-9, Figure 3.12) can explain the densities greater than quartz (pyrite density ~ 5 g/cm³). Although pyrite has elastic moduli significantly higher than quartz (Rock type is a first-order control on both mineralogy and porosity, which are usually the main factors influencing the elastic moduli and density of rocks and hence their seismic velocity. The velocity of low-porosity igneous and metamorphic rocks is generally higher than sedimentary rocks, with velocities in sedimentary rocks typically controlled by variation in quartz content (Mavko et al., 2009a; Schön, 2015; Wyllie et al., 1956). Sedimentary rocks, including volcanoclastics, have a wider range of velocities due to their generally more porous nature and more diverse mineralogy. Due to the dominance of seismic surveying techniques in imaging oil and gas reservoirs, a vast amount of research, both theoretical and empirical, has been conducted on the controls of seismic velocity in sedimentary rocks.

Table 3.1), the average abundance appears to be too low to have an observable impact on V_p for these tuffs. Pyrite does however appear to have an observable impact on V_p for the clastic unit ('Clastic') between the lower tuffs and the andalusite altered ('Anl Tuff') tuff with V_p higher than would be expected for pure quartz-porosity mixing (Figure 3.21). Density for the

clastic unit is also mostly above that for quartz, with an average of 2.8 g/cm³ (Figure 3.22). Both the elevated V_p and higher density can be explained by the abundance of pyrite (5.5% from automated mineralogy and 18.3% from XRD) and consequent dilution of quartz for this unit (Figure 3.11). The abundant pyrite likely formed during the high-sulphidation mineralisation during the Ngatamariki intrusion event as supported by the presence of pyrophyllite and kaolinite in the XRD and automated mineralogy data for the clastic unit (Figure 3.12) (Chambefort et al., 2017).

There is clear evidence that alteration by a high temperature (>375 °C), low pH fluid generated during the intrusion event at Ngatamariki has dramatically altered the chemical, mineralogical and physical properties from those of the original tuff-protolith for the andalusite tuff unit ('Anl Tuff' unit). The presence of andalusite, with accompanying pyrophyllite and kaolinite, provides evidence for acidic alteration above 375 °C (Chambefort et al., 2017; Henley and McNabb, 1978; Holdaway, 1971; Tosdal et al., 2009). The aggressive acidic alteration resulted in base cation leaching as shown by the strong depletion of Ca to below detectable levels (<0.05%, Figure 3.11) and the corresponding loss of plagioclase (<2%, Figure 3.12) (Chambefort et al., 2017; Vernon et al., 1987). This was likely countered by deposition of quartz (60-65%), andalusite (5-12%) and pyrophyllite (9-19%) which together comprise over 75% of the rock (Figure 3.12).

Logged bulk density values for the andalusite tuff ('Anl Tuff') unit are mostly above that of pure quartz (Figure 3.22). Pyrite (TIMA/XRD, Figure 3.12), Fe and S (pXRF, Figure 3.11) are very low for this unit, therefore the higher density is most likely due predominantly to the higher density of andalusite (3.15 g/cm³, Schön, (2015)). Porosity is very low for the unit (0-11% with a mean of 5%) and quartz abundance is consistently high relative to the tuffs in NM10 (55-65%, Figure 3.12) as is Si (27-36% with a mean of 32%, Figure 3.11), suggesting deposition of quartz and other aluminosilicates (pyrophyllite and andalusite) may have played a part in the porosity loss. It also appears that ductile/plastic deformation has taken place within this interval due to temperatures above the brittle-ductile transition (>375°C inferred from andalusite Chambefort et al., 2017; Fournier, 1999; Violay et al., 2017) during the intrusion event. Deformed textures identified from formation image logging (FMI) over this interval provide evidence for this (Figure 3.23) (Halwa, 2013).

High V_p and very low porosity continues within the weak potassic altered tuff ('WP Tuff') unit, however the causes of this are not immediately clear from the geochemistry and

mineralogy, which are markedly different from the overlying andalusite tuff ('Anl Tuff') unit (Figure 3.11 and Figure 3.12). The high abundance of plagioclase (~30%) and low abundance of acidic minerals (andalusite ~ 0.4 %, pyrophyllite ~ 0.3 %, kaolinite ~0.3%) demonstrate this unit has not undergone the same degree of acidic alteration as the overlying andalusite tuff ('Anl Tuff') unit (Figure 3.12). The proportion of illite and quartz is also much lower than all overlying tuff units suggesting limited phyllic alteration (Figure 3.12). There also appears to be little propylitic alteration formed by more the geothermal system after the intrusion event with epidote, chlorite, calcite, albite all being <2% abundance. Together this gives the appearance that the unit has been relatively unaltered both during and after the intrusion event despite being between the andalusite altered tuff, that was >375°C and contained highly acidic fluids, and the underlying intrusion which would have been >600°C when it intruded (Christenson et al., 1997; Otamendi et al., 2009).

However, biotite (up to 0.2%) and amphiboles (up to 2.3%, mostly identified as actinolite but with 0.19% hornblende, which was also observed by Arehart et al. (2002) in NM4) identified in the automated mineralogy provide evidence of weak potassic alteration as was observed by Chambefort et al. (2017). Pb and Zn are also elevated at the base of the unit suggesting Pb-Zn mineralization due to exsolved hypersaline magmatic fluids at temperatures >500 °C as seen adjacent to intrusions in Cu-Pb-Zn porphyry systems (Figure 3.11) (e.g. Hedenquist and Lowenstern, 1994; Henley and McNabb, 1978). Given the potassic alteration, possible Pb-Zn mineralization and position of this unit directly above the intrusion, it is very likely the temperatures within the unit were once well above the brittle-ductile transition.

The FMI image log over the weak potassic altered tuff ('WP Tuff') does not show the same deformation textures as seen in the andalusite tuff ('Anl Tuff' unit), however the texture and fracture character within this unit is very different from the other volcanoclastic units in the well and in formation image logs for NM8 and NM10 (Figure 3.23). Texture is described by Halwa (2013) as 'micro-fractured', characterised by abundant, small aperture fractures (average aperture of 0.07 mm compared with an average of 0.97 mm for all fractures within the well). Approximately one quarter of the fractures over the 'WP Tuff' unit are low-angle (<20° dip, mean dip 10°, with no well-defined strike direction between 2730-2930 mRF), suggesting a very different stress regime than that which produced the bulk of fractures in the well (dip >50, dominant NE-SW striking) (Figure 3.23).

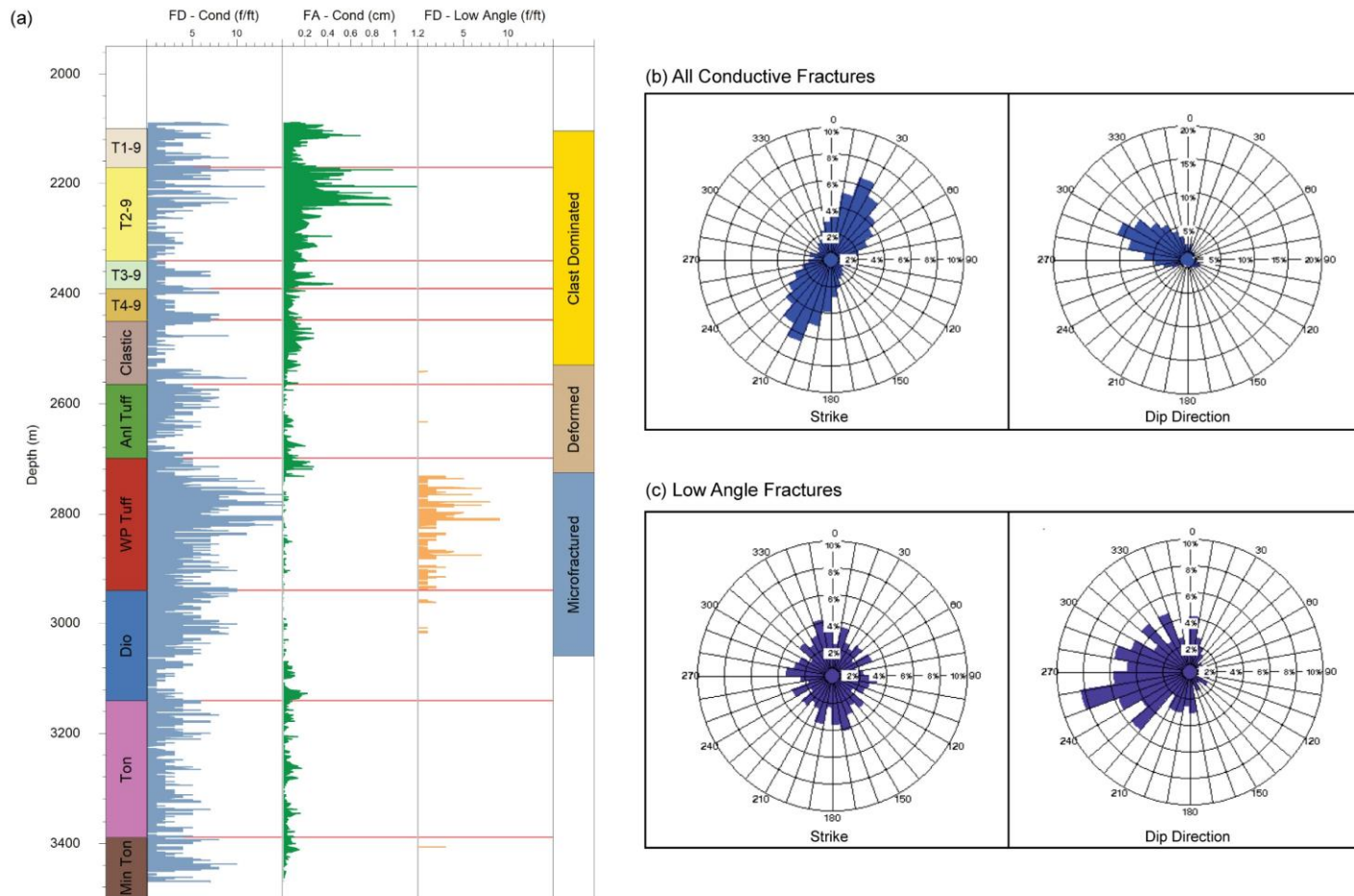


Figure 3.23. FMI log data from NM9 (a) Fracture data (FD Cond = Conductive Fracture Density, FA Cond = Conductive Fracture Aperture, FD – Low Angle = Low Angle Fracture Density. Fracture density units are fractures per foot) and textural zones (rightmost column) identified from an analysis of the FMI log in NM9. (b) Fracture strike and dip direction for all conductive fractures in the well and (c) the low angle fractures that are mostly within the ‘WP Tuff’ unit. Modified from Halwa (2013).

A possible explanation for this is hydraulic fracturing that occurred during the intrusion event when pressures close to the intrusion were close to lithostatic and pressure transients (e.g. during the release of gas from the magma) caused fracturing as was proposed by Christenson et al., (1997) for Ngatamariki, as observed in other geothermal systems where temperatures above 350°C have been encountered (Fournier, 1991; Reinsch et al., 2017) and as observed and modelled in porphyry systems (e.g. Fournier, 1999; Koide and Bhattacharji, 1975). Similar abundant low-angle fractures were identified in an FMI log from the Kakkonda geothermal system in Japan where present-day measured temperatures are 350–400°C above a granitic intrusion where measured temperatures are >500°C (Ikeuchi et al., 1998; Muraoka et al., 1998). Muraoka et al., (1998) attribute these fractures to hydraulic fracturing caused by the dehydration front associated with contact metamorphism. It is likely that quartz deposition in this zone may have also played a role in lowering porosity (e.g. Christenson et al., 1997; Scott and Driesner, 2018; White and Mroczek, 1998), however, since quartz abundance is observed to be lower in the ‘WP Tuff’ unit, this would presumably have been secondary to the closing of pore space by ductile deformation. Therefore, ductile deformation and consequent closing of pore space during the emplacement of the pluton is proposed as the explanation for the particularly high velocity and very low porosity of the weak potassic altered tuff (‘WP Tuff’ unit). This would have limited further fluid-rock reactions explaining the low amount of phyllic or propylitic alteration compared to other tuffs in NM9 and in NM10. As this unit is highly fractured, deformation whilst the intrusion event was occurring was not entirely ductile, but was likely within the ‘elastic-plastic’ zone (Fournier, 1991; Watanabe et al., 2020, 2017). It is possible also that quartz deposition played a role in lowering porosity and elevating velocity as is proposed for the other tuff units within the well.

The lack of abundant acidic alteration within the weak potassic altered (‘WP Tuff’) tuff, as is seen in the andalusite altered tuff (‘Anl Tuff’) above it, can also be attributed to the closing of pore space and rock matrix permeability by ductile deformation which limited fluid-rock interaction. It is also likely that the fluids within this zone during the intrusion event were mostly in a supercritical condition ($T > 374\text{ °C}$, $P > 221\text{ bar}$ for pure water, Reinsch et al., 2017) and therefore lacked a water phase for alteration reactions. The formation of andalusite above the WP Tuff unit demonstrates that temperatures were likely above supercritical temperature (>375 °C). The very low porosity of the WP tuff, and implied low permeability, along with the horizontal fracturing observed in the FMI log, suggest that the pressure in this zone was likely close to lithostatic and therefore above supercritical pressure (>221 bar). The

zonation of low-pH fluid above a neutral-pH supercritical fluid zone has been observed at the Krafla field where wells have produced both very acidic fluids in the zone overlying the supercritical zone and supercritical fluids themselves (Heřmanská et al., 2019). Heřmanská et al., (2019) modelled that no alteration would take place within the supercritical zone and that condensation above the supercritical zone would form a very low-pH fluid through formation of HCl and SO₄ acid. The andalusite-pyrophyllite zone ('Anl Tuff') overlying a relatively unaltered zone ('WP Tuff') at Ngatamariki in NM9 appears to reflect this process.

High velocity and low porosity continue within the upper part of the diorite intrusion ('Dio' unit) to around 3050 mRF depth (mean of 5.08 km/s, P5-P95 of 4.73-5.34 km/s). Below 3050 mRF, velocity decreases slightly to a mean of 4.81 km/s, and P5-P95 of 4.37-5.29 km/s (Figure 3.13). There are no clear reasons for the change in average velocity from the geochemistry and mineralogy, however spikes in the neutron porosity log above 10% suggest open fractures as a possible cause. There is no apparent change in velocity or porosity for the transition between the diorite and the underlying tonalite, which is largely as expected given the relatively subtle changes in bulk mineralogy for tonalite versus diorite (Figure 3.13).

The lowermost unit in NM9 ('Min Ton') has lower and more variable velocity than the overlying tonalite and quartz diorite units (Figure 3.13). The unit has similar geochemistry to the overlying tonalite with the exception of Cu, Pb and Zn which are in their highest concentrations for the well (peak values at 3430 mRF of Cu ~ 740 ppm, Pb ~ 205 ppm and Zn ~ 5470 ppm) (Figure 3.11). There are however notable differences in mineralogy with relatively high albite (~10-15%), calcite (~1.5-3%) and epidote (~0.9-1.2%) and lower plagioclase (~4%) suggesting stronger propylitic alteration (Figure 3.12). Porosity is also substantially higher and more variable within the unit than the overlying tonalite (Figure 3.13). Although there is an observable trend between Vp and porosity, there is considerably more spread in Vp-porosity space when compared to other units in this study (Figure 3.21). Numerous spikes in porosity above 10%, that generally correspond with lows in Vp, provide evidence of open-space fracturing. Taken together, the mineralised tonalite ('Min Ton' unit) appears to be a highly fractured zone that experienced mineralisation during the time of the intrusion event and propylitic alteration during more recent hydrothermal activity. The zone may represent the edge of the intrusion as Cu-Pb-Zn mineralization often occurs adjacent to intrusions in porphyry systems (Henley and McNabb, 1978).

3.4.3 NM10

The velocity-porosity relationship for the Tahorakuri Formation tuffs in NM10 follows relatively closely the Wyllie time average relationship, indicating that most of the variation in velocity can be accounted for by variation in porosity (Figure 3.21). Since the mineralogy within the tuffs is relatively constant and dominated by minerals with density close to that of quartz (quartz~30-40%, albite~20-40%, Figure 3.16), it is possible to use the density log to derive porosity. Comparison between the neutron porosity and density porosity shows that the neutron porosity is ~5-10% higher than the porosity obtained from the density log (Figure 3.24). This indicates the presence of clay-bound porosity, the neutron log being more sensitive to clay than the density log (due to the neutron log measuring H content which is in both OH and H₂O in clays) (Ellis et al., 2004). Variation in V_p also appears to be inversely correlated with the gamma log (and hence K), suggestive of the influence of illite clay, on both the porosity log and velocity log (clay-bound water) (Figure 3.17). Plotting the TIMA clay abundance versus V_p and V_s reveals a possible slight decrease in V_p and V_s with increasing illite and total clay (which is dominated by illite) for NM9 and NM10 in this study however this is not well defined (Figure 3.25).

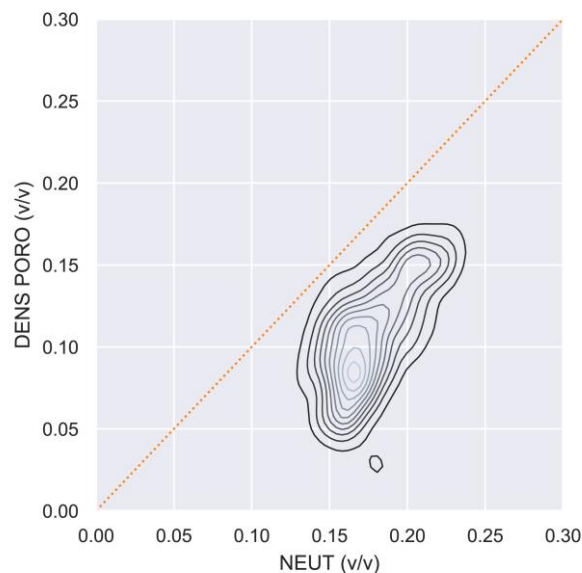


Figure 3.24. Neutron porosity versus porosity derived from the density log (using a matrix density of 2.65 g/cm³ and fluid density of 1 g/cm³) for the tuffs in NM10 ('Tuffs 10'). The neutron porosity log gives porosity ~5-10% higher than the density log which is attributed to the neutron porosity log being more affected by clays (neutron log is sensitive to hydrogen atoms in both OH and H₂O in clays whereas the density log is sensitive only to H₂O).

The transition from the Tahorakuri Formation tuffs into the andesite is clearly visible in the geochemical (Figure 3.15), mineralogical (Figure 3.16) and geophysical data (Figure 3.17). The transition in the geophysical logs is characterised by increasing velocity, decreasing porosity and increasing density whereas the transition in the mineralogy is characterised by lower quartz, lower albite, higher plagioclase, higher K-feldspar, lower illite, higher chlorite and higher epidote. The velocity variation within the andesite units ('Alt And' and 'And' units) appears to be mostly controlled by porosity but with the additional effect of more abundant higher density minerals (Figure 3.21). Both the altered andesite ('Alt And') and andesite ('And') units plot above the Wyllie-time average line, with the andesite unit being above both the quartz-porosity line and the altered andesite data. This is most likely due to the changes in bulk mineralogy resulting in an overall increase in the density and therefore elastic moduli of the rock matrix (lower quartz, higher plagioclase, higher epidote, higher chlorite) (Table 3.1, Figure 3.16). Lower illite (which is reflected in the gamma log), and overall lower total clay (illite + chlorite) suggests some of the increase in Vp and Vs in the andesites may be due to lower clay.

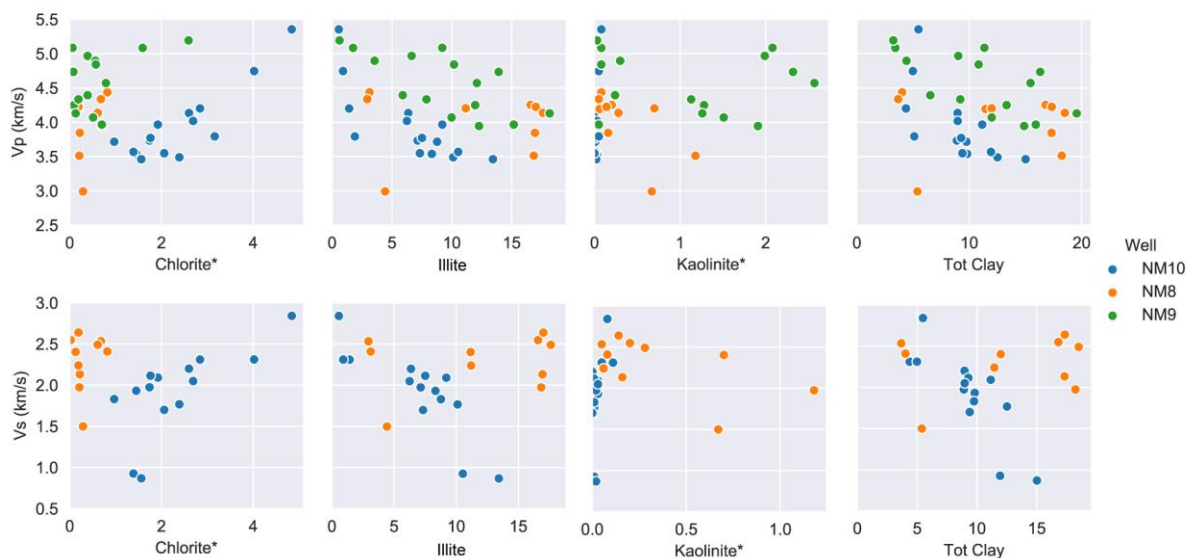


Figure 3.25. Vp and Vs versus clay content for chlorite, illite, kaolinite, and total clay (Chlorite* + Muscovite + Kaolinite*) from the TIMA data. The Vp value used is the average over a 5 m window centred on the sample depth.

There is greater variability in Vp and Vs within the altered andesite and andesite units than the overlying tuffs, which appears to be due to fracturing (Figure 3.17). A zone of particularly low Vp (relative to the rest of the andesite) occurs at the top of the altered andesite unit which corresponds to a zone of high porosity (2490 mRF depth, Vp ~3.5 km/s, porosity ~30%) and

loss of Vs signal. The highest values of epidote and K-feldspar (adularia) also occur at the top of the altered andesite unit, consistent with high permeability and fracturing at this depth (Browne, 1978). Two further zones of slightly lower Vp (~4.7 km/s at 2630 mRF and ~4.2 km/s at 2670 mRF) occur within the lower andesite unit ('And' unit) which also correlate with higher porosity (13 and 23% respectively) and loss of Vs signal (Figure 3.17). It therefore appears that some of the variability in Vp and Vs within the andesite is due to fracturing, however the primary control on the variation in velocity appears to be the matrix porosity.

3.4.4 Comparison Between Northern (NM8 and NM9) and Southern (NM10) Tahorakuri Formation

The geochemistry, mineralogy and petrophysical properties of the Tahorakuri Formation tuffs differ greatly between the northern wells (NM8 and NM9) and NM10 in the south. The alteration mineralogy assemblage of albite, illite, chlorite, calcite in NM10 is characteristic of propylitic alteration within a geothermal system (Figure 3.16) (Browne, 1978), consistent with the conceptual model for the field (Boseley et al., 2010; Chambefort et al., 2016). By contrast, mineralogy in the north reflects both an older magmatic-hydrothermal system (potassic, advanced argillic, and phyllic) and the younger, neutral pH geothermal system. Mineralogy (and hence geochemistry) is hence markedly different between south and north, with NM10 having lower quartz (~30-40% in NM10 cf. ~45-65% in NM9 and 40-75% in NM8), lower plagioclase (<2% in NM10 cf. 0-35% in NM9 and 1-20% in NM8), higher albite (22-29% in NM10 cf. 0-5% in NM9 and 1-5% in NM8), lower illite (6-13% in NM10 cf. 0-18% in NM9 and 1-18% in NM8), higher chlorite (0-3% in NM10 cf. 0-1% in NM9 and 0-1% in NM8) and higher calcite (4-10% in NM10 cf. 0-2% in NM9 and 1-3% in NM8) (Figure 3.12 and Figure 3.16). The petrophysical properties are also markedly different with lower Vp, Vs, and Vp/Vs, lower density and higher porosity in the NM10 Tahorakuri Formation relative to NM8 and NM9 (Table 3.3).

Table 3.3. Petrophysical property differences for the Tahorakuri Formation between the north (NM8 and NM9) and south (NM10).

	NM8			NM9			NM10		
Property	P5	Mean	P95	P5	Mean	P95	P5	Mean	P95
Vp (km/s)	3.51	4.09	4.46	3.83	4.59	5.29	3.38	3.78	4.17
Vs (km/s)	1.91	2.39	2.67	NA	NA	NA	1.58	1.94	2.31
Vp/Vs	1.58	1.72	1.93	NA	NA	NA	1.66	2.02	2.25
Neutron Porosity (%)	NA	NA	NA	0	7.5	17	14	18	22
Density (g/cm³)	NA	NA	NA	2.50	2.64	2.76	2.38	2.47	2.57

Intrusion-related alteration, particularly quartz deposition, and ductile deformation are the primary factors creating the differences in mineralogical and petrophysical properties between the northern and southern Tahorakuri Formation tuffs (Figure 3.26). The increase in velocity in the northern tuffs is due primarily to a reduction in the matrix porosity on the order of 10% and there are a number of processes that appear to cause this. Close to the intrusion and extending several hundred metres above it in NM9, a zone of ductile deformation and quartz precipitation has lowered porosity below 5%, creating particularly high velocities (4.5-5.5 km/s). This zone likely extends around the intrusion as suggested by the potassic alteration found in NM8 and fluid inclusion temperatures exceeding 500 °C in NM4 and NM8 (Chambefort et al., 2013; Christenson et al., 1997). Quartz deposition and consequent reduction of matrix porosity appears to have resulted in elevated velocities within the Tahorakuri Formation tuffs in NM8 and the uppermost tuffs in NM9 (Tuffs Lo 9, Anl Tuffs Up 9 geochemical groups) relative to those in NM10 (Table 3.3). Given the documented pervasive nature of phyllic alteration and quartz deposition in the north (Chambefort et al., 2017), the elevated velocities likely extend over a wide region in the north below the Whakamaru Group Ignimbrites.

The logged section of the Tahorakuri Formation in NM10 appears to be representative of the general alteration seen in this part of the field and is characteristic of the lower temperature, deep margin of the reservoir. Currently no logging data exist for the central, higher temperature (270-280 °C) part of the reservoir (NM7-NM11 area) and therefore there is some uncertainty whether there is significant velocity variation within the Tahorakuri Formation towards the hotter upflow area. However, widespread quartz deposition infilling the matrix porosity, as is observed in the north of the field, is not expected above 2 km and below 350 °C based on quartz solubility controls and the modelling results of White and Mroczek (1998). There is also some uncertainty as to the extent of deformation and alteration of the Tahorakuri Formation to the south of the intrusion and it is possible that reduction of matrix porosity from quartz deposition during the intrusion event extends into the current upflow area. Further pXRF, automated mineralogy, quantitative XRD and seismic velocity logging in additional wells throughout the field would address these uncertainties.

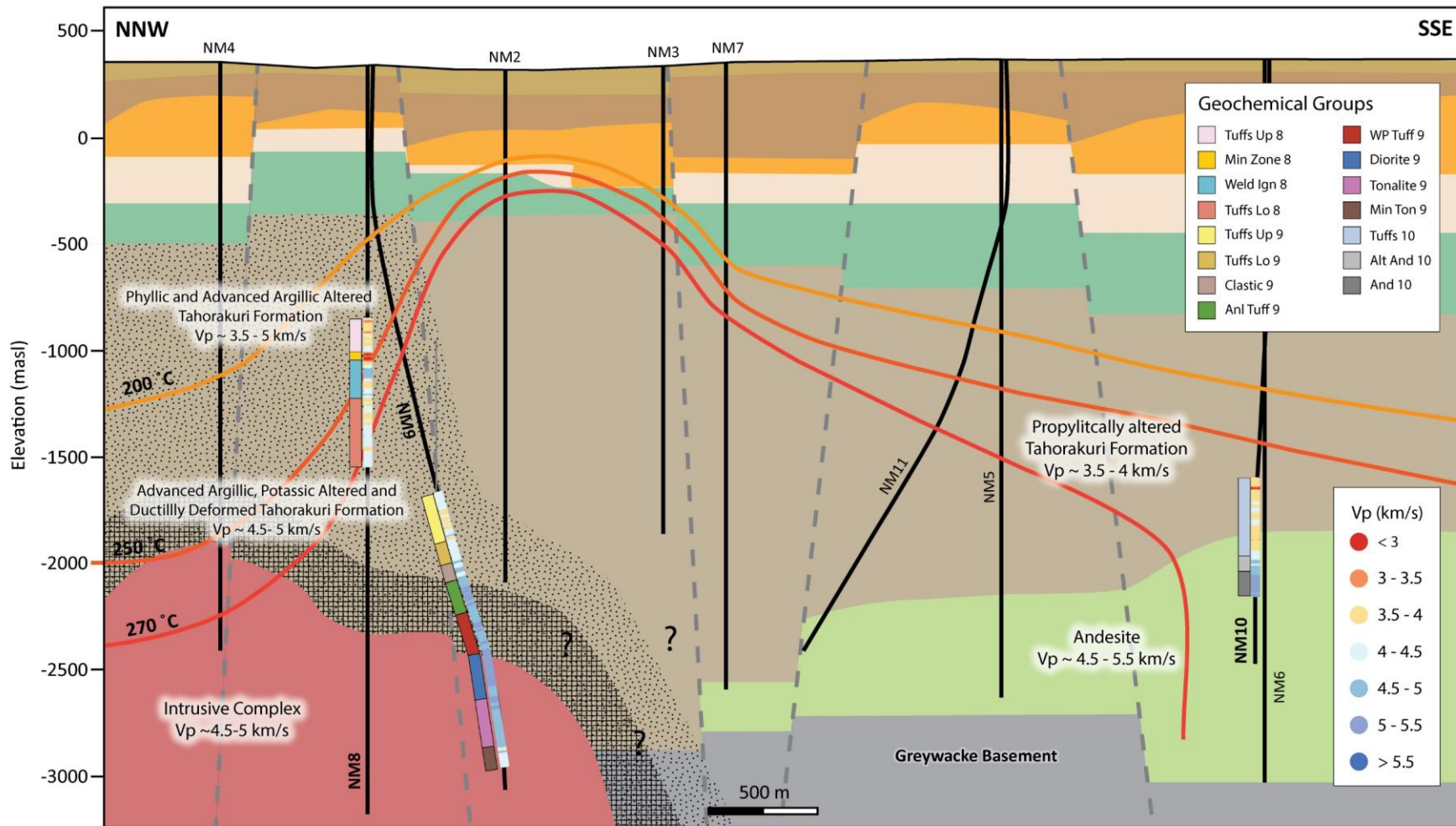


Figure 3.26. Schematic cross-section showing the interpreted large-scale velocity structure below -500 masl at Ngatamariki based on the well log and cuttings analysis.

Overall, the logging dataset analysed in this study suggests that most of the variation in V_p and V_s can be accounted for by variation in porosity (Figure 3.21 and Figure 3.27). It is likely that at least some of this porosity exists as clay-bound water, which is mostly in illite clays for the formations in this study. Porosity is in turn controlled by primary lithology and alteration with the additional effect of ductile deformation closing pore space several hundred metres above the intrusion in the north of the field. The alteration (phyllic, advanced argillic and potassic) and ductile deformation that appears to have dramatically reduced porosity and increased velocity in the Tahorakuri Formation tuffs in this study are not commonly encountered in geothermal reservoirs. The dataset here suggests the effect of more common propylitic alteration on porosity and therefore velocity is minor and that lithology plays a larger role. Variation in the elastic moduli of matrix minerals is an important factor in some cases where quartz is <40% (e.g. the andesites in NM10 and clastic unit in NM9 with high abundance of pyrite), however this is a smaller effect than porosity. The effect of fracturing and highly fractured zones is evident in all three wells and acts to lower V_p and V_s dramatically over relatively small depth intervals (<50m) and/or results in higher variability in velocity.

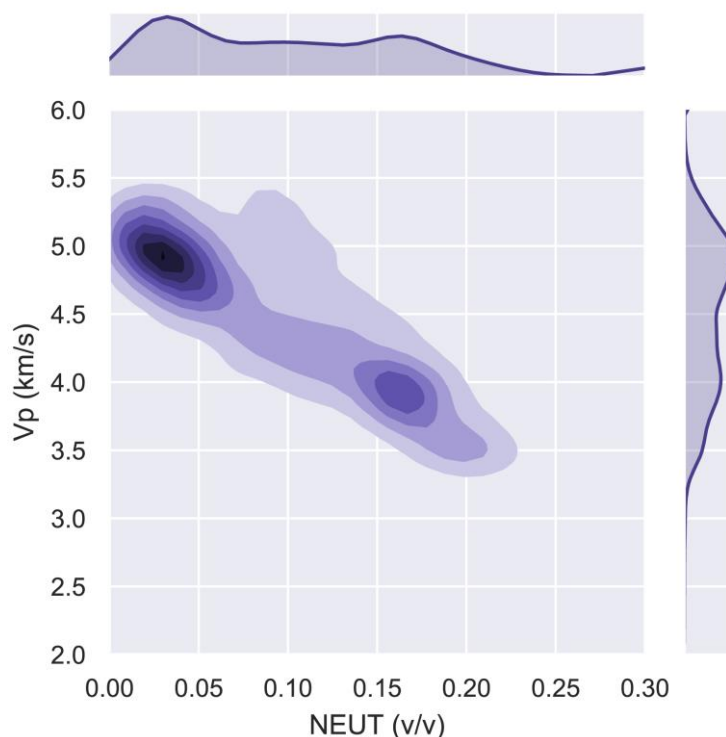


Figure 3.27. Neutron porosity vs. V_p for NM9 and NM10 in this study.

3.5 Conclusions

Variation in porosity is the largest factor effecting seismic velocity in the Ngatamariki geothermal reservoir at the log-scale, however other factors such as the elastic moduli of matrix minerals and fracturing are also important. Porosity is primarily controlled by rock type (tuffs, andesite lava, tonalite/diorite intrusion), however this study shows that alteration and ductile deformation above intrusion heat sources in geothermal fields can dramatically change porosity and therefore velocity. The intrusion event in the north of the Ngatamariki field has greatly altered the geochemical, mineralogical and physical properties of the tuff-dominated Tahorakuri Formation. Porosity in the north of the field has been decreased and seismic velocity increased in the north by both wide-spread quartz deposition and ductile deformation in a zone extending several hundred metres above the intrusion complex. The lowest porosities (0-5%) and highest seismic velocities (V_p 4.5-5.5 km/s) occur within this zone that directly overlies the tonalite/quartz-diorite intrusion in NM9. Evidence from mineralogy and an FMI log indicate this particularly low porosity zone is due mostly to ductile deformation when past-temperatures within this zone exceeded 375°C and the fluid was likely in a supercritical state. This has implications for geophysical imaging of magma bodies (i.e. low velocity zones associated with molten magmas may have overlying high velocity zones associated with ductile deformation). It also provides insight into the physical property changes, and therefore hydrologic processes, that may take place close to the heat sources of geothermal systems (e.g. that porosity and permeability reduction due to ductile deformation limits fluid circulation directly above a large silicic magma body).

More generally, this study suggests that major formation changes and alteration processes that cause a significant reduction in matrix porosity are first-order controls on large-scale velocity variation and therefore need to be closely considered when interpreting seismic velocity images in geothermal fields. Clay-bound water within the reservoir also appears to be a possible factor in controlling V_p and V_s , however the dataset in this study spans only a relatively small variation in clay type and abundance and therefore further logging and mineralogical data is needed to further investigate this.

4 Monte Carlo 1D Velocity Inversion of the 2017-2018 Expanded Array Data

Abstract

In order to perform a preliminary investigation of the spatial patterns of velocity variation at the Rotokawa and Ngatamariki geothermal fields and define appropriate starting models for 3D tomography inversions, the program VELEST was used to perform coupled 1D velocity, hypocentre and station correction inversions. To do this, 1000 1D velocity starting models were randomly generated from normal velocity distributions defined based on a combination of measured velocities from three geothermal wells and the known geological variation from wells across the two geothermal fields. The program VELEST was then used to perform combined 1D velocity, hypocentre and station correction inversions for these 1000 different starting models. Travel-time data from 351 microseismic events, mostly from three clusters of seismic activity around injection wells within the fields, were used in the inversions. These events were recorded on an expanded seismic array of ~55 seismometers deployed across the two geothermal fields during 2017 and 2018. The P and S arrival times used in the inversions were from both manual picking (90 events) and high-quality automatic picks (261 events). The inversions consisted of seven iterations of coupled hypocentre, velocity and station corrections resulting in a decrease in root-mean-squared (RMS) residual from a starting range of 0.18 – 0.275 s to a final range of 0.085 – 0.125 s for all models. Grouping of the models by their final RMS value showed that a local minima or ‘best-fitting’ 1D velocity model was defined by the data. The models with the lowest RMS values compared well with measured velocity data from well NM10, which is close to the centre of the array, above 2 km bsl. Measured velocities from wells NM8 and NM9 from northern Ngatamariki however appear to be high relative to the range of 1D velocity models obtained from VELEST over depths of 1-2 km bsl (average of 4.72 km/s for V_p in measured data for NM9 versus an average of 3.75 km/s for the VELEST models). This suggests the measured velocities from these wells are above average for the study area. Several areas of negative and positive station corrections were observed, implying that 3D velocity variations occur across the two geothermal fields that are manifest in the traveltime dataset. An area of both negative V_p (10 stations with average station correction of -0.21 s) and negative V_s (10 stations with average station correction of -0.34 s) station corrections suggesting faster velocity in northwest Ngatamariki, consistent with the measured velocities in

wells NM8 and NM9 from this area being above average. This is likely due to a reduction of porosity in this area between 1 to 2 km bsl due to intense alteration and deformation of the Tahorakuri Formation above a magmatic intrusion that has been identified from wells NM4, NM8 and NM9 drilled in the north of the field. A less prominent area of negative V_p station corrections is also apparent over NW Rotokawa (six stations with average station correction of -0.14 s), which may be related to the presence of thicker shallow rhyolite lavas in this area of the field. An area of positive V_s station corrections (12 stations with average station correction of 0.31 s) occurs over the eastern side of the Ngatamariki field, suggesting slower V_s in this area. The cause of this is not as clear as for NW Ngatamariki as there are no wells drilled in this area. However, it may be due to a thicker, deeper smectite clay cap and/or thicker and deeper Tahorakuri Formation in this area which is relatively high porosity and therefore lower velocity. The central Rotokawa area where production and injection wells have been drilled was observed to have similar, relatively small, negative V_s station corrections (< -0.1 s) across the field, suggesting V_s remains relatively constant across the field. In general, the range of the final 1D velocity models and the consistent spatial patterns of station corrections show that a 3D velocity inversion is warranted for the dataset. Suitable starting velocity models for the 3D inversions should be based on the best-fitting 1D velocity models obtained from the VELEST inversions.

4.1 Introduction

As discussed in Section 2.2.2, seismic tomography is most commonly formulated as a non-linear problem and, as such, most widely-used seismic tomography programs may find a *local* rather than the global minimum of the objective function. Hence, the solutions obtained can be dependent on the initial or starting velocity model used in the inversion (Kissling et al., 1994; Rawlinson et al., 2014; Thurber and Ritsema, 2007). Hence, finding an appropriate starting velocity model is critical to obtaining robust solutions (Thurber and Ritsema, 2007). If a priori knowledge of the velocity is available for a study area (e.g. sonic logs, refraction or checkshot surveys, geology), this can be used to narrow the range of plausible starting models. However, in many cases such information is limited or entirely absent. If such information is available, it may not be representative of the entire study region and therefore the range of possible initial models is typically large. Many of the metrics used to assess seismic tomography model robustness and uncertainty, such as model resolution and co-variance matrices and ray coverage statistics such as derivative weight sum (DWS), are insensitive to the uncertainty in the initial model, and therefore do not provide any indication of whether the

starting model is appropriate for the particular dataset (Thurber and Ritsema, 2007). Testing of a wide range of possible starting models is required in local earthquake tomography to assess the range of final models that provide the best-fit to the observed traveltime data.

To address this, Kissling et al. (1994) proposed the use of their VELEST code (Kissling, 1995) to obtain a ‘minimum 1D model’ by performing multiple inversions for 1D velocity using different starting models. The ‘minimum 1D model’ is the 1D model and station corrections that obtains the lowest RMS traveltime residual value for all earthquakes used in the inversion. Their code uses a similar inversion procedure to that of standard 3D tomography (i.e. similar to the SIMULPS code of Thurber, 1983), but inverts only for hypocentres, 1D velocity and station corrections. The resultant 1D velocity model is thus approximately equal to the average velocity for the particular layer depth range for the region that is sampled by the ray-paths (Kissling et al., 1994). Station correction terms for each seismometer are used in the inversion and partially account for velocity variation from the 1D average velocity model (which includes local, shallow velocity structure and larger scale 3D velocity variation). The station correction terms can therefore also provide an initial indication of the relative 3D velocity variation within an area (i.e. which areas are on average higher velocity and which areas slower velocity) relative to the reference station used (e.g. Clarke et al., 2009).

Using VELEST, Kissling et al. (1994) proposed a recipe to obtain an initial model or models that could be used as the basis for starting models in subsequent 3D tomography. They advocate a trial and error approach whereby a range of different layer geometries and velocities are trialled with the goal of finding the range of possible 1D velocity models that provide the lowest RMS residual misfit between observed and calculated traveltimes. Sherburn et al. (2006) provide a good example of the approach of using a minimum 1D velocity model obtained using VELEST that was subsequently used as a starting model in 3D tomographic inversions for the Taranaki volcanoes in New Zealand.

Clarke et al. (2009) took a more systematic approach of determining a minimum 1D velocity model by trialling 1000 different starting velocity models generated from randomised normal distributions of velocity values for each layer based on the expected range of subsurface velocities for their study areas, the Rotorua and Kawerau geothermal fields in New Zealand. In this study, a similar approach to that of Clarke et al. (2009) was used with the 2017-2018 Rotokawa-Ngatamariki expanded array dataset in order to establish a suitable starting model for 3D tomography, to investigate whether the travel-time dataset warranted a 3D inversion

and to assess the relative 3D velocity variation across the study area using the station corrections obtained.

4.2 Data and Methodology

4.2.1 Travel-time data

The travel-time data used consisted of both manually picked and automatically picked P and S wave arrival times from 302 earthquakes mostly from the three main clusters of activity (Rotokawa, Ngatamariki South and Ngatamariki North) near injection areas in the geothermal fields (Figure 4.1 and Figure 4.2 and Table 4.1). 100 well-recorded events (those with >30 P picks and >10 S picks) were initially selected from a catalog of automatically located hypocentres (see Appendix A.2 for methodology used) that were then manually re-picked. These events were distributed across the study area with an emphasis on selecting events that occurred outside of the three main clusters of microseismic activity. The manual picking followed the procedure of Diehl and Kissling, (2009) and included manually picking arrival time uncertainties. Figure 2.6 demonstrates that 90% of the manually picked uncertainties were within ± 0.04 s of each arrival time pick for P picks and were within ± 0.09 s of each arrival time pick for S picks. In total, P and S picks were available for 63 stations, or 61 if excluding stations with <10 picks (SS32 and SS35).

The manual picking resulted in a catalog with more events at Rotokawa than at Ngatamariki South and Ngatamariki North as manually reviewed events for Ngatamariki South and Ngatamariki North were often found to be of poorer quality (as they are lower magnitude than events at Rotokawa). To obtain an approximately even distribution of events for each of the main clusters and to increase the total number of picks, automatically picked events were added to the catalog. The automatically picked events were selected based on having at least 10 P and 1 S picks with high pick SNR. Comparison of results using only the manual picks and the manual and automatic picks showed little difference in the final velocity models, station corrections and RMS residuals for each model which indicates that there was no significant increase in the amount of pick noise by adding the automatic picks. The final catalog used consisted of 302 events with 7,829 total P picks and 3332 total S picks (Table 4.1). The distribution of the number of P picks and S picks per event is shown in Figure 4.3. Starting locations for the events were produced using NonLinLoc (Lomax et al., 2000) using both the P and S picks with weighting as described in Appendix A.2.

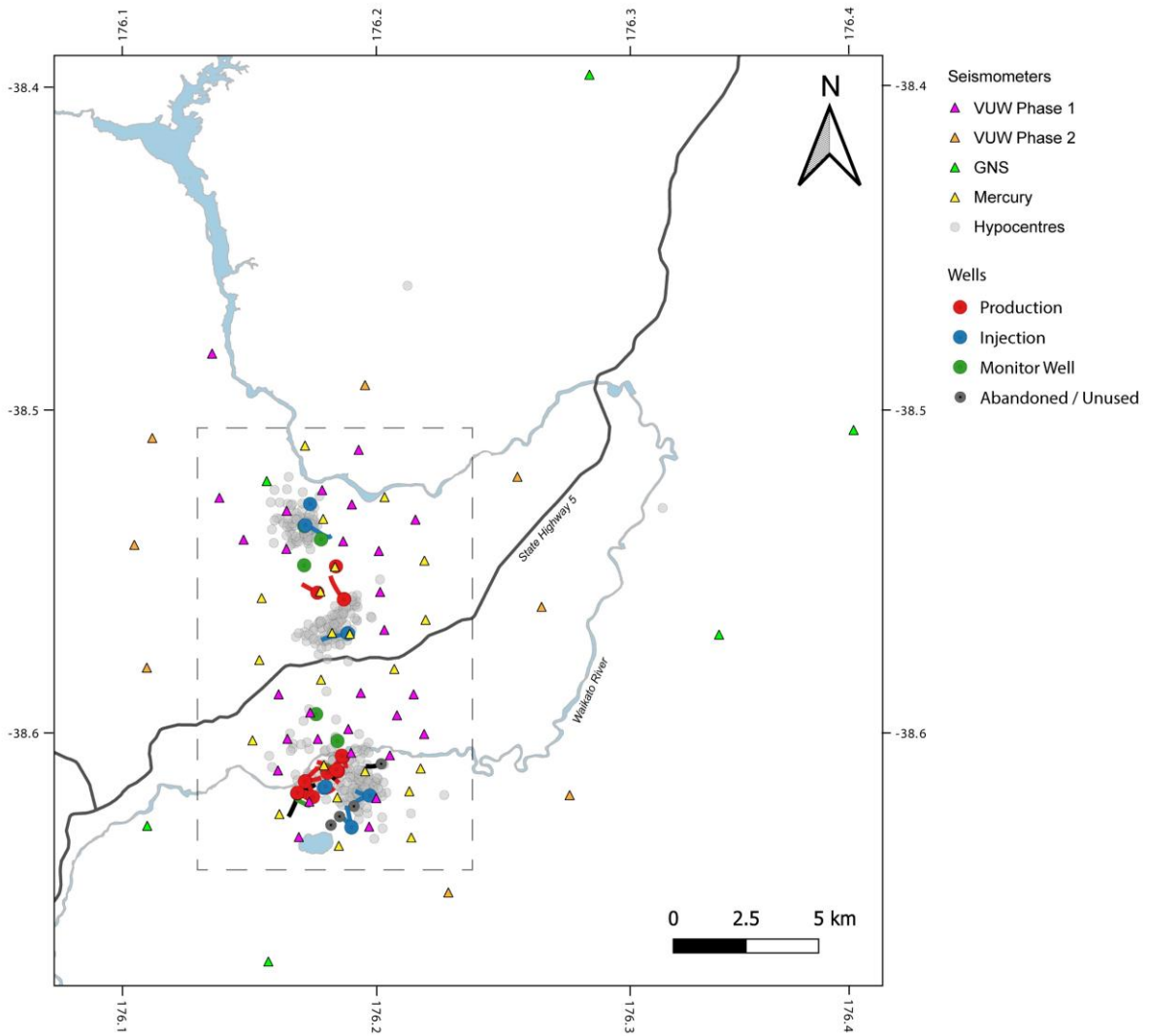


Figure 4.1. Seismometers and the starting event locations used in the VELEST analysis (obtained from NonLinLoc). The dashed outline shows the location of Figure 4.2.

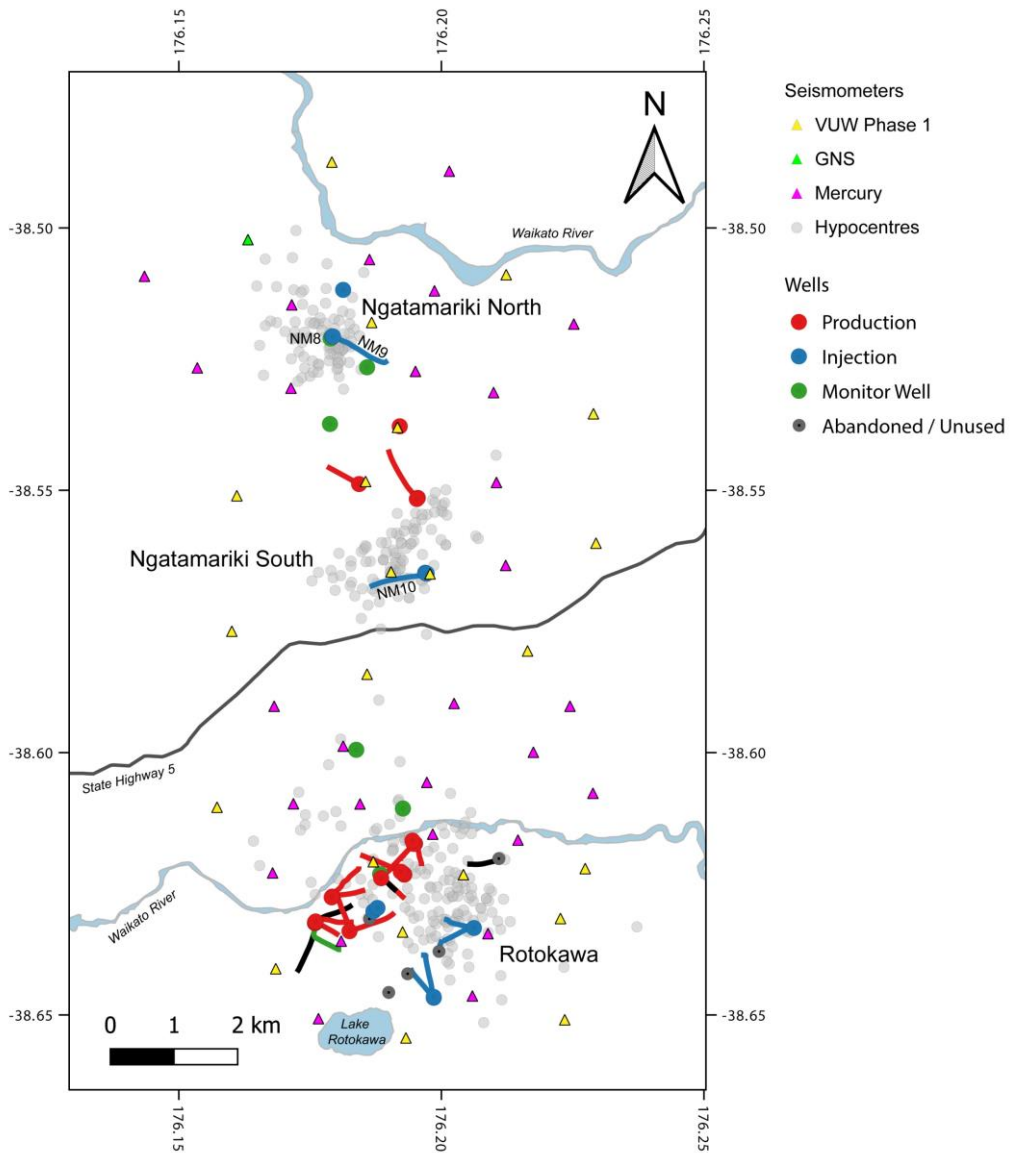


Figure 4.2. Close-up of seismometers and the starting event locations used in the VELEST analysis (obtained from NonLinLoc) over the two geothermal fields. The three main clusters of microseismicity (Ngatamariki North, Ngatamariki South and Rotokawa) are labelled. Wells for which measured velocity data is available (NM8, NM9 and NM10) are also labelled.

Table 4.1. Number of events and picks and whether manually or automatically picked for all events and for each cluster of events.

	All	Rotokawa	NM South	NM North
Total Events	302	122	96	84
Manually picked Events	87	50	18	19
Auto picked Events	215	72	78	65
Manual P picks	2557	1507	559	491
Auto P picks	5272	2293	1748	1231
Manual S picks	769	483	165	121
Auto S picks	2563	1601	531	431
Total picks	11161	5884	3003	2274

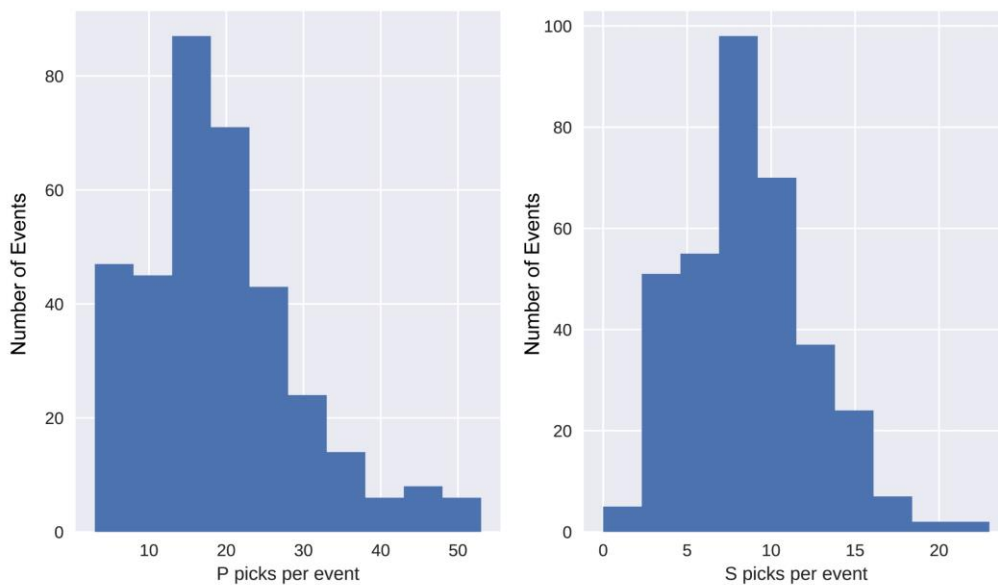


Figure 4.3. Number of P and S picks per event.

4.2.2 VELEST Using Monte Carlo Starting Models

The VELEST seismic tomography code (Kissling et al., 1994) solves the coupled hypocentre-velocity problem for layered, one-dimensional velocity models. The final 1D model layer velocities obtained from VELEST are representative of the average velocity for the particular layer depth range through which the rays pass (Kissling et al., 1994). VELEST also solves for ‘station correction’ terms for each seismometer used in the inversion. These terms account to some degree for systematic velocity variations from the 1D average velocity model (which includes local, shallow velocity structure and larger-scale 3D velocity variation). The station correction terms can therefore indicate relative 3D velocity variation within an area (i.e. which areas are on average higher velocity and which areas slower velocity) (Clarke et al., 2009). The station correction terms are calculated relative to a reference station which, according to Kissling et al. (1994), should be a station approximately within the centre of the array that recorded a high proportion of the total events used. RT21 was therefore used as the reference station as it operated continuously, recorded most of the total possible P and S arrivals from the events and is located in the approximate centre of the array. Station correction terms are therefore relative to this station (i.e. areas with positive station corrections are, on average, slower seismic velocity than RT21 and areas with negative station corrections are, on average, faster velocity than RT21). The choice of reference station does not have any effect on the 1D model velocities and only effects the station correction terms (Kissling, 1995).

VELEST uses damping regularization and therefore seeks solutions that minimise the RMS misfit between the observed and calculated travel-times. As VELEST uses a linearised iterative scheme, and the model solution space is likely strongly non-linear, the model determined may be a local minima. The result of this is that the final model can be strongly dependent on the starting model. It is therefore important to test a range of starting models spanning the expected range of possible seismic velocities for the particular area (Clarke et al., 2009). To do this, a set of 1000 V_p starting models were generated at random from a normal distribution for each layer. The layer depth intervals and mean V_p for each layer were estimated based on the available velocity measurements in wells at Ngatamariki (i.e. checkshot survey in NM8 and velocity logs in NM8, NM9 and NM10) and the geological layering across the two fields. Most of the earthquakes used occurred between 1-3 km and hence 0.5 km thick layers were used over this interval. Standard deviations of ± 1 km/s were used to define the normal distribution for each layer from which velocities were randomly generated with the constraint that all starting velocities are positive. The generated velocity distribution for each layer covers most

of the range of velocities measured within the field (Figure 4.4). S velocity models were generated from the P velocity models using a V_p/V_s ratio of 1.75 based on V_p/V_s values obtained from full waveform logs in NM8 and NM10 (Chapter 3). Each of the 1000 starting models were then inverted using VELEST with seven iterations of joint hypocentre and velocity model adjustment. Of the 1000 models run, only one failed to converge to lower final RMS.

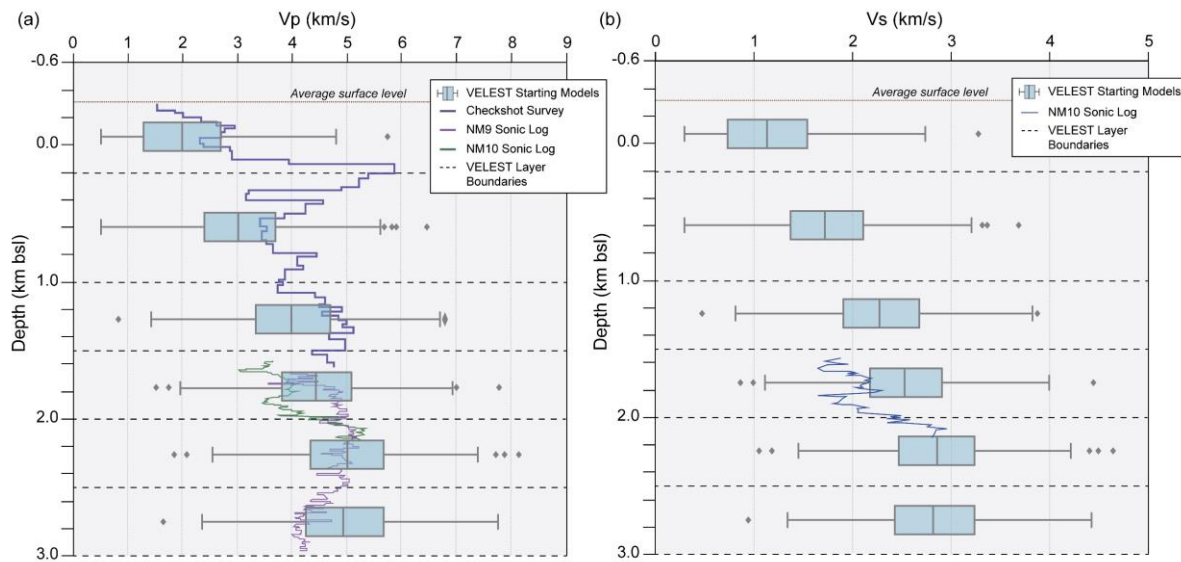


Figure 4.4. Starting (a) V_p and (b) V_s models compared to checkshot and V_p and V_s logs. N.b. the checkshot survey was conducted in well NM9 located in the north of the Ngatamariki field. The particularly high velocity in the NM9 checkshot survey at between 0 to 0.4 km bsl is due to a welded ignimbrite layer. An additional layer at 5 km bsl is not shown but has the same velocity distribution as that for the 2.5 to 3 km bsl layer. An additional layer below that extends to infinity, again with the same distribution as 2.5 to 3 km bsl.

4.3 Results

4.3.1 Data fit

The RMS residual for 999 of the 1000 models improved over the seven iterations from a range of 0.18 – 0.275 s after the first iteration to a range of 0.085 – 0.125 s after the seventh iteration (Figure 4.5). The distribution of RMS for the final models was approximately log-normal with a long tail of RMS values above 0.95 s (Figure 4.6). In order to analyse the models that best fit the data (i.e. to find the ‘minimum’ 1D velocity model), the 10th percentile (P10) and 50th percentile of the RMS distribution were calculated and models were grouped according to whether they had RMS below these values (i.e. if a model had a final RMS \leq the 10th percentile

of all RMS values it was part of the P10 group of models, if a model had final RMS < the 50th percentile but > the 10th percentile of all RMS values it was part of the P50 group of models). All references to P10 and P50 discussed hereafter relate to this.

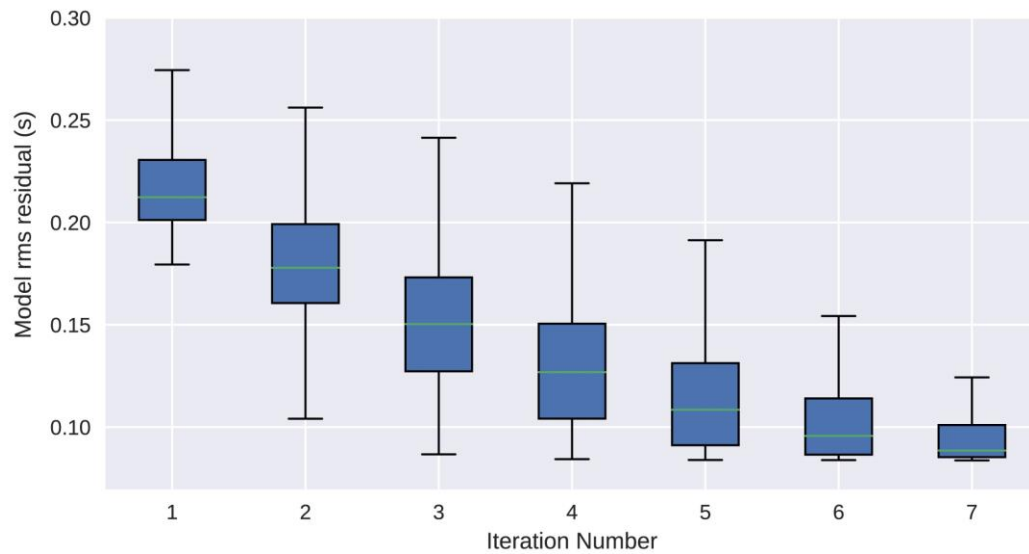


Figure 4.5. RMS residual misfit between observed and calculated traveltimes for each iteration for all 999 final models obtained.

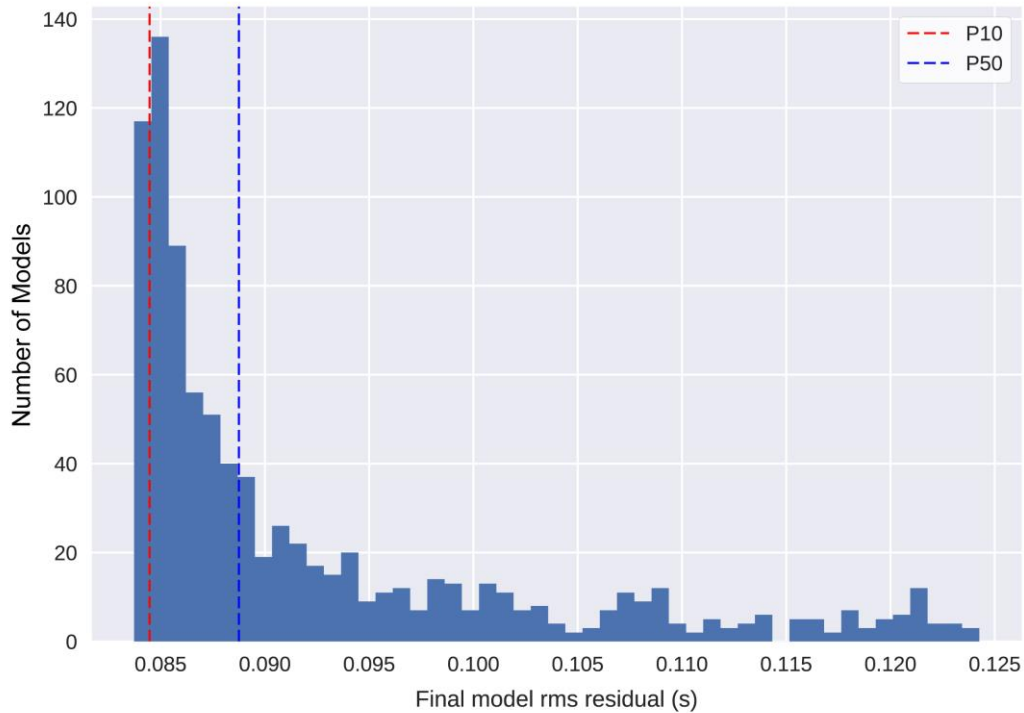


Figure 4.6. Distribution of the final RMS residual misfit for all 999 final models obtained after seven iterations. The dashed red and blue lines indicate the 10th percentile and 50th percentile values respectively.

4.3.2 Final Velocity Models

The final V_p and V_s models versus the starting models are shown in Figure 4.7 and Figure 4.8 respectively. In all cases, the range of the final V_p models was reduced from the range of the starting V_p models. For both V_p and V_s , the final models were mostly lower in velocity than their starting models with the lowest values of V_p and V_s relatively unchanged between starting and final. The range of final velocities narrows when analysing only the P50 models and further again for the P10 models. The mean of the final velocity models was relatively unchanged between the different subsets of models with $RMS < \text{the P10 RMS}$ and models with $RMS < \text{the P50 RMS}$. This, together with the narrowing range of velocities for the P10 and P50 models, suggests the velocity model solutions are gravitating toward a common velocity model with the lowest RMS, even though the variation between the final RMS values is relatively low (from 0.085 to 0.125 s, Figure 4.6).

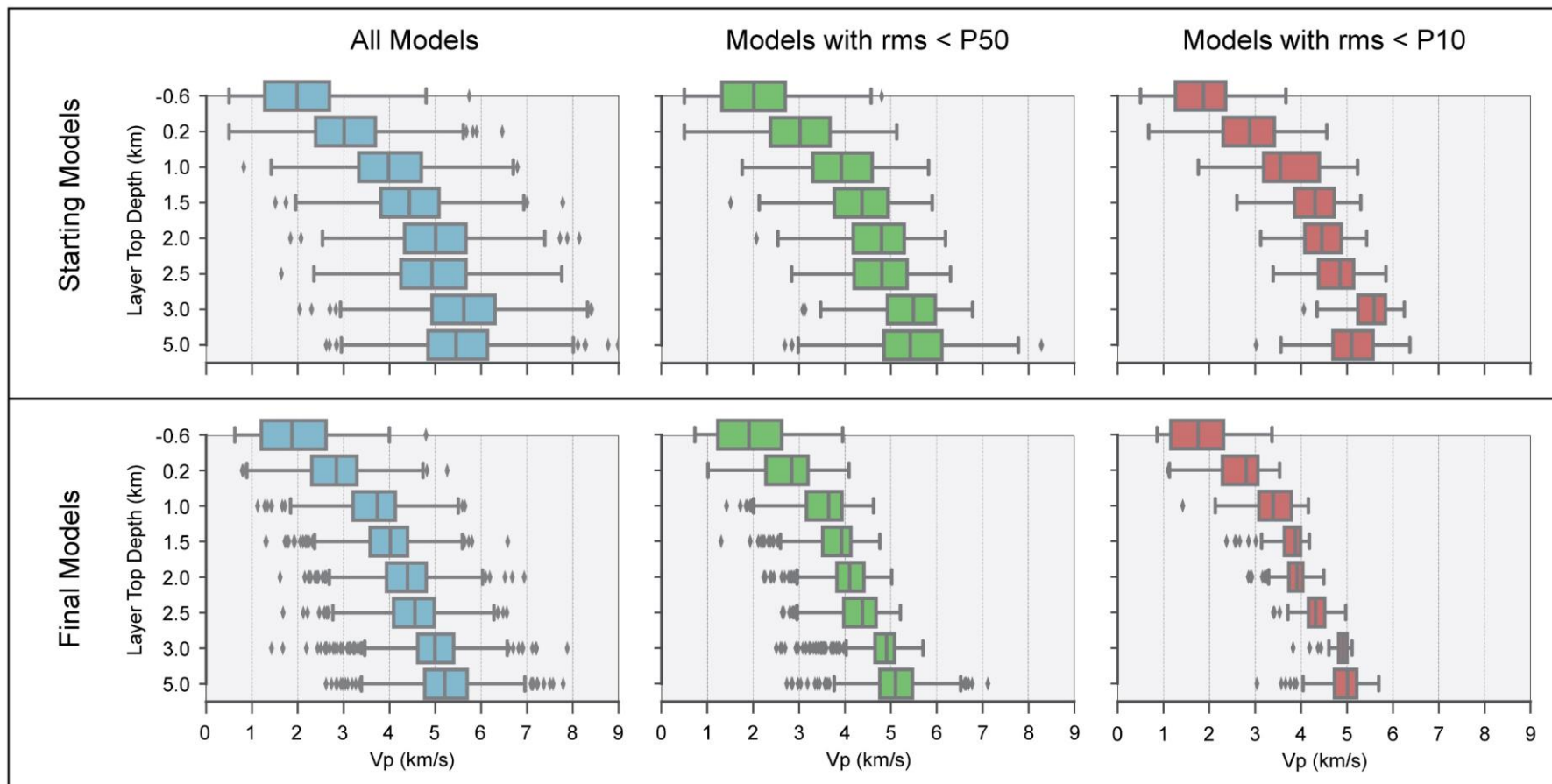


Figure 4.7. Box and whisker plot of the starting and final V_p for each layer of the VELEST inversions. The leftmost panel shows the distribution of all 999 models, the middle panel the distribution of the P50 models (models that obtained final RMS < the 50th percentile of all the models) and the right panel the distribution of the P10 models (models that obtained final RMS < the 10th percentile of all the models). See glossary for explanation of box and whisker plots.

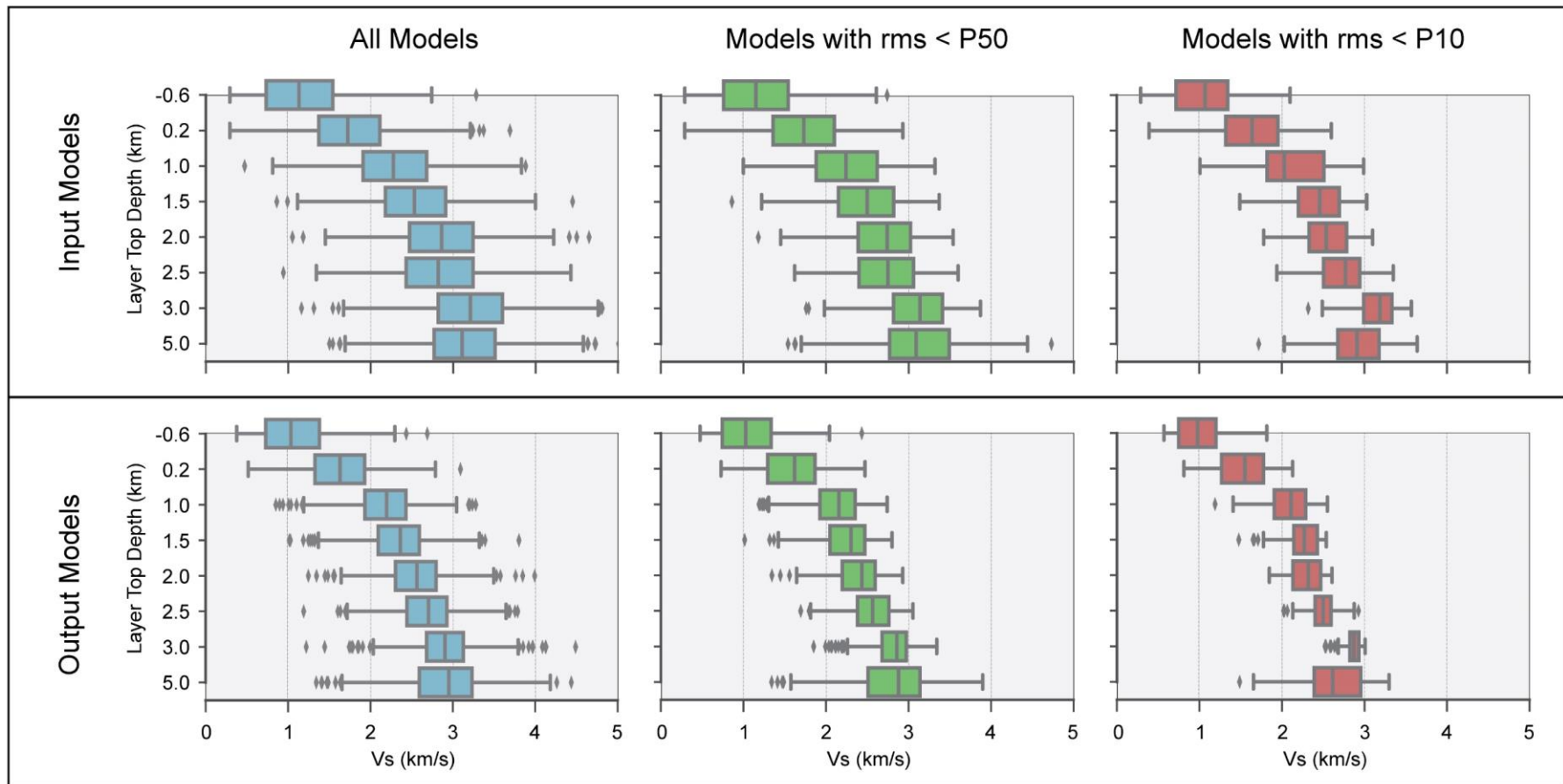


Figure 4.8. Box and whisker plot of the starting and final V_s for each layer of the VELEST inversions. The leftmost panel shows the distribution of all 999 models, the middle panel the distribution of the P50 models (models that obtained final RMS < the 50th percentile of all the models) and the right panel the distribution of the P10 models (models that obtained final RMS < the 10th percentile of all the models). See glossary for explanation of box and whisker plots.

4.3.3 Station Corrections

The station corrections for the models are plotted in map view for the models with RMS less than the P50 RMS in Figure 4.9 and Figure 4.10 for Vp and Figure 4.11 and Figure 4.12 for Vs. Numeric values for the station corrections are provided in Appendix A.5. Similar mean values in the station corrections are observed when using all of the models and for the models with RMS less than the P10 RMS of all models (Appendix A.5). However, the standard deviation in the station corrections grows between the different subsets of final solutions, with the smallest standard deviation for the P10 models and largest standard deviation when considering all models. Again, these observations suggest the station correction terms are converging toward a common set of station corrections with the lowest RMS, although the variation between the RMS values is relatively small (Figure 4.6).

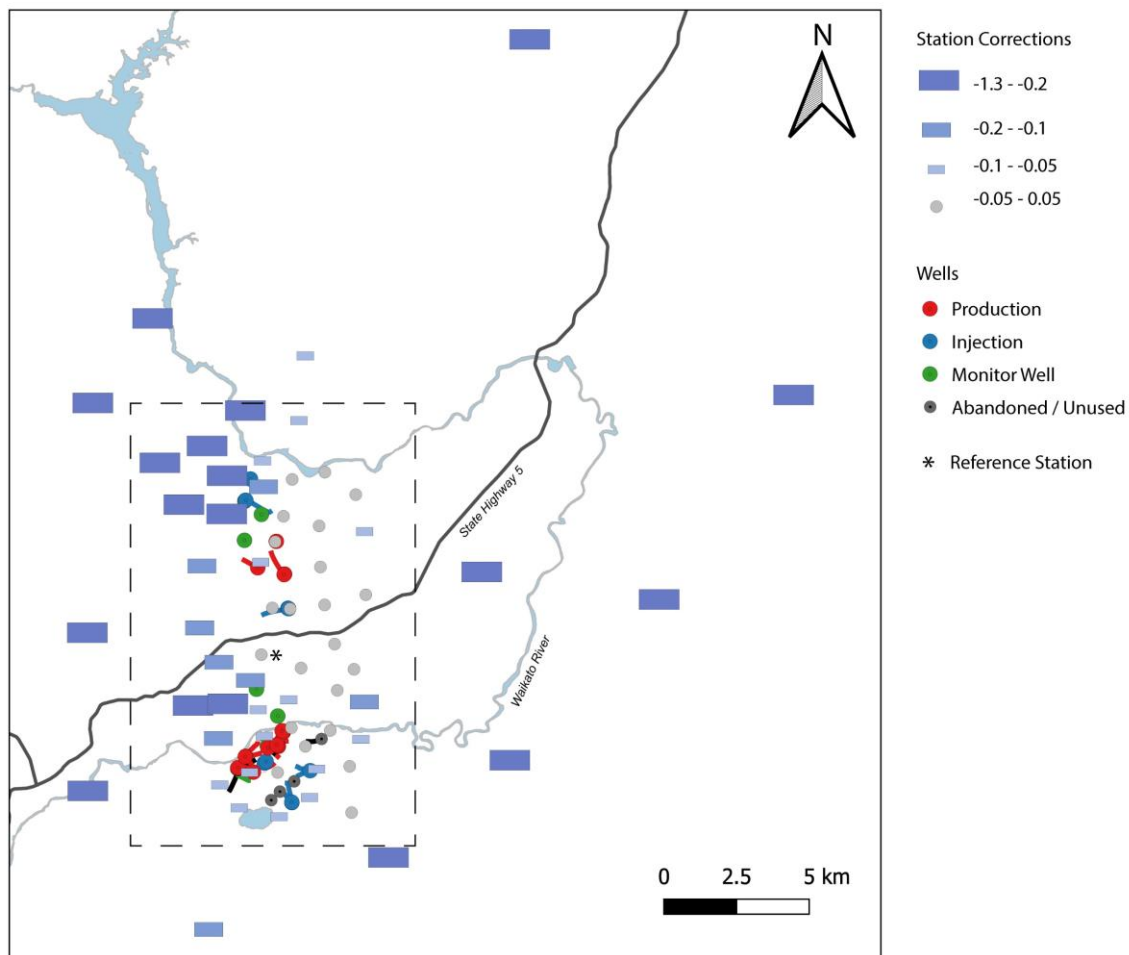


Figure 4.9. Vp station corrections. Negative station corrections are, on average, faster velocity than the reference station in southern Ngatamariki and vice versa for positive corrections. Station corrections units are seconds. Dashed box shows the location of Figure 4.10.

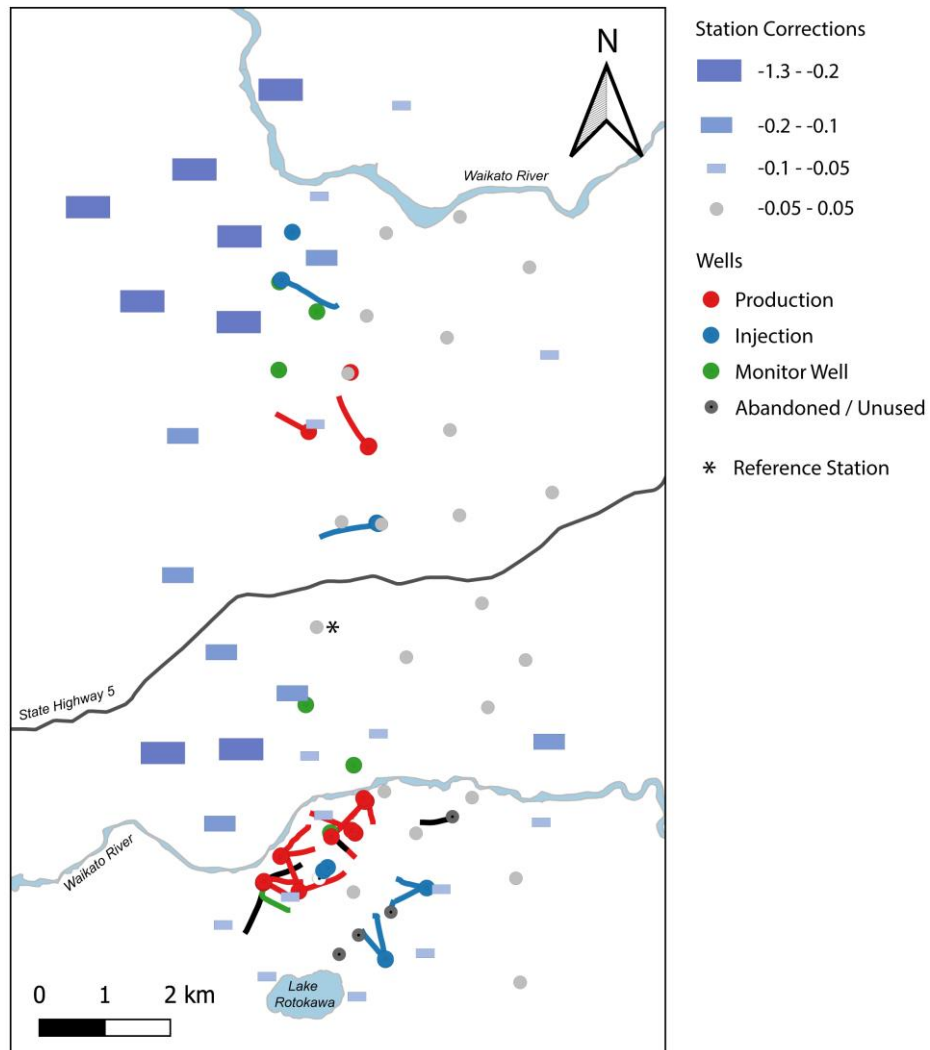


Figure 4.10. Vp station corrections zoomed in. Negative station corrections are, on average, faster velocity than the reference station in southern Ngatamariki and vice versa for positive corrections. Station corrections units are seconds.

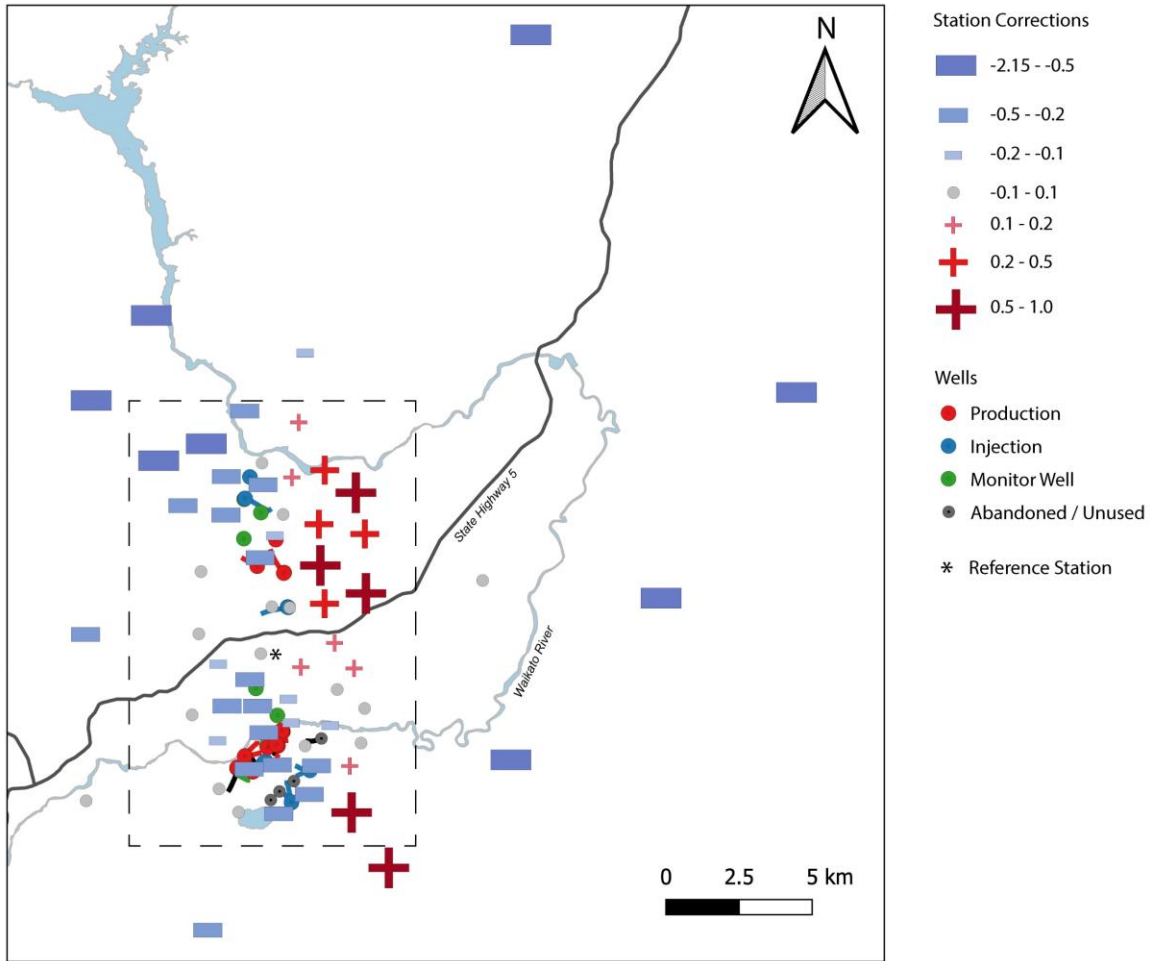


Figure 4.11. Vs station corrections. Negative station corrections are, on average, faster velocity than the reference station in southern Ngatamariki and vice versa for positive corrections. Station corrections units are seconds. Dashed outline shows location of Figure 4.12.

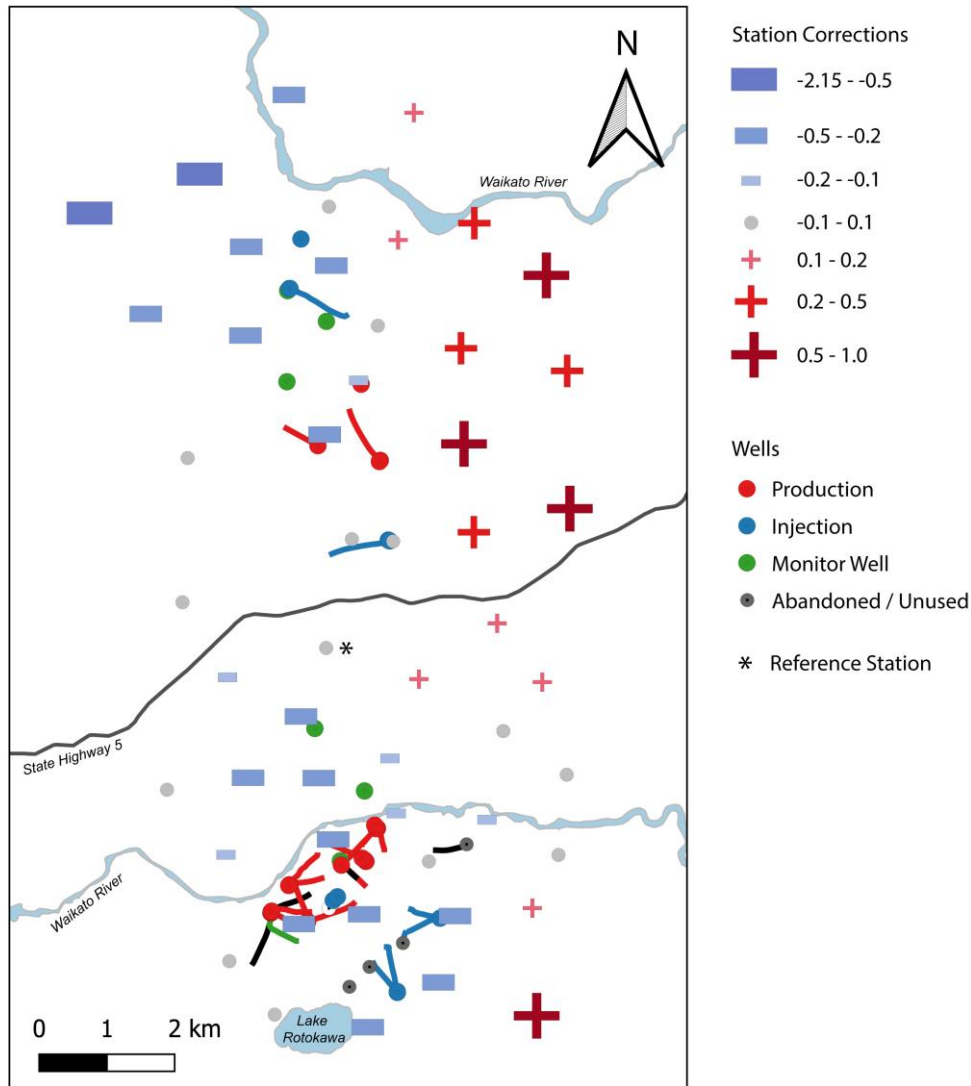


Figure 4.12. Vs station correction zoomed in. Negative station corrections are, on average, faster velocity than the reference station in southern Ngatamariki and vice versa for positive corrections. Station corrections units are seconds.

A distinct area of high, negative Vp station corrections (8 stations below -0.1 s, average = -0.2 s, standard deviation = 0.07 s) occurs over northwest Ngatamariki. An area of relatively high Vp station corrections also occurs for northwest Rotokawa, although this is both smaller in spatial extent, occurs on fewer stations and is lower in magnitude than the northwest Ngatamariki area (6 stations below -0.1 s, average = -0.14 s, standard deviation = 0.02 s). The highest magnitude Vp station corrections occur for stations outside of the field, which are all negative (10 stations, average = -0.42 s, standard deviation = 0.32 s, max value = -1.09 s).

An area of negative Vs station corrections also occurs over northwest Ngatamariki (7 stations below -0.2 s, average = -0.36 s, standard deviation = 0.17 s). A distinct area of positive Vs

station corrections occurs over the eastern side of Ngatamariki (7 stations above 0.2 s, average = 0.43 s, standard deviation = 0.16 s). The Rotokawa area is characterised by generally negative Vs station corrections with values ranging mostly between -0.1 s and -0.41 s (14 stations, average = -0.19 s, standard deviation = 0.1 s). Again, the largest magnitude Vs station corrections are observed for the stations surrounding the two fields which were mostly negative ranging between 0 s to -1.78 s except for two stations southeast of Rotokawa which had values of 0.72 s and 0.55 s.

4.3.4 Hypocentres

The average locations for the final hypocentres obtained from VELEST were notably different to their starting locations for the Ngatamariki events, with the Ngatamariki North cluster of events shifting approximately 1 km southeast and the Ngatamariki South cluster shifting approximately 800 m east (Figure 4.13). The average location from all VELEST runs for the Rotokawa cluster was similar to the starting locations. The hypocentres were observed to shift amongst the VELEST runs (Figure 4.14). Given the distribution of shifts was approximately normal, 95% of the hypocentres (2x the standard deviation) were within 286 m of the mean location in east-west, 360 m of the mean location in north-south and within 658 m of the mean location in depth. Origin time shifts amongst the models were approximately ± 0.025 s (Figure 4.15).

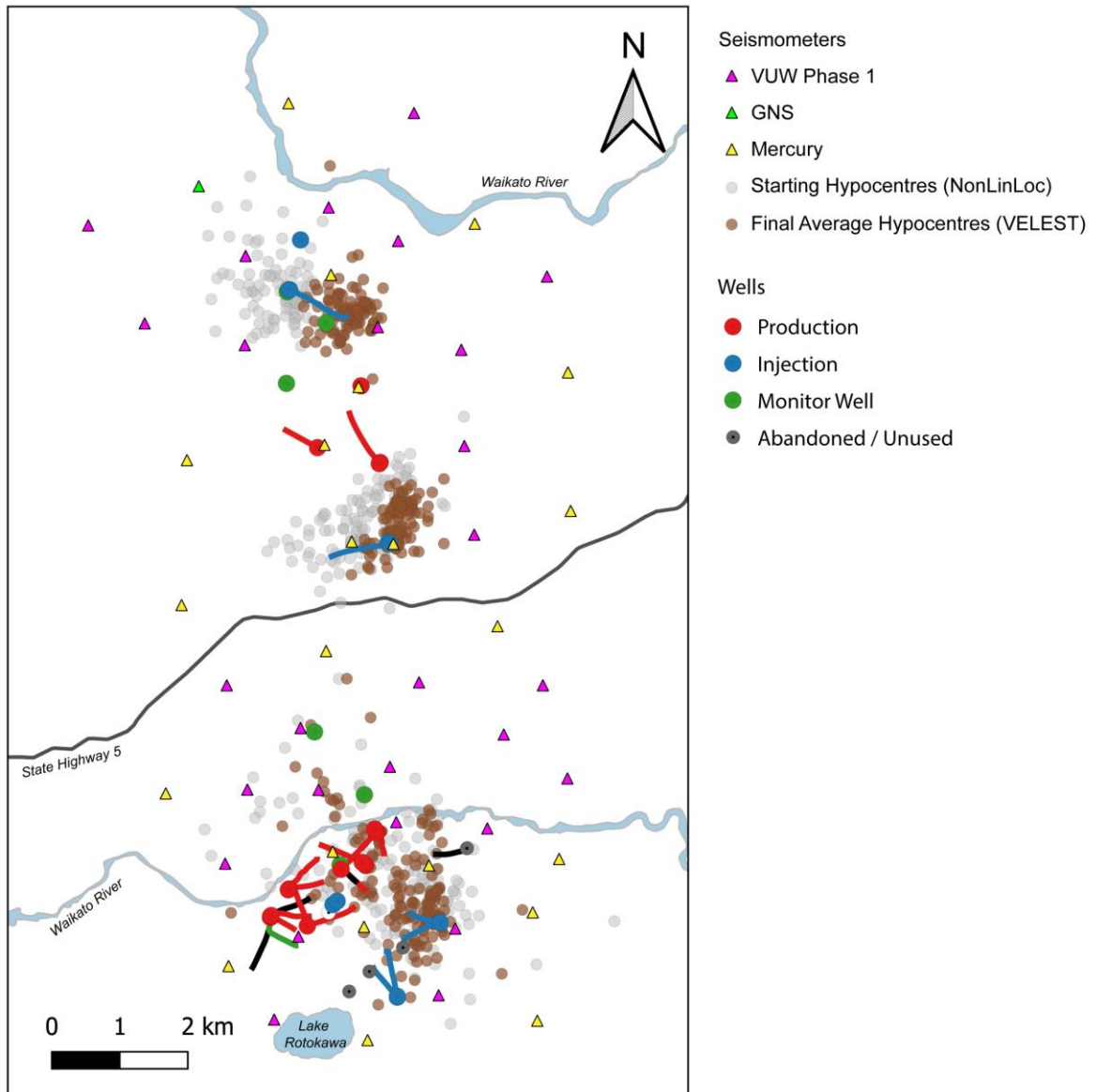


Figure 4.13. Starting (obtained from NonLinLoc) versus the final average hypocentre locations (i.e. average location from all 999 VELEST runs).

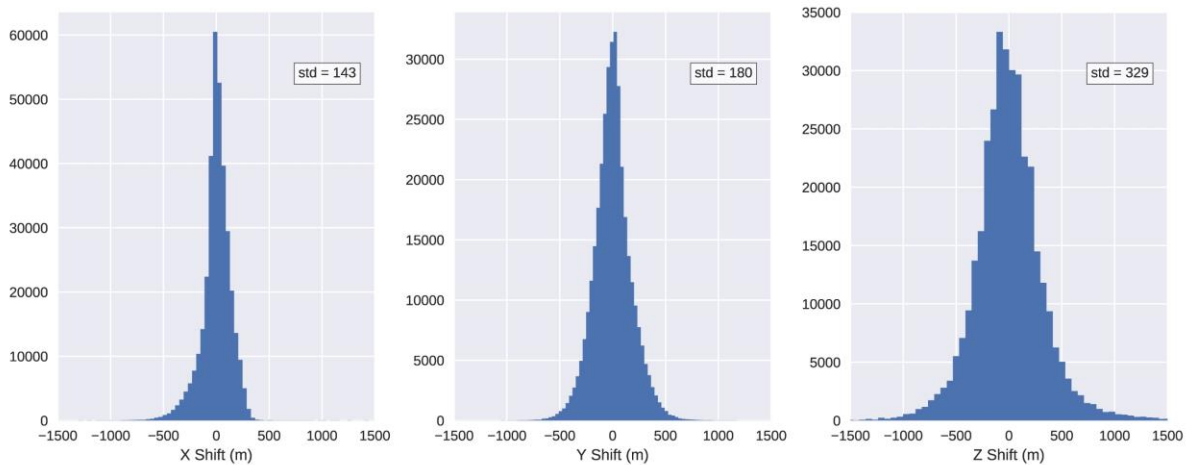


Figure 4.14. Distribution of hypocentre shifts in x (east-west), y (north-south) and z (depth) from the average location for all models. std = standard deviation in metres.

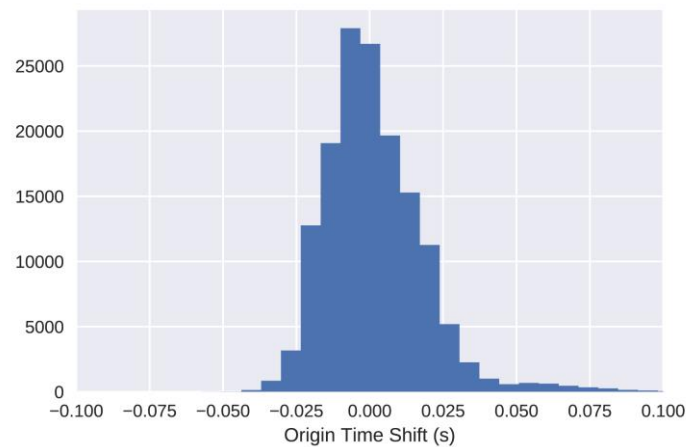


Figure 4.15. Distribution of origin time shifts for all models.

4.4 Discussion

The 1D velocity models obtained from the Monte Carlo VELEST inversions produced well-defined 1D ‘minimum’ V_p and V_s models (Figure 4.7 and Figure 4.8). The station corrections also provided an initial assessment of the spatial variation of V_p and V_s over the study area (Figure 4.10 and Figure 4.12). The variation in final RMS for all of the models was however relatively small, indicating that all 999 of the final velocity model, hypocentre and station correction solutions provided a similar fit to the traveltimes data (Figure 4.6). The distribution of the RMS is approximately log-normal and models with $RMS > 0.95s$ in the tail of the distribution are therefore relatively high RMS when compared to models with $RMS < 0.95 s$,

although the magnitude of difference in RMS is small (0.085 – 0.125 s). Grouping models into RMS < P10 and RMS < P50 shows less variation in the final velocity models (Figure 4.7 and Figure 4.8). This suggests that a ‘minimum 1D velocity’ (the 1D model that best fits the data) is being defined, particularly for layers below 1.5 km bsl.

The layers with lowest variability in the final velocity models were those that contained the hypocentres, which were mostly between 1.5 km bsl and 3 km bsl (Figure 4.7 and Figure 4.8, Table 4.2). Much higher variability in the shallower layers (from surface to 1.5 km bsl) was observed in the final models, consistent with rays travelling sub-vertically through these with few crossing rays in these layers from the microseismic events occurring in the study area.

Table 4.2. Hypocentre and ray length statistics for each layer for all final models. Nhyp = number of hypocentres, %len = % of refracted ray length in this layer, nhit = number of rays passing through this layer. Ave = average, std = standard deviation.

Layer top depth (km bsl)	nhyp ave	nhyp std	%len ave	%len std	nhit ave	nhit std
-0.6	1	1	0	0	9648	10
0.2	2	1	0	1	9650	24
1	6	6	2	7	9650	77
1.5	30	19	5	14	9678	270
2	73	23	16	29	9230	682
2.5	107	29	23	35	7872	1476
3	127	26	46	42	4501	1053
5	0	0	9	16	0	0

The hypocentre distribution results in ray-paths mostly crossing in the regions between the hypocentres (i.e. between Rotokawa and Ngatamariki and southern Ngatamariki). Hence the final velocity models should be representative of the average velocity within these regions. The final velocity models agree well with the Vp and Vs logs in NM10 from southern Ngatamariki, consistent with the final velocity models being more representative of the southern Ngatamariki

region (Figure 4.16). Measured velocities from the NM8 checkshot and NM9 Vp log on the other hand are at or above the highest velocities from VELEST for the layers between 1 to 2 km bsl (Figure 4.16). This suggests that the measured values from these wells are above average for the study area. The observation that the log velocities in NM8 and NM9 are relatively high when compared to the final VELEST velocity models is consistent with findings of Chapter 3 – where the higher log velocities for northern Ngatamariki (NM8 and NM9) for the Tahorakuri Formation were related to lowering of porosity due to emplacement of the Ngatamariki intrusion complex.

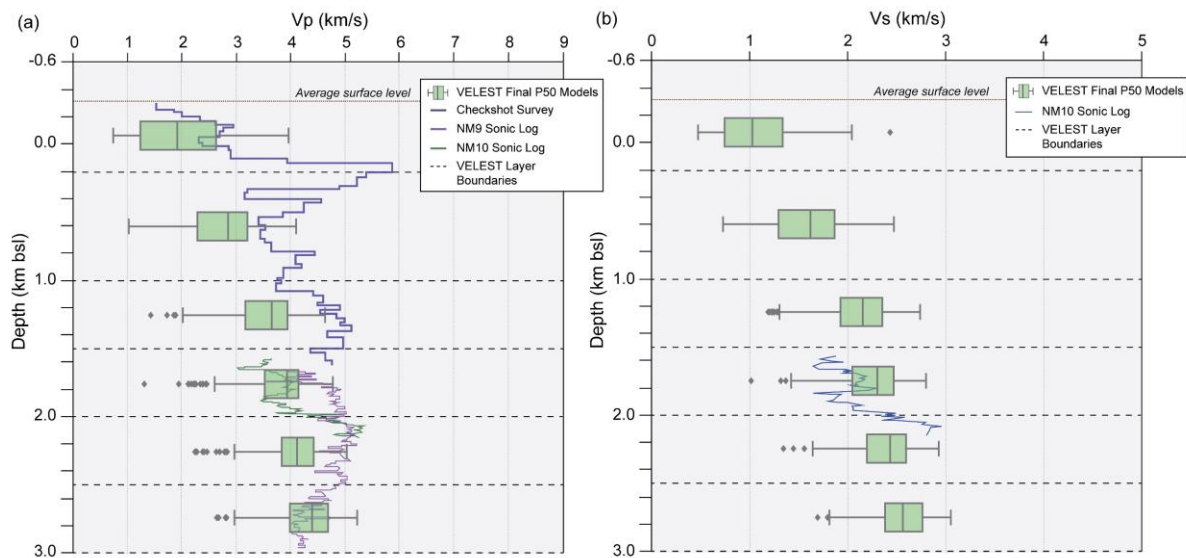


Figure 4.16. Comparison between measured Vp and Vs in wells NM9 (checkshot and sonic logs) and NM10 (sonic logs) and the distribution of the final 500 models with RMS < P50 from VELEST shown as box and whiskers for each layer.

The station correction terms show several, well-defined areas of relatively high and low velocity across the two fields (Vp station corrections Figure 4.9 and Figure 4.10 and Vs station corrections Figure 4.11 and Figure 4.12). The distinct area of high negative Vp and Vs station corrections over northwest Ngatamariki reinforces that this area is anomalously high velocity. This is interpreted to be related to the pervasive alteration above the Ngatamariki intrusion which lowered porosity and therefore increased velocity relative to the south of the field over the depth range of the Tahorakuri Formation (approximately 1 to 2 km bsl) (Chapter 3). It's possible also that thicker rhyolite lavas in the upper 1 km in this area are a significant factor in the Vp and Vs station corrections. A prominent rhyolite dome occurs in the northwest of the field, so it is likely rhyolite occurs close to surface in this area (Figure 1.2). Rhyolite lavas would be expected to have higher velocity than the shallow formations encountered in the

currently drilled wells at Ngatamariki (Huka Falls lake sediments and Oruanui Formation which consists of pumice and recently deposited sediments - Chambefort et al. (2016)), particularly if the rhyolites are unaltered and unfractured.

An explanation for the high V_p station corrections in the northwest area of Rotokawa is less obvious, although rhyolite lavas do outcrop north of the Waikato River in this area suggesting thicker rhyolite within the upper 1 km may be the cause (Figure 1.2). Further evidence for this comes from the two wells drilled north of the Waikato River, RK6 and RK8, which have thick sequences of rhyolite lava from near-surface to approximately 800 mbsl (McNamara et al., 2016; Sewell et al., 2015). The V_s station corrections for Rotokawa however do not have the same pattern as the V_p station corrections, with V_s station corrections being similar across the field. This suggests that there may be variation in V_p/V_s across the field, with lower V_p/V_s south of the Waikato River.

An area of positive V_s station corrections occurs over the western side of the Ngatamariki field, suggesting slower V_s in this area. The cause of this is not immediately apparent as there are no wells drilled in this area, but it may be due to a thicker, deeper smectite clay cap and/or thicker and deeper Tahorakuri Formation in this area which is relatively high porosity.

That the highest negative station corrections occur for the stations surrounding the field suggests the geothermal fields are relatively lower velocity on average than the surrounding area. There are a number of possible factors that may act to lower velocity within the fields relative to the surrounding area which can be broadly characterised as geological variation (e.g. the thickness of volcanoclastic formations that overlie andesite and greywacke within the region) and effects due to the presence of the geothermal fields (e.g. higher temperature, higher fracturing and high steam and gas within the pore space). The two easternmost stations are located close to the edge of the Taupō Volcanic Zone and hence the large negative station corrections for these two stations (V_p station corrections of -1.09 s and -0.89 s, V_s station corrections of -1.78 s and -1.52 s) are most likely due to much shallower greywacke in these areas as imaged by Stern and Benson (2011).

The shifts in hypocentres between models and the overall high variability of the final output models with little variation in RMS residuals suggests that the coupled hypocentre-1D velocity inversion is not well determined (Figure 4.14 and Figure 4.6). This may be due to several factors including unmodelled 3D velocity variation, the accuracy with which arrivals can be determined (~0.05 s for P and ~0.1 s for S based on the manual picking performed on this

dataset, Figure 2.6), and that the use of surface only seismometers does not constrain event depths well such that traveltimes differences can be attributed to either a shift in location and/or a velocity variation. These possible factors should be further investigated when performing 3D tomography inversions. The station corrections, and the consistency of the pattern of station corrections when using all hypocentres, suggests that a 3D velocity inversion is warranted.

The 1D velocity inversions have defined a minimum 1D velocity model that can be used as the basis for starting models in 3D tomography inversions. The spatial consistency of the station corrections (i.e. that distinct areas of negative and positive V_p and V_s station corrections have been defined) strongly suggests 3D velocity variations are present within the study area and that these are manifest in the traveltimes data acquired by the expanded array that was deployed between 2017 and 2018. The location of the high V_p and V_s station corrections in northwest Ngatamariki suggests higher velocities in this area, which compares well with measured velocities from wells in the field and is well explained by the intense alteration and deformation that occurred during the emplacement of the intrusion in the north of the field (Chapter 3). The cause of other variations observed in the station corrections are less certain but may be the result of variations in rhyolite lava thickness in the upper 1 km.

4.5 Conclusions

The program VELEST was used to perform 1000 1D velocity, hypocentre and station correction inversions for a traveltimes dataset consisting of both manual and automatic picks from the expanded array deployed over the Rotokawa and Ngatamariki geothermal fields during 2017 and 2018. The objective of this was to determine a best-fitting 1D velocity model that can be used as the basis for starting models in 3D inversion and to investigate whether 3D velocity variations are apparent within the dataset. The final velocity models from 999 successful runs of VELEST were analysed with the best-fitting models comparing well to measured velocities from V_p and V_s logs in well NM10, which is close to the centre of the array. Measured velocities from NM8 and NM9 (checkshot and sonic logs) are however at or slightly above the highest velocity values obtained with VELEST between 1 km bsl and 2 km bsl. This is consistent with the findings of Chapter 3, that higher velocities are apparent in the north of the field within the Tahorakuri Formation approximately between 1 to 2 km bsl and are related to alteration and deformation during the intrusion of magma in the north of the Ngatamariki field. A prominent area of negative V_p and V_s station corrections (V_p station corrections < -0.1 s, V_s station corrections < -0.2 s) over NW Ngatamariki was also observed,

further supporting this area of the field being on average higher velocity than the rest of the field. A less prominent area of negative V_p station corrections is apparent over NW Rotokawa, which may be related to the presence of thicker shallow rhyolite lavas in this area of the field. An area of positive V_s station corrections occurs over the eastern side of the Ngatamariki field, suggesting slower V_s in this area. The cause of this is not immediately apparent as there are no wells drilled in this area, but it may be due to a thicker, deeper smectite clay cap and/or thicker and deeper Tahorakuri Formation in this area which is relatively high porosity. Similar, relatively small, negative V_s station corrections (< -0.1 s) across the Rotokawa field suggests V_s is relatively constant across the field and slightly faster than the southern Ngatamariki area around RT21. Overall, the variations in station corrections over the study area shows that 3D velocity variations are apparent in the traveltimes dataset and that a 3D tomography inversion is warranted.

5 3D Velocity Inversion of the 2017-2018 Expanded Array Data

Abstract

Imaging of velocity variations within geothermal fields can potentially provide important information on the geology and reservoir properties that can be used to target wells and inform reservoir models. In this chapter, 3D velocity models were determined by local earthquake tomography using P and S wave traveltimes from a set of 351 microseismic events recorded on an expanded seismic array of ~50 seismometers deployed across the Rotokawa and Ngatamariki geothermal fields during 2017 and 2018. These events were mostly from three clusters of seismic activity around injection wells within the fields. The P and S arrival times used in the inversions were from both manual picking (90 events) and high-quality automatic picks (261 events) with estimated arrival times accurate to approximately ± 0.05 s for P and ± 0.1 s for S. The tomography code *tomoDD* was used for the inversions that progressed from 2D to coarse to fine inversion grids in order to examine the improvement in traveltime residuals with increasing model discretization. A 1D layered velocity starting model that was previously determined from Monte Carlo VELEST (Chapter 4) was used for most models. In addition to this, a further fine inversion grid was constructed with a 3D starting velocity model based on available well-logging data (checkshot and sonic logs) and geological information. Model solution robustness and spatial resolution were assessed by plotting Derivative Weight Sum (DWS) values that give a measure of ray-path coverage in conjunction with synthetic recovery tests (spike test and interpretation model test). The inversion models strongly indicate that a west to east, high to low velocity variation of at least $\pm 10\%$ V_p and V_s exists across northern Ngatamariki. The high velocity in the west is likely associated, at least in part, with very low porosity and low permeability that formed within the Tahorakuri Formation due to high temperature magmatic alteration and deformation during intrusion of a diorite-tonalite magma. The location of the transition from high to low velocity agrees well with the transition from high to low gravity from the available gravity data in the area. Relatively low V_p and V_s is imaged in the east of Ngatamariki and is most likely due to either a greater proportion of volcanoclastics and sediments and less rhyolite lava in the upper 1 km and/or deeper smectite and smectite-illite clay alteration in that area, as suggested by magnetotelluric data. High V_s is seen at Rotokawa, which is interpreted as being due to higher-elevation contact of the andesite and greywacke. An alternative explanation would be less volcanoclastics/sediments and more

rhyolite lava in the upper 1 km. The results also highlight some of the challenges with obtaining high spatial resolution of velocity variations at or below 1 km depth using local earthquake tomography within geothermal fields, including poor ray-path coverage from concentrated earthquake clusters; a lack of seismicity above 1 km depth and arrival time uncertainty which has a similar magnitude to the time residuals caused by the velocity variations with a scale of 1 km or less.

5.1 Introduction

Seismic velocity is known to vary with respect to important geothermal reservoir properties such as porosity/permeability, temperature and water/steam saturation (e.g. Boitnott, 1995; Jaya et al., 2010; Siratovich et al., 2014) and therefore techniques that provide images of seismic velocity have potential application to geothermal resource well targeting, monitoring and management. Seismic tomography is one such technique that can provide seismic velocity images of the subsurface, commonly using P and S wave arrival times from local earthquakes (e.g. Rawlinson and Sambridge, 2003; Thurber and Ritsema, 2007). Velocity variations deduced from seismic tomography studies in geothermal areas have been related to both reservoir fluid properties and geology. The largest geothermal field in the world, the Geysers field in California, has been widely studied due to its large size, ongoing seismic monitoring, widespread seismic activity and the steam-dominated nature of the reservoir. Foulger et al. (1997) and Julian et al. (1996) first identified a low V_p/V_s anomaly (~9% lower than surrounding areas) at the field that coincided with the highly produced part of the reservoir. This was related to low pore pressure and boiling in pore space resulting in increasing steam content. Subsequent studies at the Geysers have reproduced these findings (Gunasekera et al., 2003; Lin and Wu, 2018). Theoretical considerations and laboratory experiments suggest that this low V_p/V_s anomaly represents a zone where the pore fluid is predominately vapor, pressure is low, and the shear modulus is increased as a result of the drying of argillaceous (illite clay) material in the reservoir rocks (Boitnott & Boyd, 1996; Boitnott & Kirkpatrick, 1997). De Matteis et al. (2008) and Vanorio et al. (2004) report similar low V_p/V_s at the steam-dominated Larderello-Travale field in Italy, which is interpreted as due to steam-bearing formations. They also find a high velocity transition at depth within the field that they relate to lithology variation or to less fractured parts of the crystalline basement. Foulger & Toomey, (1989) and Jousset et al. (2011) identified several high velocity bodies beneath the Hengill field in Iceland that they related to solidified magma bodies. A low velocity body was also identified that was interpreted to possibly contain partial melt and represent the heat source for the Hengill

field. A low-velocity body was also identified by Zhang & Lin, (2014) beneath the Coso geothermal field in the US which was interpreted as being due to felsic magmatic intrusions. Muksin et al. (2013) presented results of a seismic tomography study for the Tarutung basin in Indonesia that contains several high temperature geothermal fields. They found high Vp/Vs values near to the surface within the Sarulla graben and northeast of the Tarutung basin that were interpreted as fluid bearing sediments with fracturing.

Although no seismic tomography work has been published for the Ngatamariki and Rotokawa geothermal fields, a number of large-scale seismic velocity variations are expected within the fields based on geological variations and seismic velocity logging data. For instance, the northern part of Ngatamariki is known to be low permeability due to the presence of an old intrusion and its associated alteration halo (Chambefort et al., 2016). Measured velocities at Ngatamariki from wireline sonic logs show that the highly altered rock above the intrusion in the north of the field has higher Vp (approximately 0.5-1 km/s faster) than the same formation in the south of the field (Chapter 3). Sherburn et al., (2003) also report a high Vp anomaly (>15% above background) in the north of Ngatamariki that they attribute to the intrusion. However, this feature was not well resolved spatially as the study used a regional seismic monitoring network with wide spacing between seismometers. As the intrusion and its alteration is associated with low permeability, imaging the high velocity with tomography can allow future wells drilled at Ngatamariki to be targeted away from this low permeability area. Unlike the Ngatamariki reservoir, the Rotokawa reservoir has a thick 2-phase zone (steam + liquid) at the top of the reservoir (approximately from 1 to 2 km depth) that has grown and increased in its steam content during the operation of the field (e.g. Hernandez et al., 2015; McNamara et al., 2016; Sewell et al., 2015). The presence of steam in the reservoir is expected to reduce Vp and if imaged with tomography might assist with better defining the extent of the field. A sharp lateral temperature gradient is also known to exist at Rotokawa in the north-northeast of the field (340°C measured in well RK24 to ~200°C in well RK19 within 1 km distance) (Sewell et al., 2015). This is associated with a transition from high (initial injectivity greater than 1 t/h.bar and convective, isothermal temperature profiles) to very low permeability (initial injectivity less than 1 t/h.bar and conductive, linear temperature-with-depth profiles) and there may be Vp and Vs changes associated with this, which if adequately imaged, would inform future drilling on the field.

The primary purpose of this study was to investigate the 3D velocity structure of the Ngatamariki and Rotokawa fields using local earthquake tomography. To do this, a dense array

of 50 seismometers was deployed across the two fields for a one-year period over 2017 and 2018 with the aim of improving the spatial resolution of velocity variations within the field (Figure 2.2). This work builds on a Monte Carlo 1D inversion of the same dataset that determined the average 1D velocity structure across the two fields and serves as a basis for the 3D inversion work presented here (Chapter 4). The 1D inversion also included inverting for station correction terms that provided an indication of the general 3D velocity variation in the area.

5.2 Data and Methodology

5.2.1 Travel-time Data

The P and S arrival time data used was the same as that used for the Monte Carlo VELEST analysis presented in Chapter 4 and consisted of both manually picked and automatically picked P and S wave arrival times from 302 microseismic events mostly from the three main clusters of activity (Rotokawa, Ngatamariki South and Ngatamariki North) near injection areas in the geothermal fields (Figure 4.1 and Table 4.1). Chapter 4 describes how this arrival time catalog was generated. Starting locations for the hypocentres were the average locations from the Monte Carlo VELEST analysis. In total, the absolute arrival time dataset consisted of 7829 P arrivals and 3332 S arrivals.

The python program, hypoDDpy (Krischer, 2015), which uses the Obspy framework (Beyreuther et al., 2010), was used to generate the differential traveltime data. Catalog differential times were generated for all event pairs within 1 km of each other (effectively linking most event pairs within each of the three main clusters of seismicity – northern Ngatamariki, southern Ngatamariki and Rotokawa). Cross-correlation differential times were also generated for all phase and event pairs within 1 km of each other, however only cross-correlation differential times for event pairs within 0.5 km of each other were used in the inversions. In total, 111,858 catalog P, 19,972 catalog S, 61,533 cross-correlation P and 10,928 cross-correlation S traveltimes were generated.

5.2.2 Inversion code tomoDD

The program tomoDD (Zhang, 2003) was used to invert both absolute and differential traveltime data to obtain V_p and V_s models. The inclusion of differential traveltime data in the inversion has been shown to sharpen velocity contrasts within and surrounding the clusters of seismicity for which the differential data are calculated (Zhang, 2003). The large-scale velocity

structure is however dominantly determined by the absolute traveltimes data. The inversion code tomoDD utilises the ‘pseudo-bending’ ray-tracing method of Um and Thurber, (1987) to determine ray paths and calculate traveltimes. Velocity model parameterisation is via a grid of nodes with tri-linear interpolation of velocity between the nodes to obtain a continuous velocity media. Inversion is via the LSQR damped least-squares algorithm of Paige and Saunders, (1982). Both damping and smoothing regularization are used to stabilise the inversion and obtain a model that is close to the starting model and minimises the velocity model complexity required to fit the traveltimes data down to the noise level. Three data types are able to be used in tomoDD – absolute traveltimes, catalog differential times and cross-correlation traveltimes. These are implemented in the inversion in a hierarchical scheme whereby each data type is weighted differently throughout the inversion.

To investigate the velocity model complexity that is required to obtain an adequate fit to the absolute data, inversions were first performed using only the absolute data with six different model parameterisations with increasing complexity from a 2D grid through to a fine grid with 1 km node spacings (Figure 5.1). For all of these inversions, nodes with derivative weight sum values (a measure of ray path coverage e.g. Thurber and Eberhart-Phillips, (1999)), less than 0.1 times the average of all nodes were fixed in the inversion, thereby preventing nodes that are not sampled by the ray paths from changing. Damping only was used in the 1D and 2D inversions whereas both damping and smoothing were used in the coarse and fine 3D models. In each of the 3D models, an L-curve test was performed to obtain appropriate values for the damping and smoothing values (Figure 5.2). Inversions for the absolute data were run for 5 iterations of hypocentre only followed by 5 iterations of joint hypocentre-velocity. The change in residual RMS between the 4th and 5th and 9th and 10th iterations was small for all inversions ($\sim < 5$ ms RMS), showing that the hypocentre and velocity model solutions had converged.

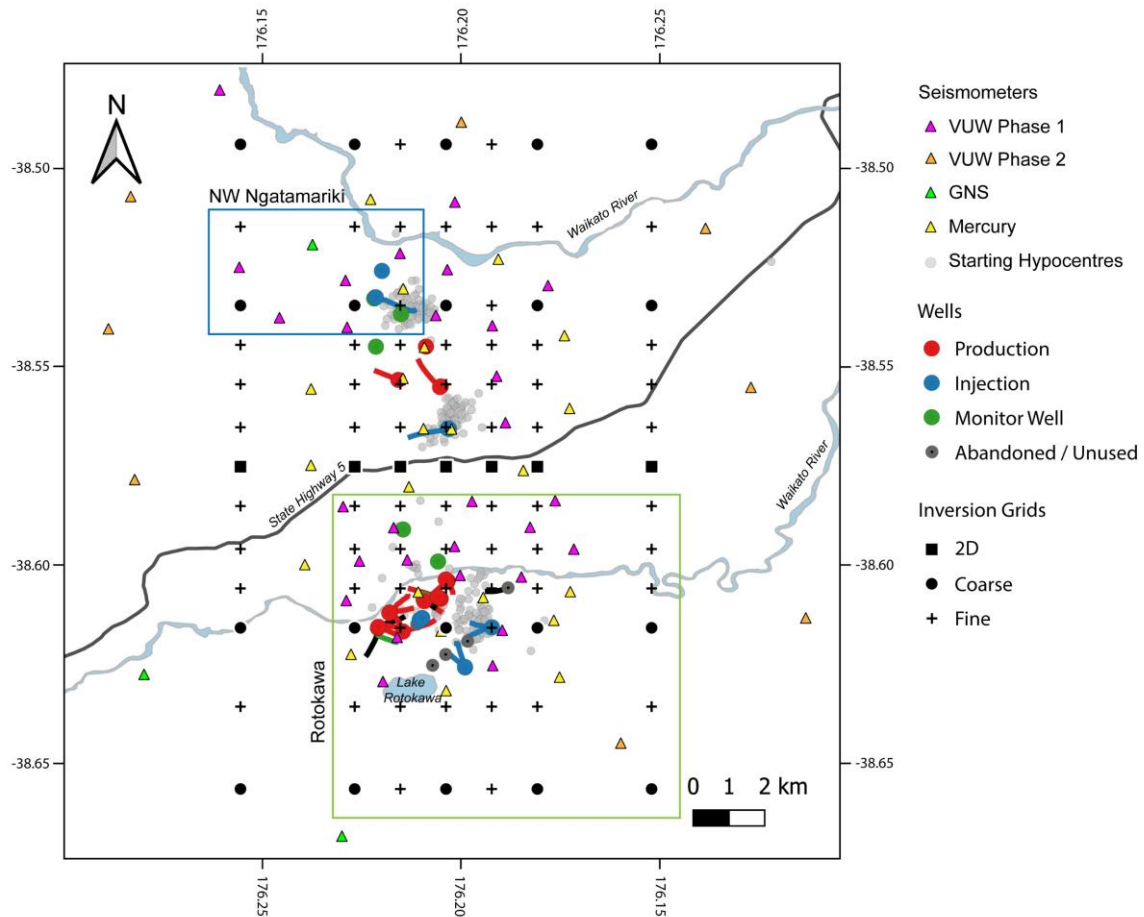


Figure 5.1. Location of nodes for the different grids used for absolute data inversion. The blue and green rectangles show the areas for which the starting velocity values were changed in the ‘geo’ starting models. N.b. The coarse model includes the nodes of the 2D model and likewise the fine model includes the nodes of both the 2D and coarse models.

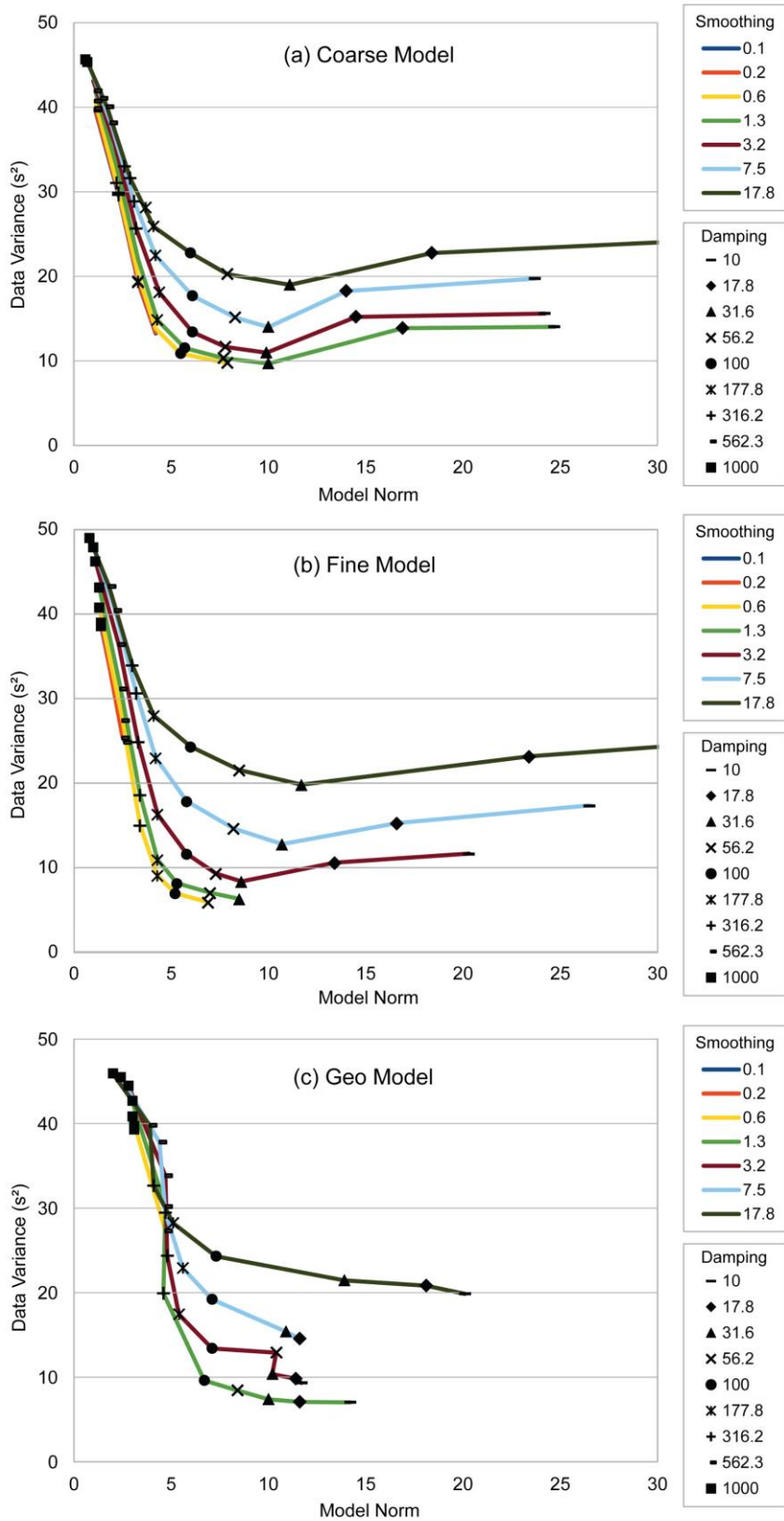


Figure 5.2. Trade-off curves for the absolute traveltimes data for (a) the coarse 3D model, (b) the fine 3D model and (c) the fine 3D model with geological starting model. Coloured lines are for varying smoothing and symbols are for varying damping.

All models except one used a 1D starting velocity model based on the average of the 50% best-fitting VELEST models (Figure 5.3). To make use of available a-priori velocity information and to test sensitivity of the final model to the starting velocity model, a 3D starting velocity model (referred to as the ‘geo’ model) was developed based on the checkshot survey, well-logging data and geological information. In this starting model, both the northwest corner of Ngatamariki and Rotokawa were given higher starting velocities (Figure 5.1 and Figure 5.3). For northwest Ngatamariki, the starting velocities approximate those obtained from the checkshot survey and Vp log in NM9. For the Rotokawa area, higher starting velocities between 1 km bsl and 2 km bsl approximate those obtained for andesite and greywacke from sonic logs (Vp and Vs for andesite in NM10) and the core measurements of Mielke et al. (2016) and seismic refraction survey velocities of Stern and Benson, (2011) for greywacke. The starting model hence accounts for the difference in elevation of the top of andesite between Ngatamariki and Rotokawa (approximately 2 km bsl for Ngatamariki (Chambefort et al., 2014) versus approximately 1-1.5 km bsl for Rotokawa (McNamara et al., 2016)). Everywhere else in the 3D geo starting model the starting values were as per the 1D starting model. In all starting models, the Vp/Vs ratio was set to be 1.8 based on the average obtained from the dipole sonic logs in NM8 and NM10 (Chapter 3, Figure 3.20).

Two starting velocity models were constructed using the node locations for the ‘fine’ model; an inversion grid using the 1D VELEST starting model with constant velocity for each depth (hereafter referred to as the ‘fine’ model) and a 3D starting model based on the geology, checkshot and logs (‘hereafter referred to as the ‘geo’ model) (Figure 5.1). The inversion scheme placed 100 times higher weight on the absolute data in the first two sets of iterations in order to establish the absolute hypocentre location and bulk velocity structure first. Subsequent iterations placed higher weight on the catalog differentials followed lastly by the cross-correlation differentials. As with the inversions using absolute data only, the first set of iterations were hypocentre only in order to allow hypocentre movement to reduce residuals prior to joint inversion of both velocity and hypocentre. Nodes with DWS values higher than 10 times the average DWS were fixed in the velocity model inversion during the inversion sets with higher weight on the differentials. This was to limit any velocity model changes occurring far outside of the source regions, in accordance with double-difference tomography theory (Zhang, 2003; Zhang and Thurber, 2006). Again, trade-off curve tests were performed to select the optimal settings for damping and smoothing.

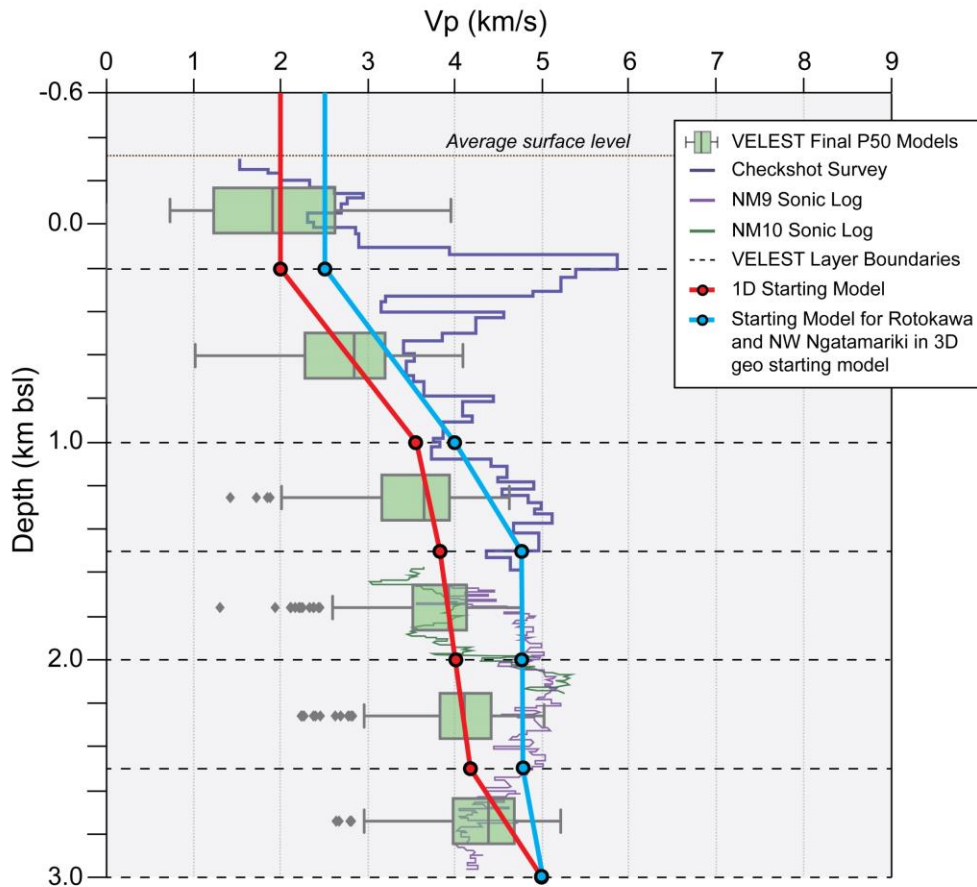


Figure 5.3. 1D starting model used in the 3D inversions (red line) and velocity starting values applied to NW Ngatamariki and Rotokawa in the 3D ‘geo’ starting model (blue line, see Figure 5.1 for areas where these velocities were applied). Also shown are the box and whisker plots for the 50% best-fitting VELEST models and the sonic and checkshot velocity data.

5.2.3 Synthetic testing

Based on the recommendations of Rawlinson and Spakman, (2016), a discrete spike test involving a sparse distribution of velocity spikes (or alternatively described by Rawlinson and Spakman, (2016) as a sparse checkerboard test), was performed rather than the more commonly used checkerboard resolution test that involves tightly-spaced, alternating high/low velocities between each set of nodes (e.g. Rawlinson and Sambridge, 2003). This was done to better assess smearing of velocity onto nodes that are not well constrained by the available ray paths, particularly above 1 km bsl where ray-paths are mostly vertical and there is little crossing of ray-paths. Synthetic arrival times were generated through a velocity model consisting of velocity spikes 1 x 1 x 1 km in size and with $\pm 10\%$ velocity variation from the 1D starting velocity. The spikes were separated by one node in east-west and two nodes in north-south and were placed between 1.5 and 2.5 km bsl. The synthetic arrivals were then inverted using the

same parameters as were used in the inversion of the real data. Synthetic recovery tests of the main interpreted velocity structures were also performed to assess how well resolved spatially these features are. All synthetic tests were performed both with and without randomly generated Gaussian pick noise with a standard deviation of 0.05 s for P and 0.1 s for S which was based on the standard deviation of the manually picked uncertainties (Figure 2.6).

5.3 Results

5.3.1 Data Fit

The 1D and 2D velocity models were not able to fit the data to the level of noise (approximately ± 0.05 s for P and ± 0.1 s for S) and 3D velocity structure (coarse, fine and geo models) was required to provide an adequate fit to the data (Figure 5.4). The coarse model provides a reasonably good fit to both the P and S data, with most residuals less than ± 0.1 s for P and less than ± 0.2 s for S. The fine and geo models show improvement in residual fit relative to the coarse model, however the improvement is smaller than when moving from the 2D to the coarse model. The fine and geo models both fit the P and S residuals close to the expected level of uncertainty in the pick data. The difference in data fit between the fine and geo model is relatively minor with the fine model obtaining a slightly better fit to the data than the geo model. The catalog and cross-correlation differentials for the double difference runs were well fit with RMS residuals of 61 ms for catalog and 25 ms for cross-correlation data for the fine model and 73 ms for catalog and 16 ms for cross-correlation in the geo model.

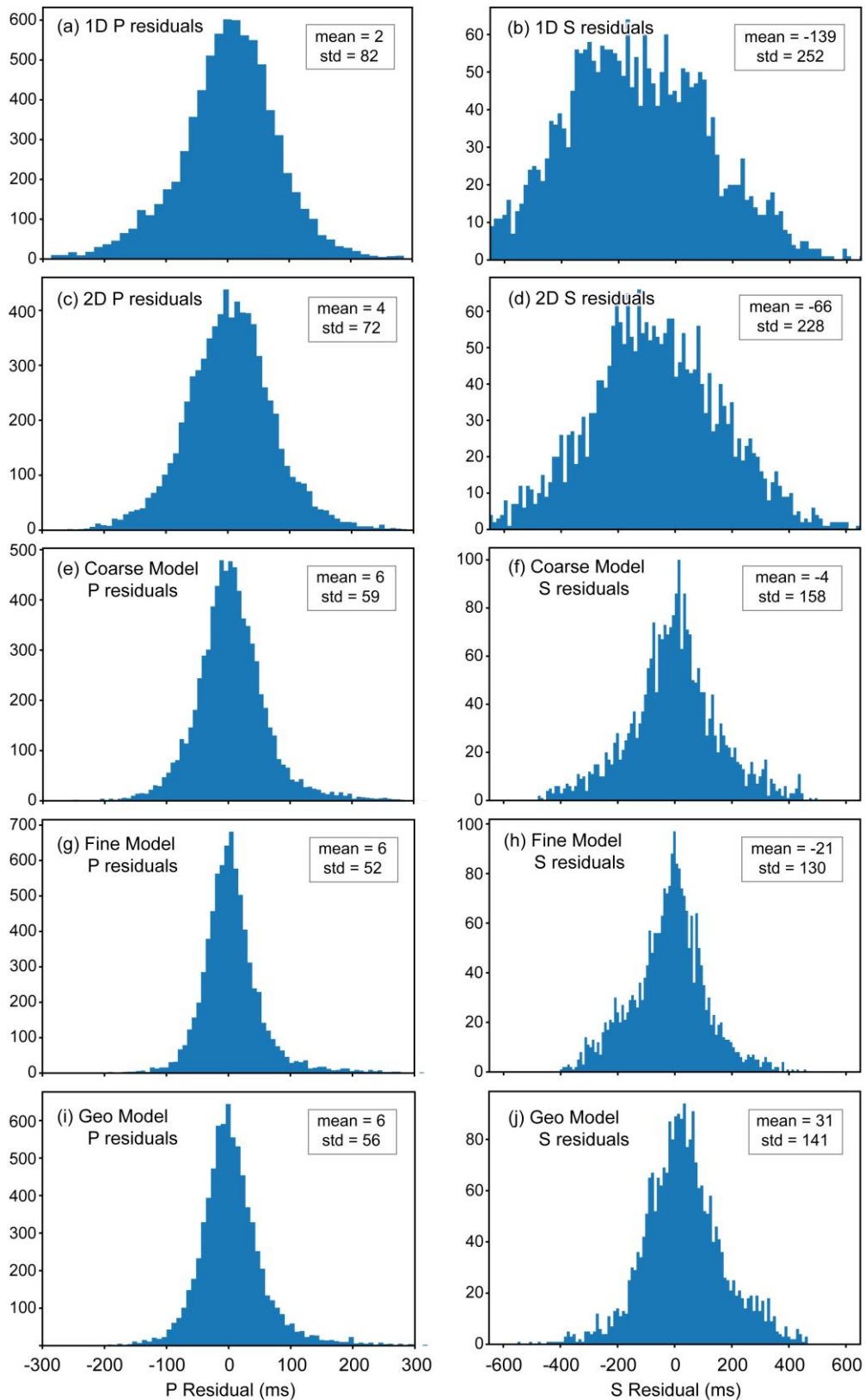


Figure 5.4. Distribution of P and S residuals for the absolute arrivals for the 1D (a and b), 2D (c and d), coarse 3D (e and f), fine 3D (g and h) and 3D geo model (i and j). Means and standard deviations are in milliseconds.

5.3.2 Data Coverage

DWS values for V_p and V_s clearly show that the area between the earthquake clusters and between 1 to 2 km bsl has the best ray-path coverage (Figure 5.5 and Figure 5.6). There is relatively poor coverage for all depths outside of the dense array which is partly because relatively few events were recorded by the outer array due to data acquisition issues. The highest DWS values were obtained at 1.5 and 2 km depths for both P and S waves with values of >1000 for P and >100 for S in an area extending between the main earthquake clusters. Events at southern Ngatamariki and Rotokawa are larger magnitude than those for northern Ngatamariki and are therefore better recorded across the array. This is likely the reason for very high DWS in the south between RK and NM south at 2 km depth. DWS values at 1 km bsl are approximately half those at 1.5 and 2 km for the area between earthquakes (~ 500 for P, ~ 50 for S). Relatively low DWS values for 0.2 km bsl is due to ray paths at this depth travelling mostly vertically and therefore the average length of ray travelling close to each node is low. DWS values are low for 2.5 and 3 km depth as the earthquakes are mostly at or above these depths. The DWS values agree well with the results of the synthetic testing that further show that depths between 1.0 and 2.0 km bsl are best resolved for this dataset and that there is poor constraint at 0.2, 2.5 and 3 km bsl (see Synthetic Testing below).

5.3.3 Final Velocity Models

All four models (2D, coarse, fine and geo) show a west to east, high to low variation in V_p and V_s across northern Ngatamariki between 0.2 and 2 km depth. Depth slices for the fine model are shown in Figure 5.7 for V_p and Figure 5.8 for V_s and for the geo model in Figure 5.9 for V_p and Figure 5.10 for V_s . Comparisons between the fine and geo models on the same velocity scale are shown in Figure 5.11 and Figure 5.12 for V_p and Figure 5.13 and Figure 5.14. The transition between high to low velocity in all cases occurred approximately through the middle of the Ngatamariki field with the transition being sharper in the fine and geo models. The inclusion of high V_s at Rotokawa was a common result for all of the 3D models (coarse, fine and geo) and resulted in a significant change in S residuals between the 2D and coarse model (Figure 5.4).

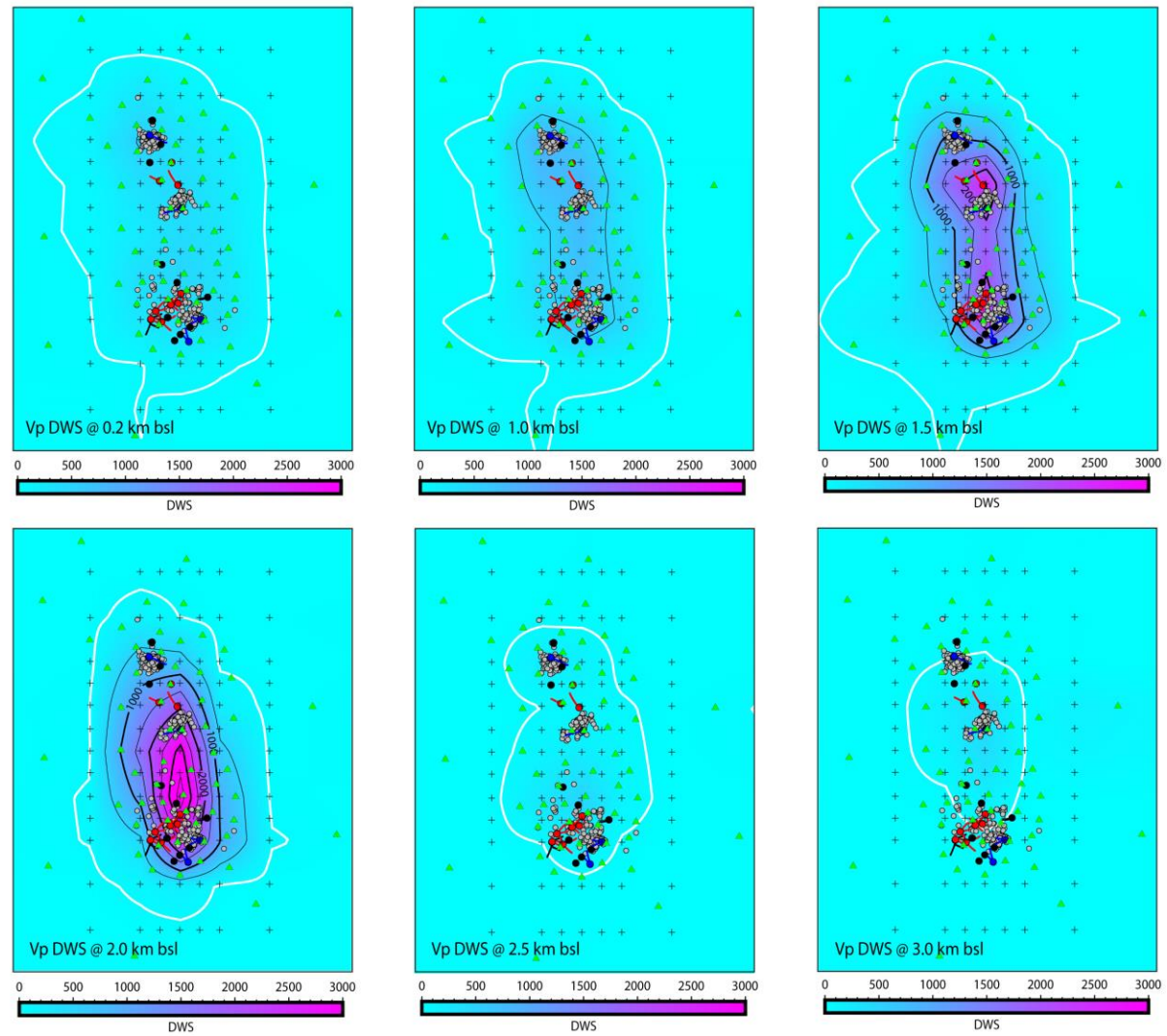


Figure 5.5. Derivative weight sum (DWS) for Vp. Green triangles show the location of seismometers, grey dots the location of hypocentres. The white contour is DWS equals 50.

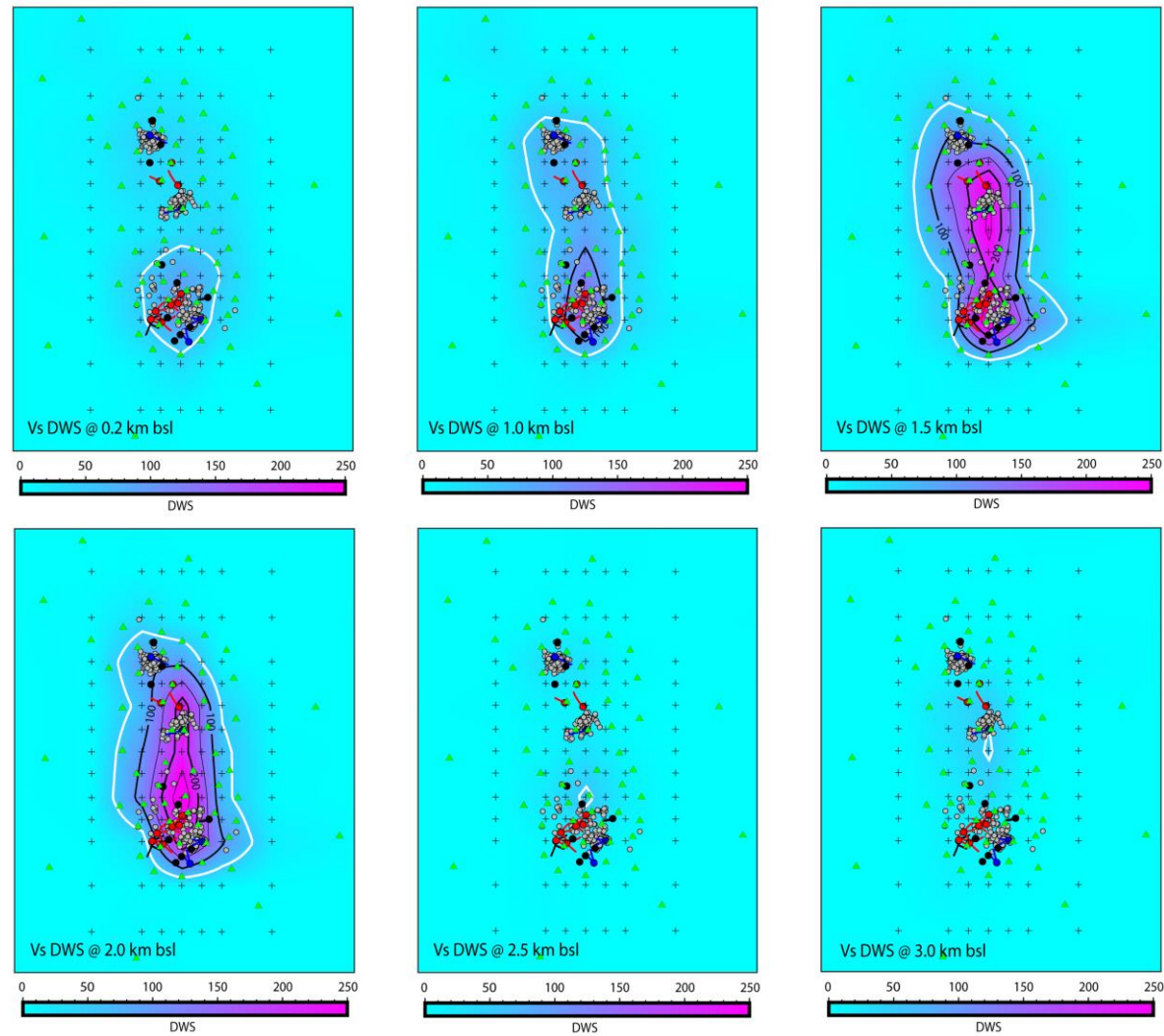


Figure 5.6. Derivative weight sum (DWS) for Vs. Green triangles show the location of seismometers, grey dots the location of hypocentres. Note the difference in the colour scale between Vp DWS and Vs DWS. The white contour is DWS equals 50.

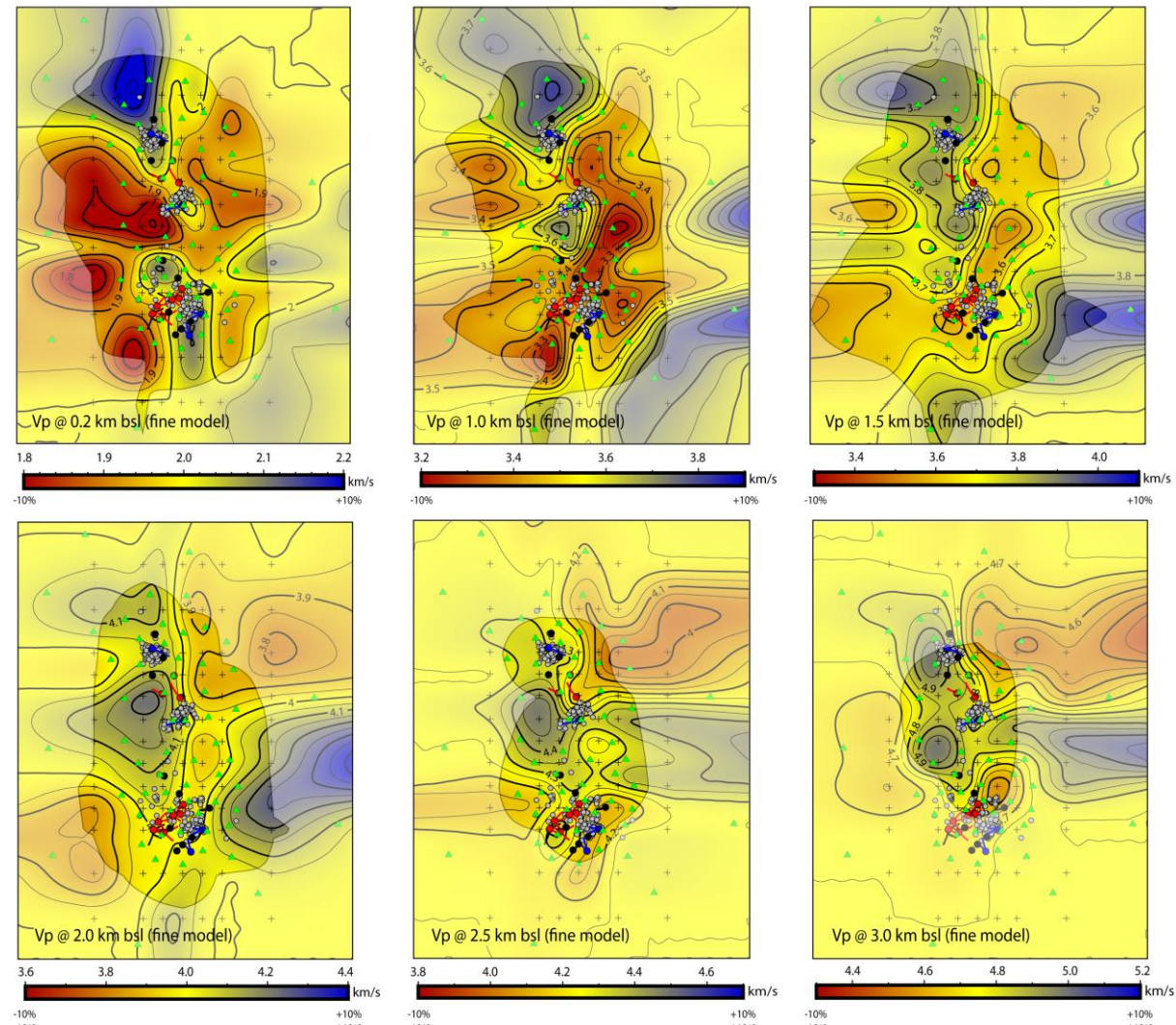


Figure 5.7. V_p for the fine model. The area with good ray coverage ($DWS > 500$) is highlighted. Green triangles show the seismometers, grey dots the earthquakes. The colour scale ranges between $\pm 10\%$ of the 1D starting velocity model.

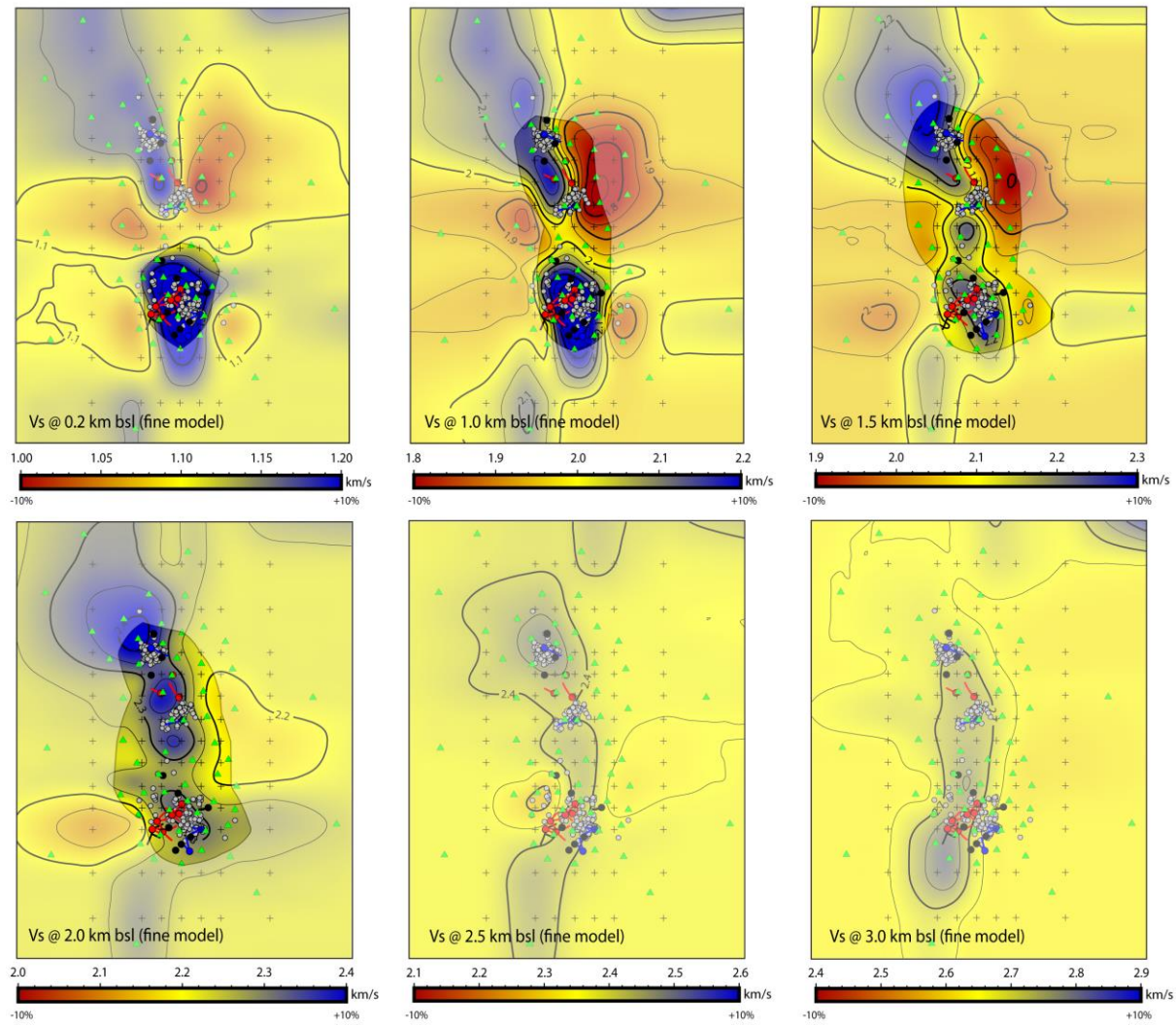


Figure 5.8. V_s for the fine model. The area with good ray coverage ($DWS > 50$) is highlighted. Green triangles show the station locations, grey dots the earthquakes. The colour scale ranges between $\pm 10\%$ of the 1D starting velocity model.

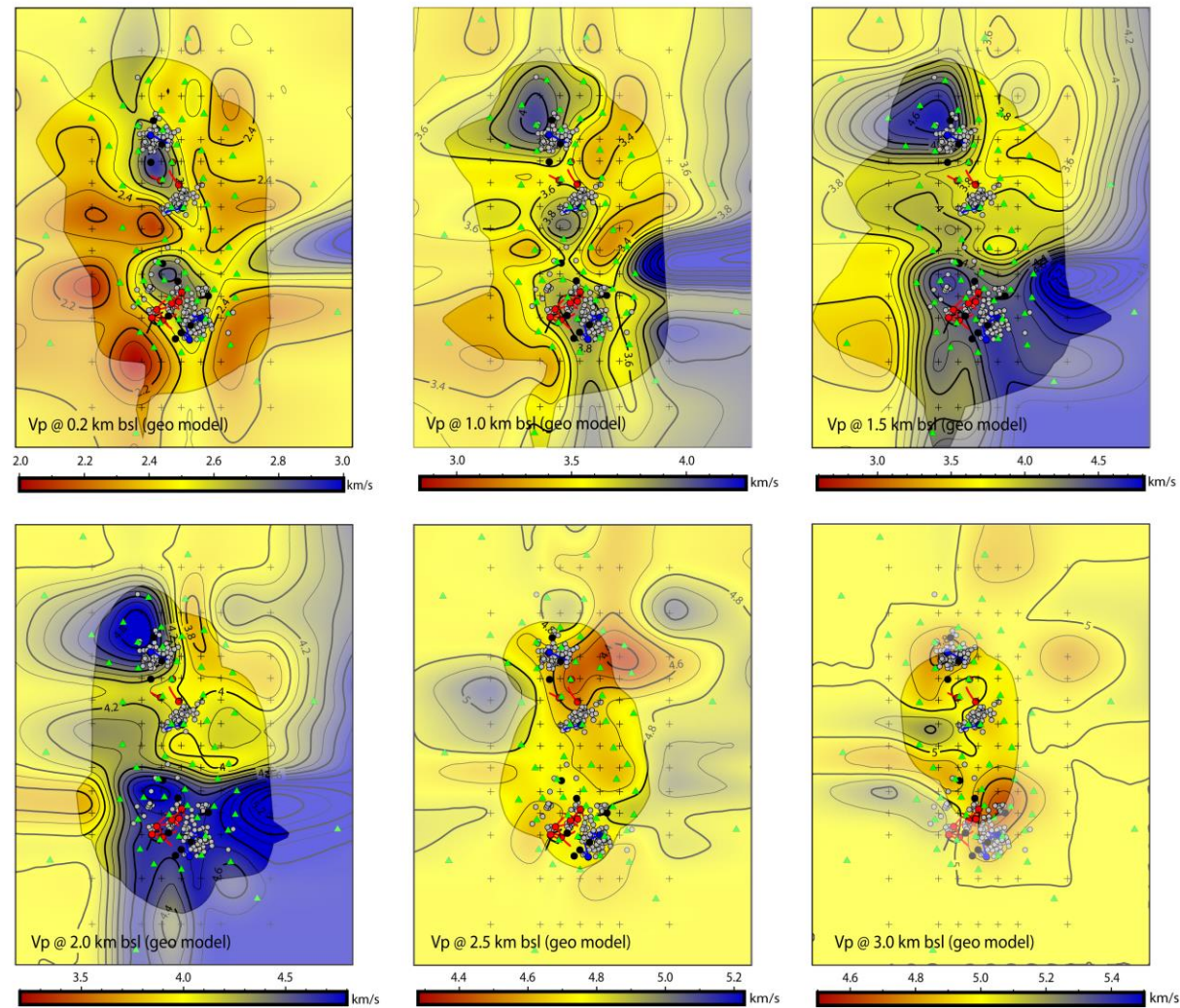


Figure 5.9. Vp for the geo model. The area with good ray coverage (DWS > 500) is highlighted. Green triangles show the station locations, grey dots the earthquakes. Note the difference in velocity scale from Figure 5.7.

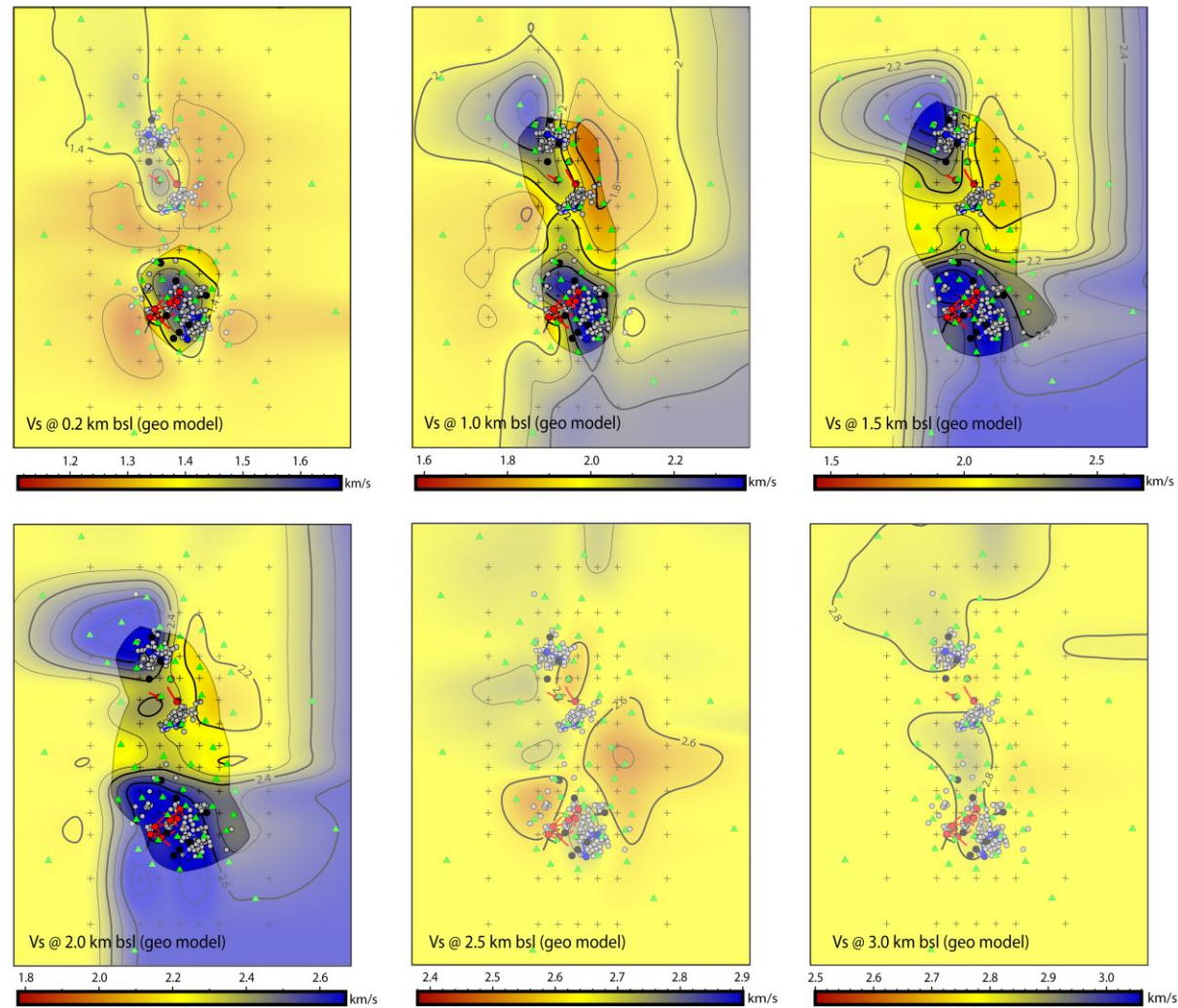


Figure 5.10. Vs for the geo model. The area with good ray coverage ($DWS > 50$) is highlighted. Green triangles show the station locations, grey dots the earthquakes. Note the difference in velocity scale from Figure 5.8

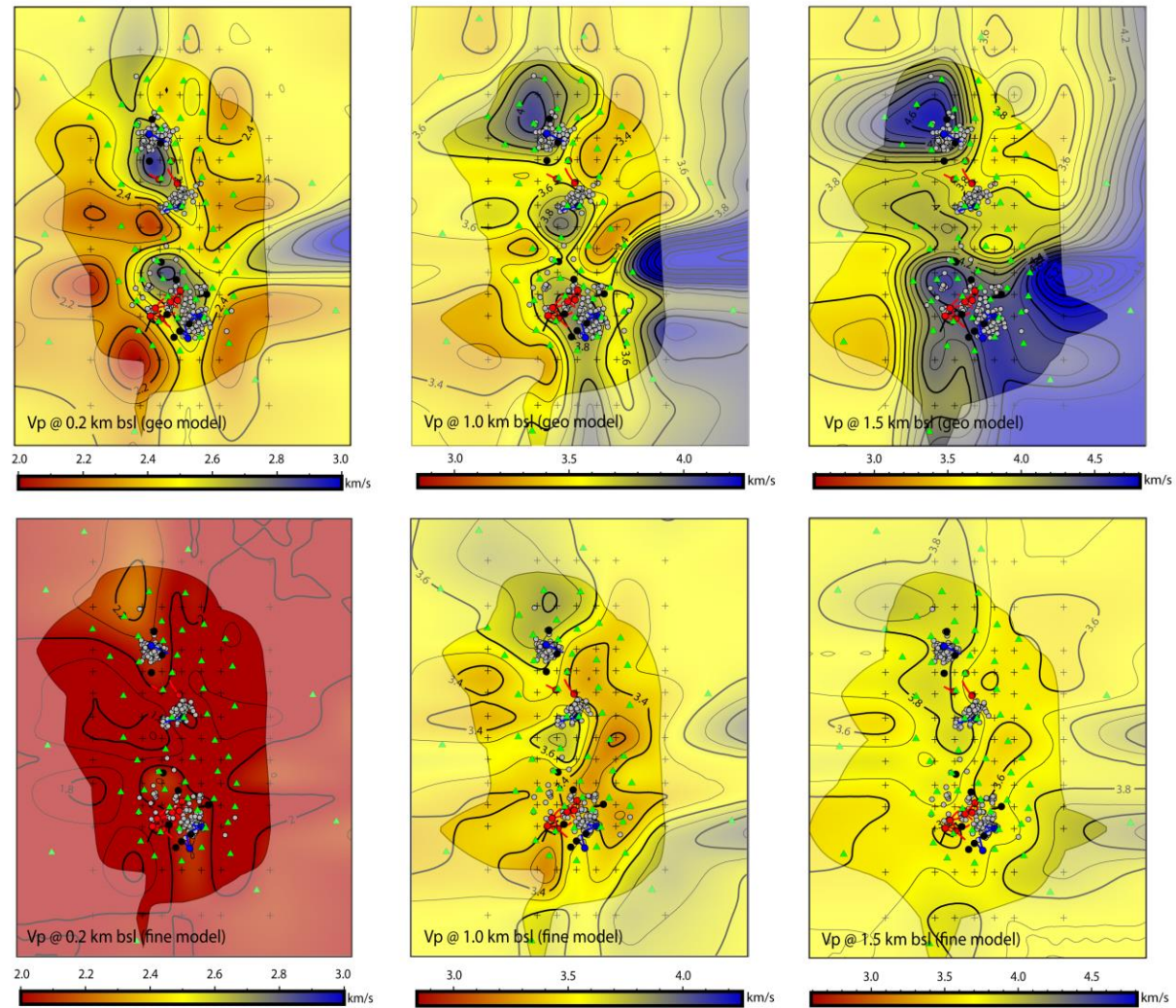


Figure 5.11. Comparison between the geo and fine model with the same velocity scale for Vp. The area with good ray coverage (DWS > 500) is highlighted. Green triangles show the station locations, grey dots the earthquakes.

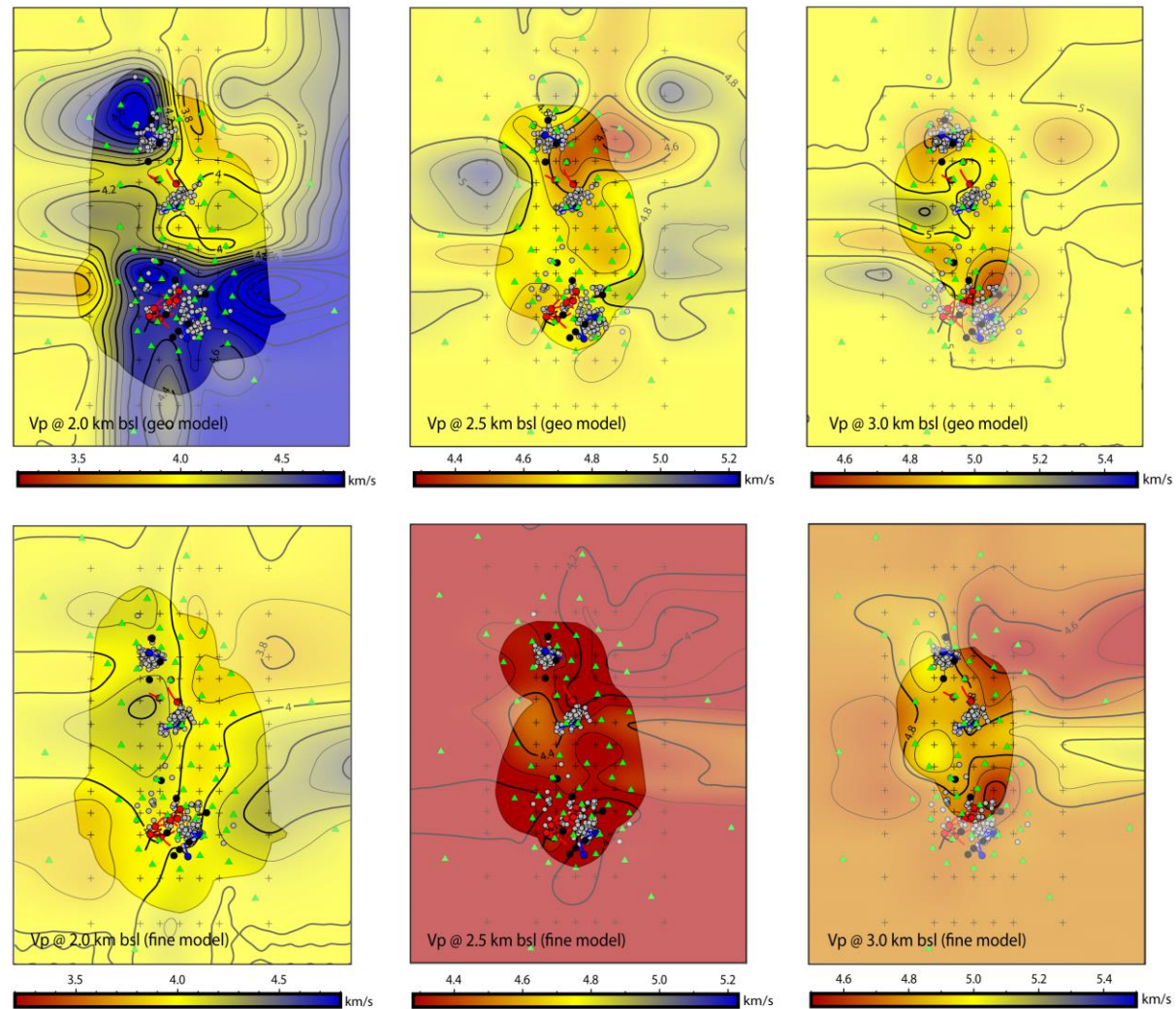


Figure 5.12. Comparison between the geo and fine model with the same velocity scale for V_p . The area with good ray coverage ($DWS > 50$) is highlighted. Green triangles show the station locations, grey dots the earthquakes.

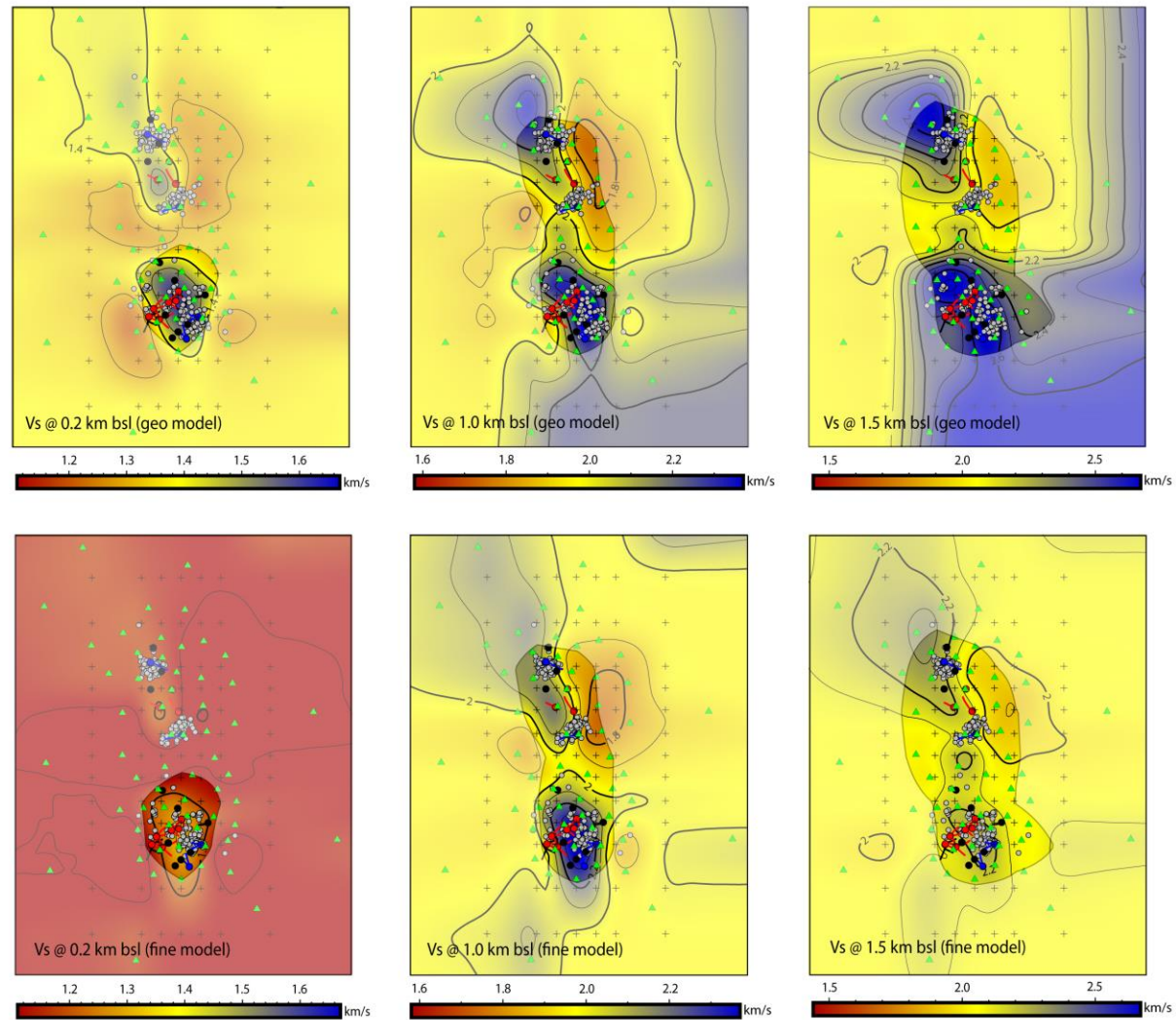


Figure 5.13. Comparison between the geo and fine model with the same velocity scale for V_s . The area with good ray coverage ($DWS > 50$) is highlighted. Green triangles show the station locations, grey dots the earthquakes.

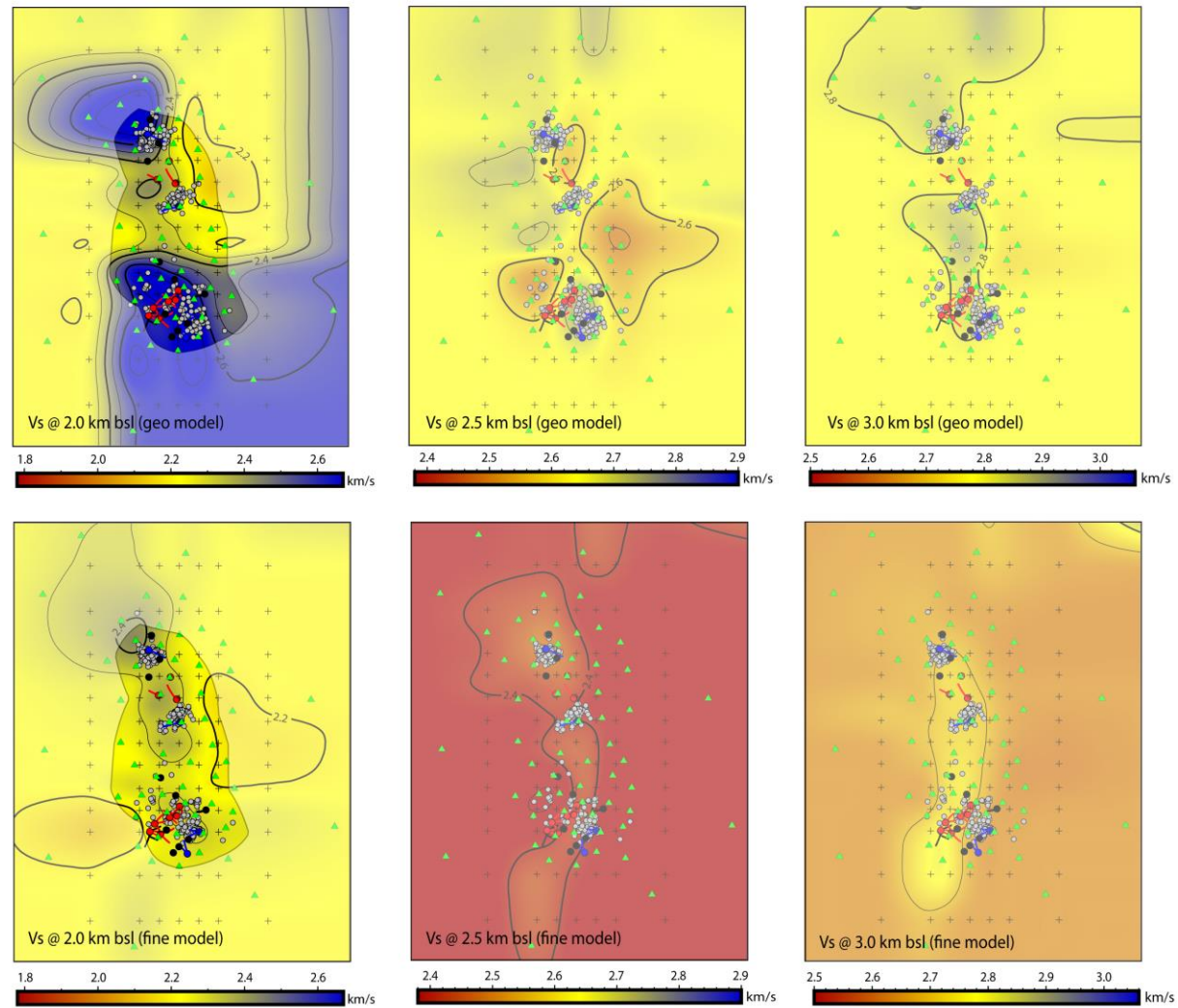


Figure 5.14. Comparison between the geo and fine model with the same velocity scale for V_s . The area with good ray coverage ($DWS > 50$) is highlighted. Green triangles show the station locations, grey dots the earthquakes.

For the fine model, high V_p (up to 7% higher than the starting model) was observed in NW Ngatamariki from 0.2 to 2.0 km bsl (Figure 5.7). The high velocity is only in the NW from 0.2 to 1.0 km bsl and extends to the south at 1.5 and 2.0 km bsl. Lower V_p (up to 10% lower than the starting model), occurs to the east of Ngatamariki between 0.2 and 2 km bsl which extends over Rotokawa at 1.0 and 1.5 km bsl, but is less apparent at Rotokawa for 2 km bsl (Figure 5.7). In general, the V_s variations are stronger than V_p over the 0.2 – 2 km bsl depth range (Figure 5.8). High V_s (up to 10% higher than the starting model) to low V_s (up to 10% lower than the starting model) occurs across Ngatamariki over 0.2 to 1.5 km bsl similar to the spatial variation for V_p . High V_s (up to 10%) is observed for Rotokawa between 0.2 to 1.5 km bsl (Figure 5.8). Higher V_s , up to 10% higher than the starting model, extends across the two fields at 2 km bsl in the area between the earthquake clusters.

The geo model had similar overall spatial variations to the fine model (Figure 5.9 and Figure 5.10). Again, a high to low velocity variation is seen across Ngatamariki for both V_p and V_s . V_p and V_s from 1.0-2.0 km bsl for NW Ngatamariki were however higher than the fine model and were relatively unchanged from the starting model that had high velocity in this area based on the checkshot data from NM9. Higher V_p and V_s than the starting model is still observed to the southwest of NM with values similar to the fine model. The low V_p in the east of Ngatamariki had similar V_p to that of the fine model between 1 and 2 km bsl. V_p is different than the fine model over the 1.0-2.0 km bsl depth interval at Rotokawa (3.3-4 km/s V_p for the fine model versus 4-4.8 km/s V_p for the geo model). These values of V_p for Rotokawa are relatively unchanged from the starting model which had higher V_p and V_s based on the shallower andesite and greywacke. V_s again shows a high to low variation across northern Ngatamariki similar to the fine model. The V_s values for the high velocity to the NW of Ngatamariki are higher than for the fine model, and, as was the case for the V_p , are similar to the geo starting model. V_s values for Rotokawa are also similar to the geo starting model, being higher than the fine model. The values of V_s for the low to the east of Ngatamariki are similar to that of the fine model. The low in the east at Ngatamariki and the extension of high velocity to the southwest of Ngatamariki are the main velocity variations added by the inversion relative to the geo starting model for both V_p and V_s .

There appeared to be little improvement in the fit to residuals for both the fine and geo models during velocity and hypocentre inversions involving catalog and cross-correlation data (< 5 ms for both catalog and cross-correlation data, Figure 5.15). The velocity models obtained from the double-difference inversions were also relatively unchanged from those obtained using just

the absolute data. Together these results suggest that there is little improvement in the velocity model from incorporating the differential data and that most of the residual improvement in these data can be achieved by small relative hypocentre movements.

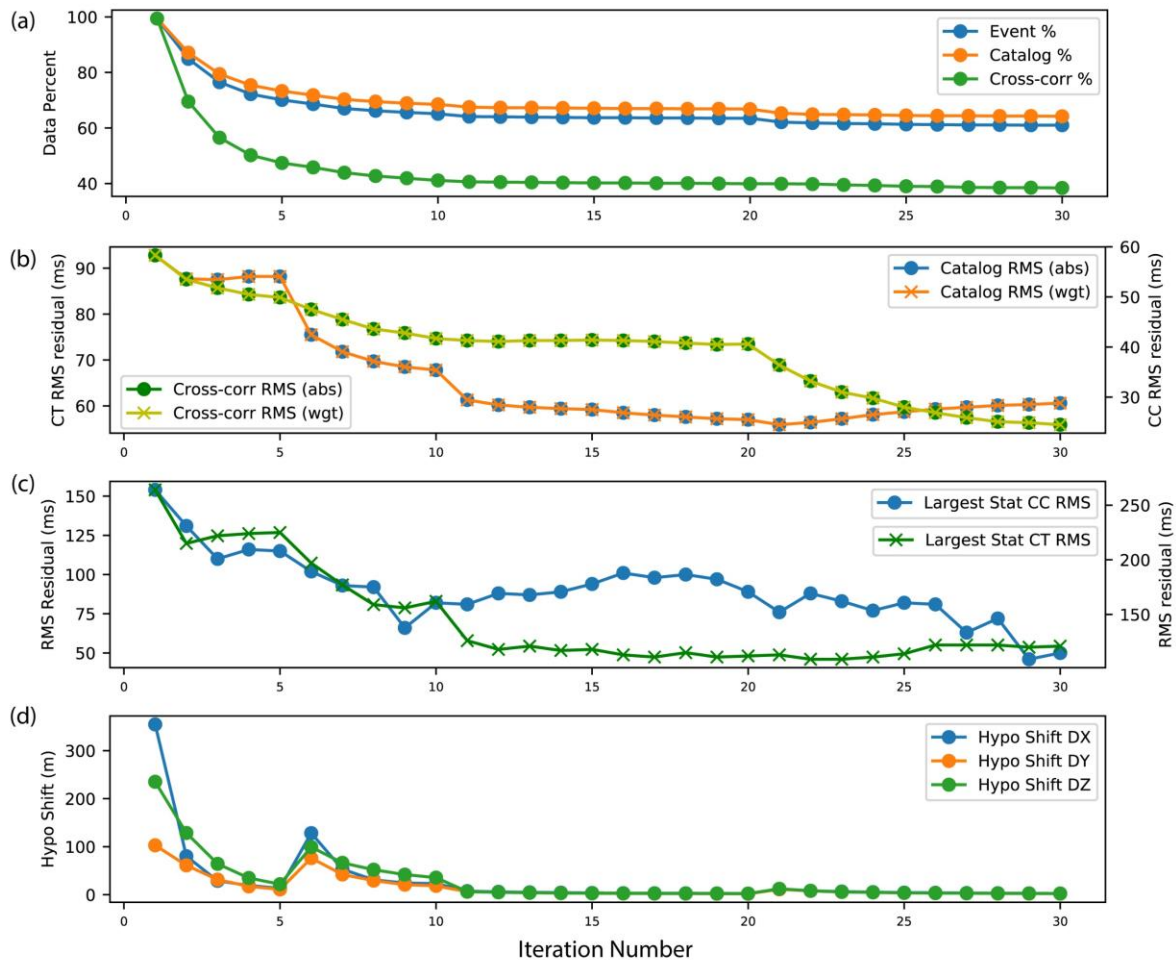


Figure 5.15. Change in data percent, data fit and hypocentre shift for each iteration. (a) Percent of each data type, (b) RMS residual for catalog and cross-correlation data, (c) largest overall station RMS for catalog and cross-correlation data and (d) hypocentre shifts for each iteration for the fine model. Little improvement in RMS residual is made for catalog and cross-correlation data when inverting for both hypocentre and velocity model (iterations 15-20 for catalog and 25-30 for cross-correlation).

5.3.4 Synthetic Testing

The best recovery for the spike test for both V_p and V_s was at 1.5 km bsl with reasonable recovery also obtained for 2 km bsl (Figure 5.16, Figure 5.17, Figure 5.18, Figure 5.19, Figure 5.20 and Figure 5.21). At both of these depths, and for both V_p and V_s , the region encompassing the earthquakes was best recovered, with both the shape of velocity variations

and whether the velocity was relatively high or low being generally recovered. The recovery of the shape of the velocity variations is slightly worse with the addition of pick noise to the synthetic data. Recovery directly adjacent to the area between the hypocentres but still within the dense array is partially recovered for V_p at 1.5 and 2 km bsl but not for V_s . This likely reflects the overall lower amount of S wave data as shown by the lower DWS values for V_s relative to V_p (Figure 5.5 and Figure 5.6). Areas outside of the dense array and at 2.5 km bsl were poorly recovered again due to the lack of ray coverage. Velocity variations were introduced by the inversion at 0.2 and 1.0 km bsl despite the synthetic model having the same constant velocity as the starting model for the inversion. These variations became more prominent with the addition of pick noise to the synthetic data. In all cases, the absolute velocity values were underestimated by the inversion. For the best recovered area between the earthquakes at 1.5 km bsl, the percent difference in velocity between the synthetic model and the recovered model is approximately $\pm 50\%$ (i.e. the recovered velocity values are approximately half those of the synthetic model). Recovery of the true velocity values was worse for 2 km bsl.

The recovery of the synthetic interpretation model was generally good between 1 and 2 km bsl, with poorer recovery at 2.5 km bsl for both V_p and V_s (Figure 5.22, Figure 5.23, Figure 5.24, Figure 5.25, Figure 5.26 and Figure 5.27). The high to low velocity variation across northern Ngatamariki was well recovered for both V_p and V_s between 1 and 2 km bsl and was reasonably well recovered for 2.5 km bsl, however the transition between high and low velocity was smoother than the actual model in all cases. There was more evidence of smearing of the velocity variation along the general north-south ray-path direction in the recovery of the synthetic interpretation model than was apparent in the spike test. For example, the low velocity area in eastern Ngatamariki appears to be smeared in a NS direction for V_p . The smearing was less apparent for V_s than for V_p , possibly because the traveltime perturbations are larger for V_s than they are for V_p . The high velocity area in northwest Ngatamariki also shows some north-south smearing for V_p , which is more prominent with the addition of noise. High V_p at Rotokawa is generally not well recovered, however high V_s in the same area is reasonably well recovered.

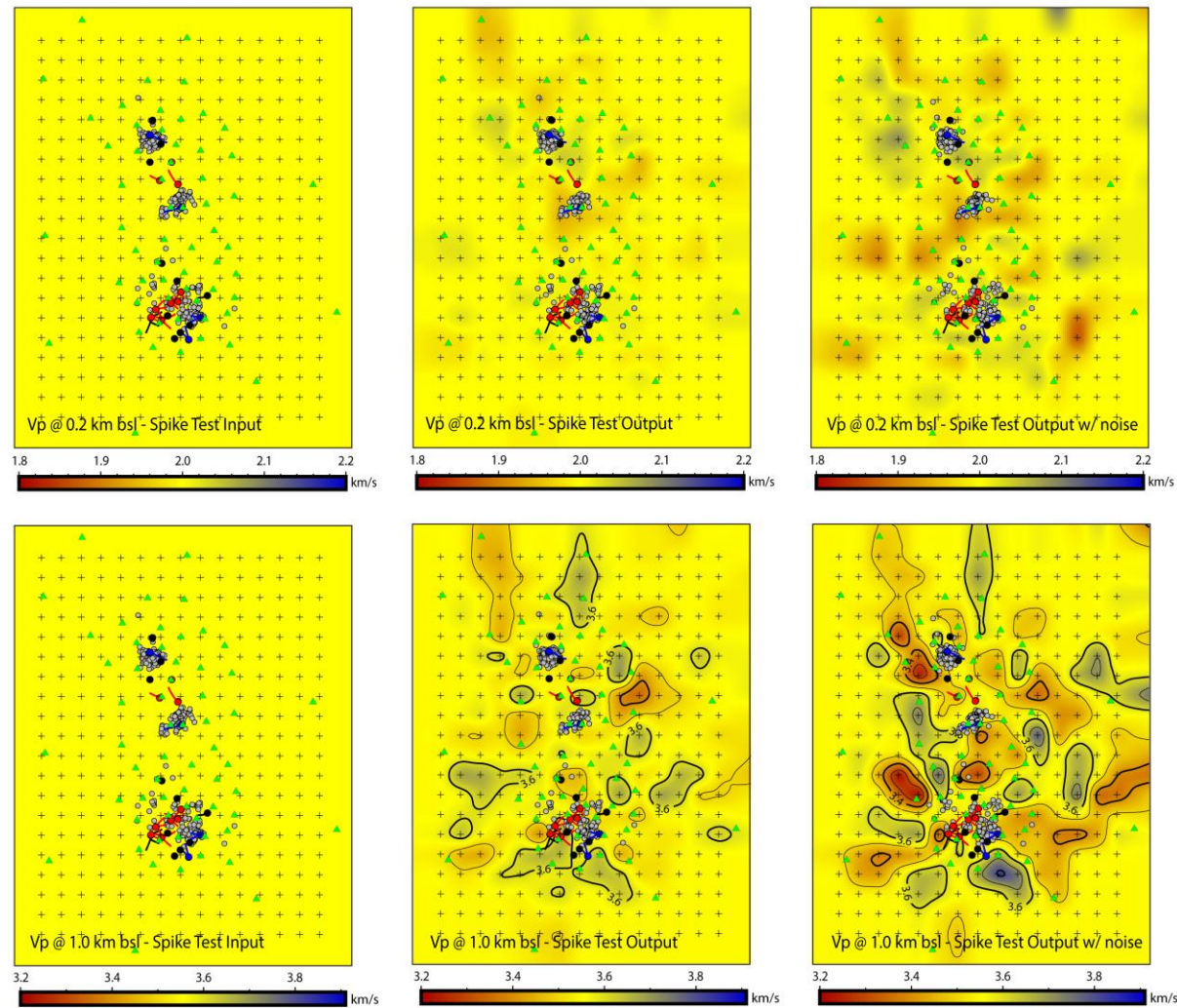


Figure 5.16. Spike test for Vp at 0.2 and 1 km bsl. Note that no velocity variations were included in these two layers. Plus signs show the locations of nodes used to calculate the synthetic data. Green triangles show seismometers, grey dots the earthquakes used in the inversion.

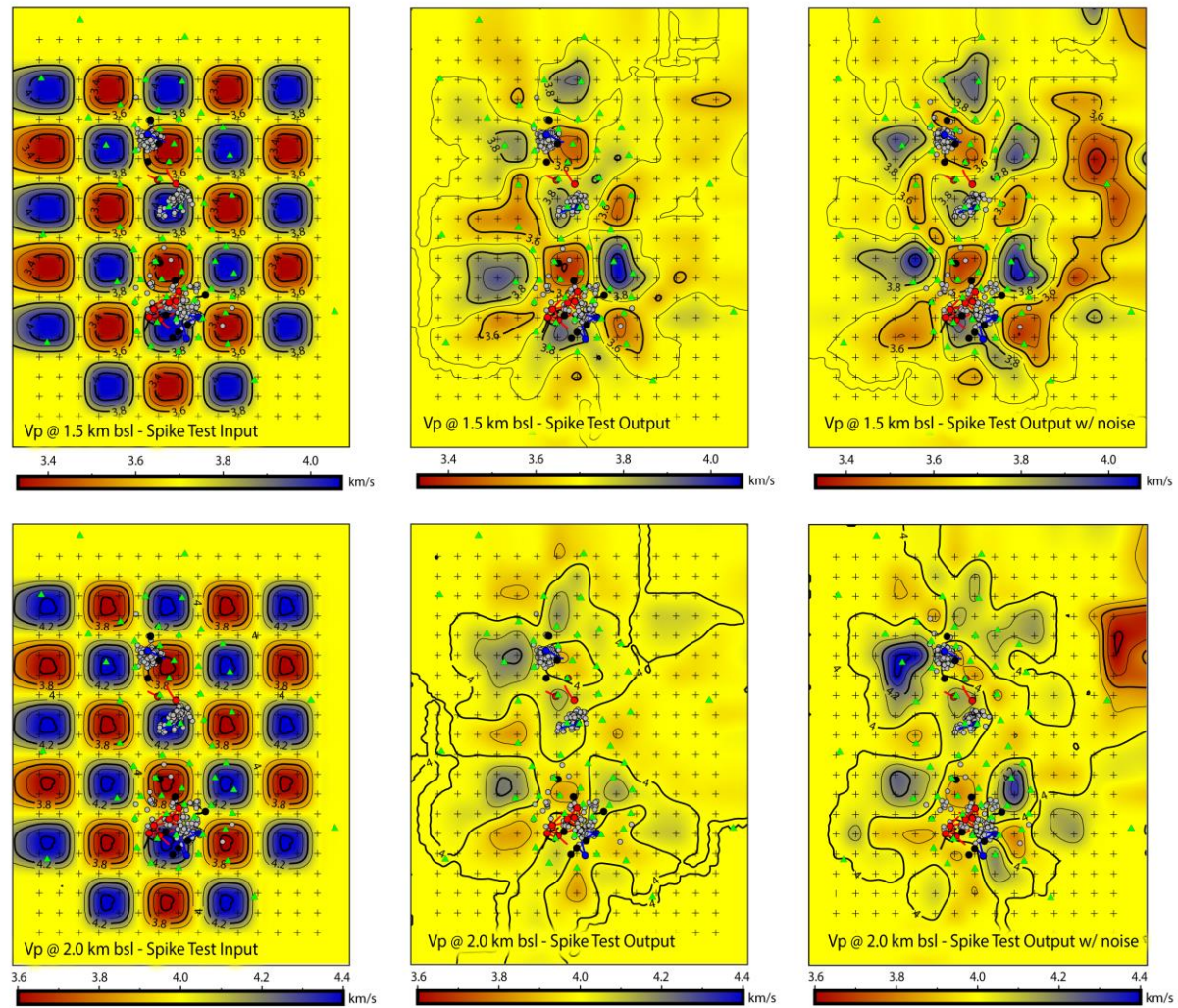


Figure 5.17. Spike test for V_p at 1.5 and 2.0 km bsl. Plus signs show the locations of nodes used to calculate the synthetic data. Green triangles show seismometers, grey dots the earthquakes used in the inversion.

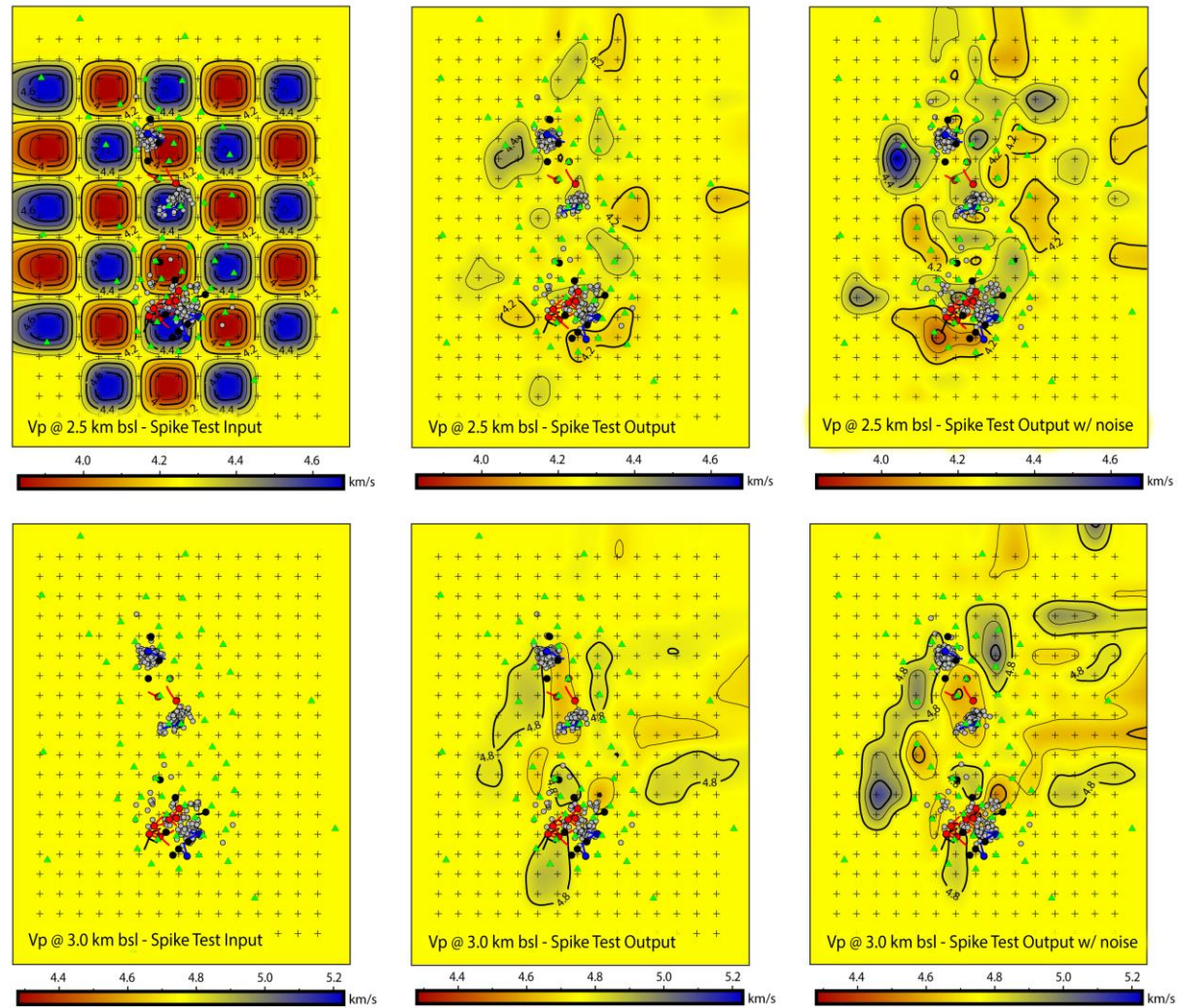


Figure 5.18. Spike test for Vp at 2.5 and 3.0 km bsl. Note that no velocity variations were included in the 3 km bsl layer. Plus signs show the locations of nodes used to calculate the synthetic data. Green triangles show seismometers, grey dots the earthquakes used in the inversion.

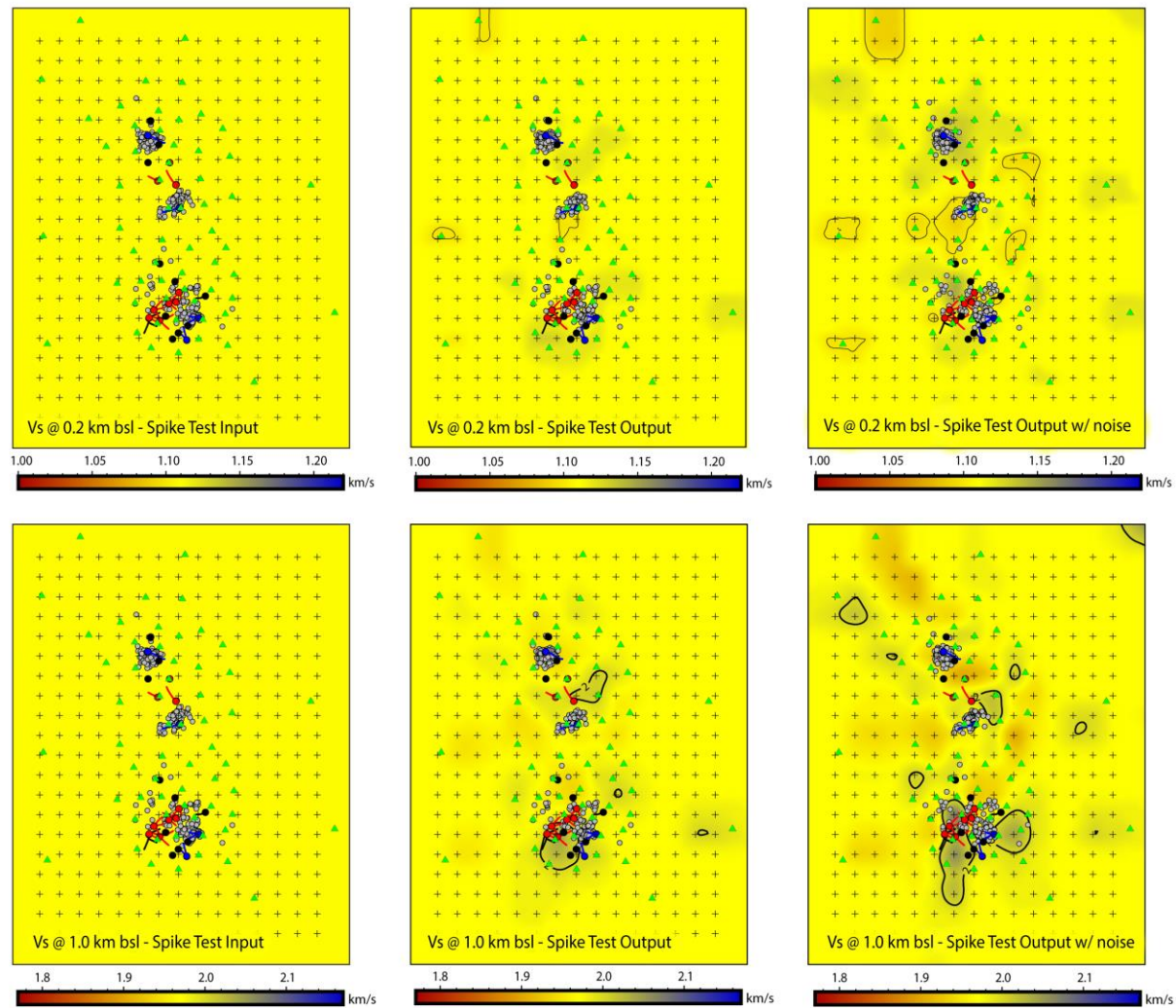


Figure 5.19. Spike test for Vs at 0.2 and 1 km bsl. Note that no velocity variations were included in these two layers. Plus signs show the locations of nodes used to calculate the synthetic data. Green triangles show seismometers, grey dots the earthquakes used in the inversion.

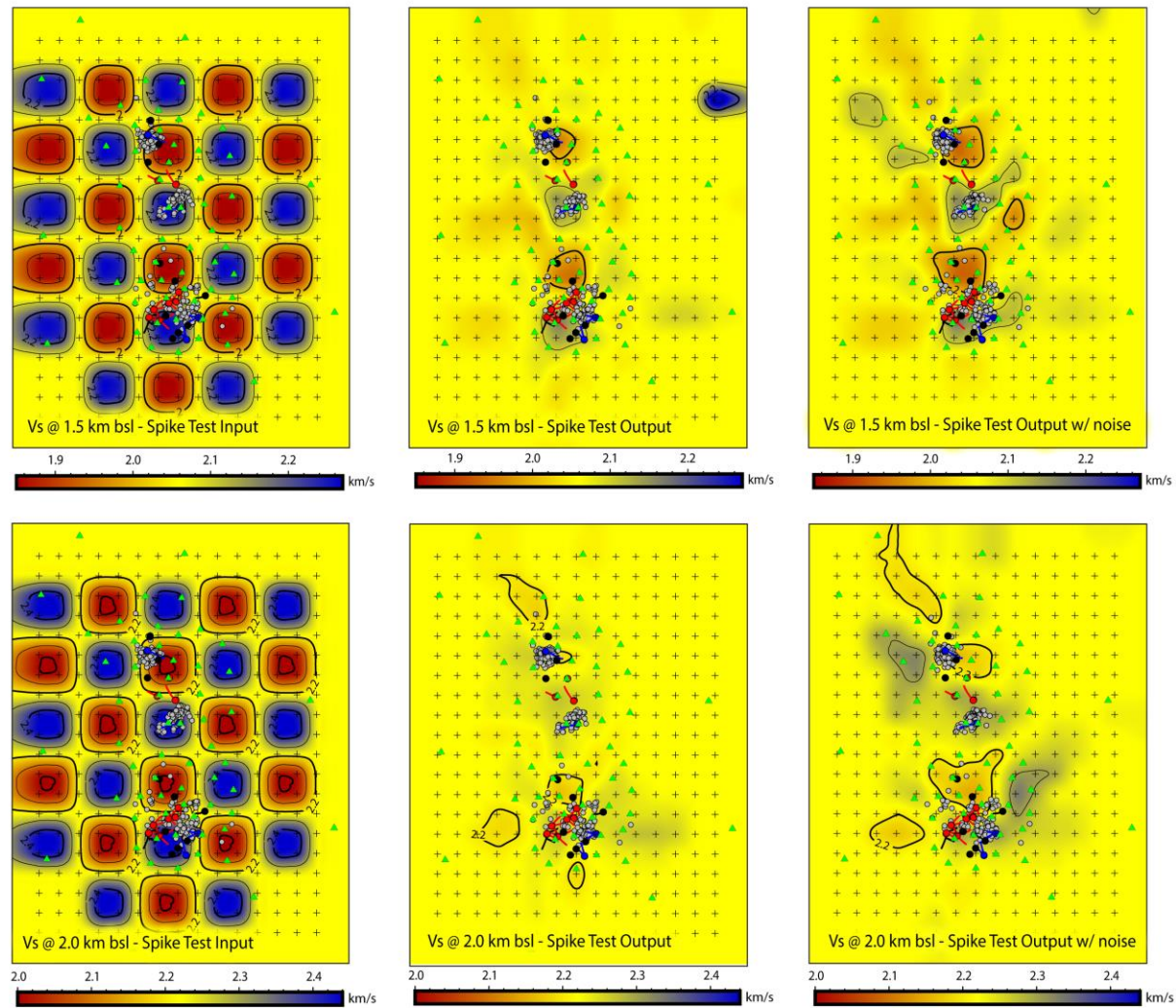


Figure 5.20. Spike test for V_s at 1.5-2 km bsl. Plus signs show the locations of nodes used to calculate the synthetic data. Green triangles show seismometers, grey dots the earthquakes used in the inversion.

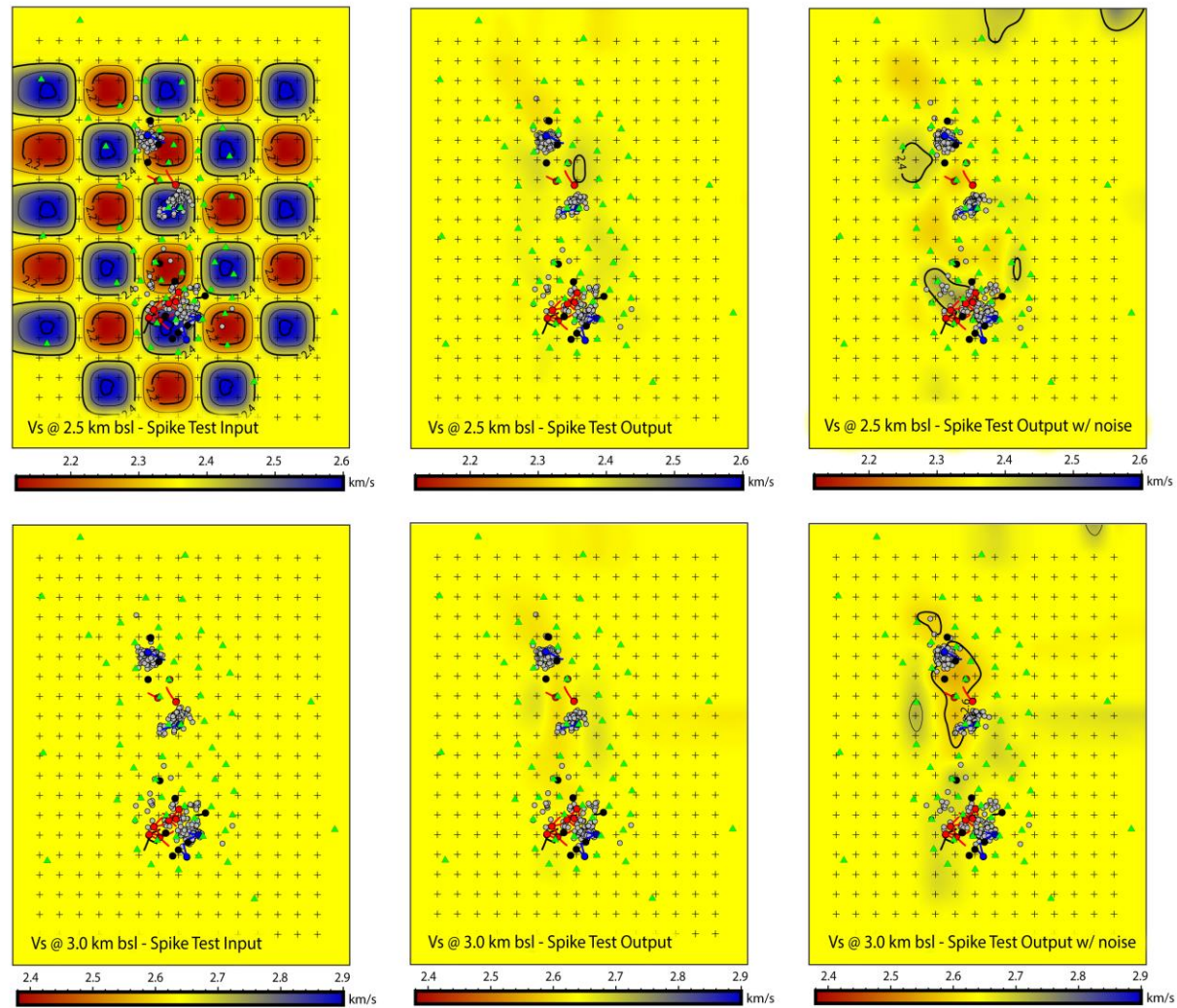


Figure 5.21. Spike test for V_s at 2.5 and 3.0 km bsl. Note that no velocity variations were included in the 3 km bsl layer. Plus signs show the locations of nodes used to calculate the synthetic data. Green triangles show seismometers, grey dots the earthquakes used in the inversion.

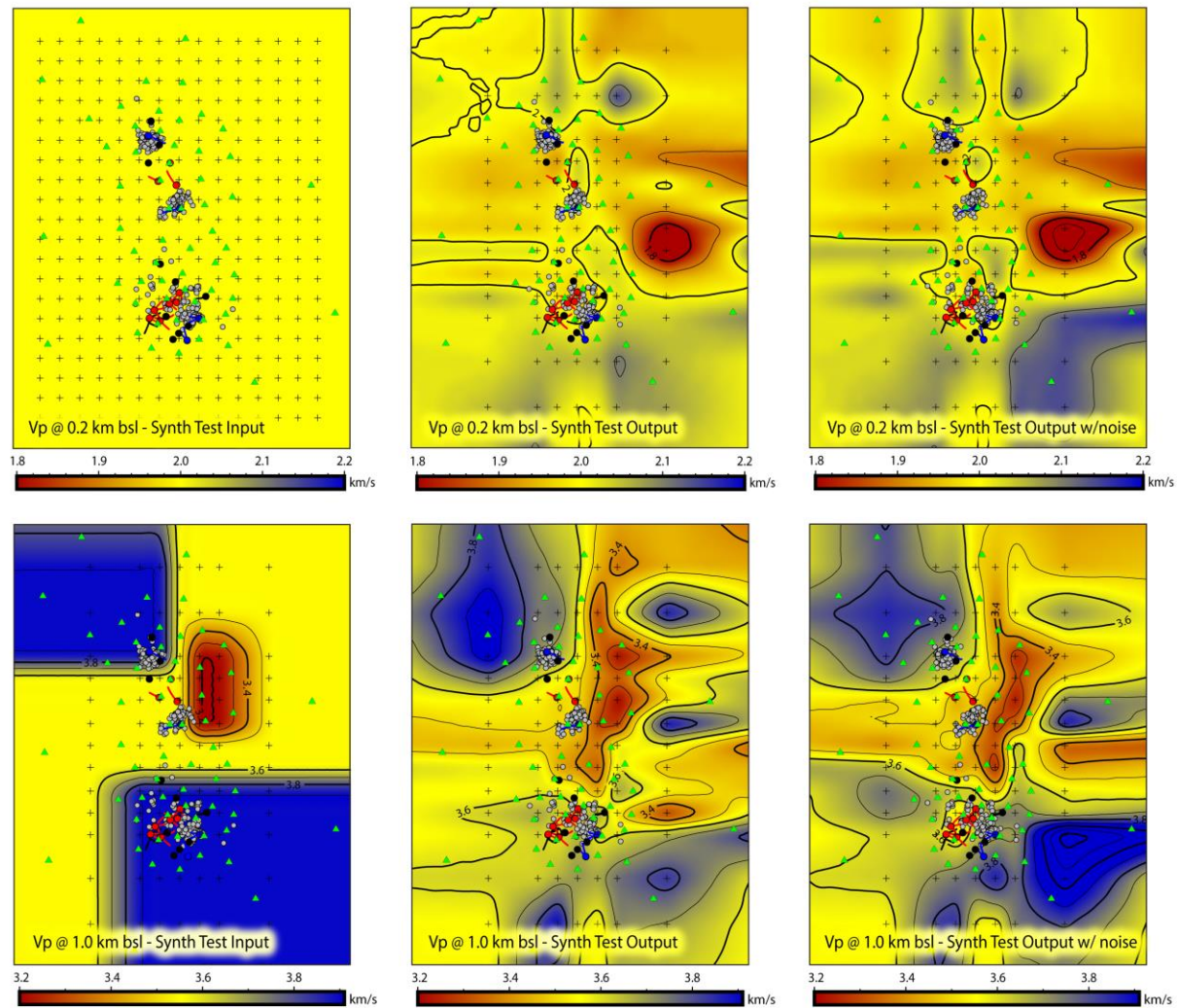


Figure 5.22. Synthetic recovery of the main interpreted features for Vp at 0.2 and 1 km bsl. Plus signs show the locations of nodes used to calculate the synthetic data. Green triangles show seismometers, grey dots the earthquakes used in the inversion.

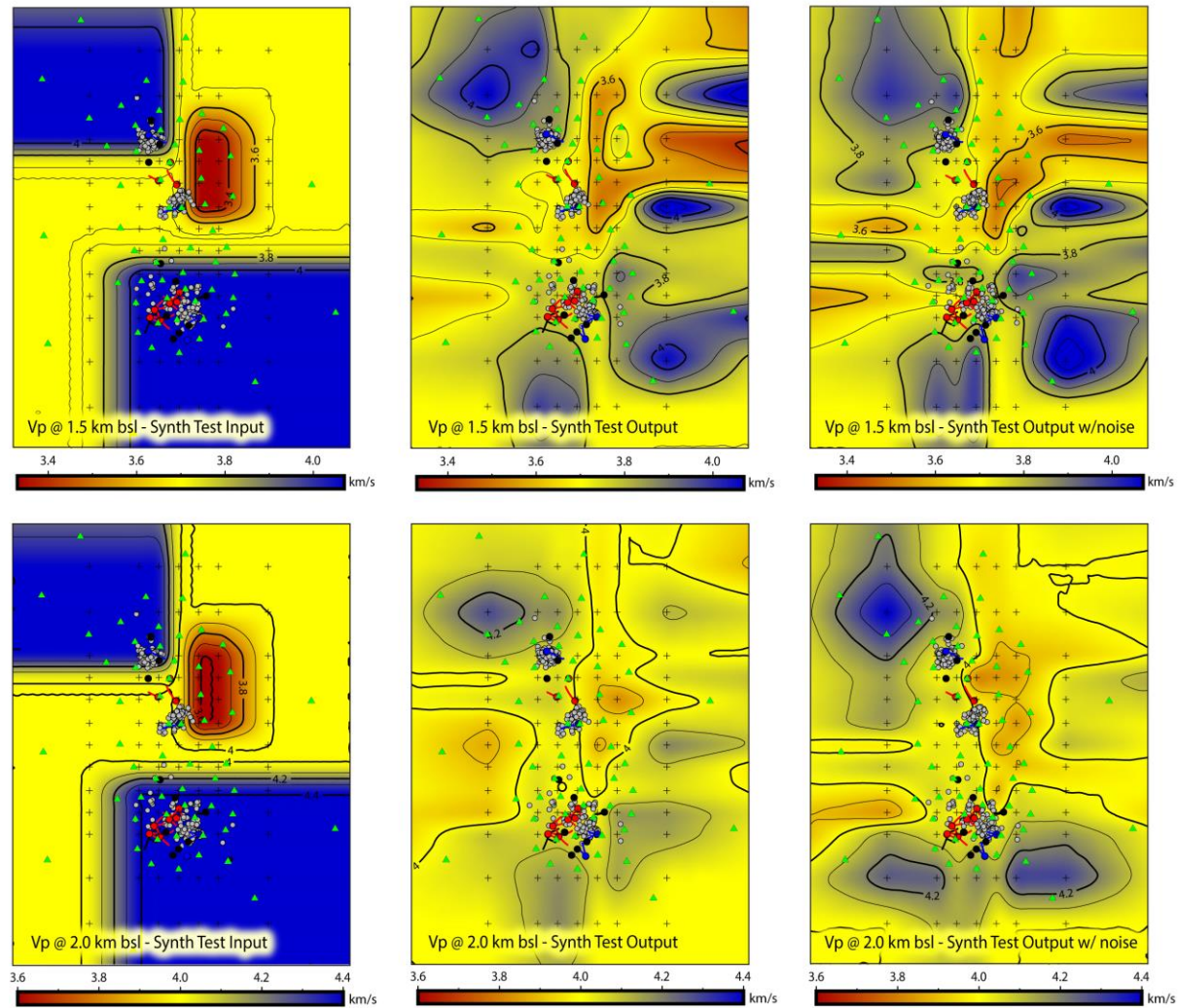


Figure 5.23. Synthetic recovery of the main interpreted features for Vp at 1.5 and 2km bsl. Plus signs show the locations of nodes used to calculate the synthetic data. Green triangles show seismometers, grey dots the earthquakes used in the inversion.

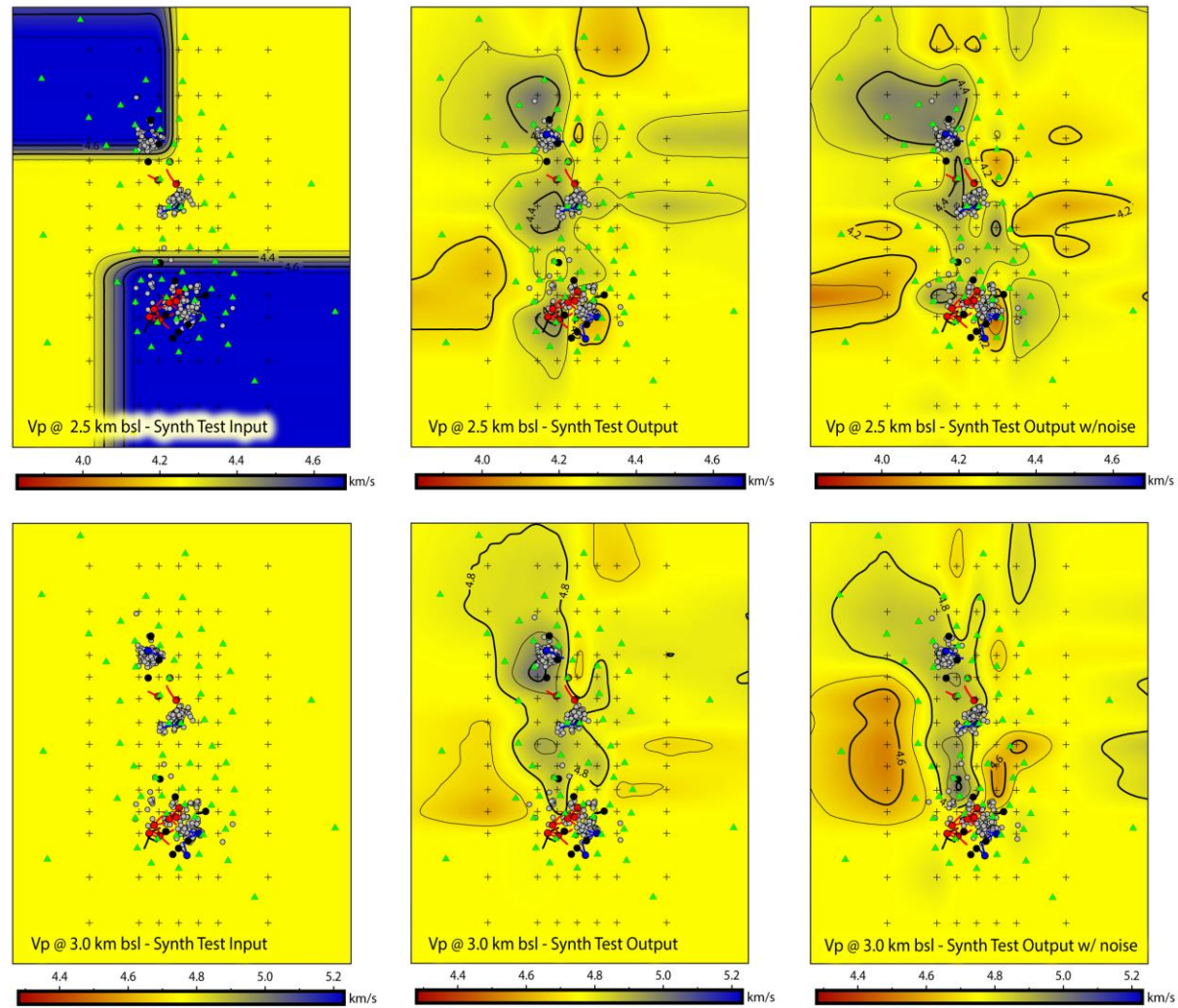


Figure 5.24. Synthetic recovery of the main interpreted features for Vp at 2.5 and 3 km bsl. Plus signs show the locations of nodes used to calculate the synthetic data. Green triangles show seismometers, grey dots the earthquakes used in the inversion.

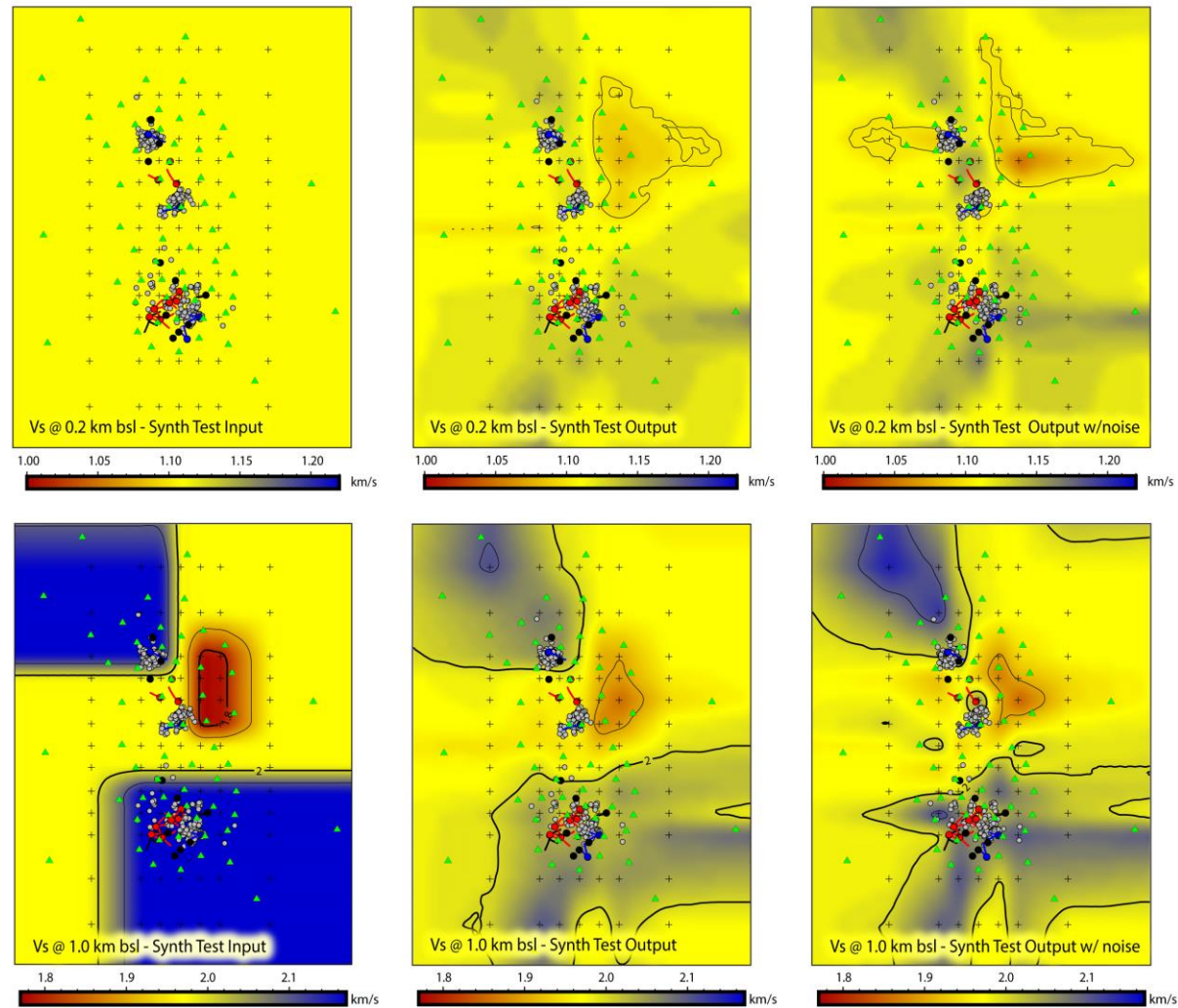


Figure 5.25. Synthetic recovery of the main interpreted features for V_s at 0.2 and 1 km bsl. Plus signs show the locations of nodes used to calculate the synthetic data. Green triangles show seismometers, grey dots the earthquakes used in the inversion.

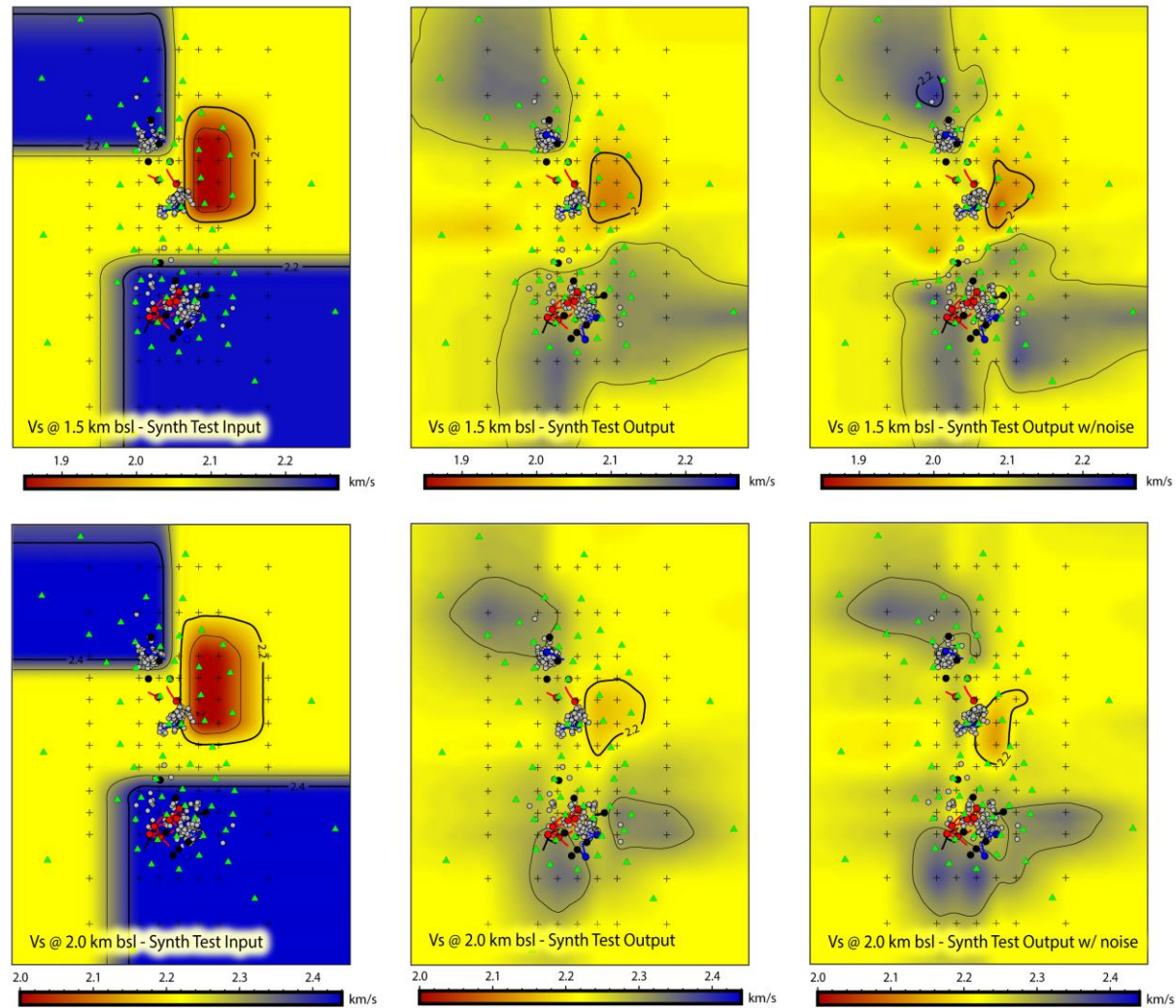


Figure 5.26. Synthetic recovery of the main interpreted features for V_s at 1.5 and 2km bsl. Plus signs show the locations of nodes used to calculate the synthetic data. Green triangles show seismometers, grey dots the earthquakes used in the inversion.

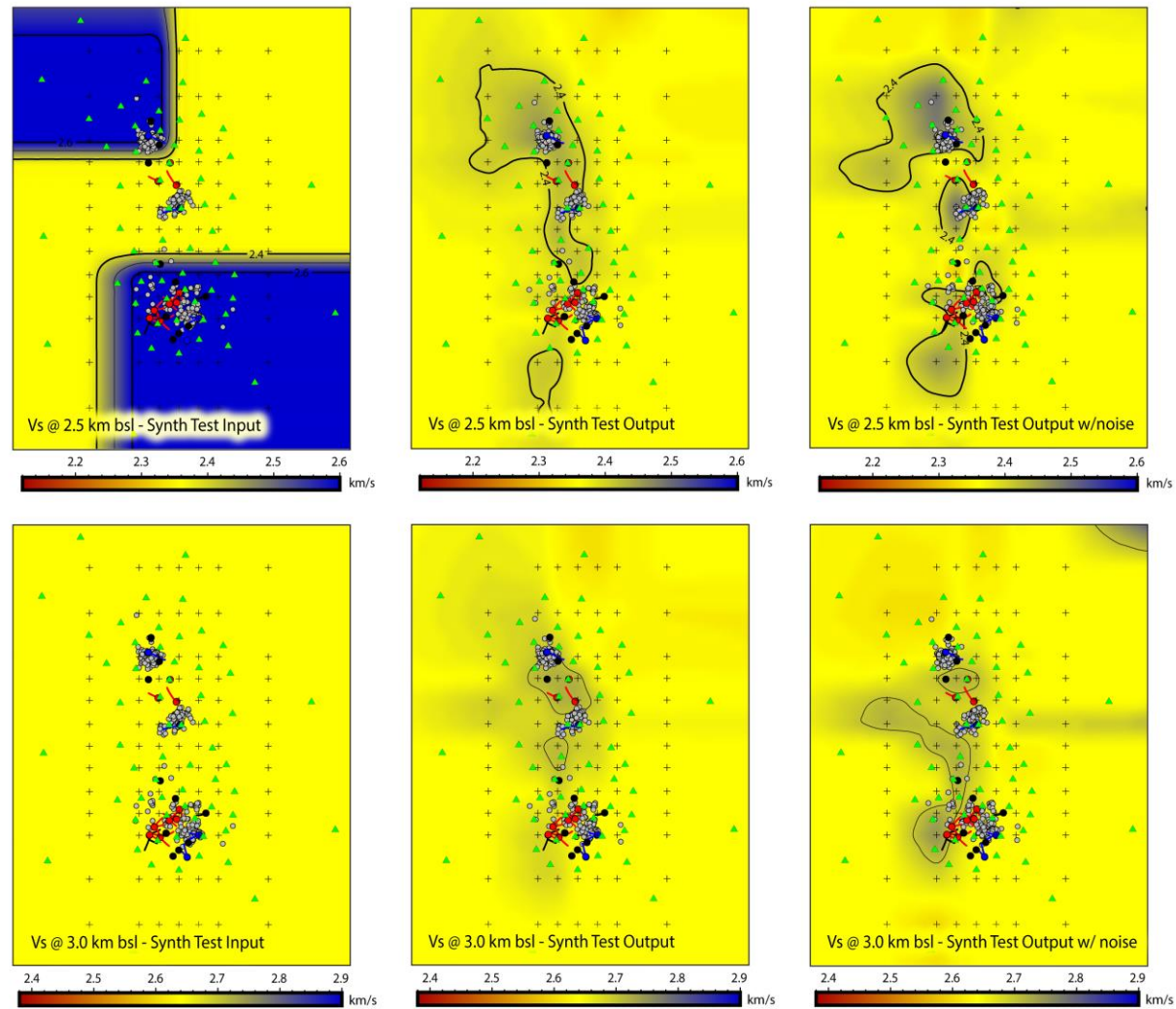


Figure 5.27. Synthetic recovery of the main interpreted features for Vs at 2.5 and 3 km bsl. Plus signs show the locations of nodes used to calculate the synthetic data. Green triangles show seismometers, grey dots the earthquakes used in the inversion.

5.4 Discussion

As was indicated by the VELEST station corrections in Chapter 4, there is good evidence for significant 3D velocity structure across the Ngatamariki and Rotokawa area. This is demonstrated by the improvement in residual fit when moving from the 2D model to the 3D models (Figure 5.4). A high to low, west to east velocity variation is consistently observed across northern Ngatamariki for both V_p and V_s between 0.2 and 2 km bsl in all of the 3D models (coarse, fine and geo) (Figure 5.7, Figure 5.8, Figure 5.9 and Figure 5.10). High V_s (and V_p in the geo model) relative to the 1D VELEST starting model is observed in the Rotokawa area between 0.2 and 2 km bsl. The location of the velocity variations and whether high or low relative to the 1D VELEST starting model is very similar to that indicated by the VELEST station corrections (Figure 5.28). The spike test and recovery of the interpretation model suggest that spatial resolution is greatest between the earthquake clusters at depths of 1.0 and 2.0 km. The spike test also provides evidence that in the area between the earthquake clusters, features larger than $1 \times 1 \times 1$ km and greater than $\pm 10\%$ variation in velocity should be detected and their general location known. Outside of this, resolution is poorer, particularly in areas outside of the dense array and at depths below 2 km bsl.

Consistent with expectations based on Chapter 3 and 4, high velocity (V_p and V_s) in NW Ngatamariki (and possibly extending to the SW of Ngatamariki) is likely due, at least in part, to the alteration and deformation that occurred within the Tahorakuri Formation during the emplacement of the diorite-tonalite intrusion. As was shown in Chapter 3, the logging and checkshot data from wells NM9 in the north and NM10 in the south shows a difference in V_p on the order of 1 km/s for the Tahorakuri Formation which was shown to be due to a porosity difference on the order of 10-15% between north and south. The high velocity is unlikely to be directly due to the intrusion itself as the DWS and synthetic testing both show that this dataset is relatively insensitive to velocity variations at the depth of the intrusion (below 2 km bsl). It is possible that some of the high velocity may be due to higher velocity within the upper 1 km related to thicker rhyolite lavas that outcrop in the northwest.

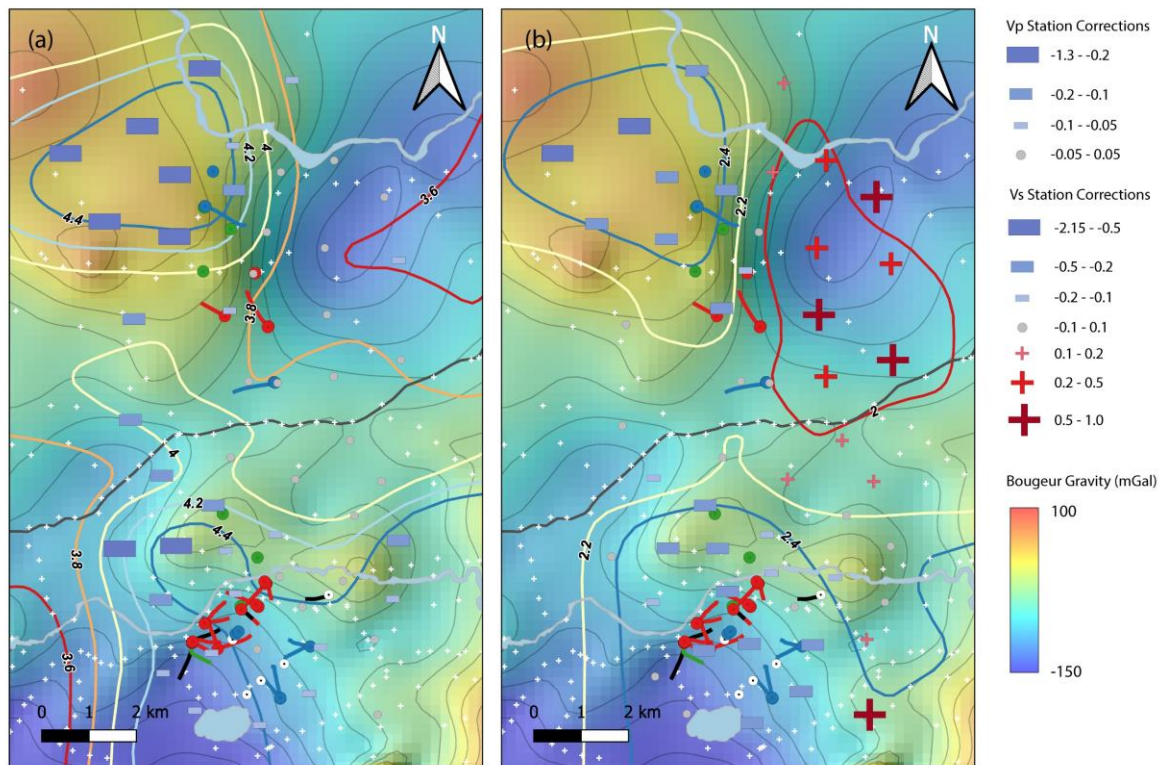


Figure 5.28. Comparison between velocity and gravity data. (a) Contours of Vp at 1.5 km bsl from the geo model and Vp VELEST station corrections overlain on Bouguer gravity. (b) Contours of Vs at 1.5 km bsl from the geo model and Vs station corrections overlain on Bouguer gravity. White plus signs show the location of gravity stations. Station corrections units are seconds.

The transition from high velocity in the west to low velocity in the east across Ngatamariki was consistently placed across the NM9 well in the north in all models (2D, coarse, fine and geo). The transition was more sharply defined in the fine and geo models, again being placed across the NM9 well (Figure 5.7, Figure 5.8, Figure 5.9, Figure 5.10). This suggests that NM9 may be close to the edge of the intrusion and its alteration and deformation halo that caused lower porosity and increased velocity in NM9 (Chapter 3). The location of the transition is also consistent with the available gravity data which shows a relatively large change of approximately 100 mGal (Figure 5.28). The west-east transition from high to low velocity in the interpretation model synthetic test was well recovered between 1.0 and 2.0 km bsl and the spike test showed good recovery in the area of the transition for both Vp and Vs (spike test Figure 5.16 - Figure 5.21, interpretation model synthetic recovery Figure 5.22 - Figure 5.27). Therefore, the high to low transition should be relatively well resolved (on the order of ± 1 km) in the east-west direction by the available travelttime data. There is clear evidence of smearing

into the shallow layers in the interpretation model recovery for both V_p and V_s , and this suggests the velocity structure is not well determined with depth (Figure 5.22 and Figure 5.25). It is therefore difficult to distinguish how much of the high velocity is above 1 km or below 1 km for northwest Ngatamariki. Given the checkshot and wireline logging data clearly show elevated velocities between 1-2 km bsl in NM9 (Figure 5.3), most of the high velocity is likely below 1 km bsl. The rhyolite dome and shallow rhyolites in NW Ngatamariki that effectively displace low velocity volcanoclastics and sediments above 1 km may, however, play a part in elevating velocity in this area (Figure 1.2).

Low velocity (V_p and V_s) in the east of Ngatamariki occurs between 0.2-2 km bsl and, given the results of the interpretation model synthetic recovery which showed smearing across these depths, it is difficult to tell whether the low velocity in this area is dominantly between 0.2-1 km bsl or 1-2 km bsl. One possible explanation for the low velocity to the east of Ngatamariki is the deepening of smectite and smectite-illite alteration within the Tahorakuri Formation. Wells drilled at Ngatamariki show that the Tahorakuri Formation in the south of the field (NM7-NM5-NM6) is smectite and smectite-illite altered to depths of up to 1.5 km bsl (Boseley et al., 2010; Chambeft et al., 2016). MT surveys conducted at Ngatamariki image this alteration (Boseley et al., 2010) as a thick conductive layer that deepens to the east and southeast of the field (Figure 5.29). Smectite and smectite-illite clays have been widely shown to lower seismic velocity relative to illite and chlorite clays (e.g. Eberhart-Phillips et al., 1989; Khadeeva and Vernik, 2014; Wyering et al., 2014) and the deepening of the smectite and smectite-illite alteration to the east of Ngatamariki is one possible explanation for the low velocity.

Gravity data also show a low to the east of Ngatamariki, however this is not well defined spatially due to the sparse station spacing (Figure 5.28). The gravity low is part of a broader low gravity region termed as the 'Mihi' gravity low which Stagpoole et al. (2020) interpreted as possibly due to the Mihi Breccia, a pyroclastic flow unit interpreted to have formed during subaqueous rhyolite dome building (Downs, 2016). The Mihi low is part of a broader low gravity feature across the Taupō-Reporoa basin (Stagpoole et al., 2020; Wilson and Rowland, 2016). Given that the area east of Ngatamariki is more towards the axis of the Taupō-Reporoa Basin, it is also possible that some of the low velocity in this area can be attributed to a greater proportion of pyroclastic and sedimentary rocks and less rhyolite lava in the upper 1 km (Downs et al., 2014; Wilson and Rowland, 2016).

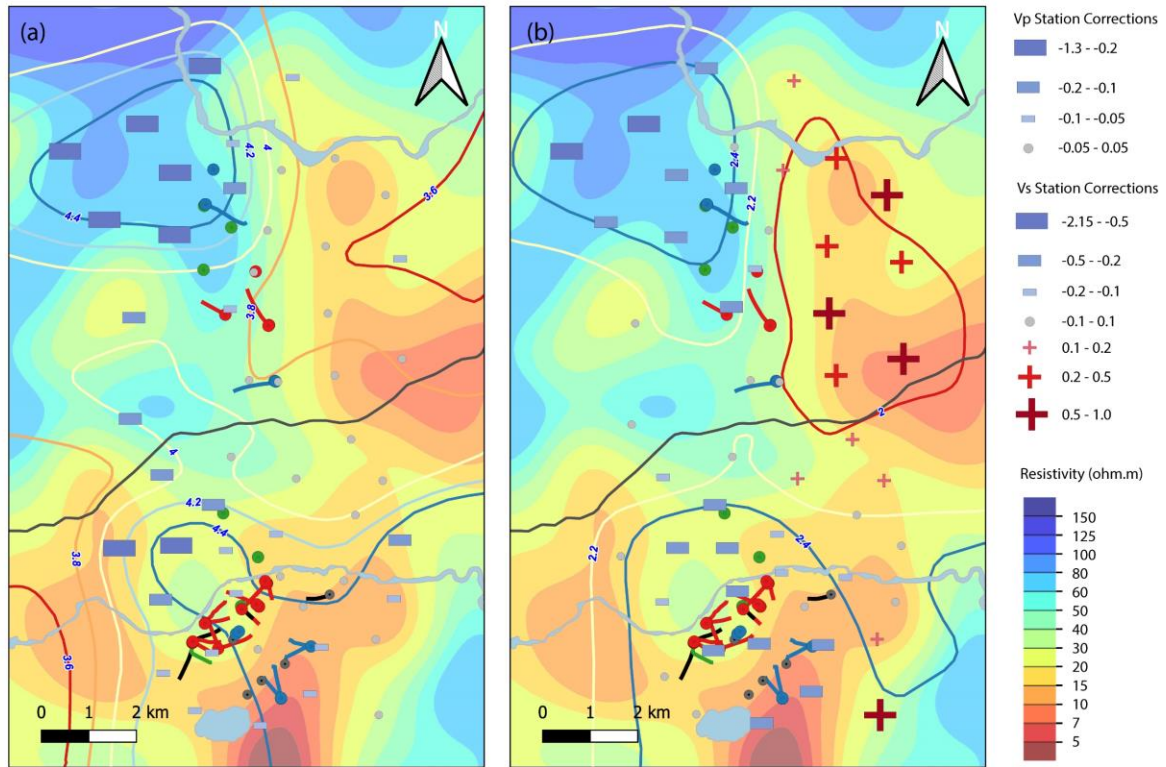


Figure 5.29. Comparison of resistivity at 1.5 km bsl from a 3D inversion of magnetotelluric data across the two fields and velocity from the geo model. (a) Vp contours at 1.5 km bsl from the geo model and Vp station corrections from VELEST and (b) Vs at 1.5 km bsl and Vs station corrections from VELEST. Station corrections units are seconds.

The high Vs at Rotokawa (Figure 5.8 and Figure 5.10) appears to be, at least in part, due to the higher elevation of the greywacke and andesite contacts relative to Ngatamariki (-1000 to -1500 masl at Rotokawa versus -2000 to -2500 masl at Ngatamariki, Figure 1.4 and Figure 1.5). Vp appears to be not well constrained by the data at Rotokawa, as shown by the very different results for Vp between the fine and geo models (Figure 5.7 and Figure 5.9). This is despite relatively high DWS and the relatively good spike test recovery in this area. This may be due to smearing of the low Vp for eastern Ngatamariki into Rotokawa by the dominantly north-south directed ray-paths, as was indicated by the interpretation model recovery test (Figure 5.22 - Figure 5.27). Given that high Vs occurs between 1 km and 2 km bsl for Rotokawa in both the fine and geo models, and the known high Vp for andesite from the NM10 log (Chapter 3) and for greywacke from core studies (Mielke et al., 2016) and refraction survey results (Stern and Benson, 2011), it is more likely that Vp values are high at Rotokawa and closer to those of the geo starting model. Part of the high Vs (and likely Vp) at Rotokawa may also be due to the greater thicknesses of rhyolite lavas which outcrop to the north and northeast (McNamara et

al., 2016) (Figure 1.2). The lack of independent constraints on the velocity above 1 km again makes it difficult to determine whether this is the case.

The results highlight some of the challenges to obtaining good spatial resolution of velocity variations at a scale on the order of or less than 1 km from local earthquake tomography in geothermal fields. The concentrated earthquake clusters for these fields clearly affects the ray-path coverage and therefore spatial resolution of velocity variations. The three main clusters of activity around the injection wells at Rotokawa, Ngatamariki South and Ngatamariki North result in most of the ray-paths between fields travelling in an approximate north-south line at depths between the earthquake depths (dominantly 1.5 and 2.0 km bsl) (Figure 5.5 and Figure 5.6). This results in a lack of good spatial resolution outside of this north-south corridor and also creates some smearing of velocity along the north-south ray paths (Figure 5.22 and Figure 5.27). Although effort was made to include as many of the earthquakes that occurred outside of the three main areas of activity, these are relatively sparse (typically a single event or two) and therefore do not provide much additional constraint on the velocities. Obtaining ray-path coverage outside of the main earthquake areas was hampered to some extent by poor data recovery from the second instrument deployment (Figure 2.4). However, as most of the ray-paths to the instruments of the second deployment would still be from the three main areas of seismicity, it is unlikely this data would have provided significant new constraints on the velocity model within the fields. The problem of concentrated earthquake locations may be a common challenge in many geothermal fields where activity is often concentrated at injection locations and there is little natural seismicity within the fields.

There is a particular problem with ray-path coverage above 1 km bsl in this study, that is likely a common problem for most geothermal areas due to the general low levels of seismicity above ~1 km depth (e.g. Gritto and Jarpe, 2014; Millett et al., 2018; Vanorio et al., 2004). The effect of this is readily apparent in the synthetic testing results obtained here; the lack of constraint on shallow velocities results in smearing of deeper velocity variations into the shallower parts of the model (Figure 5.22 and Figure 5.25). The reverse could also be true, shallow velocity variations could become smeared into deeper layers without constraint on the shallow layers. Having external constraints on the shallow velocities, for example from active-source refraction and/or further checkshot/VSP surveys in other wells, would help to constrain both the shallow and deep parts of the model.

It is also apparent in the results of the synthetic testing that the absolute velocity values are likely underestimated. This problem has been recognised for some time and is partly a consequence of the damped-least squares inversion (e.g. Rawlinson et al., 2014). The underestimation of velocity values is apparent in synthetic testing which showed that input velocity variations of $\pm 10\%$ were, at best, recovered as $\pm 5\%$ velocity variations (spike test Figure 5.16 - Figure 5.21 and interpretation model recovery Figure 5.22 - Figure 5.27). The differences in velocity values for the two different starting models (1D and 3D geo starting models) also indicate that the velocity values themselves are not well constrained (Figure 5.11, Figure 5.12, Figure 5.13 and Figure 5.14). For instance, the maximum V_p for the high velocity area in NW Ngatamariki at 2 km bsl was 4.1 km/s for the 1D VELEST model whilst in the geo model it was 4.8 km/s. The inclusion of a priori information provided by the checkshot survey and logs in the geo model likely results in velocity values in this area that are closer to actual values.

Obtaining additional constraints on the shallow velocity structure across the two fields would benefit definition of both the shallow and deeper velocity structure, filling the data gap that arises from the lack of earthquakes above 1 km. This would probably be most effectively done by performing checkshot/VSP surveys in inactive wells (or in injection wells during plant shut downs) with various offsets and azimuths from the wells in conjunction with refraction surveying that would provide more detailed information on shallow variations across the fields in the upper few hundred metres as was done at the Ohaaki field (Henry and Hochstein, 1990; Stagpoole, 1994). Another possible constraint on shallow velocities is noise cross-correlation as undertaken by Civilini et al. (2016), however the use of 4.5 Hz seismometers may limit the depths for which velocity can be obtained. Obtaining ray-path coverage below 1 km bsl in the areas surrounding the fields by deploying seismometers in similar locations as the second phase of deployment but for a longer recording period would also help (Figure 2.2). Further gravity surveying across the two fields and adjacent to them would also help to further define the high gravity in the northwest of Ngatamariki and thereby the location of the intrusion and its low permeability deformation/alteration halo. Gravity surveying would also help to guide the location of refraction surveying lines (i.e. refraction lines would ideally be located across significant changes in gravity).

The imaging of the transition from high velocity to low velocity across northern Ngatamariki in this study suggests that the low porosity and permeability Tahorakuri formation above the intrusion does not extend to the east and northeast of the current northern injection wells at

Ngatamariki. Therefore, future wells in the field targeted to the east and northeast of the current northern injection wells would be unlikely to encounter the low permeability associated with the highly altered and deformed Tahorakuri Formation. Ideally the velocity transition would be better defined spatially by active source methods (e.g. checkshot/VSP with sensors in inactive wells in the north of the field and various offsets from those wells to the east) prior to drilling in this area. A more detailed gravity survey may also assist in further defining the transition from low porosity / high density Tahorakuri Formation above the intrusion to higher porosity / lower density Tahorakuri Formation away from the intrusive.

5.5 Conclusions

This study has shown that at least three large-scale 3D velocity variations exist across the Rotokawa and Ngatamariki fields. High velocity (V_p and V_s) is evident for northwest Ngatamariki from 0.2 to 2.0 km bsl which possibly extends to the southwest of the field. This is associated, at least in part, with the very low porosity and low permeability Tahorakuri Formation that was highly altered and deformed during emplacement of the Ngatamariki diorite-tonalite intrusion.

The high velocity coincides with a large positive gravity anomaly (up to 100 mGal), providing further evidence for an area of low porosity in NW Ngatamariki. As the high velocity (and gravity) correlates with low permeability, future wells at Ngatamariki might target the area to the east of the current northern injection wells where the velocity transitions to values similar to or lower than the southern, more permeable, part of the field. Low velocity (V_p and V_s) occurs to the east of Ngatamariki, with the most likely possible explanations for this being a higher proportion of volcanics and sediments (less rhyolite) in the upper 1 km than in the currently drilled area and/or a deeper smectite clay-cap within the Tahorakuri Formation that is imaged by MT resistivity data.

High velocity (V_s and most likely V_p) is observed at Rotokawa, that is likely due, at least in part, to the higher elevation of andesite/greywacke at Rotokawa relative to Ngatamariki. A higher proportion of rhyolite lava and less volcanics and sediments in the upper 1 km is another possible contributing factor.

Synthetic testing shows that the general location of the velocity variations and whether they are high or low velocity is well resolved, with spatial resolution on the order of 1 km between the clusters of earthquakes and worse outside of this. However, the synthetic testing also

highlights some of the issues in resolving velocity variations at spatial resolution at and below 1 km in geothermal fields with local earthquake tomography alone. These issues include poor ray-path coverage due to highly clustered earthquakes, poor ray-path coverage above 1 km due to a lack of seismicity above 1 km, arrival time noise, and the underestimation of the true velocity values due to the damped least-squares inversion.

Including some active-source techniques (such as VSP/checkshot and refraction surveys) would likely help with addressing some of the ray-path coverage issues. Significant improvements to the velocity imaging could be made by conducting refraction surveys in conjunction with VSP/checkshot which together would provide constraints on velocity above 1 km bsl and thereby reduce uncertainty in velocity variations below this depth from the earthquake data. Improving the gravity survey coverage across the two fields would also further define the low porosity and permeability within the Tahorakuri Formation associated with the intrusion in the north of Ngatamariki, as well as provide guidance for planning the refraction surveys and checkshot/VSP.

6 Synthesis

One of the main objectives of this study was to investigate the factors that control seismic velocity and to use that knowledge to interpret the seismic velocity images provided by tomographic methods. This objective was largely achieved and the results of this study have implications both for well targeting and reservoir management of the Ngatamariki and Rotokawa geothermal fields and for the application of seismic tomography methods as applied to geothermal fields.

6.1 Summary

The specific findings and implications of each chapter and implications are summarised below.

Chapter 3:

- A method for characterizing lithology and alteration in geothermal wells was developed by combining high depth resolution portable XRF, XRD and automated mineralogy (Section 3.2.6). Although each method has been utilised before in geothermal wells, this is the first time the combination of techniques has been applied to characterise lithologies and alteration.
- A method for depth correction of drill cuttings was established utilizing potassium (K) concentrations obtained from portable XRF measurements on rock cuttings and gamma ray logging (Section 3.2.5). This method improves the ability to compare rock cuttings properties to log properties and therefore potentially has wide application in geological characterization of wells. As the method potentially improves the accuracy of depths from which cuttings were derived it may also improve geologic structural models based on offset of lithologies downhole as is commonly done in geothermal reservoirs (e.g. Wallis et al., 2013).
- The principal control on seismic velocity measurements from the geophysical logging at Ngatamariki is porosity, which is in turn controlled by rock type, alteration and ductile deformation above an intrusion (Section 3.4).
- An approximately 1 km/s difference in seismic velocity exists between the tuff-dominated Tahorakuri formation in the north (NM8 and NM9) and the south (NM10) of the Ngatamariki field (Section 3.4.4, Figure 3.26). This was shown to be due to

reduction of porosity in the north of the field due to alteration (quartz-deposition) and ductile deformation that occurred during the intrusion of a tonalite/quartz-diorite magma body approximately 600 kya.

- The zone directly overlying the Ngatamariki diorite-tonalite intrusion ('WP Tuff') is very weakly altered and very low porosity. An FMI log through this zone shows it to be highly fractured, but all fractures have very small aperture. Together these suggest that the zone directly above the intrusion was very low permeability for most of the time during and after the intrusion event. If the zone was very low permeability, then this likely hydraulically isolated this zone, resulting in near-lithostatic pressure. Given the evidence for temperatures above 375°C within this zone and near-lithostatic pressure, it is likely that fluids within the zone were in a supercritical state for most of the time during the intrusion event (i.e. temperature >374 °C and pressure >221 bar), similar to that encountered by geothermal wells in other field directly above large silicic intrusives (e.g. Kakkonda - Ikeuchi et al. (1998)). Further work, such as more detailed geochemistry and fluid inclusion analyses, may confirm or refute this interpretation.
- Although not directly related to the goals of this work, the detailed geochemistry and mineralogy dataset obtained may have wider implications for the geochemical and mineralogical changes that occur adjacent to magmatic intrusions (Sections 3.4.2 and 3.4.4). This is potentially of interest to both the geothermal sectors, particularly for utilizing super-critical geothermal resources (e.g. Chambefort et al., 2020; Reinsch et al., 2017) and mining of porphyry systems.

Chapter 4:

- A 1D velocity model was established for the two geothermal fields that can be used as the basis for 3D tomography work and/or hypocentre locations (Section 4.3.2, Figure 4.7 and Figure 4.8).
- High variation in the shallow velocity layers (above 1 km bsl) indicated that the arrival time dataset from only the microearthquakes does not constrain shallow velocities well (Section 4.3.2, Figure 4.7 and Figure 4.8).
- Station correction terms obtained defined the major spatial variations in velocity across the two fields (Vp station corrections - Figure 4.9 and Figure 4.10, Vs station corrections - Figure 4.11 and Figure 4.12). A west-east, high to low velocity variation

was indicated by the VELEST station correction terms. High V_s was also indicated by the station correction terms for Rotokawa.

Chapter 5:

- The improvement in residual fit from velocity inversions that progressed from 2D to coarse to fine grid parameterisations demonstrated that 3D velocity variation is apparent in the arrival time dataset for Rotokawa and Ngatamariki (Figure 5.4).
- The velocity models produced a consistent spatial pattern across northern Ngatamariki (V_p - Figure 5.7 and Figure 5.8 and V_s - Figure 5.9 and Figure 5.10). High velocity (both V_p and V_s) was observed in northwest Ngatamariki with low velocity in the east. V_s was observed to be particularly low in the east of Ngatamariki.
- High velocity in the northwest of Ngatamariki is interpreted as being due to the low-porosity Tahorakuri formation tuffs that have been altered and ductily deformed during the emplacement of the diorite/tonalite intrusion in the north of the field (V_p - Figure 5.7 and Figure 5.8 and V_s - Figure 5.9 and Figure 5.10). High velocity (both V_p and V_s).
- That the high velocity in the NW of Ngatamariki does not continue to the northeast of the field suggests that the low-permeability encountered in wells previously drilled in the north of the field (NM4 and NM8) does not continue to the northeast (V_p - Figure 5.7 and Figure 5.8 and V_s - Figure 5.9 and Figure 5.10). Future wells may therefore be targeted in the northeast and in the transition zone between high and low velocity which may be an area of particularly high permeability, as has been observed in other geothermal fields (e.g. Stimac et al., 2019).
- The spatial variation of velocity across Ngatamariki agrees well with variations in density from gravity surveying (Figure 5.28) and resistivity from MT surveys (Figure 5.29).
- Particularly low V_s in the east of Ngatamariki is likely related to deeper smectite alteration, which may be related to thicker Tahorakuri Formation, as shown by the deepening of the low-resistivity layer imaged by MT surveying (Figure 5.29). Higher porosity within the Tahorakuri Formation may also be a factor in lowering V_s in the east.

- Higher V_p and V_s at Rotokawa is most likely related to the higher elevation of the contact between the Tahorakuri Formation and andesite relative to Ngatamariki (V_p - Figure 5.7 and Figure 5.8 and V_s - Figure 5.9 and Figure 5.10).
- A 3D velocity model was obtained that utilises both measured data (well logs and checkshot) and arrival times provided from earthquakes (V_p - Figure 5.9 and V_s - Figure 5.10). The 3D velocity model can be utilised in on-going seismic monitoring at Ngatamariki and Rotokawa providing improved accuracy of hypocentres, particularly the depths of events.

6.2 Implications for the Rotokawa and Ngatamariki Geothermal Fields

6.2.1 Ngatamariki

There are a number of important implications from this thesis for the Ngatamariki geothermal field. Chapter 3 demonstrates that the Tahorakuri Formation in the north of the field is very different geochemically and physically from that in the south of the field. Porosity for the Tahorakuri Formation in the north has been lowered by both mechanical deformation and acidic alteration that occurred due to the very high temperatures ($>375^{\circ}\text{C}$) during the time the intrusion was emplaced. This likely resulted in the closure of most large aperture, permeable fractures which explains the relatively low permeabilities of NM8 and NM4 as shown by their low injectivities and conductive temperature profiles (Chapter 3). Due to the low porosity of the Tahorakuri Formation in the north of the field, the seismic velocity, both V_p and V_s , has increased which is imaged in the seismic tomography analysis presented in Chapters 4 and 5. The seismic tomography, gravity and MT resistivity datasets all suggest that the low permeability, alteration halo (and therefore the underlying intrusion) does not continue east of the current injection wells (NM4, NM8, NM9) (Figure 6.1). Therefore, future wells in the field that are targeted in the northeast sector are unlikely to encounter the same low permeability as observed in NM4 and NM8. The transition from high to low velocity, high to low gravity/density and high to low resistivity consistently occurs east to west across the north of the field, approximately at the location of the NM9 well. This suggests that the deeper part of this well may be close to the edge of the intrusion and its alteration halo. Since NM9 has relatively high permeability it follows that other wells targeted into the transition zone may

encounter good permeability. Enhanced permeability in the contact zones around intrusions has been noted to occur in other geothermal fields around the world (e.g. the Muara Laboh field in Indonesia, Stimac et al., (2019)). How far the intrusion and its alteration/deformation halo extends in the southwest sector of the field is somewhat uncertain due to the lack of good ray-path sampling in the tomography and the sparse available gravity data. The data that is available, particularly the gravity and MT data, suggest that the intrusion and its alteration/deformation halo does not continue to the southwest.

Low velocities (both V_p and V_s) were consistently imaged in the seismic tomography to the east of the currently drilled wells at Ngatamariki. Comparison to the MT data suggests that this is associated with deepening of the low resistivity smectite clay cap (Figure 6.1). Since this low resistivity zone is known to be low permeability, wells drilled in the east would likely encounter a deeper top of reservoir.

The seismicity pattern from the 1209 events that were detected and located during the 2017-2018 deployment is consistent with that of previous studies (Hopp, 2019; Sewell et al., 2015; Sherburn et al., 2015) (Figure 6.2). For northern Ngatamariki there is a clear set of events that occurs relatively shallow (~1 km bsl) and a set of events that are much deeper (~2 km bsl). Since most of the deep injection in this part of the field is through NM9, the deeper events are likely associated with injection in that well. The events in the south of the field show a NE-SW trending structure, the Aratiatia Fault Zone, that extends from the injection wells (NM10 and NM6) back to the southern production wells (NM5 and NM11), consistent with a permeable pathway between the wells as shown in tracer testing (Buscarlet et al., 2015). The Rotokawa events are mostly on the injection side of the Central Field fault, as was observed in previous studies. The improved velocity model produced as part of this thesis shows the event depths at Ngatamariki are mostly at the same depths as the injection well feedzones, but extend to as deep as 5 km bsl (Figure 6.3).

6.2.2 Rotokawa

There are comparatively fewer implications for the Rotokawa field when compared to that for Ngatamariki. This is due to a number of factors; the variable results obtained for the tomography work for V_p ; that most of the high V_s that was consistently observed in the tomography results is likely due to the higher elevation of greywacke and andesite, which was already known from the drilling; and that there is no measured velocity data from the wells at Rotokawa that could be used to examine velocity controls as could be performed for

Ngatamariki (Figure 6.1). There is no clear observable effect of the presence of steam in the ~1 km thick two-phase zone at Rotokawa in the tomography results, as might have been expected based on the impact of steam that has been observed in some core studies (Boitnott, 1995) and at a number of geothermal fields (e.g. the Geysers field, Gritto and Jarpe, (2013)). There may be a number of reasons why this is not observable at Rotokawa (e.g. the smaller spatial scale of the two-phase zone at Rotokawa compared to other fields, the lower resolution of the tomography due to highly concentrated earthquakes at Rotokawa). It's also possible that most of the steam at Rotokawa resides in the fracture space, which makes up only a small percentage of the total pore space, and that predominantly liquid is contained in the pore spaces (Grant, 2013).

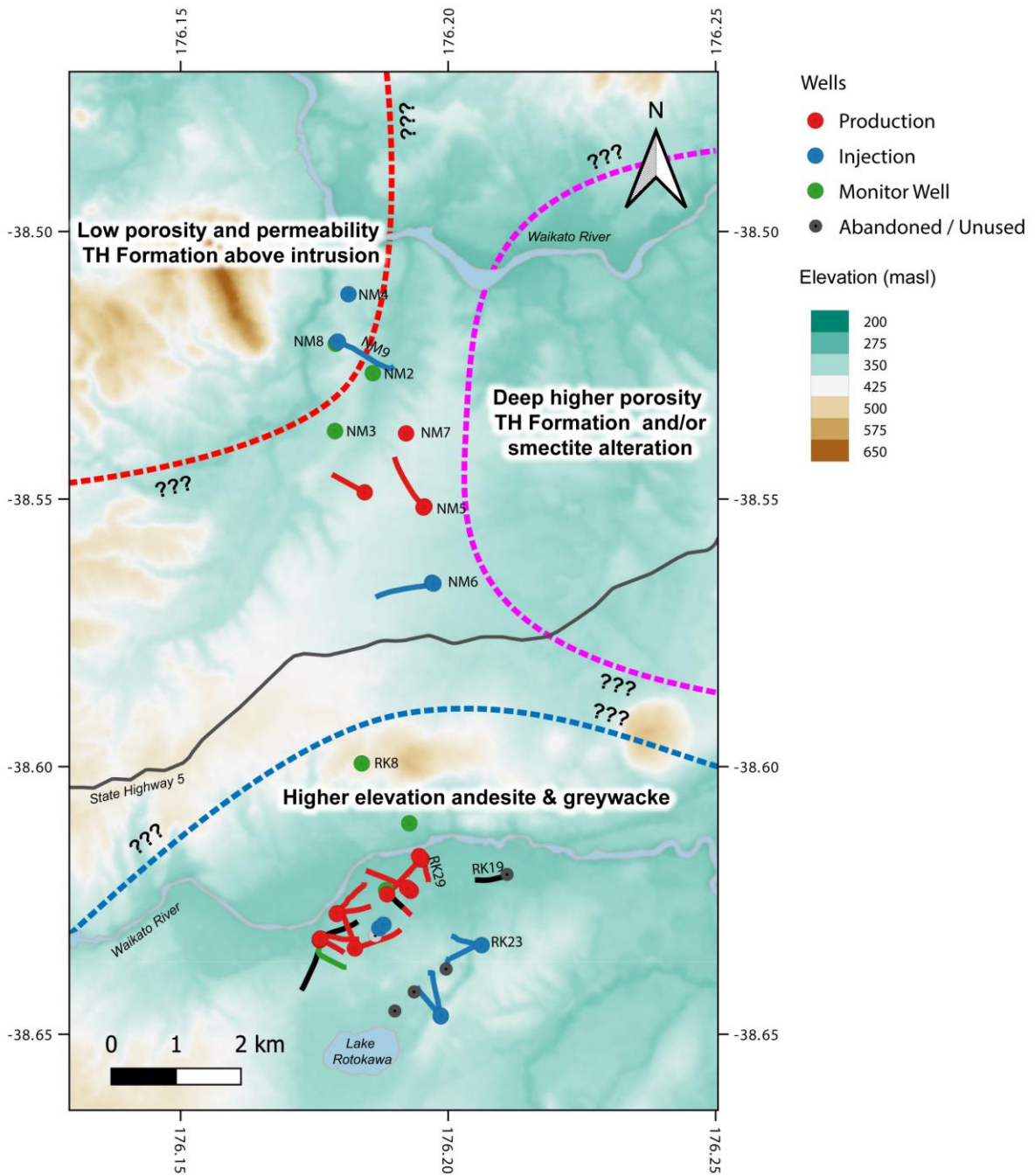


Figure 6.1. Summary of interpretation based on the work in this thesis. Question marks indicate where the interpretation is particularly uncertain which is due mostly to lack of ray-path coverage in the seismic tomography.

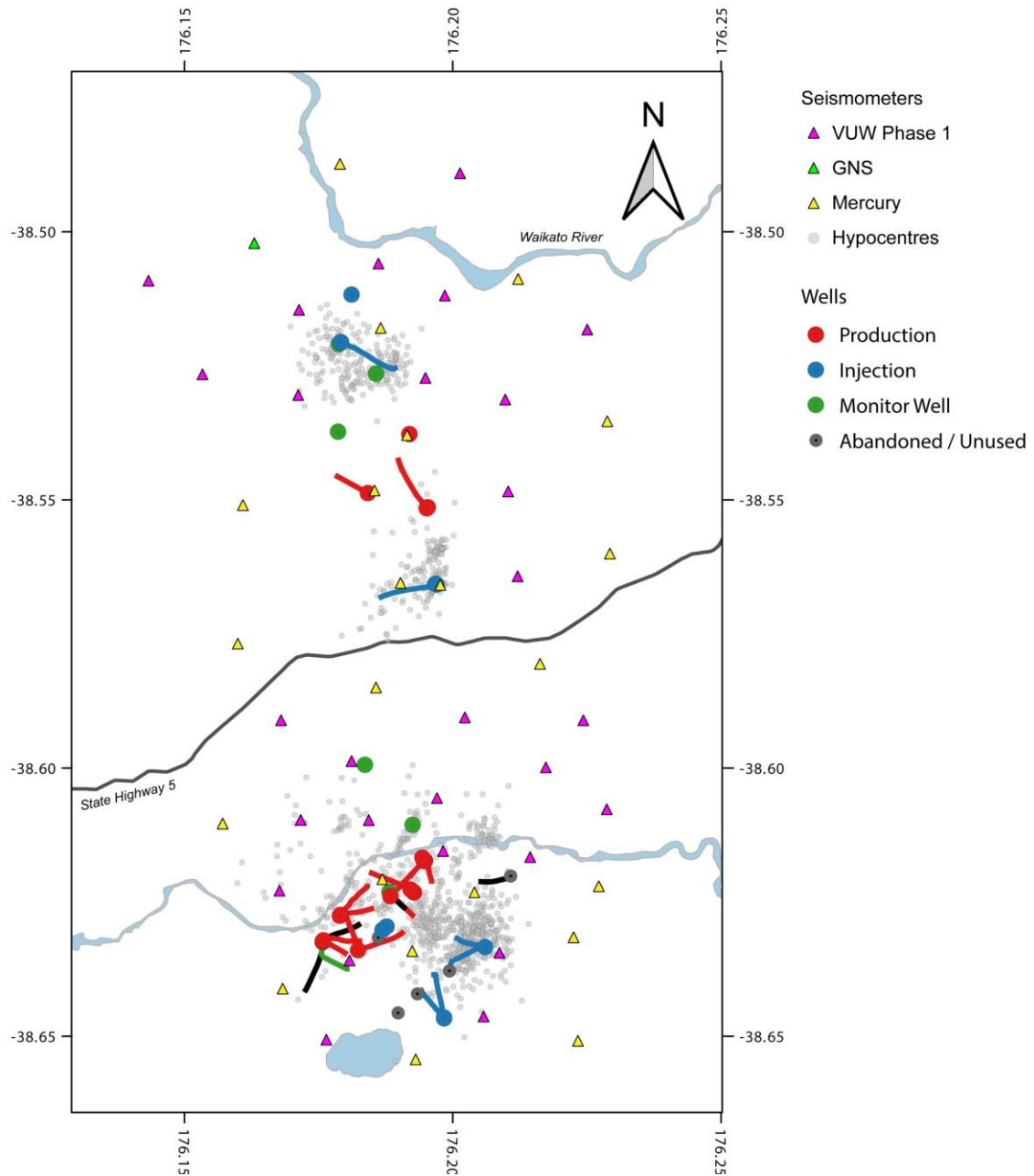


Figure 6.2. Hypocentres for the 1209 earthquakes recorded and located during the 2017-2018 field deployment.

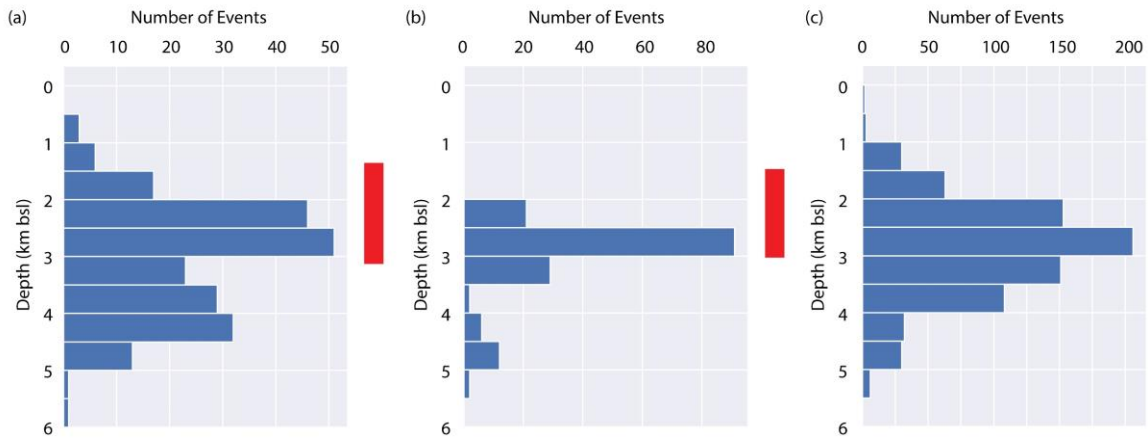


Figure 6.3. Hypocentre depths for (a) Ngatamariki North, (b) Ngatamariki South and (c) Rotokawa for the 1209 earthquakes recorded and located during the 2017-2018 field deployment. Red bars indicate the depth range of injection feedzones in each of the areas.

The improved velocity model that was obtained for Rotokawa in this thesis does provide improved earthquake locations for the field, particularly the depths of events. Locations obtained for the Rotokawa earthquake cluster during the 2017-2018 deployment agree well with the elevation of the injection feedzones at Rotokawa (Figure 6.3). The depths are shallower than those obtained by using a 1D velocity model for the entire Rotokawa-Ngatamariki seismic monitoring network as was used by Hopp (2019). The main driver of the difference is likely the relatively higher velocities that are observed at Rotokawa, a consequence of the higher elevation of greywacke and andesite at Rotokawa.

The general seismicity pattern obtained from the 2017-2018 expanded array at Rotokawa is mostly consistent with the patterns and interpretations that have been presented by Hopp (2019); Sewell et al. (2015); Sherburn et al. (2015). As observed in those studies, the majority of the seismicity at Rotokawa is on the injection side of the Central Field Fault which appears to impede the flow of injection back to production wells, as observed in injection tracer tests (Winick et al., 2015). The 2017-2018 hypocentres do appear to contain more events in the production area and the area north of the Waikato River (Figure 6.2). A lineament of events across the northwest production wells may be associated with a fault in that area as was interpreted from microseismic monitoring and tracer testing at Rotokawa during injection in that part of the field in 2008 (Addison et al., 2015; Sewell et al., 2015). Events here may be induced by the influx of cooler fluids in the western production area, as was outlined by Clearwater et al. (2016). The events north of the river appear to be natural seismic events associated with the Aratiatia Fault zone.

6.3 Implications for Application of Seismic Tomography in Geothermal Areas

The synthetic testing performed as part of the 3D inversion work suggests that obtaining resolution at less than 1 km is challenging, as was discussed in Chapter 5. Some of the factors at play are; the uncertainty in travel times (picking accuracy and origin time), lack of well distributed earthquakes and coupling of the hypocentre and velocity inversion problem. Achievable resolution is also likely limited by the dominant wavelength of the P and S waves that are recorded due to Fresnel zone limits (Williamson and Worthington, 1993). Williamson (1991) derived an approximate relation for the smallest feature (r_{min}) that can be expected to be resolved via ray-based tomography methods based on the width of the first Fresnel zone.

$$r_{min} \sim \sqrt{L\lambda} \quad (6.1)$$

Where L is the propagation distance and λ is the wavelength of the seismic wave. Given that the dominant frequencies P and S waves in this study (and likely for local earthquakes in geothermal fields recorded with surface seismometers in general) are on the order of 10 Hz and 2 Hz respectively, and that propagation lengths are approximately 2-3 km, implies the smallest features that could theoretically be resolved by ray-based tomography are on the order of 200 m for Vp and 1000 m for Vs.

6.4 Prospects for Further Research

There are many avenues for further research that arise from this thesis, both on the seismic velocity imaging applied to the Rotokawa and Ngatamariki geothermal fields and for seismic velocity imaging in geothermal fields in general. The extent of the low permeability, highly altered and deformed rock above the intrusion in the north of the Ngatamariki field could be further defined in a number of ways. Further pXRF, XRD and automated mineralogy on additional wells at Ngatamariki (e.g. NM4, NM2, NM3, NM7) might be used to define the north-south extent and examine variations in the thickness of the zone above the intrusion that has been affected by the intrusion processes. Further fluid inclusion analyses could also be performed on wells in the north of the field (NM4, NM8 and NM9) to more directly define the vertical extent of the Tahorakuri Formation above the intrusion that has been exposed to temperatures above the brittle-ductile threshold ($> 375^{\circ}\text{C}$).

The unique and rich geophysical, geochemical and mineralogical dataset from the NM9 well logs and cuttings analyses above the diorite-tonalite intrusive body acquired in this work could be the basis for further investigation of the processes that occurred during the intrusion event at Ngatamariki. For example, more detailed geochemistry, such as those undertaken by Muraoka et al. (1998)), and/or fluid inclusion studies of the zone directly overlying the intrusive (WP Tuff unit) may confirm or refute the processes occurring above the intrusion proposed in this work (i.e. ductile deformation and supercritical fluid conditions). This may be beneficial to assessing the potential for use of supercritical fluids above magmatic bodies in New Zealand and overseas (Climo et al., 2020; Reinsch et al., 2017). Expanding the geophysical datasets and joint inversion of them could be used to better define the extent of the low permeability associated with the intrusion in the northwest of Ngatamariki. Collection of additional gravity measurements across the field accompanied by gravity modelling, with constraints provided by the wireline logging dataset (e.g. use of density and porosity logs) and checkshot survey, would be a cost-effective way to potentially further constrain the low permeability area. However, as the high-density body is at 2-3 km depth, the spatial resolution of the gravity may be insufficient. This could be tested though by performing 2.5D forward modelling.

The best option for high resolution imaging of the extent of low permeability in the north is acquisition of further active source seismic data (e.g. VSP). This could be done by installing a Distributed Acoustic Sensing (DAS) fibre-optic in idle wells (e.g. NM4) and/or into wells (NM8 and NM9) during the annual power plant shut down for maintenance. Vibroseis or an air-gun could be used as seismic sources with shot-points at varying distances and azimuth to the east of the northern NM wells. Nodal seismometers at relatively close spacing (<100 m) could also be used at the surface during the survey to better constrain the shallow velocities. Similar approaches have been utilised in other geothermal fields (e.g. Kästner et al., 2020; Parker et al., 2018). Recording any microseismic activity during the survey could also provide useful constraints. Kim et al. (2020) describe how they utilised dense seismic sensors at the surface and microearthquakes in the Krafla geothermal field to image 'bright-spots' that were interpreted as magma.

The lack of data constraints on the seismic velocity from local earthquake seismic tomography in the shallower parts (particularly above 1.0 km bsl) of the Ngatamariki and Rotokwa geothermal fields was clearly demonstrated in this study. This is due to the depth range of the available earthquakes in the fields (mostly between 1 and 3 km bsl) and it is likely that most

seismic tomography using local earthquakes in geothermal fields will suffer from the same lack of data constraints on the shallower parts of the velocity models. This might be overcome by combined use of geophysical methods that can characterise physical properties from surface to ~1 km depth. Seismic refraction lines might be utilised to obtain direct velocity measurements between 100m and 1 km bsl, perhaps including measurements from downhole seismometers at Ngatamariki. A more detailed gravity survey would be useful for identifying short-wavelength gravity changes that might be associated with possible variations in density, and therefore seismic velocity, in the upper few hundred metres. The gravity survey should include gravity measurements already available for the two fields from microgravity monitoring undertaken as part of the geothermal system monitoring. Ideally any gravity surveying would be performed prior to refraction surveys such that the location of survey lines could be optimised to image any apparent shallow density/velocity contrasts. Further ambient noise tomography utilizing the expanded array data may also add direct constraints on shear wave velocity in the upper few hundred metres. Identification and delineation of shallow rhyolite lava bodies, which likely have relatively high seismic velocity, might be aided by use of aeromagnetic survey data.

Finally, joint-inversion of the available geophysical datasets (gravity, seismic, resistivity, geophysical logging) could be performed, leveraging the high-quality and coverage of the geophysical datasets at Ngatamariki and Rotokawa. This approach utilises the fact that geophysical properties commonly co-vary to better constrain the inversion of each property (e.g. density, seismic velocity and resistivity). This is being increasingly utilised in geothermal areas where multiple geophysical datasets are available (Soyer et al., 2017).

There is also the question of why the NW of Ngatamariki has remained low permeability despite continued tectonic activity since emplacement of the intrusion approximately 65 kya. Presumably this is due to the Tahorakuri formation in the north becoming mechanically much stronger and therefore more difficult to fracture relative to the Tahorakuri formation in the rest of the field. Hopp, (2019) noted that stress inversions in the north of the Ngatamariki field reveal an unconventional stress state with no vertical principal axis, whereas stress results in the south show the expected normal-faulting regime with NE-SW-oriented S_{Hmax} . Further geomechanical modelling, as was suggested by Hopp, (2019), of this may provide insight into why permeability is low in this area and more generally around intrusions in geothermal fields. This might be aided by further stress inversions utilizing the expanded array seismic data. There is abundant geophysical and geological data available for Ngatamariki to undertake such geomechanical modelling which is relatively rare for geothermal fields. Additionally, the

modelling may indicate that permeability between the mechanically-strong intrusion and its alteration and the relatively mechanically-weak Tahorakuri Formation is likely higher, which could be important for well targeting in the area.

There is also more that could be done with the expanded seismic array dataset that was collected for this thesis. Full waveform inversion could be performed, which may provide better spatial resolution of velocity than ray-based tomography, particularly better definition of sharp velocity contrasts such as that in the north of the Ngatamariki field (Brittan et al., 2013; Liu and Gu, 2012). The double-difference, full waveform adjoint inversion method of Yuan et al., (2016) looks to be particularly promising in this regard, offering both improved accuracy of source terms (e.g. origin time) through double-difference of station pairs for the same event, as well as the benefits of full waveform inversion (higher spatial resolution and better definition of velocity contrasts).

The expanded array data might also be integrated with seismic array data available for the Wairakei geothermal field, 5-10 km's south of Rotokawa, and data acquired by Bannister et al., (2015). This data would potentially add constraints on the areas surrounding the Ngatamariki and Rotokawa fields, outside the coverage provided by the expanded array deployed for this work. Deep earthquakes, that were either not well-recorded (possibly due to strong attenuation of high frequencies below and within the geothermal fields) or were outside of the expanded array, might also be added providing better constraints on velocities below the geothermal fields.

Seismic attenuation tomography inversion could also be performed. Seismic attenuation is more sensitive to the presence of gas and steam and therefore may provide more information on the extent of steam, particularly within the Rotokawa reservoir. Focal mechanisms and stress tensor inversions as was done by Hopp, (2019), S-wave splitting, possibly as a tomographic approach as done by Mroczek et al. (2019) and S-wave velocity structure from ambient noise cross-correlation as done by Civilini et al., (2016) might also be performed using the expanded seismic array data. The denser deployment of seismometers obtained for this thesis might provide improved data constraints and higher spatial resolution for each of these methods.

6.5 Concluding Statement

This thesis adds to a growing body of work on the utility of seismic velocity imaging in geothermal fields by providing both a robust case-study of velocity imaging via tomographic methods and furthering the understanding of the factors that control seismic velocities within geothermal fields. Examination of seismic velocity logs, in conjunction with geochemistry and mineralogy techniques, has shown that porosity variation is the largest factor that controls seismic velocities, although other factors appear to be important as well (e.g. fracturing, changes in the density of the matrix minerals, clay abundance). Porosity variation within the Ngatamariki field has in-turn been shown to be due to both primary lithology types, alteration (particularly quartz infilling of pore spaces) and ductile-deformation during an intrusion event in the field. The low-porosity altered and deformed Tahorakuri Formation tuffs above the intrusion has been imaged by the seismic tomography methods applied here and suggest that the intrusion and its alteration/deformation halo does not extend to the northeast of the field. Since the intrusion alteration/deformation process have lowered permeability, this study has implications for well targeting and reservoir modelling and management in the Ngatamariki geothermal field. More generally, the thesis demonstrates that very low porosity, high seismic velocity zones form above intrusions due to ductile deformation, a finding that may have implications for seismic imaging of magma bodies, for understanding the deep heat sources of geothermal systems and for utilization of supercritical geothermal resources.

References

- Addison, S.J., Winick, J.A., Mountain, B.W., Siega, F.L., 2015. Rotokawa reservoir tracer test history, in: Proc. NZ Geothermal Workshop 2015.
- Ahmed, A.D., Hood, S.B., Gazley, M.F., Cooke, D.R., Orovan, E.A., 2019. Interpreting element addition and depletion at the Ann Mason porphyry-Cu deposit, Nevada, using mapped mass balance patterns. *J. Geochemical Explor.* 196, 81–94. <https://doi.org/10.1016/j.gexplo.2018.09.009>
- Aitchison, J., 1982. The Statistical Analysis of Compositional Data. *J. R. Stat. Soc. Ser. B* 44, 139–160. <https://doi.org/10.1111/j.2517-6161.1982.tb01195.x>
- Aki, K., Lee, W.H.K., 1976. Determination of three-dimensional velocity anomalies under a seismic array using first P arrival times from local earthquakes 1. A homogenous initial model. *J. Geophys. Res.* 81, 4381–4399.
- Arehart, G.B., Christenson, B.W., Wood, C.P., Foland, K.A., Browne, P.R.L., 2002. Timing of volcanic, plutonic and geothermal activity at Ngatamariki, New Zealand. *J. Volcanol. Geotherm. Res.* 116, 201–214. [https://doi.org/https://doi.org/10.1016/S0377-0273\(01\)00315-8](https://doi.org/https://doi.org/10.1016/S0377-0273(01)00315-8)
- Avseth, P., Mukerji, T., Mavko, G., Dvorkin, J., 2010. Rock-physics diagnostics of depositional texture, diagenetic alterations, and reservoir heterogeneity in high-porosity siliciclastic sediments and rocks — A review of selected models and suggested work flows. *GEOPHYSICS* 75, 75A31-75A47. <https://doi.org/10.1190/1.3483770>
- Bannister, S., Bourguignon, S., Sherburn, S., Bertrand, E.A., 2015. 3-D seismic velocity and attenuation in the central Taupo Volcanic Zone, New Zealand: imaging the roots of geothermal systems, in: Proceedings, World Geothermal Congress. p. 17.
- Berryman, J.G., 2007. Seismic waves in rocks with fluids and fractures. *Geophys. J. Int.* 171, 954–974. <https://doi.org/10.1111/j.1365-246X.2007.03563.x>
- Berryman, J.G., 2000. Seismic velocity decrement ratios for regions of partial melt in the lower mantle. *Geophys. Res. Lett.* 27, 421–424. <https://doi.org/10.1029/1999GL008402>
- Beyreuther, M., Barsch, R., Krischer, L., Megies, T., Behr, Y., Wassermann, J., 2010. ObsPy: A python toolbox for seismology. *Seismol. Res. Lett.* 81, 530–533.

<https://doi.org/10.1785/gssrl.81.3.530>

- Boitnott, G., Boyd, P., 1996. Permeability, electrical impedance, and acoustic velocities on reservoir rocks from The Geysers geothermal field, in: Proceedings, Twenty-First Workshop on Geothermal Reservoir Engineering.
- Boitnott, G.N., 1995. Laboratory measurements on reservoir rocks from the Geysers Geothermal Field.
- Boitnott, G.N., Kirkpatrick, A., 1997. Interpretation of Field Seismic Tomography at The Geysers Geothermal Field, California, in: Proceedings of the Twenty-Second Workshop on Geothermal Reservoir Engineering.
- Boseley, C., Cumming, W., Urzúa-Monsalve, L., Powell, T., Grant, M., 2010. A resource conceptual model for the Ngatamariki geothermal field based on recent exploration well drilling and 3D MT resistivity imaging, in: Proceedings World Geothermal Congress.
- Brevik, I., 2005. Burial processes and their control on acoustic properties in shales, in: SEG Technical Program Expanded Abstracts 2005. Society of Exploration Geophysicists, pp. 1557–1560. <https://doi.org/10.1190/1.2147989>
- Brittan, J., Bai, J., Delome, H., Wang, C., Yingst, D., 2013. Full waveform inversion—the state of the art. *First Break* 31.
- Browne, P.R.L., 1978. Hydrothermal Alteration in Active Geothermal Fields. *Annu. Rev. Earth Planet. Sci.* 6, 229–248. <https://doi.org/10.1146/annurev.ea.06.050178.001305>
- Browne, P.R.L., Lawless, J. V., 2001. Characteristics of hydrothermal eruptions, with examples from New Zealand and elsewhere. *Earth Sci. Rev.* 52, 299–331. [https://doi.org/10.1016/S0012-8252\(00\)00030-1](https://doi.org/10.1016/S0012-8252(00)00030-1)
- Buscarlet, E., Moon, H., Wallis, I., Quinao, J., 2015. Reservoir tracer test at the Ngatamariki geothermal field, in: Proceedings 37th New Zealand Geothermal Workshop. p. 20.
- Cant, J.L., 2015. Matrix Permeability of Reservoir Rocks, Ngatamariki Geothermal Field, Taupo Volcanic Zone, New Zealand. University of Canterbury. Geology.
- Carey, B., Dunstall, M., McClintock, S., White, B., Bignall, G., Luketina, K., Robson, B., Zarrouk, S., Seward, A., 2015. 2015 New Zealand Country Update, in: Proceedings World Geothermal Congress.

- Castellazzi, C., Savage, M.K., Walsh, E., Arnold, R., 2015. Shear wave automatic picking and splitting measurements at Ruapehu volcano, New Zealand. *J. Geophys. Res. Solid Earth* 120, 3363–3384. <https://doi.org/10.1002/2014JB011585>
- Chambefort, I., Buscarlet, E., Wallis, I., Sewell, S., Wilmarth, M., 2016. Ngatamariki Geothermal Field, New Zealand: Geology, geophysics, chemistry and conceptual model. *Geothermics* 59, Part B, 266–280. <https://doi.org/http://dx.doi.org/10.1016/j.geothermics.2015.07.011>
- Chambefort, I., Lewis, B., Simpson, M.P., Bignall, G., Rae, A.J., Ganefianto, N., 2017. Ngatamariki Geothermal System: Magmatic to Epithermal Transition in the Taupo Volcanic Zone, New Zealand. *Econ. Geol.* 112, 319–346. <https://doi.org/10.2113/econgeo.112.2.319>
- Chambefort, I., Lewis, B., Wilson, C.J.N., Rae, A.J., Coutts, C., Bignall, G., Ireland, T.R., 2014. Stratigraphy and structure of the Ngatamariki geothermal system from new zircon U–Pb geochronology: Implications for Taupo Volcanic Zone evolution. *J. Volcanol. Geotherm. Res.* 274, 51–70. <https://doi.org/10.1016/j.jvolgeores.2014.01.015>
- Chambefort, I., Mountain, B., Blair, A., Bignall, G., 2020. *Geothermal: The Neat Generation. World.*
- Chambefort, I.S., Dilles, J.H., Heinrich, C., 2013. Hydrothermal mineralogy and fluid inclusions chemistry to understand the roots of active geothermal systems, in: *AGU Fall Meeting Abstracts.*
- Chen, C., Holland, A.A., 2016. PhasePApy: A Robust Pure Python Package for Automatic Identification of Seismic Phases. *Seismol. Res. Lett.* 87, 1384–1396. <https://doi.org/10.1785/0220160019>
- Christenson, B.W., Mroczek, E.K., Wood, C.P., Arehart, G.B., 1997. Magma-ambient production environments: PTX constraints for paleo-fluids associated with the Ngatamariki diorite intrusion, in: *Proceedings of the 19th New Zealand Geothermal Workshop.* pp. 87–92.
- Civilini, F., Pancha, A., Savage, M., Sewell, S., 2016. Inferring shear-velocity structure of the upper 200 m using cultural ambient noise at the Ngatamariki geothermal field, Central North Island, New Zealand. *Interpretation.*

- Clarke, D., Townend, J., Savage, M.K., Bannister, S., 2009. Seismicity in the Rotorua and Kawerau geothermal systems, Taupo Volcanic Zone, New Zealand, based on improved velocity models and cross-correlation measurements. *J. Volcanol. Geotherm. Res.* 180, 50–66. <https://doi.org/10.1016/j.jvolgeores.2008.11.004>
- Clearwater, J., Hernandez, D., Sewell, S.M., Addison, S., 2016. Model-Based Decision Making to Manage Production in the Western Compartment at Rotokawa, in: *New Zealand Geothermal*
- Climo, M., Chambefort, I., Carey, B., Bendall, S., Blair, A., 2020. Advancing New Zealand's Supercritical Geothermal Opportunity, in: *Proceedings World Geothermal Congress.* p. 1.
- Cumming, W., 2016. Resource Conceptual Models of Volcano-Hosted Geothermal Reservoirs for Exploration Well Targeting and Resource Capacity Assessment: Construction, Pitfalls and Challenges, in: *Geothermal Resources Council Transactions.*
- Dahlhaus, L., 2013. NM9 Checkshot QC Report. Confidential report to Mighty River Power.
- De Matteis, R., Vanorio, T., Zollo, A., Ciuffi, S., Fiordelisi, A., Spinelli, E., 2008. Three-dimensional tomography and rock properties of the Larderello-Travale geothermal area, Italy. *Phys. Earth Planet. Inter.* 168, 37–48. <https://doi.org/10.1016/j.pepi.2008.04.019>
- Degen, T., Sadki, M., Bron, E., König, U., Nénert, G., 2014. The HighScore suite. *Powder Diffr.* 29, S13–S18. <https://doi.org/10.1017/S0885715614000840>
- Deichmann, N., Garcia-Fernandez, M., 1992. Rupture geometry from high-precision relative hypocentre locations of microearthquake clusters. *Geophys. J. Int.* 110, 501–517. <https://doi.org/10.1111/j.1365-246X.1992.tb02088.x>
- DeVilbiss, J.W., 1980. Wave dispersion and absorption in partially saturated rocks. Stanford University.
- Dickson, M.H., Fanelli, M., 2013. *Geothermal energy: utilization and technology.* Routledge.
- Diehl, T., Deichmann, N., Kissling, E., Husen, S., 2009a. Automatic S-Wave Picker for Local Earthquake Tomography. *Bull. Seismol. Soc. Am.* 99, 1906–1920. <https://doi.org/10.1785/0120080019>
- Diehl, T., Kissling, E., 2009. Users Guide for Consistent Phase Picking at Local to Regional Scales.

- Diehl, T., Kissling, E., Husen, S., Aldersons, F., 2009b. Consistent phase picking for regional tomography models: application to the greater Alpine region. *Geophys. J. Int.* 176, 542–554. <https://doi.org/10.1111/j.1365-246X.2008.03985.x>
- Downs, D.T., 2016. Mihi Breccia: A stack of lacustrine sediments and subaqueous pyroclastic flows within the Taupo Volcanic Zone, New Zealand. *J. Volcanol. Geotherm. Res.* 327, 180–191. <https://doi.org/10.1016/j.jvolgeores.2016.08.004>
- Downs, D.T., Rowland, J. V., Wilson, C.J.N., Rosenberg, M.D., Leonard, G.S., Calvert, A.T., 2014. Evolution of the intra-arc Taupo-Reporoa basin within the Taupo volcanic zone of New Zealand. *Geosphere* 10, 185–206. <https://doi.org/10.1130/GES00965.1>
- Durán, E.L., Adam, L., Wallis, I.C., Barnhoorn, A., 2019. Mineral Alteration and Fracture Influence on the Elastic Properties of Volcaniclastic Rocks. *J. Geophys. Res. Solid Earth* 124, 4576–4600. <https://doi.org/10.1029/2018JB016617>
- Eberhart-Phillips, D., Han, D.-H., Zoback, M.D., 1989. Empirical relationships among seismic velocity, effective pressure, porosity, and clay content in sandstone. *GEOPHYSICS* 54, 82–89. <https://doi.org/10.1190/1.1442580>
- Ellis, D., Case, C., Chiaromonte, J., 2004. Porosity from neutron logs II: Interpretation. *Petrophysics* 45.
- Evans, J.R., Eberhart-Phillips, D., Thurber, C.H., 1994. User's manual for SIMULPS12 for imaging vp and vp/vs: A derivative of the “Thurber” tomographic inversion SIMUL3 for local earthquakes and explosions.
- Farina, B., Poletto, F., Mendrinós, D., Carcione, J.M., Karytsas, C., 2019. Seismic properties in conductive and convective hot and super-hot geothermal systems. *Geothermics* 82, 16–33. <https://doi.org/10.1016/j.geothermics.2019.05.005>
- Foulger, G.R., Grant, C.C., Ross, A., Julian, B.R., 1997. Industrially induced changes in Earth structure at the Geysers Geothermal Area, California. *Geophys. Res. Lett.* 24, 135–137. <https://doi.org/10.1029/96GL03152>
- Foulger, G.R., Toomey, D.R., 1989. Structure and evolution of the Hengill-Grensdalur volcanic complex, Iceland: geology, geophysics, and seismic tomography. *J. Geophys. Res.* 94, 17511–17522. <https://doi.org/10.1029/jb094ib12p17511>
- Fournier, R.O., 1999. Hydrothermal processes related to movement of fluid from plastic into

- brittle rock in the magmatic-epithermal environment. *Econ. Geol.* 94, 1193–1211.
- Fournier, R.O., 1991. The transition from hydrostatic to greater than hydrostatic fluid pressure in presently active continental hydrothermal systems in crystalline rock. *Geophys. Res. Lett.* 18, 955–958. <https://doi.org/10.1029/91GL00966>
- Gazley, M.F., Bonnett, L.C., Fisher, L.A., Salama, W., Price, J.H., 2017. A workflow for exploration sampling in regolith-dominated terranes using portable X-ray fluorescence: comparison with laboratory data and a case study. *Aust. J. Earth Sci.* 64, 903–917. <https://doi.org/10.1080/08120099.2017.1367721>
- Gazley, M.F., Fisher, L.A., 2014. A review of the reliability and validity of portable X-ray fluorescence spectrometry (pXRF) data. *Miner. Resour. Ore Reserv. Estim. AusIMM Guid. to Good Pract.* 69, 82.
- Gazley, M.F., Martin, A.P., Turnbull, R.E., Frontin-Rollet, G., Strong, D.T., 2020. Regional patterns in standardised and transformed pathfinder elements in soil related to orogenic-style mineralisation in southern New Zealand. *J. Geochemical Explor.* 217, 106593. <https://doi.org/10.1016/j.gexplo.2020.106593>
- Gomberg, J.S., Shedlock, K.M., Roecker, S.W., 1990. The effect of S-wave arrival times on the accuracy of hypocenter estimation. *Bull. Seismol. Soc. Am.* 80, 1605–1628.
- Grant, M., 2013. *Geothermal reservoir engineering*. Elsevier.
- Gritto, R., Jarpe, S.P., 2014. Temporal variations of Vp/Vs-ratio at The Geysers geothermal field, USA. *Geothermics* 52, 112–119. <https://doi.org/10.1016/j.geothermics.2014.01.012>
- Gritto, R., Jarpe, S.P., 2013. Three-dimensional seismic tomography at the Geysers Geothermal Field, CA, USA, in: *Proceedings of the 38th Workshop On Geothermal Reservoir Engineering*, Stanford University, Stanford, CA.
- Gunasekera, R.C., Foulger, G.R., Julian, B.R., 2003. Reservoir depletion at The Geysers geothermal area, California, shown by four-dimensional seismic tomography. *J. Geophys. Res. Solid Earth* 108. <https://doi.org/10.1029/2001jb000638>
- Guo, Z., Chapman, M., Li, X., 2012. A shale rock physics model and its application in the prediction of brittleness index, mineralogy, and porosity of the Barnett Shale, in: *Society of Exploration Geophysicists International Exposition and 82nd Annual Meeting 2012*, SEG 2012. Society of Exploration Geophysicists, pp. 2406–2410.

<https://doi.org/10.1190/segam2012-0777.1>

- GuoXin, L., YuHua, G., Jie, Z., FengPing, Y., ChangHai, Y., Neville, T.J., Farag, S., XingWang, Y., YouQing, Z., 2007. Petrophysical Characterization Of A Complex Volcanic Reservoir.
- Halwa, L., 2013. FMI Image Interpretation Report. Mighty River Power. Ngatamariki-9.
- Han, D., Nur, A., Morgan, D., 1986. Effects of porosity and clay content on wave velocities in sandstones. *GEOPHYSICS* 51, 2093–2107. <https://doi.org/10.1190/1.1442062>
- Haslinger, F., Kissling, E., 2001. Investigating effects of 3-D ray tracing methods in local earthquake tomography. *Phys. Earth Planet. Inter.* 123, 103–114. [https://doi.org/10.1016/S0031-9201\(00\)00204-1](https://doi.org/10.1016/S0031-9201(00)00204-1)
- Hedenquist, J.W., Lowenstern, J.B., 1994. The role of magmas in the formation of hydrothermal ore deposits. *Nature* 370, 519–527.
- Henley, R.W., McNabb, A., 1978. Magmatic vapor plumes and ground-water interaction in porphyry copper emplacement. *Econ. Geol.* 73, 1–20.
- Henry, S.A., Hochstein, M.P., 1990. Geophysical structure of the broadlands/ohaaki geothermal field (New Zealand). *Geothermics* 19, 129–150. [https://doi.org/10.1016/0375-6505\(90\)90013-2](https://doi.org/10.1016/0375-6505(90)90013-2)
- Heřmanská, M., Stefánsson, A., Scott, S., 2019. Supercritical fluids around magmatic intrusions: IDDP-1 at Krafla, Iceland. *Geothermics* 78, 101–110.
- Hernandez, D., Addison, S., Sewell, S., Azwar, L., Barnes, M., 2015. Rotokawa: Reservoir response of 172 MW geothermal operation, in: *Proceedings of the New Zealand Geothermal Workshop*. Rotorua, New Zealand.
- Hochstein, M.P., Hunt, T.M., 1970. Seismic, gravity and magnetic studies, Broadlands geothermal field, New Zealand. *Geothermics* 2, 333–346. [https://doi.org/10.1016/0375-6505\(70\)90032-5](https://doi.org/10.1016/0375-6505(70)90032-5)
- Holdaway, M.J., 1971. Stability of andalusite and the aluminum silicate phase diagram. *Am. J. Sci.* 271, 97–131. <https://doi.org/10.2475/ajs.271.2.97>
- Hole, H., 2013. Geothermal drilling - keep it simple, in: *New Zealand Geothermal Workshop 2013*.

- Hopp, C., 2019. Characterizing microseismicity at the Rotokawa and Ngatamariki geothermal fields. Victoria University.
- Hopp, C., Savage, M., Townend, J., Sewell, S., 2016. Matched filter earthquake detection and double-difference relocation at Rotokawa and Ngatamariki geothermal areas: January to November, 2015. 38th New Zeal.
- Hunt, T., Bowyer, D., 2007. Reinjection and gravity changes at Rotokawa geothermal field, New Zealand. *Geothermics* 36, 421–435. <https://doi.org/10.1016/j.geothermics.2007.07.004>
- Hunt, T.M., 2012. Geothermal field monitoring and Reservoir Monitoring geothermal reservoir monitoring, in: *Encyclopedia of Sustainability Science and Technology*. Springer New York, pp. 4201–4221. https://doi.org/10.1007/978-1-4419-0851-3_298
- Hurst, A., Nadeau, P., 1995. Clay microporosity in reservoir sandstones: an application of quantitative electron microscopy in petrophysical evaluation. *Am. Assoc. Pet. Geol. Bull.* 79, 563–573.
- Hutchings, L., Jarpe, S., Boyle, K., Viegas, G., Majer, E., 2011. Inexpensive, automated micro-earthquake data collection and processing system for rapid, high-resolution reservoir analysis. *Geotherm. Resour. Coun. Transactions* 35, 1679–1685.
- Ikeuchi, K., Doi, N., Sakagawa, Y., Kamenosono, H., Uchida, T., 1998. High-temperature measurements in well WD-1a and the thermal structure of the Kakkonda geothermal system, Japan. *Geothermics* 27, 591–607. [https://doi.org/10.1016/S0375-6505\(98\)00035-2](https://doi.org/10.1016/S0375-6505(98)00035-2)
- International Finance Corporation, 2013. Success of geothermal wells: A global study.
- Ito, H., DeVilbiss, J., Nur, A., 1979. Compressional and shear waves in saturated rock during water-steam transition. *J. Geophys. Res.* 84, 4731. <https://doi.org/10.1029/JB084iB09p04731>
- Iyer, H.M., Hirahara, K., 1993. *Seismic tomography: Theory and practice*. Springer Science & Business Media.
- Jaya, M.S., Shapiro, S.A., Kristinsdóttir, L.H., Milsch, H., Spangenberg, E., 2010. Temperature dependence of seismic properties in geothermal rocks at reservoir conditions.

- Geothermics 39, 115–123. <https://doi.org/10.1016/j.geothermics.2009.12.002>
- Jeffreys, H., 1932. An Alternative to the Rejection of Observations. *Proc. R. Soc. London. Ser. A, Contain. Pap. a Math. Phys. Character* 137, 78–87.
- Jousset, P., Haberland, C., Bauer, K., Arnason, K., 2011. Hengill geothermal volcanic complex (Iceland) characterized by integrated geophysical observations. *Geothermics* 40, 1–24. <https://doi.org/10.1016/j.geothermics.2010.12.008>
- Julian, B., Gubbins, D., 1977. Three-dimensional seismic ray tracing. *J. Geophys.*
- Julian, B.R., Foulger, G.R., 2012. Geothermal seismology: the state of the art, in: *Proceedings of the 37th Workshop On Geothermal Reservoir Engineering*, Stanford University, Stanford, CA.
- Julian, B.R., Ross, A., Foulger, G.R., Evans, J.R., 1996. Three-dimensional seismic image of a geothermal reservoir: The Geysers, California. *Geophys. Res. Lett.* 23, 685–688. <https://doi.org/10.1029/95GL03321>
- Kästner, F., Giese, R., Planke, S., Millett, J.M., Flóvenz, Ó.G., 2020. Seismic imaging in the Krafla high-temperature geothermal field, NE Iceland, using zero- and far-offset vertical seismic profiling (VSP) data. *J. Volcanol. Geotherm. Res.* 391, 106315. <https://doi.org/10.1016/J.JVOLGEORES.2018.02.016>
- Keary, P., Brooks, M., Hill, I., 1992. *An introduction to exploration geophysics*, Third Edit. ed. Blackwell Publishing Ltd.
- Khadeeva, Y., Vernik, L., 2014. Rock-physics model for unconventional shales. *Lead. Edge* 33, 318–322. <https://doi.org/10.1190/tle33030318.1>
- Kim, D., Brown, L.D., Arnason, K., Gudmundsson, Ó., Ágústsson, K., Flóvenz, Ó.G., 2020. Magma “bright spots” mapped beneath Krafla, Iceland, using RVSP imaging of reflected waves from microearthquakes. *J. Volcanol. Geotherm. Res.* 391, 106365. <https://doi.org/10.1016/J.JVOLGEORES.2018.04.022>
- Kissling, E., 1995. *Program VELEST User Guide*.
- Kissling, E., Ellsworth, W.L., Eberhart-Phillips, D., Kradolfer, U., 1994. Initial reference models in local earthquake tomography. *J. Geophys. Res. Solid Earth* 99, 19635–19646.
- Klimentos, T., 1991. The effects of porosity-permeability-clay content on the velocity of

- compressional waves. *GEOPHYSICS* 56, 1930–1939. <https://doi.org/10.1190/1.1443004>
- Koide, H., Bhattacharji, S., 1975. Formation of fractures around magmatic intrusions and their role in ore localization. *Econ. Geol.* 70, 781–799. <https://doi.org/10.2113/gsecongeo.70.4.781>
- Krischer, L., 2015. hypoDDpy.
- Langridge, R., Ries, W., Litchfield, N., Villamor, P., Van Dissen, R., Barrell, D., Rattenbury, M., Heron, D., Haubrock, S., Townsend, D., Lee, J., Berryman, K., Nicol, A., Cox, S., Stirling, M., 2016. The New Zealand Active Faults Database. *New Zeal. J. Geol. Geophys.* 59, 86–96. <https://doi.org/10.1080/00288306.2015.1112818>
- Lees, J.M., 2007. Seismic tomography of magmatic systems. *J. Volcanol. Geotherm. Res.* 167, 37–56. <https://doi.org/10.1016/j.jvolgeores.2007.06.008>
- Lewis, B., Chambefort, I., Rae, A., Saunders, F., 2013. Geology of well NM9, Ngatamariki Geothermal Field.
- Lewis, B., Chambefort, I., Rae, A.J., 2012a. Geology of Injection Well NM8-NM8A, Ngatamariki Geothermal Field.
- Lewis, B., Chambefort, I., Rae, A.J., Sanders, F., 2012b. Geology of Injection Well NM10, Ngatamariki Geothermal Field.
- Lin, G., Wu, B., 2018. Seismic velocity structure and characteristics of induced seismicity at the Geysers Geothermal Field, eastern California. *Geothermics* 71, 225–233. <https://doi.org/10.1016/j.geothermics.2017.10.003>
- Liu, D., Sams, M., White, R., 2014. Rock-physics modeling of a dispersed-clay sandstone and dispersed-quartz shale sequence. *Lead. Edge* 33, 298–308. <https://doi.org/10.1190/tle33030298.1>
- Liu, Q., Gu, Y.J., 2012. Seismic imaging: From classical to adjoint tomography. *Tectonophysics* 566–567, 31–66. <https://doi.org/https://doi.org/10.1016/j.tecto.2012.07.006>
- Lomax, A., Virieux, J., Volant, P., Berge-Thierry, C., 2000. Probabilistic Earthquake Location in 3D and Layered Models. pp. 101–134. https://doi.org/10.1007/978-94-015-9536-0_5
- Mauk, J.L., Simpson, M.P., 2007. Geochemistry and stable isotope composition of altered

- rocks at the Golden Cross epithermal Au-Ag deposit, New Zealand. *Econ. Geol.* 102, 841–871.
- Mauriohooho, K., Barker, S.L.L., Rae, A., 2016. Mapping lithology and hydrothermal alteration in geothermal systems using portable X-ray fluorescence (pXRF): A case study from the Tauhara geothermal system, Taupo Volcanic Zone. *Geothermics* 64, 125–134. <https://doi.org/10.1016/j.geothermics.2016.03.005>
- Mavko, G., Mukerji, T., Dvorkin, J., 2009a. *The rock physics handbook: Tools for seismic analysis of porous media.* Cambridge university press.
- Mavko, G., Mukerji, T., Dvorkin, J., 2009b. *The rock physics handbook : tools for seismic analysis of porous media.* Cambridge University Press.
- Mayer, K., Scheu, B., Montanaro, C., Yilmaz, T.I., Isaia, R., Aßbichler, D., Dingwell, D.B., 2016. Hydrothermal alteration of surficial rocks at Solfatara (Campi Flegrei): Petrophysical properties and implications for phreatic eruption processes. *J. Volcanol. Geotherm. Res.* 320, 128–143. <https://doi.org/10.1016/j.jvolgeores.2016.04.020>
- McKinley, J.M., Hron, K., Grunsky, E.C., Reimann, C., de Caritat, P., Filzmoser, P., van den Boogaart, K.G., Tolosana-Delgado, R., 2016. The single component geochemical map: Fact or fiction? *J. Geochemical Explor.* 162, 16–28. <https://doi.org/10.1016/j.gexplo.2015.12.005>
- McNamara, D., Sewell, S., Buscarlet, E., Wallis, I., 2016. A review of the Rotokawa geothermal field, New Zealand. *Geothermics* 59, 281–293.
- Mielke, P., Weinert, S., Bignall, G., Sass, I., 2016. Thermo-physical rock properties of greywacke basement rock and intrusive lavas from the Taupo Volcanic Zone, New Zealand. *J. Volcanol. Geotherm. Res.* 324, 179–189. <https://doi.org/10.1016/j.jvolgeores.2016.06.002>
- Milicich, S.D., Chambefort, I., Wilson, C.J.N., Alcaraz, S., Ireland, T.R., Bardsley, C., Simpson, M.P., 2020. A zircon U-Pb geochronology for the Rotokawa geothermal system, New Zealand, with implications for Taupō Volcanic Zone evolution. *J. Volcanol. Geotherm. Res.* 389, 106729. <https://doi.org/10.1016/j.jvolgeores.2019.106729>
- Millett, J.M., Planke, S., Kästner, F., Blischke, A., Hersir, G.P., Halldórsdóttir, S., Flóvenz, Ó.G., Árnadóttir, S., Helgadóttir, H.M., Vakulenko, S., Buryak, S., Erlendsson, Ö., Giese,

- R., Cavailhes, J.P., Jerram, D.A., Guðmundsson, Á., Júlíusson, E., 2018. Sub-surface geology and velocity structure of the Krafla high temperature geothermal field, Iceland: Integrated ditch cuttings, wireline and zero offset vertical seismic profile analysis. *J. Volcanol. Geotherm. Res.* <https://doi.org/10.1016/J.JVOLGEORES.2018.03.024>
- Mondol, N.H., Bjørlykke, K., Jahren, J., Høeg, K., 2007. Experimental mechanical compaction of clay mineral aggregates—Changes in physical properties of mudstones during burial. *Mar. Pet. Geol.* 24, 289–311. <https://doi.org/10.1016/J.MARPETGEO.2007.03.006>
- Mondol, N.H., Jahren, J., Bjørlykke, K., Brevik, I., 2008. Elastic properties of clay minerals. *Lead. Edge* 27, 758–770. <https://doi.org/10.1190/1.2944161>
- Moos, D., Zoback, M.D., 1983. In Situ Studies of Velocity in Fractured Crystalline Rocks. *J. Geophys. Res.* 88, 2345–2358.
- Mroczek, S., Savage, M.K., Hopp, C., Sewell, S.M., 2019. Anisotropy as an indicator for reservoir changes: Example from the Rotokawa and Ngatamariki geothermal fields, New Zealand. *Geophys. J. Int.* 220, 1–17. <https://doi.org/10.1093/gji/ggz400>
- Muksin, U., Haberland, C., Bauer, K., Weber, M., 2013. Three-dimensional upper crustal structure of the geothermal system in Tarutung (North Sumatra, Indonesia) revealed by seismic attenuation tomography. *Geophys. J. Int.* 195, 2037–2049. <https://doi.org/10.1093/gji/ggt383>
- Muraoka, H., Uchida, T., Sasada, M., Yagi, M., Akaku, K., Sasaki, M., Yasukawa, K., Miyazaki, S.I., Doi, N., Saito, S., Sato, K., Tanaka, S., 1998. Deep geothermal resources survey program: Igneous, metamorphic and hydrothermal processes in a well encountering 500°C at 3729 m depth, Kakkonda, Japan. *Geothermics* 27, 507–534. [https://doi.org/10.1016/S0375-6505\(98\)00031-5](https://doi.org/10.1016/S0375-6505(98)00031-5)
- Naganawa, S., Suzuki, M., Ikeda, K., Inada, N., Sato, R., 2018. Modeling of Cuttings Lag Distribution in Directional Drilling to Evaluate Depth Resolution of Mud Logging, in: IADC/SPE Drilling Conference and Exhibition. Society of Petroleum Engineers. <https://doi.org/10.2118/189615-MS>
- Otamendi, J.E., Ducea, M.N., Tibaldi, A.M., Bergantz, G.W., de la Rosa, J.D., Vujovich, G.I., 2009. Generation of Tonalitic and Dioritic Magmas by Coupled Partial Melting of Gabbroic and Metasedimentary Rocks within the Deep Crust of the Famatinian Magmatic

- Arc, Argentina. *J. Petrol.* 50, 841–873. <https://doi.org/10.1093/PETROLOGY/EGP022>
- Paige, C., Saunders, M., 1982. LSQR: An algorithm for sparse linear equations and sparse least squares. *ACM Trans. Math.*
- Parker, L.M., Thurber, C.H., Zeng, X., Li, P., Lord, N.E., Fratta, D., Wang, H.F., Robertson, M.C., Thomas, A.M., Karplus, M.S., 2018. Active-source seismic tomography at the Brady Geothermal Field, Nevada, with dense nodal and fiber-optic seismic arrays. *Seismol. Res. Lett.* 89, 1629–1640.
- Pereyra, V., Lee, W.H.K., Keller, H.B., 1980. Solving two-point seismic-ray tracing problems in a heterogeneous medium. *Bull. Seismol. Soc. Am.* 70, 79–99.
- Pirrie, D., Rollinson, G.K., 2011. Unlocking the applications of automated mineral analysis. *Geol. Today* 27, 226–235. <https://doi.org/10.1111/j.1365-2451.2011.00818.x>
- Poletto, F., Farina, B., Carcione, J.M., 2018. Sensitivity of seismic properties to temperature variations in a geothermal reservoir. *Geothermics* 76, 149–163. <https://doi.org/10.1016/j.geothermics.2018.07.001>
- Pullammanappallil, S.K., Louie, J.N., 1993. Inversion of seismic reflection traveltimes using a nonlinear optimization scheme. *Geophysics* 58, 1607–1620.
- Rawlinson, N., 2012. FMTOMO - Fast Marching Tomography Package: Instruction Manual.
- Rawlinson, N., Fichtner, A., Sambridge, M., Young, M.K., 2014. Chapter One – Seismic Tomography and the Assessment of Uncertainty. *Adv. Geophys.* 55, 1–76. <https://doi.org/10.1016/bs.agph.2014.08.001>
- Rawlinson, N., Kool, M. de, Sambridge, M., 2006. Seismic wavefront tracking in 3D heterogeneous media: applications with multiple data classes. <http://aseg.org.au/exploration-geophysics>.
- Rawlinson, N., Pozgay, S., Fishwick, S., 2010. Seismic tomography: a window into deep Earth. *Phys. Earth Planet. Inter.* 178, 101–135.
- Rawlinson, N., Sambridge, M., 2003. Seismic traveltome tomography of the crust and lithosphere. *Adv. Geophys.* 46, 81–199.
- Rawlinson, N., Spakman, W., 2016. On the use of sensitivity tests in seismic tomography. *Geophys. J. Int.* 205. <https://doi.org/10.1093/gji/ggw084>

- Reinsch, T., Dobson, P., Asanuma, H., Huenges, E., Poletto, F., Sanjuan, B., 2017. Utilizing supercritical geothermal systems: a review of past ventures and ongoing research activities. *Geotherm. Energy* 5, 16. <https://doi.org/10.1186/s40517-017-0075-y>
- Reyes, A.G., 1990. Petrology of Philippine geothermal systems and the application of alteration mineralogy to their assessment. *J. Volcanol. Geotherm. Res.* 43, 279–309. [https://doi.org/10.1016/0377-0273\(90\)90057-M](https://doi.org/10.1016/0377-0273(90)90057-M)
- Ruan, Y., Lei, W., Modrak, R., Örsvuran, R., Bozdağ, E., Tromp, J., 2019. Balancing unevenly distributed data in seismic tomography: a global adjoint tomography example. *Geophys. J. Int.* 219, 1225–1236. <https://doi.org/10.1093/gji/ggz356>
- Sambridge, M.S., 1990. Non-linear arrival time inversion: constraining velocity anomalies by seeking smooth models in 3-D. *Geophys. J. Int.* 102, 653–677. <https://doi.org/10.1111/j.1365-246X.1990.tb04588.x>
- Saxena, V., Krief, M., Adam, L., 2018. *Handbook of Borehole Acoustics and Rock Physics for Reservoir Characterization*.
- Sayers, C.M., Den Boer, L.D., 2018. The Elastic Properties of Clay in Shales. *Wiley Online Libr.* 123, 5965–5974. <https://doi.org/10.1029/2018JB015600>
- Schlumberger, 2014. DSI Dipole Shear Sonic Imager [WWW Document]. URL <https://www.slb.com/-/media/files/fe/product-sheet/dsi-ps.ashx>
- Schön, J., 2015. *Physical properties of rocks : fundamentals and principles of petrophysics*, Second Edi. ed.
- Schulz, B., Sandmann, D., Gilbricht, S., 2020. SEM-Based Automated Mineralogy and its Application in Geo-and Material Sciences. *Minerals* 10, 1004.
- Scott, S.W., Driesner, T., 2018. Permeability Changes Resulting from Quartz Precipitation and Dissolution around Upper Crustal Intrusions. *Geofluids* 2018, 1–19. <https://doi.org/10.1155/2018/6957306>
- Sewell, S., Addison, S., Hernandez, D., Azwar, L., Barnes, M., 2015. Rotokawa Conceptual Model Update 5 years After Commissioning of the 138 MWe NAP Plant, in: *Proc. NZ Geothermal Workshop*.
- Sewell, S., Savage, M.K., Townend, J., Bannister, S., Hutchings, L., 2017. Preliminary

- investigation of seismic velocity variation at the Rotokawa and Ngatamariki Geothermal Fields, in: Geothermal Resources Council Transactions.
- Sewell, S M, Cumming, W., Bardsley, C.J., Winick, J., Quinao, J., Wallis, I.C., Sherburn, S., Bourguignon, S., 2015. Interpretation of microseismicity at the Rotokawa Geothermal Field, 2008 to 2012, in: World Geothermal Congress 2015. p. 25.
- Sherburn, S., Bannister, S., Bibby, H., 2003. Seismic velocity structure of the central Taupo Volcanic Zone, New Zealand, from local earthquake tomography. *J. Volcanol. Geotherm. Res.* 122, 69–88. [https://doi.org/10.1016/S0377-0273\(02\)00470-5](https://doi.org/10.1016/S0377-0273(02)00470-5)
- Sherburn, S., Sewell, S.M., Bourguignon, S., Cumming, W., Bannister, S., Bardsley, C., Winick, J., Quinao, J., Wallis, I.C., 2015. Microseismicity at Rotokawa geothermal field, New Zealand, 2008–2012. *Geothermics* 54, 23–34. <https://doi.org/10.1016/j.geothermics.2014.11.001>
- Sherburn, S., White, R.S., 2005. Crustal seismicity in Taranaki, New Zealand using accurate hypocentres from a dense network. *Geophys. J. Int.* <https://doi.org/10.1111/j.1365-246X.2005.02667.x>
- Sherburn, S., White, R.S., Chadwick, M., 2006. Three-dimensional tomographic imaging of the Taranaki volcanoes, New Zealand. *Geophys. J. Int.* 166, 957–969. <https://doi.org/10.1111/j.1365-246X.2006.03040.x>
- Simpson, M.P., Gazley, M.F., Stuart, A.G.J., Pearce, M.A., Birchall, R., Chappell, D., Christie, A.B., Stevens, M.R., 2019. Hydrothermal Alteration at the Karangahake Epithermal Au-Ag Deposit, Hauraki Goldfield, New Zealand. *Econ. Geol.* 114, 243–273. <https://doi.org/10.5382/econgeo.2019.4630>
- Simpson, M.P., Mauk, J.L., 2000. Geochemistry of wall rock alteration at the Golden Cross deposit, New Zealand: New Zealand Minerals and Mining Conference, 2000, in: Proceedings. pp. 197–208.
- Simpson, M.P., Mauk, J.L., Castendyk, D.N., 2003. Geochemistry of wall rock alteration at the Waihi and Favona epithermal deposits, New Zealand, in: Proceedings of New Zealand Branch of the Australasian Institute of Mining and Metallurgy 36th Annual Conference. p. 270.
- Siratovich, P., Heap, M., Villeneuve, M., Cole, J., Reuschlé, T., 2014. Physical property

- relationships of the Rotokawa Andesite, a significant geothermal reservoir rock in the Taupo Volcanic Zone, New Zealand. *Geotherm. Energy* 2, 31. <https://doi.org/10.1186/s40517-014-0010-4>
- Siratovich, P.A., von Aulock, F.W., Lavallée, Y., Cole, J.W., Kennedy, B.M., Villeneuve, M.C., 2015. Thermoelastic properties of the Rotokawa Andesite: A geothermal reservoir constraint. *J. Volcanol. Geotherm. Res.* 301, 1–13. <https://doi.org/10.1016/j.jvolgeores.2015.05.003>
- Soyer, W., Mackie, R., Hallinan, S., Pavesi, A., Nordquist, G., Suminar, A., Intani, R., Nelson, C., 2017. Multi-physics imaging of the Darajat field. *GRC Trans.* 41.
- Stagpoole, V., 1994. Interpretation of refraction seismic and gravity data across the eastern margin of the Taupo Volcanic Zone, New Zealand. *Geothermics* 23, 501–510. [https://doi.org/10.1016/0375-6505\(94\)90015-9](https://doi.org/10.1016/0375-6505(94)90015-9)
- Stagpoole, V., Miller, C., Caratori Tontini, F., Brakenrig, T., Macdonald, N., 2020. A two million-year history of rifting and caldera volcanism imprinted in new gravity anomaly compilation of the Taupō Volcanic Zone, New Zealand. *New Zeal. J. Geol. Geophys.* 1–14. <https://doi.org/10.1080/00288306.2020.1848882>
- Stern, T., Benson, A., 2011. Wide-angle seismic imaging beneath an andesitic arc: Central North Island, New Zealand. *J. Geophys. Res. Solid Earth* 116. <https://doi.org/10.1029/2011JB008337>
- Stimac, J., Ganefianto, N., Baroek, M., Sihotang, M., Ramadhan, I., Mussofan, W., Sidik, R., Alfiady, Dyaksa, D.A., Azis, H., Putra, A.P., Martikno, R., Irsamukhti, R., Santana, S., Matsuda, K., Hatanaka, H., Soeda, Y., Cariou, L., Egermann, P., 2019. An overview of the Muara Laboh geothermal system, Sumatra. *Geothermics* 82, 150–167. <https://doi.org/10.1016/j.geothermics.2019.05.008>
- Stimac, J., Goff, F., Goff, C.J., 2015. Intrusion-Related Geothermal Systems, in: *The Encyclopedia of Volcanoes*. Elsevier, pp. 799–822. <https://doi.org/10.1016/b978-0-12-385938-9.00046-8>
- Streck, M.J., Grunder, A.L., 1995. Crystallization and welding variations in a widespread ignimbrite sheet; the Rattlesnake Tuff, eastern Oregon, USA. *Bull. Volcanol.* 57, 151–169. <https://doi.org/10.1007/BF00265035>

- Taylor, J.C., Clapp, R.A., 1991. New Features and Advanced Applications of Siroquant: A Personal Computer XRD Full Profile Quantitative Analysis Software Package. *Adv. X-Ray Anal.* 35, 49–55. <https://doi.org/10.1154/S037603080000865X>
- Thurber, C., Eberhart-Phillips, D., 1999. Local earthquake tomography with flexible gridding. *Comput. Geosci.* 25, 809–818. [https://doi.org/10.1016/S0098-3004\(99\)00007-2](https://doi.org/10.1016/S0098-3004(99)00007-2)
- Thurber, C., Ritsema, J., 2007. Theory and Observations – Seismic Tomography and Inverse Methods, in: *Treatise on Geophysics*. Elsevier, pp. 323–360. <https://doi.org/10.1016/B978-044452748-6.00009-2>
- Thurber, C.H., 1983. Earthquake locations and three-dimensional crustal structure in the Coyote Lake Area, central California. *J. Geophys. Res.* 88, 8226. <https://doi.org/10.1029/JB088iB10p08226>
- Tosaya, C., Nur, A., 1982. Effects of diagenesis and clays on compressional velocities in rocks. *Geophys. Res. Lett.* 9, 5–8. <https://doi.org/10.1029/GL009i001p00005>
- Tosdal, R.M., Dilles, J.H., Cooke, D.R., 2009. From source to sinks in auriferous magmatic-hydrothermal porphyry and epithermal deposits. *Elements* 5, 289–295. <https://doi.org/10.2113/gselements.5.5.289>
- Um, J., Thurber, C., 1987. A fast algorithm for two-point seismic ray tracing. *Bull. Seismol. Soc. Am.* 77, 972–986.
- Ussher, G., Harvey, C., Johnstone, R., Anderson, E., 2000. Understanding the resistivities observed in geothermal systems, in: *Proceedings World Geothermal Congress*. Kyushu, pp. 1915–1920.
- Vanorio, T., De Matteis, R., Zollo, A., Batini, F., Fiordelisi, A., Ciulli, B., 2004. The deep structure of the Larderello-Travale geothermal field from 3D microearthquake travelttime tomography. *Geophys. Res. Lett.* 31, n/a-n/a. <https://doi.org/10.1029/2004GL019432>
- Vanorio, T., Prasad, M., Nur, A., 2003. Elastic properties of dry clay mineral aggregates, suspensions and sandstones. *Geophys. J. Int.* 155, 319–326. <https://doi.org/10.1046/j.1365-246X.2003.02046.x>
- Vernon, R.H., Flood, R.H., D’Arcy, W.F., 1987. Sillimanite and andalusite produced by base-cation leaching and contact metamorphism of felsic igneous rocks. *J. Metamorph. Geol.* 5, 439–450. <https://doi.org/10.1111/j.1525-1314.1987.tb00395.x>

- Violay, M., Heap, M.J., Acosta, M., Madonna, C., 2017. Porosity evolution at the brittle-ductile transition in the continental crust: Implications for deep hydro-geothermal circulation. *Sci. Rep.* 7, 7705. <https://doi.org/10.1038/s41598-017-08108-5>
- Waldhauser, F., Ellsworth, W., 2000. A double-difference earthquake location algorithm: Method and application to the northern Hayward fault, California. *Bull. Seismol. Soc.*
- Wallis, I., Bardsley, C., Powell, T., Rowland, J. V., O'Brien, J., 2013. A Structural Model for the Rotokawa Geothermal Field, New Zealand, in: *New Zealand Geothermal Conference 2013*.
- Wallis, I., McCormick, S., Sewell, S., Boseley, C., 2012. Formation assessment in geothermal using wireline tools-application and early results from the Ngatamariki Geothermal Field, New Zealand, in: *Proceedings of the New Zealand Geothermal Conference 2012*.
- Wang, Z., 2001. Fundamentals of seismic rock physics. *Geophysics* 66, 398–412.
- Wang, Z., Dilmore, R.M., Harbert, W., 2020. Inferring CO₂ saturation from synthetic surface seismic and downhole monitoring data using machine learning for leakage detection at CO₂ sequestration sites. *Int. J. Greenh. Gas Control* 100, 103115. <https://doi.org/10.1016/j.ijggc.2020.103115>
- Watanabe, N., Numakura, T., Sakaguchi, K., Saishu, H., Okamoto, A., Ingebritsen, S.E., Tsuchiya, N., 2017. Potentially exploitable supercritical geothermal resources in the ductile crust. *Nat. Geosci.* 10, 140–144. <https://doi.org/10.1038/ngeo2879>
- Watanabe, N., Saito, K., Okamoto, A., Nakamura, K., Ishibashi, T., Saishu, H., Komai, T., Tsuchiya, N., 2020. Stabilizing and enhancing permeability for sustainable and profitable energy extraction from superhot geothermal environments. *Appl. Energy* 260, 114306. <https://doi.org/10.1016/J.APENERGY.2019.114306>
- Watton, T.J., Cannon, S., Brown, R.J., Jerram, D.A., Waichel, B.L., 2014. Using formation micro-imaging, wireline logs and onshore analogues to distinguish volcanic lithofacies in boreholes: Examples from Palaeogene successions in the Faroe-Shetland Basin, NE Atlantic. *Geol. Soc. Spec. Publ.* 397, 173–192. <https://doi.org/10.1144/SP397.7>
- White, S.P., Mroczek, E.K., 1998. Permeability Changes During the Evolution of a Geothermal Field Due to the Dissolution and Precipitation of Quartz. *Transp. Porous Media* 33, 81–101. <https://doi.org/10.1023/A:1006541526010>

- Wiles, D.B., Young, R.A., IUCr, 1981. A new computer program for Rietveld analysis of X-ray powder diffraction patterns. urn:issn:0021-8898 14, 149–151. <https://doi.org/10.1107/S0021889881008996>
- Williamson, P.R., 1991. A guide to the limits of resolution imposed by scattering in ray tomography. *Geophysics* 56, 202–207. <https://doi.org/10.1190/1.1443032>
- Williamson, P.R., Worthington, M.H., 1993. Resolution limits in ray tomography due to wave behavior: Numerical experiments. *GEOPHYSICS* 58, 727–735. <https://doi.org/10.1190/1.1443457>
- Wilson, C., Houghton, B., McWilliams, M., Lanphere, M., Weaver, S., Briggs, R., 1995. Volcanic and structural evolution of Taupo Volcanic Zone, New Zealand: a review. *J. Volcanol. Geotherm. Res.* 68, 1–28. [https://doi.org/10.1016/0377-0273\(95\)00006-G](https://doi.org/10.1016/0377-0273(95)00006-G)
- Wilson, C.J.N., Rowland, J. V., 2016. The volcanic, magmatic and tectonic setting of the Taupo Volcanic Zone, New Zealand, reviewed from a geothermal perspective. *Geothermics* 59, 168–187. <https://doi.org/10.1016/j.geothermics.2015.06.013>
- Winick, J., Siega, F., Addison, S., Richardson, I., 2015. Coupled Iodine-125 and 2NSA Reservoir Tracer Testing at the Rotokawa Geothermal Field, New Zealand. . *World Geotherm.*
- Wyering, L.D., Villeneuve, M.C., Wallis, I.C., Siratovich, P.A., Kennedy, B.M., Gravley, D.M., Cant, J.L., 2014. Mechanical and physical properties of hydrothermally altered rocks, Taupo Volcanic Zone, New Zealand. *J. Volcanol. Geotherm. Res.* 288, 76–93. <https://doi.org/http://dx.doi.org/10.1016/j.jvolgeores.2014.10.008>
- Wyllie, M., Gregory, A., Gardner, L., 1956. Elastic wave velocities in heterogeneous and porous media. *GEOPHYSICS* 21.
- Xinmin, S., Qiquan, R., Yuanhui, S., Yongjun, W., Lin, Y., Fuli, C., 2010. Fine description and geologic modeling for volcanic gas reservoirs. *Pet. Explor. Dev.* 37, 458–465. [https://doi.org/10.1016/S1876-3804\(10\)60047-X](https://doi.org/10.1016/S1876-3804(10)60047-X)
- Yuan, Y.O., Simons, F.J., Tromp, J., 2016. Double-difference adjoint seismic tomography. *Geophys. J. Int.* 206, 1599–1618. <https://doi.org/10.1093/gji/ggw233>
- Zhang, H., 2003. Double-difference seismic tomography method and its applications.

- Zhang, H., Thurber, C., 2006. Development and Applications of Double-difference Seismic Tomography. *pure Appl. Geophys.* 163, 373–403. <https://doi.org/10.1007/s00024-005-0021-y>
- Zhang, H., Thurber, C.H., 2007. Estimating the model resolution matrix for large seismic tomography problems based on Lanczos bidiagonalization with partial reorthogonalization. *Geophys. J. Int.* 170, 337–345. <https://doi.org/10.1111/j.1365-246X.2007.03418.x>
- Zhang, H., Thurber, C.H., 2003. Double-Difference Tomography: The Method and Its Application to the Hayward Fault, California. *Bull. Seismol. Soc. Am.* 93, 1875–1889. <https://doi.org/10.1785/0120020190>
- Zhang, Q., Lin, G., 2014. Three-dimensional Vp and Vp/Vs models in the Coso geothermal area, California: Seismic characterization of the magmatic system. *J. Geophys. Res. Solid Earth* 119, 4907–4922. <https://doi.org/10.1002/2014JB010992>
- Zhao, D., 2015. *Multiscale Seismic Tomography*.
- Zhu, Y., Liu, E., Martinez, A., Payne, M.A., Harris, C.E., 2011. Understanding geophysical responses of shale-gas plays. *Lead. Edge (Tulsa, OK)* 30, 332–338. <https://doi.org/10.1190/1.3567265>
- Zucca, J.J., Hutchings, L.J., Kasameyer, P.W., 1994. Seismic velocity and attenuation structure of the Geysers geothermal field, California. *Geothermics* 23, 111–126. [https://doi.org/10.1016/0375-6505\(94\)90033-7](https://doi.org/10.1016/0375-6505(94)90033-7)

Appendices

A.1. Expanded array seismic network

Table A1.1. Seismometer information for the first phase of the expanded array deployment. All instruments used ANU's LPR-200 recorders. Co-ordinates are WGS84.

Site	Longitude	Latitude	Date installed	Sensor Type	Sensor Serial	Recorder Serial
SS03	176.1982	-38.5089	1/04/2017	Lennartz 3D-Lite MKII (1 Hz)	F-0351	47
SS04	176.1844	-38.5218	31/03/2017	L28-3D (4.5 Hz)	307	50
SS05	176.1963	-38.5259	31/03/2017	L28-3D (4.5 Hz)	13	215
SS06	176.1707	-38.5285	1/04/2017	L28-3D (4.5 Hz)	315	186
SS07	176.2217	-38.5299	31/03/2017	Lennartz 3D-Lite MKII (1 Hz)	A-039	211
SS08	176.1933	-38.5375	31/03/2017	L28-3D (4.5 Hz)	310	182
SS09	176.1541	-38.538	1/04/2017	Lennartz 3D-Lite MKII (1 Hz)	D0210	208
SS10	176.2076	-38.5401	31/03/2017	L28-3D (4.5 Hz)	5	129
SS11	176.1711	-38.5404	1/04/2017	L28-3D (4.5 Hz)	305	46
SS12	176.2087	-38.5527	31/03/2017	L28-3D (4.5 Hz)	9	103
SS14	176.2109	-38.5645	30/03/2017	L28-3D (4.5 Hz)	24	30
SS15	176.2235	-38.584	29/03/2017	L28-3D (4.5 Hz)	320B	53
SS16	176.2025	-38.5843	31/03/2017	L28-3D (4.5 Hz)	319	150
SS17	176.1701	-38.5856	29/03/2017	Lennartz 3D-Lite MKII (1 Hz)	A-024	171
SS18	176.1827	-38.5908	29/03/2017	L28-3D (4.5 Hz)	1	144
SS19	176.2171	-38.5907	31/03/2017	L28-3D (4.5 Hz)	325	51
SS20	176.198	-38.5955	31/03/2017	L28-3D (4.5 Hz)	6	189
SS21	176.228	-38.5963	29/03/2017	L28-3D (4.5 Hz)	306	227
SS22	176.1862	-38.599	29/03/2017	L28-3D (4.5 Hz)	16	132
SS23	176.1742	-38.5992	30/03/2017	L28-3D (4.5 Hz)	11	42
SS24	176.2149	-38.6032	28/03/2017	L28-3D (4.5 Hz)	304	237
SS25	176.1995	-38.6028	28/03/2017	L28-3D (4.5 Hz)	4	138
SS26	176.171	-38.6091	30/03/2017	L28-3D (4.5 Hz)	320A	31

SS27	176.2101	-38.6166	30/03/2017	L28-3D (4.5 Hz)	323	105
SS28	176.1838	-38.6184	29/03/2017	L28-3D (4.5 Hz)	309	93
SS29	176.2077	-38.6255	30/03/2017	L28-3D (4.5 Hz)	2	198
SS30	176.1802	-38.6295	30/03/2017	Lennartz 3D-Lite MKII (1 Hz)	D-0194	217

Table A1.2. Seismometer information for the second phase of the expanded array deployment. All instruments used ANU's LPR-200 recorders. Co-ordinates are WGS84.

Site	Longitude	Latitude	Date installed	Sensor Type	Sensor Serial	Recorder Serial
SS01	176.1392	-38.4807	12/05/2017	L28-3D (4.5 Hz)	313	193
SS02	176.144	-38.5253	12/05/2017	L28-3D (4.5 Hz)		
SS03	176.1982	-38.5089	1/04/2017	Lennartz 3D-Lite MKII (1 Hz)	F-0351	47
SS04	176.1844	-38.5218	31/03/2017	L28-3D (4.5 Hz)	307	50
SS07	176.2217	-38.5299	31/03/2017	Lennartz 3D-Lite MKII (1 Hz)	A-039	211
SS08	176.1933	-38.5375	31/03/2017	L28-3D (4.5 Hz)	310	182
SS09	176.1541	-38.538	1/04/2017	Lennartz 3D-Lite MKII (1 Hz)	D0210	208
SS10	176.2076	-38.5401	31/03/2017	L28-3D (4.5 Hz)	5	129
SS11	176.1711	-38.5404	1/04/2017	L28-3D (4.5 Hz)	305	46
SS12	176.2087	-38.5527	31/03/2017	L28-3D (4.5 Hz)	9	103
SS15	176.2235	-38.584	29/03/2017	L28-3D (4.5 Hz)	320B	53
SS16	176.2025	-38.5843	31/03/2017	L28-3D (4.5 Hz)	319	150
SS18	176.1827	-38.5908	29/03/2017	L28-3D (4.5 Hz)	1	144
SS20	176.198	-38.5955	31/03/2017	L28-3D (4.5 Hz)	6	189
SS21	176.228	-38.5963	29/03/2017	L28-3D (4.5 Hz)	306	227
SS22	176.1862	-38.599	29/03/2017	L28-3D (4.5 Hz)	16	132
SS25	176.1995	-38.6028	28/03/2017	L28-3D (4.5 Hz)	4	138
SS26	176.171	-38.6091	30/03/2017	L28-3D (4.5 Hz)	320A	31
SS27	176.2101	-38.6166	30/03/2017	L28-3D (4.5 Hz)	323	105
SS28	176.1838	-38.6184	29/03/2017	L28-3D (4.5 Hz)	309	93

SS30	176.1802	-38.6295	30/03/2017	Lennartz 3D-Lite MKII (1 Hz)	D-0194	217
SS31	176.1999	-38.4888	13/12/2017	L28-3D (4.5 Hz)	2	198
SS32	176.1166	-38.5075	13/12/2017	L28-3D (4.5 Hz)	325	51
SS33	176.2613	-38.5157	14/12/2017	L28-3D (4.5 Hz)	315	186
SS34	176.1117	-38.5408	15/12/2017	L28-3D (4.5 Hz)	13	215
SS35	176.2733	-38.5555	14/12/2017	L28-3D (4.5 Hz)	A-024	171
SS36	176.1178	-38.5787	15/12/2017	L28-3D (4.5 Hz)	24	30
SS37	176.2864	-38.6135	12/12/2017	L28-3D (4.5 Hz)	304	237
SS38	176.2399	-38.645	12/12/2017	L28-3D (4.5 Hz)	11	42

Table A1.3. Seismometers owned by Mercury. NS12, NS13 and NS14 are downhole instruments installed in groundwater monitoring wells.

Station	Longitude	Latitude	Elevation	Sensor Type	Start_date
NS01	176.177	-38.5082	349	GS-11D (4.5 Hz)	29/08/2012
NS03	176.2091	-38.5233	327	GS-11D (4.5 Hz)	16/05/2012
NS04	176.2257	-38.5425	345	GS-11D (4.5 Hz)	15/05/2012
NS07	176.227	-38.5608	345	GS-11D (4.5 Hz)	15/05/2012
NS11	176.1903	-38.5659	409	GS-11D (4.5 Hz)	30/08/2012
NS12	176.1905	-38.5454	-164	IESE F41-15 (15 Hz)	1/02/2013
NS13	176.1851	-38.5532	130	IESE F41-15 (15 Hz)	12/02/2013
NS14	176.1973	-38.566	163	IESE F50-4.5 (4.5 Hz)	1/03/2013
NS15	176.2154	-38.5764	382	GS-11D (4.5 Hz)	1/05/2015
NS16	176.162	-38.5751	450	GS-11D (4.5 Hz)	23/04/2015
NS18	176.1852	-38.5307	348	GS-11D (4.5 Hz)	23/04/2015
RT01	176.1721	-38.6226	371	GS-11D (4.5 Hz)	2/07/2008
RT05	176.196	-38.6318	369	GS-11D (4.5 Hz)	2/07/2008
RT12	176.2231	-38.6141	400	GS-11D (4.5 Hz)	30/05/2011
RT17	176.2272	-38.6069	342	GS-11D (4.5 Hz)	29/10/2012
RT18	176.189	-38.607	308	GS-11D (4.5 Hz)	14/03/2013
RT19	176.2053	-38.6084	312	GS-11D (4.5 Hz)	15/03/2013
RT21	176.2245	-38.6284	250	GS-11D (4.5 Hz)	28/08/2013
RT22	176.187	-38.5804	423	GS-11D (4.5 Hz)	24/06/2015
RT23	176.1605	-38.6001	447	GS-11D (4.5 Hz)	25/06/2015

Table A1.4. Seismometers used in this thesis that are owned by GNS Science and are part of the GeoNet array. THQ2 is a downhole instrument.

Station	Longitude	Latitude	Elevation	Sensor Type	Start_date
ALRZ	176.343	-38.562	405	L4C-3D (1 Hz)	7/11/2007
ARAZ	176.1201	-38.6277	420	L4C-3D (1 Hz)	20/05/2007
HRRZ	176.2838	-38.3901	590	L4C-3D (1 Hz)	22/03/2007
PRRZ	176.393	-38.4971	392	L4C-3D (1 Hz)	12/11/2007
THQ2	176.1698	-38.6684	370	Duke 4.5 (4.5 Hz)	18/12/2012
WPRZ	176.1624	-38.5196	519	LE-3Dlite MkII (1 Hz)	24/03/2010

A.2 Automatic Data Processing for Local Earthquake Seismic Tomography: Rotokawa and Ngatamariki 2012-2017 Dataset

Introduction

Local earthquake tomography requires accurate determination of seismic phase arrival times. In general, the level of uncertainty in arrival times used for local earthquake tomography will increase the range of potential velocity models that fit the data (Rawlinson et al., 2014). Manual picking of arrivals arguably provides the highest accuracy determination of arrival times, although even experienced analysts can disagree on arrival times and their uncertainties (e.g. Chen and Holland, 2016; Diehl and Kissling, 2009). Manual picking is also time consuming, particularly for large arrays with 10's or 100's of stations. Automated picking techniques have the potential to produce more consistent arrival time picks and greatly reduce the time and effort required by manual picking. However, automated picking techniques are prone to false triggering, particularly for low signal-to-noise ratio arrivals (i.e. small magnitude events in noisy environments). S-wave automated picks are particularly prone to false triggering due to the inherent nature of S-wave arrivals (i.e. secondary arrivals embedded within P-wave energy and the generally lower frequency content of these arrivals). Filtering of bad picks and applying a weighting scheme to picks based on their uncertainty are also important for obtaining accurate hypocentres and high quality tomographic inversions (e.g. Diehl et al., 2009).

To facilitate the analysis of both the existing data at Rotokawa and Ngatamariki (~20 stations, 5 years of data, many thousands of events) and the expanded array data, an automated picking and location procedure was developed. The goal was to obtain arrival times and initial earthquake locations similar to those obtained via manual picking.

The automated processing workflow developed makes use mostly of existing software packages and the Obspy framework. A flow-chart of the general processing steps is shown in Figure A2.1.

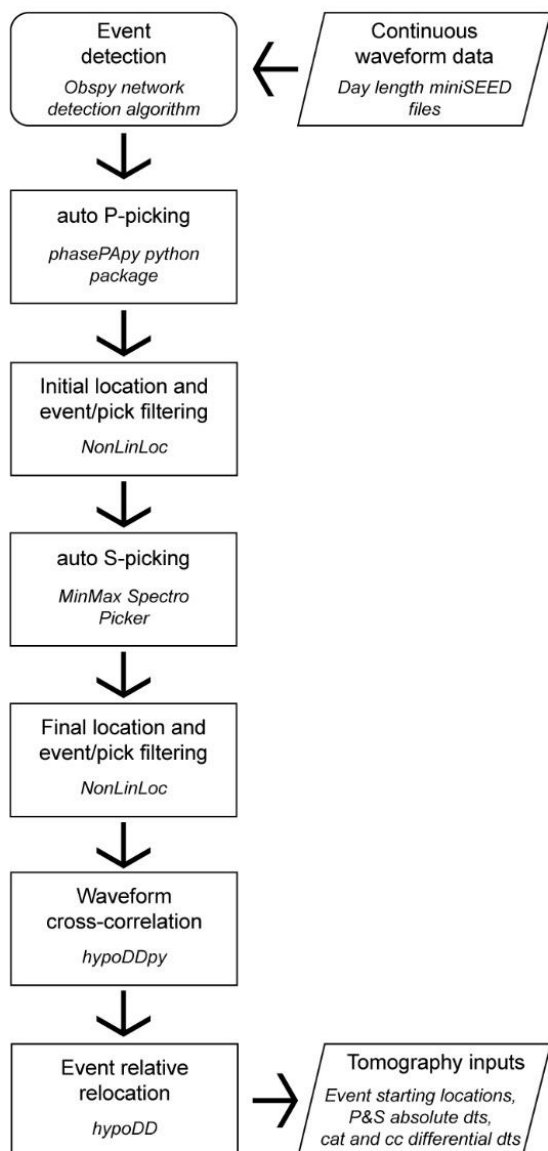


Figure A2.1. A flow chart summarizing the automated processing workflow used for the 2012-2017 dataset.

Rotokawa-Ngatamariki 2012-2017 dataset

A microseismic array that covers both Rotokawa and Ngatamariki has been operating since 2012. Since that time there have been many changes to seismometer locations, however the overall network geometry has been relatively consistent throughout the monitoring period (Figure A2.2).

A set of 124 events from the 2012-2013 period were manually picked which provide a calibration dataset for automatic picking. These events occurred in the three main clusters of seismicity throughout the study area (~50 events at Rotokawa, ~40 for southern Ngatamariki and ~30 for northern Ngatamariki) and are hence representative of the majority of seismic events of interest that occur in the area. The picking procedure of Diehl and Kissling (2009)

was followed for the manual picking that includes making estimates of pick uncertainty (Figure A2.3). These manual picks form the basis for calibrating and assessing the performance of the P and S phase automatic pickers.

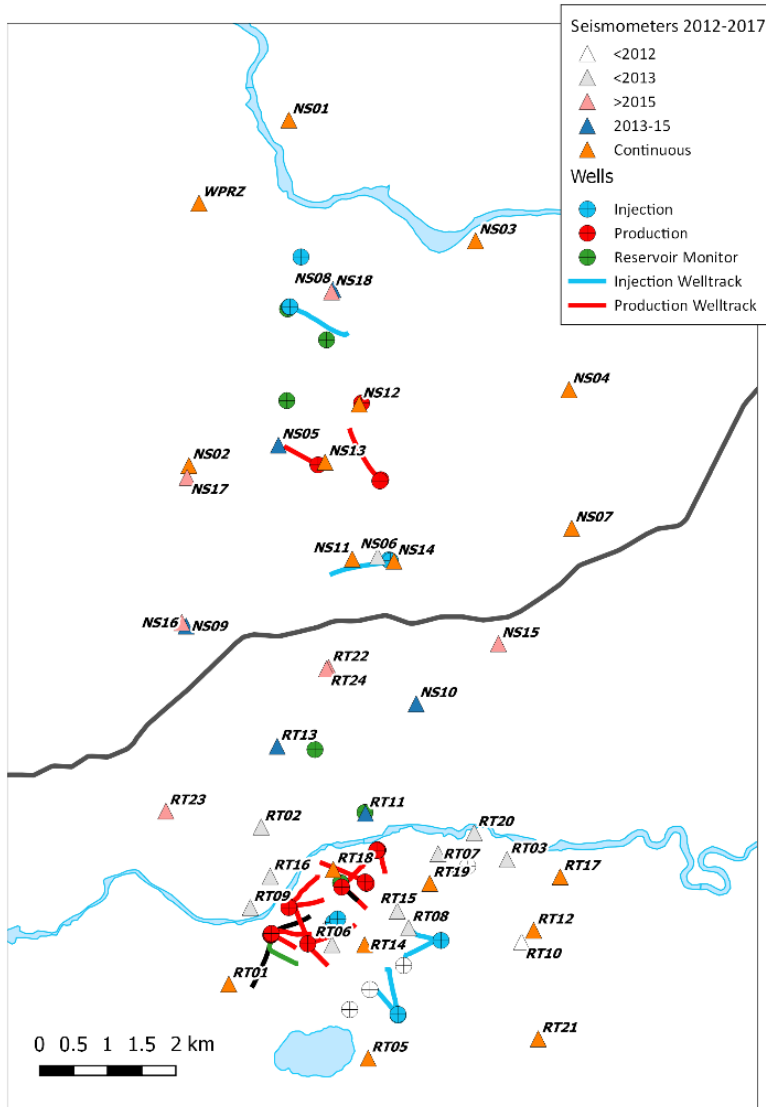


Figure A2.2. The microseismic monitoring network at Rotokawa and Ngatamariki during the 2012-2017 period.

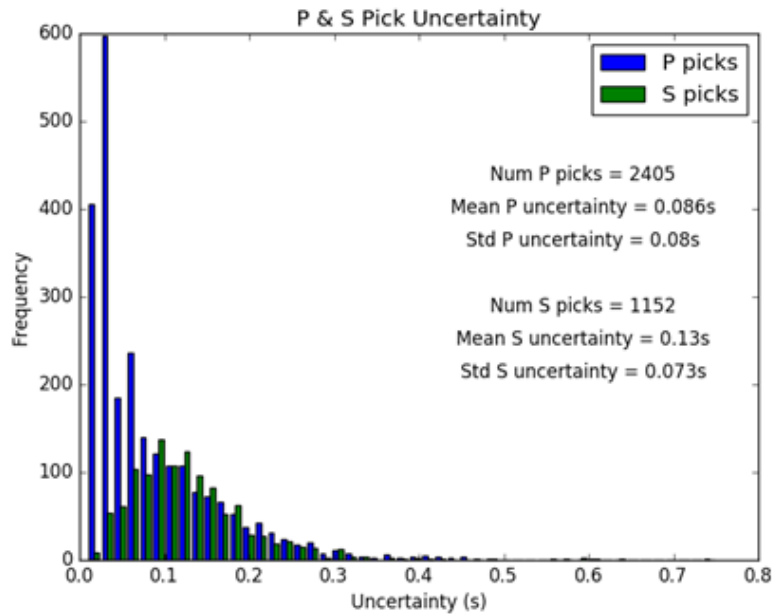


Figure A2.3. Histogram of P and S pick uncertainties determined via manual picking following the procedure outlined by Diehl et al. (2009b).

Network event detection

Event detection was carried out using the ‘Network Coincidence Trigger’ module within Obspy (Beyreuther et al., 2010). This routine works by applying one of several triggering algorithms (e.g. STA/LTA, recursive STA/LTA, Z-detect) to all waveform data provided. It then compiles a chronological list of triggers and finds overlapping single station triggers and calculates a coincidence sum (which is determined according to the weighting applied to each station in the network). If the coincidence sum exceeds a user specified threshold then an event is declared.

The network coincidence trigger implemented for the 2012-2017 dataset used the recursive STA/LTA trigger on all Z-component data from all stations (with STA over 0.5 s, LTA over 5 s, threshold on of 3 and threshold off of 1). Events were only declared if triggers occurred on at least 6 stations across the network. Based on preliminary runs and previous monitoring by GNS Science, Rotokawa is much more seismically active than Ngatamariki. Therefore, to attempt to detect more events at Ngatamariki, the Ngatamariki stations and some northern Rotokawa stations were weighted slightly higher than the Rotokawa stations (1 versus 0.7). 9967 events were detected using this algorithm for the May, 2012 to July, 2017 period.

Automated P picking

Automated P picking was performed using the PhasePapy python package developed by Chen and Holland, (2016). The package contains three separate picking algorithms:

- Akaike Information Criteria (AIC) picker
- Frequency Band (FB) picker
- Kurtosis (KT) picker

Each picker produces a characteristic function (CF) which is then used as the basis for triggering picks. The reader is referred to the paper by Chen and Holland, (2016) for information on how each algorithm computes the characteristic function from a seismic trace. Each of the pickers utilise a dynamic triggering threshold which is determined by multiplying the RMS of the CF in a moving window with a user-defined coefficient. Therefore, using a lower dynamic threshold level can identify a greater number of smaller signal to noise ratio arrivals but will likely cause a greater number of false picks. A high threshold-triggering level will trigger only on high signal to noise ratio arrivals with fewer false picks but will likely miss a greater number of lower signal to noise arrivals. The implementation of a dynamic threshold as opposed to the fixed threshold used by many pickers is intended to minimise false triggering due to transient noise sources (e.g. passing vehicles, wind, etc) (Figure A2.4).

Several user defined parameters are required for each of the pickers. The two main parameters that control when picks are triggered for all three pickers are

- ‘t_ma’ – the time in seconds of the moving average window for the dynamic threshold
- ‘n_sigma’ – which controls the level at which a pick is triggered

In addition to these, the FB picker has additional parameters that control when picks are triggered

- ‘t_long’ – the time in seconds of the moving window over which the characteristic function is calculated for each bandpass filtered data

And the KT picker also has an additional parameter that controls when picks are triggered of

- ‘t_win’ – the time in seconds of the moving window over which the kurtosis characteristic function is calculated

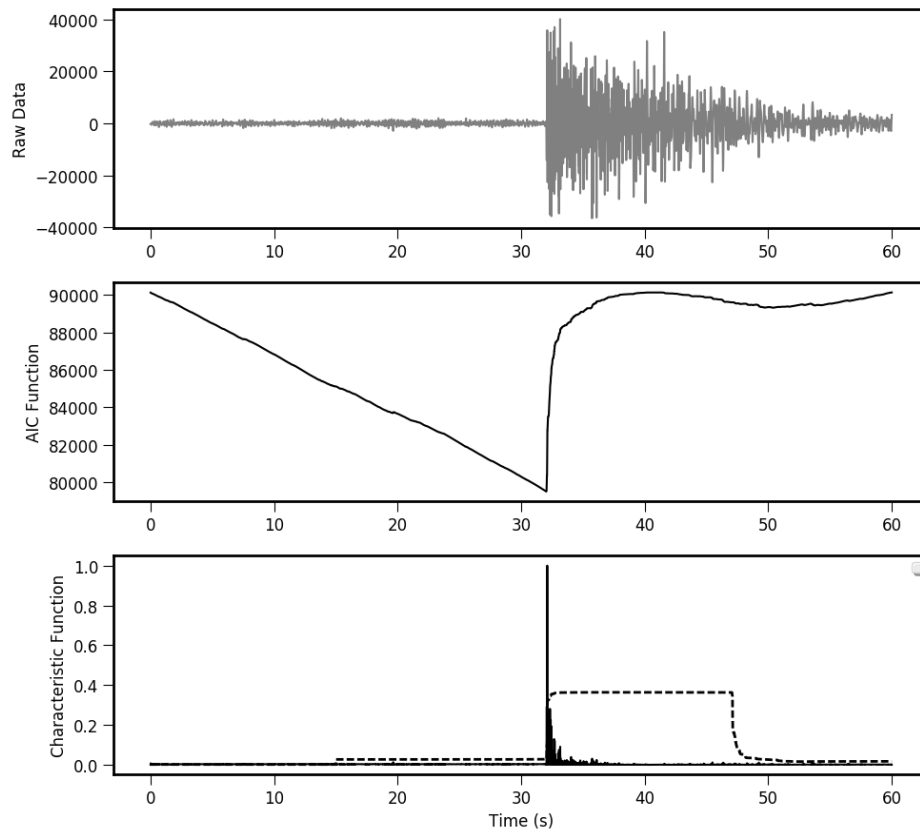


Figure A2.4. Example of the AIC picker for a magnitude 2 event at Ngatamariki. A pick is triggered when the characteristic function (solid line in lowermost panel) exceeds the dynamic threshold (dashed line in lowermost panel).

The usual approach to determining what these parameters should be for a particular dataset involves a trial-and-error approach of manually examining how well the picker performs on individual arrivals for a relatively small number of events and stations. However, due to variations in signal-to-noise ratios, how well particular parameters work can vary between events and stations. This is exacerbated by the generally low magnitudes of the events and high cultural noise environment of the Rotokawa and Ngatamariki area. Therefore, a range of possible parameters were tested for each of the pickers on the manually picked dataset described previously. This then provided a statistical basis for selecting the optimal parameters for each picker.

Each of the pickers outputs a signal-to-noise ratio of the characteristic function (CF-SNR) for each pick made. The CF-SNR of each pick is determined by the ratio of the first local maximum CF after the pick to the RMS of CF in the previous time window. As expected, higher CF-SNR picks show generally better agreement with manual picks (Figure A2.5). This relationship

between CF-SNR and time difference to the manual picks was used to determine a pick weighting scheme for all picks made by each of the pickers (Figure A2.5).

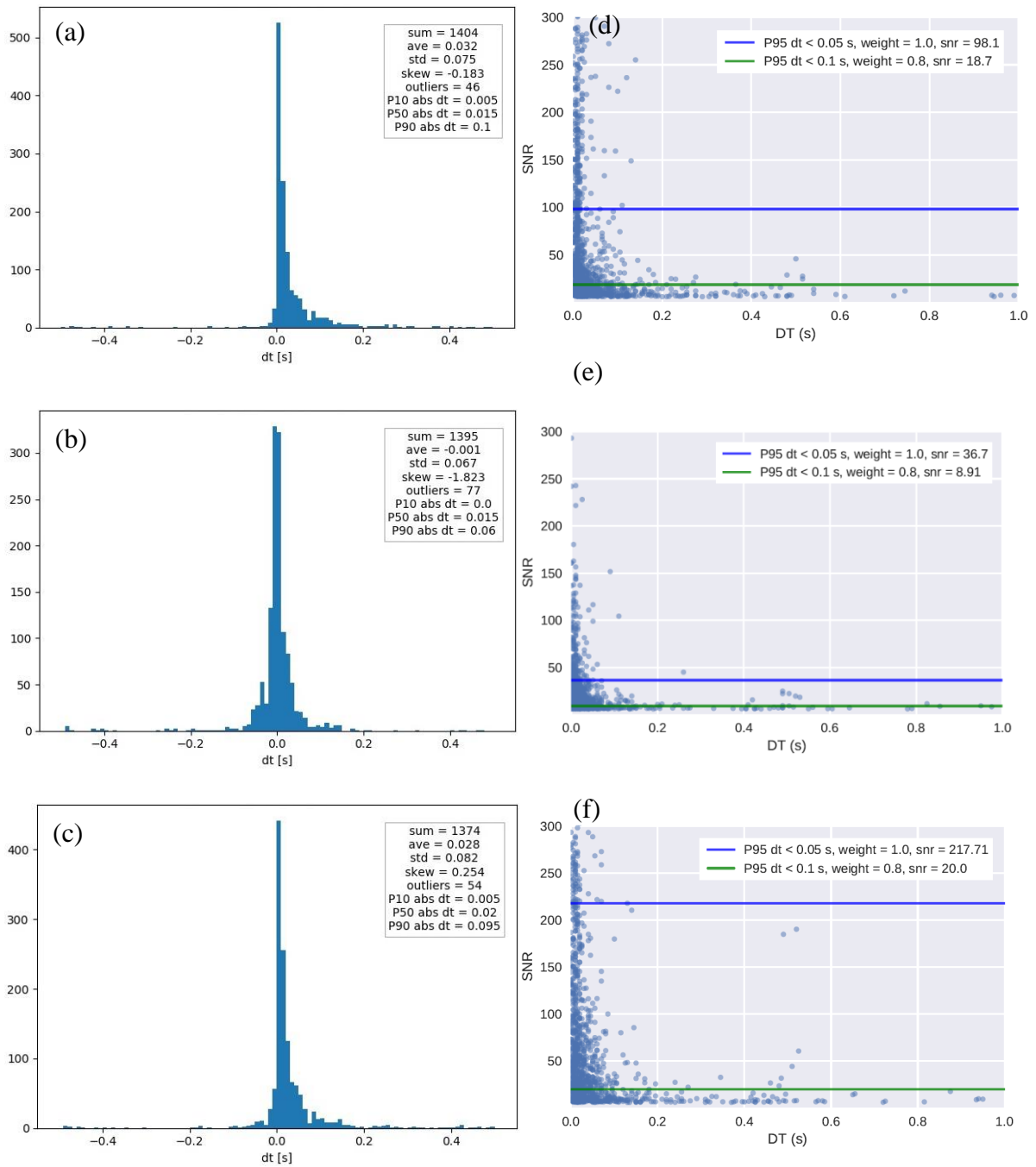


Figure A2.5. Comparison between auto and manual picks ($dt = \text{auto} - \text{manual}$) for the three different P pickers and the absolute dt versus the signal to noise of the picker characteristic functions (SNR). (a) and (d) the AICD picker, (b) and (e) the FB picker and (c) and (f) the KT picker. The relationship between the picker SNR and the absolute dt was used as the basis for assigning pick weights and uncertainties. The blue and green horizontal lines on the dt versus SNR plots show the SNR value at which 95% of the picks above the line have a dt of less than 0.05 s and 0.1 s respectively and were therefore given weights of 1 and 0.8 respectively in subsequent location analysis. All other picks were given weighting of 0.2. Statistics on the performance of each picker relative to the manual picks are shown in the inset of a,b and c. Outliers were defined as picks that with dt greater than 0.5 s and were excluded from the statistics shown. The 10th, 50th and 90th percentile of the absolute dt is shown showing that in all cases 50% of the auto picks are within 0.02 s of the manual pick and 90% of the auto picks are within 0.1 s of the manual pick for each of the three pickers.

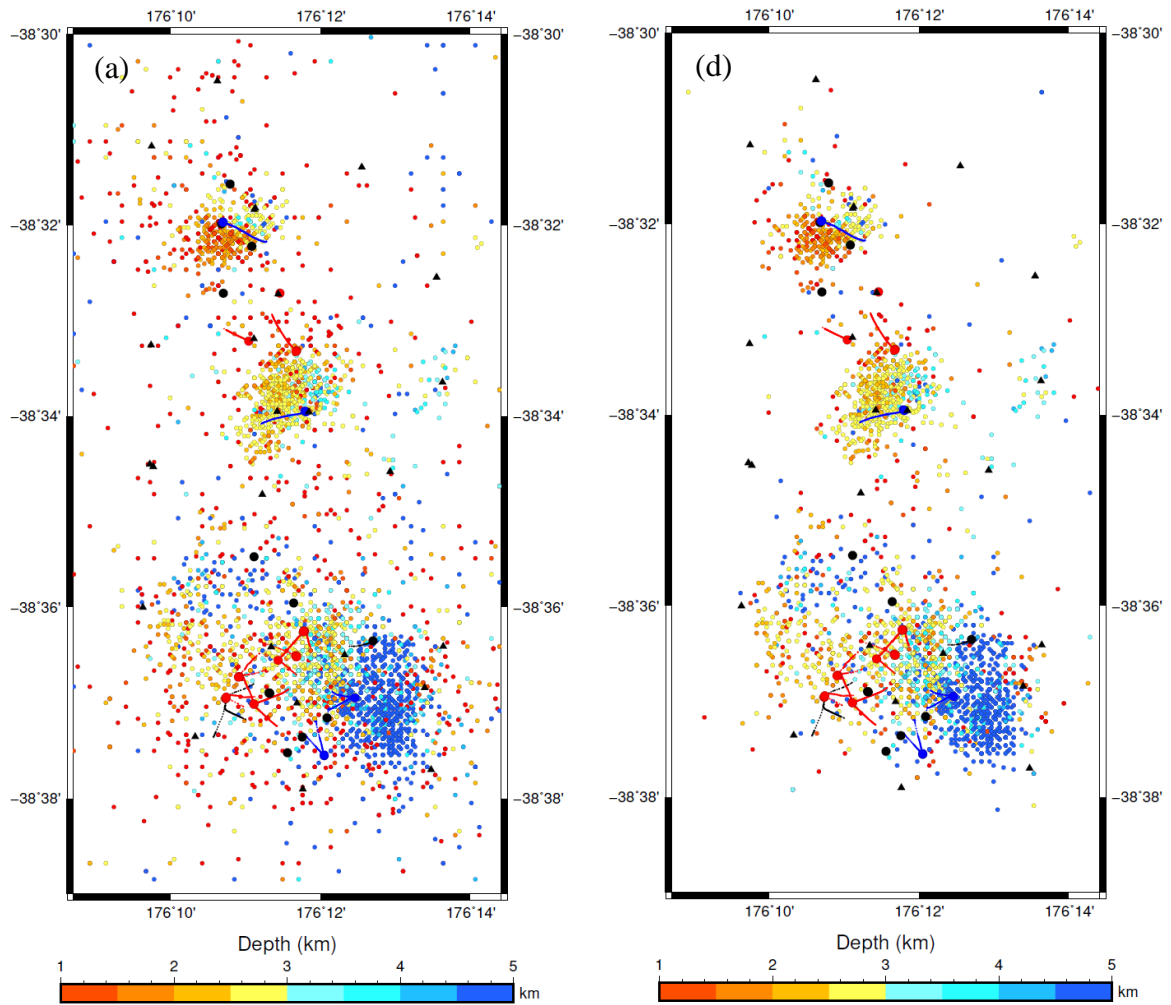
Auto-picking was performed for the 2012-2017 data on 60 s Z-component records centred on the detection time of each events for each station active during the particular event. The highest weighted pick from each of the three pickers was used for the final pick time and weighting. If two or more picks for the same event-station had the same weighting then the pick times were averaged. For a P pick to be declared, at least two out of the three pickers were required to have picks within 0.5 s of each other. Of the 9967 events detected, 8001 events had 6 or more P picks and were therefore considered locatable. Of the 116,292 P picks for these 8001 events, 12,134 (10 %) were given a weight of 1, 65,698 (57 %) were given a weight of 0.8 and 38,460 (33 %) were given a weight of 0.2.

Preliminary event locations using P picks

The NonLinLoc event location algorithm of Lomax et al. (2000) was used to obtain preliminary event locations and to perform QA/QC checks on the automatic P picks. NonLinLoc locates events via a non-linear grid search technique using P and S picks and their uncertainties and produces probability density functions in xyz space for each hypocentre. The maximum likelihood of the PDF is usually taken as the event location if a single location is desired.

The average 1D velocity model from the Monte Carlo VELEST work of Sewell et al. (2017) was used to create the travel time grid for all NonLinLoc runs. Preliminary event locations were then determined using only the automatic P picks and their uncertainties and weights (Figure A2.6). Pick uncertainties were assigned to be gaussian using the uncertainties assigned

via the CF-SNR versus dt analysis (Figure A2.5). The initial run included 116,292 P picks from 8001 events which were then filtered to remove poorly constrained events and picks with very



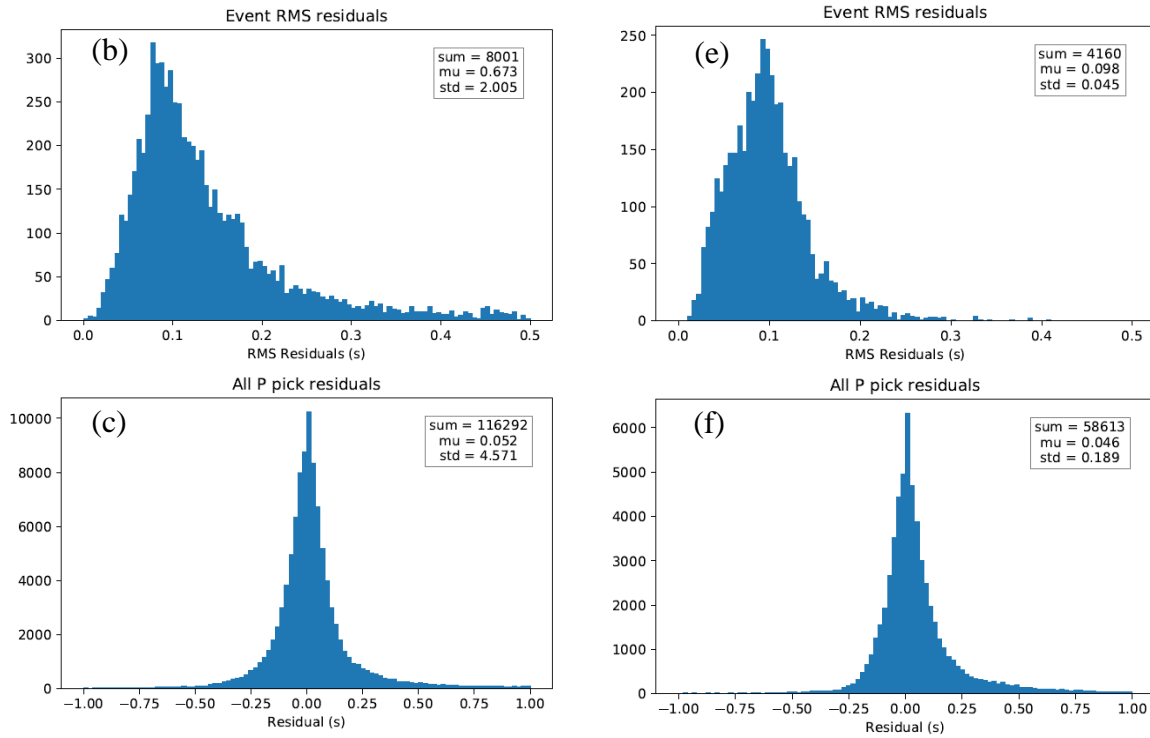


Figure A2.6. Event locations – (a) and (d), event RMS residuals – (b) and (f) and P pick residuals - (c) and (e) before (a, b, c) and after (d, f, e) filtering events and picks. N.B. A large proportion of the removed events were located outside the map area.

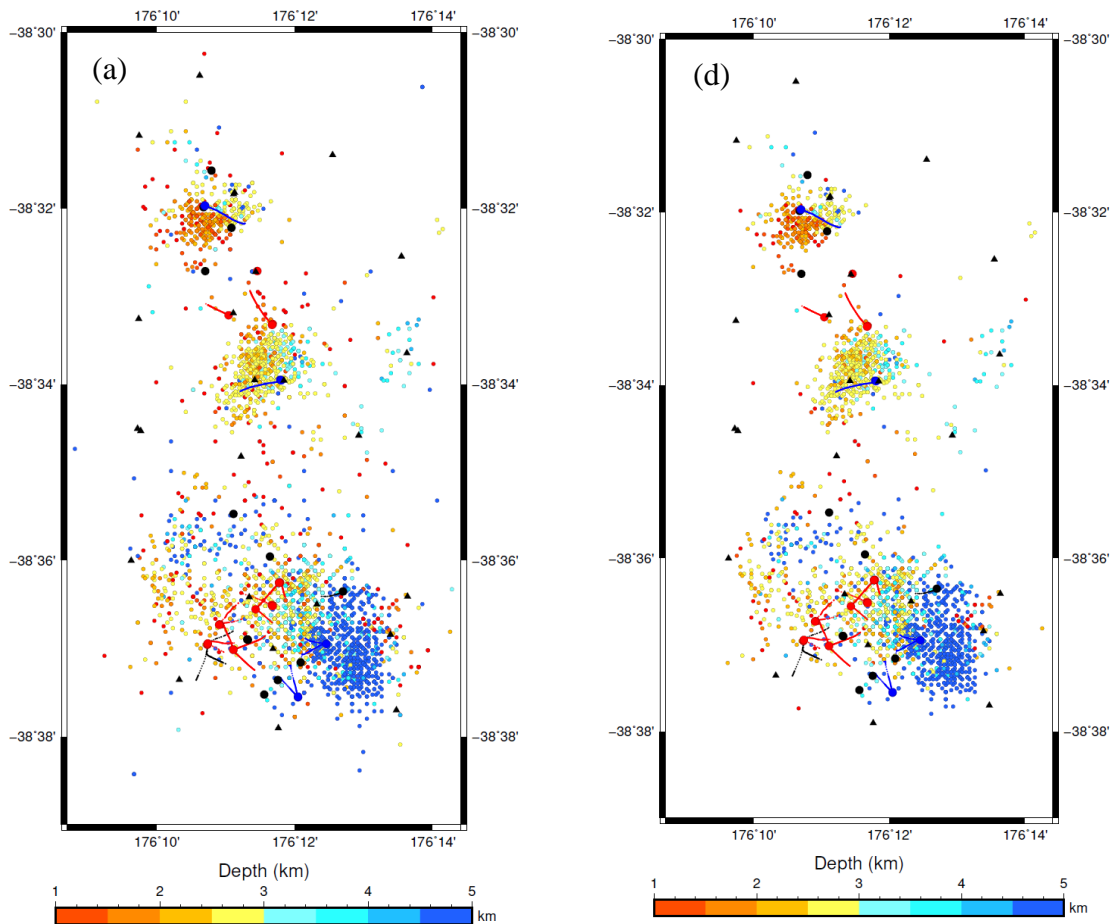
high residuals (Table A2.1). A total of 4160 events were left after event filtering with 58,613 P picks which were re-run in NLLoc (Figure A2.6). Most of the events removed appear to have occurred in the surrounding region, in particular in the adjacent Wairakei Geothermal Field approx. 10 km southwest of Rotokawa.

Table A2.1. Event and pick filters applied to the initial NLLoc run. The filters were applied in succession in order from top to bottom of the table. The percentage of events/picks removed by each filter relative to the input catalog is also shown.

Filter	Events/Picks removed	%age removed
Region filter (remove events outside RK-NM array bounds)	2796	35%
Azimuth gap < 180	462	6%
Event RMS < 1s	516	6%

P pick residual < 1s	4287	0.03%
Events with < 6 P picks	67	0.8%

The distribution of P pick residuals following the initial run exhibited a long positive tail of residuals (Figure A2.6e). A manual review of events during 2014 showed that the vast majority of these are due to late automatic picks on low CF-SNR arrivals. Therefore, picks with low CF-SNR (picks with assigned weights of 0.2) were filtered if their residuals were greater than ± 0.2 s. This removed 5569 of the 58,613 picks ($\sim 1\%$). Re-running these picks in NLLoc had a minor effect on event locations but removed the long positive tail of relatively high residuals resulting in a near gaussian distribution of residuals (Figure A2.7a and A2.7c). It also shifted the distribution on event RMS residuals, showing more clearly a population of high RMS residual outliers (Figure A2.7b). These events were again filtered, mostly to remove the outlier events with relatively high RMS residuals, but also to remove events with less than 8 P picks as these were unlikely to provide well constrained events in the double difference relocation.



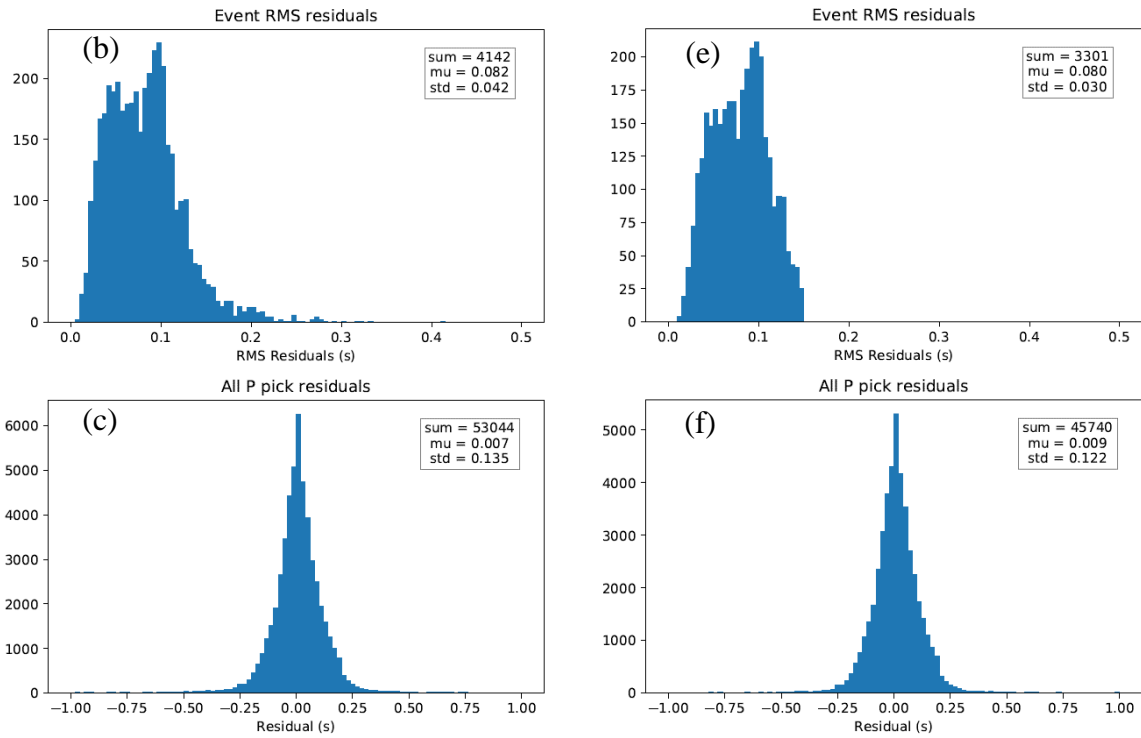


Figure A2.7. Event locations – (a) and (d), event RMS residuals – (b) and (f) and P pick residuals - (c) and (e) before (a, b, c) and after (d, f, e) filtering events and picks.

The filtering resulted in removal of a lot of the apparent scattered events outside the three main clusters of seismicity and approximately gaussian distributions for both the event RMS residuals and P pick residuals.

Table A2.2. Event and pick filters applied to the second NLLoc run. The filters were applied in succession in order from top to bottom of the table. The percentage of events/picks removed by each filter relative to the input catalog is also shown.

Filter	Events/Picks removed	%age removed
Region filter (remove events outside RK-NM array bounds)	13	0.3%
Azimuth gap < 180	171	4%
Event RMS < 0.15s	201	5%
Events with < 8 P picks	547	13%

Automated S picking

Automatic S-wave picking was performed on the event catalog on all stations for which a P pick existed. Event locations determined using only the P picks were used to rotate the three-component seismic data from ZNE co-ordinates to LQT co-ordinates prior to automatic S picking to attempt to improve the signal-to-noise of the S-wave arrival on the transverse (QT) components.

Both the automated S-wave picking of Castellazzi et al. (2015) and application of the phasePapy pickers to S-wave picking were initially trialled with reasonable results. However, neither of these appeared to produce results with a comparable number of S picks per event and similar level of uncertainty to manual picking for S waves (average of 2-3 S picks per event, S to P ratio of ~20% and S uncertainty of ~0.2-0.3 s. Given the importance of determining accurate S-wave arrivals for constraining event depths, for constraining Vp/Vs inversions and constraining possible Vp/Vs variations over time, a new S-wave picking approach was developed. The picker uses two different characteristic functions; one based on a moving window of the absolute value of the maximum minus the minimum amplitude (MinMax Picker), the other on a spectrogram of the data that is stacked for frequencies below a cut-off (Spectro Picker). The picker therefore exploits the main characteristics that typify S-wave arrivals; namely high amplitude and low frequency. The resulting characteristic functions exhibit a step-change for S-wave arrivals of sufficient signal-to-noise. The step change in the characteristic function is then located by comparing the forward average to the backward average of the characteristic function over different moving windows.

S-wave automatic picker

Accurate determination of S-wave arrivals is important for determining accurate microseismic event locations, particularly event depths, and for deriving Vs and Vp/Vs tomographic models (Diehl et al., 2009a; Gomberg et al., 1990). Manual picking of seismic arrivals is generally more accurate than automated approaches however the time taken to perform manual picking is often prohibitive, particularly for large datasets of many thousands of events recorded on many tens of seismometers. Automatic S-wave picking is however difficult due mostly to the inherent nature of the S-arrival as a secondary phase that is superposed on P wave coda (e.g. Diehl et al., 2009a). Most existing automatic S-wave picking approaches have drawn on algorithms that have been successfully applied to P wave picking. However, the S-wave arrival is fundamentally different from the P-wave arrival in a number of ways. For example, noise

prior to the P-wave arrival is generally consistent over time windows of tens of seconds whereas the ‘noise’ (often P-wave coda) prior to the S-wave arrival can often contain amplitude spikes which can cause false triggering of automatic pickers.

S waves are typically characterised by high amplitude, low frequency (~1-10 Hz) transverse motion and the S-wave picking algorithms developed here are designed with this in mind. Two different S wave picking characteristic functions have been developed; one based on the absolute value of the maximum minus the minimum amplitude over a small moving time window (MinMax Picker), the other on a spectrogram of the data that is stacked for frequencies below a cut-off (Spectro Picker). The resulting characteristic functions exhibit a step-change for S-wave arrivals of sufficient signal-to-noise. The step change in the characteristic function is then located by comparing the forward average to the backward average of the characteristic function over different moving time windows.

Pre-processing

Prior to the automated picking, data is rotated from ZNE to LQT co-ordinates. This requires an initial event location accurate enough to define station-event back azimuths and the inclination angle of the arrival to the station. A sufficiently accurate initial location for data rotation can usually be determined from P-wave arrival times from more than 8 stations with an azimuthal gap of less than ~180°. The rotation of data, although not essential to the functioning of the picking algorithms, improves the signal to noise of the S wave arrival. The automatic picking algorithms could be applied to horizontal components in the ZNE co-ordinate system.

MinMax amplitude picker

The basis of the MinMax picker is finding the time when the change in transverse motion is greatest. The absolute difference between the maximum and minimum amplitude is calculated for a small, user-defined time window (Figure A2.8). This is then normalised to the maximum value so that all values fall between 0 and 1. As the S-wave arrival is often associated with large-amplitude movement on the transverse components it will typically be associated with a step-change in the normalised min-max function. The step change in the characteristic function is then located by comparing the forward average to the backward average of the characteristic function over different moving time windows.

Spectrogram picker

The min-max picker works well for S-wave arrivals characterised by sharp changes in amplitude (Figure A2.9). However, often S-wave arrivals are more emergent with the largest change in amplitude occurring sometime after the first-arrival. In these cases, the S-wave arrival can often be identified by a change in frequency content of the waveform data. This is often done during manual picking of S-wave data by visual inspection of spectrogram plots. The spectrogram picker works on a similar principle, attempting to automate the process of identifying a change in frequency content of the waveforms.

Signal-to-noise of the characteristic functions

The signal-to-noise ratio of each pickers is calculated as the ratio of the average of the characteristic function (for the MinMax picker the normalised min-max function, for the Spectro picker the normalised stacked spectrogram) over a user-specified time window before and after the S pick. A signal-to-noise cut-off can then be used to exclude S picks with low SNR and/or a SNR weighting scheme can be applied in location programs.

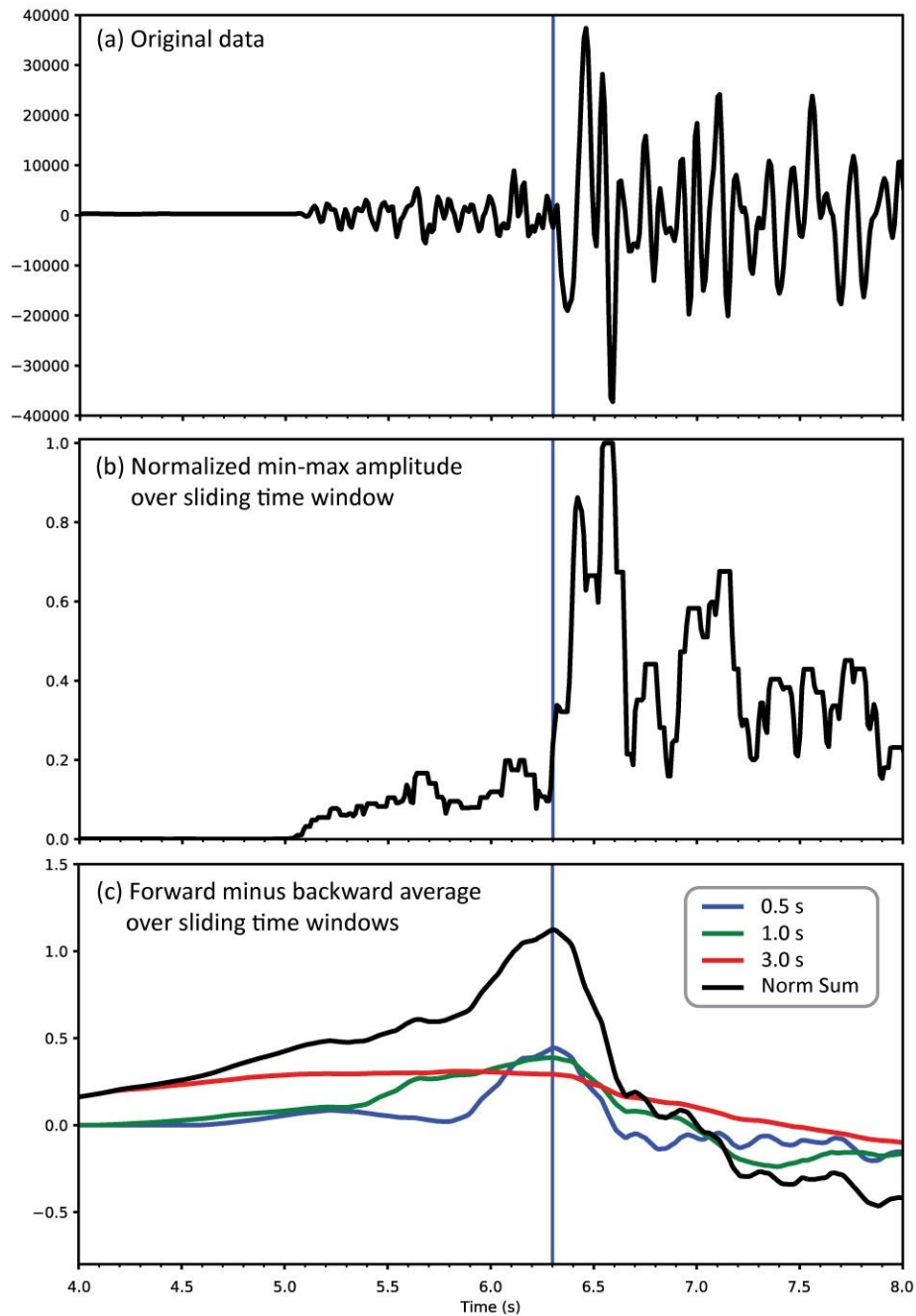


Figure A2.8. Example of the min-max automatic S picking for a good signal-to-noise S arrival. (a) shows the original data (the T channel of the rotated 3-component data), (b) shows the normalised maximum minus minimum amplitude over a sliding time window of 0.1s and (c) shows the three forward minus backward averages of the normalised min-max amplitude shown in (b) over sliding windows of 0.5, 1.0 and 3.0 seconds. The black line is the summation of the three normalised to the maximum value. The automatic S pick (blue vertical line) is triggered at the maximum value of the normalised sum.

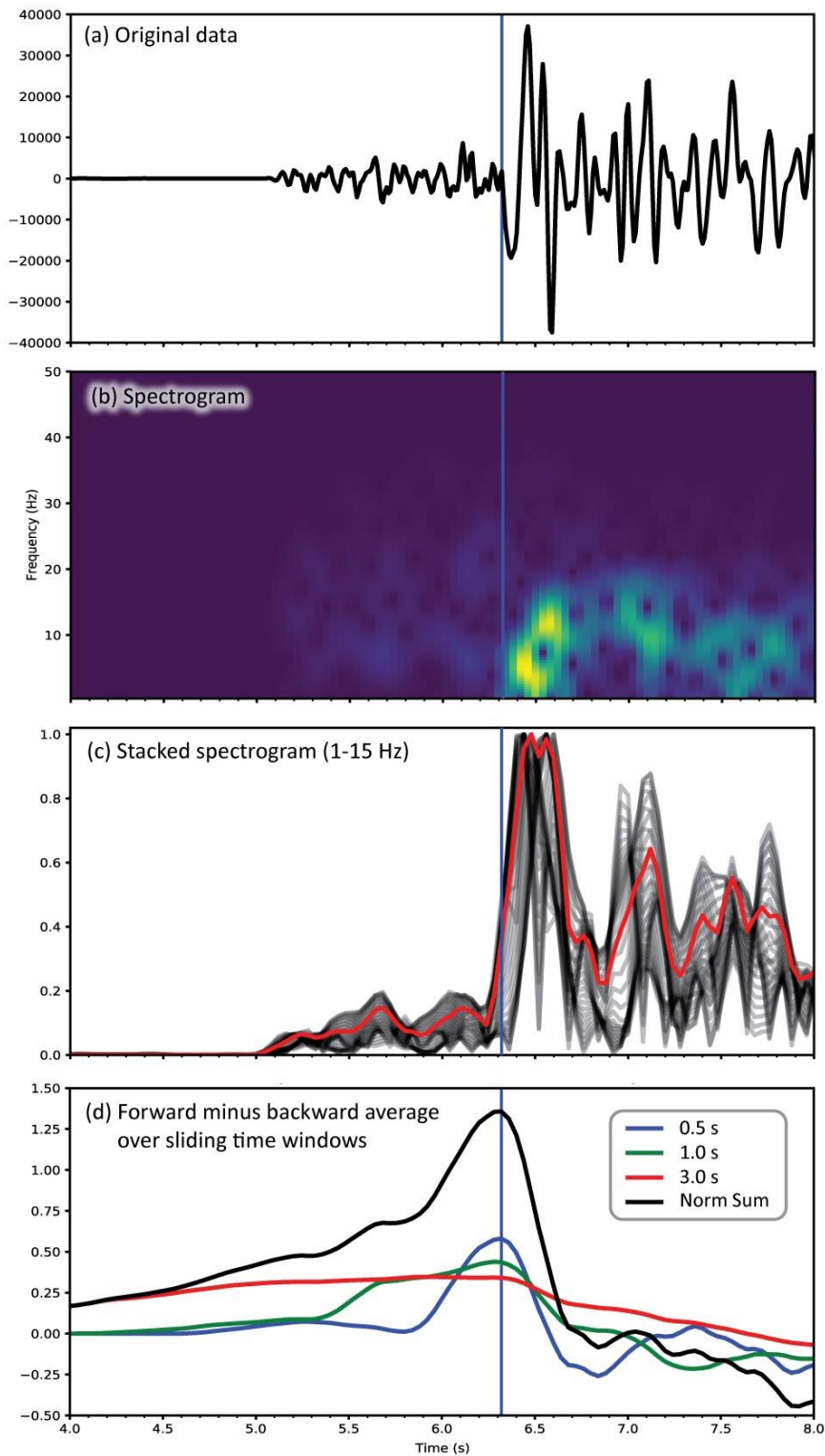


Figure A2.9. Example of the spectro automatic S picking for the same arrival as in Figure A2.8. (a) shows the original data (the T channel of the rotated 3-component data), (b) shows a graphical representation of the spectrogram (c) shows the individual frequency components (grey transparent lines) of the spectrogram normalised to the maximum amplitude for

frequencies between 1 and 15 Hz. The red line shows the summed or stacked individual frequency components normalised to the maximum value. (d) shows the three forward minus backward averages of the stacked frequency components, red line in (c), over sliding windows of 0.5, 1.0 and 3.0 seconds. The black line is the summation of the three normalised to the maximum value. The automatic S pick (blue vertical line) is triggered at the maximum value of the normalised sum.

The main user defined picking parameters for each of the S-wave pickers are;

MinMax Picker

- 'samp_wind' – the time window over which the maximum – minimum amplitude value is calculated
- 'ave_winds' – the time windows over which the running forward average minus backward average is calculated

Spectro Picker

- 'wlen' – the window length over which the fft is performed
- 'ave_winds' – the windows over which the running forward average minus backward average is calculated
- 'freq_high' – the high frequency cut-off (frequencies above this are not included in the calculation of the stacked spectrogram trace)

As with the automatic P picking, the optimal picking parameters for each of the two pickers were determined by trialling a range of different parameters and comparing the automatic picks to all S picks in the manually picked dataset. This then provided a statistical basis for selecting the optimal parameters. The MinMax picker was able to pick 77% of the manual picks with 90% of the picks within 0.265 s of the manual pick (Figure A2.10). The Spectro picker was able to pick 72% of the manual picks with 90% of the picks within 0.2 s of the manual pick (Figure A2.10).

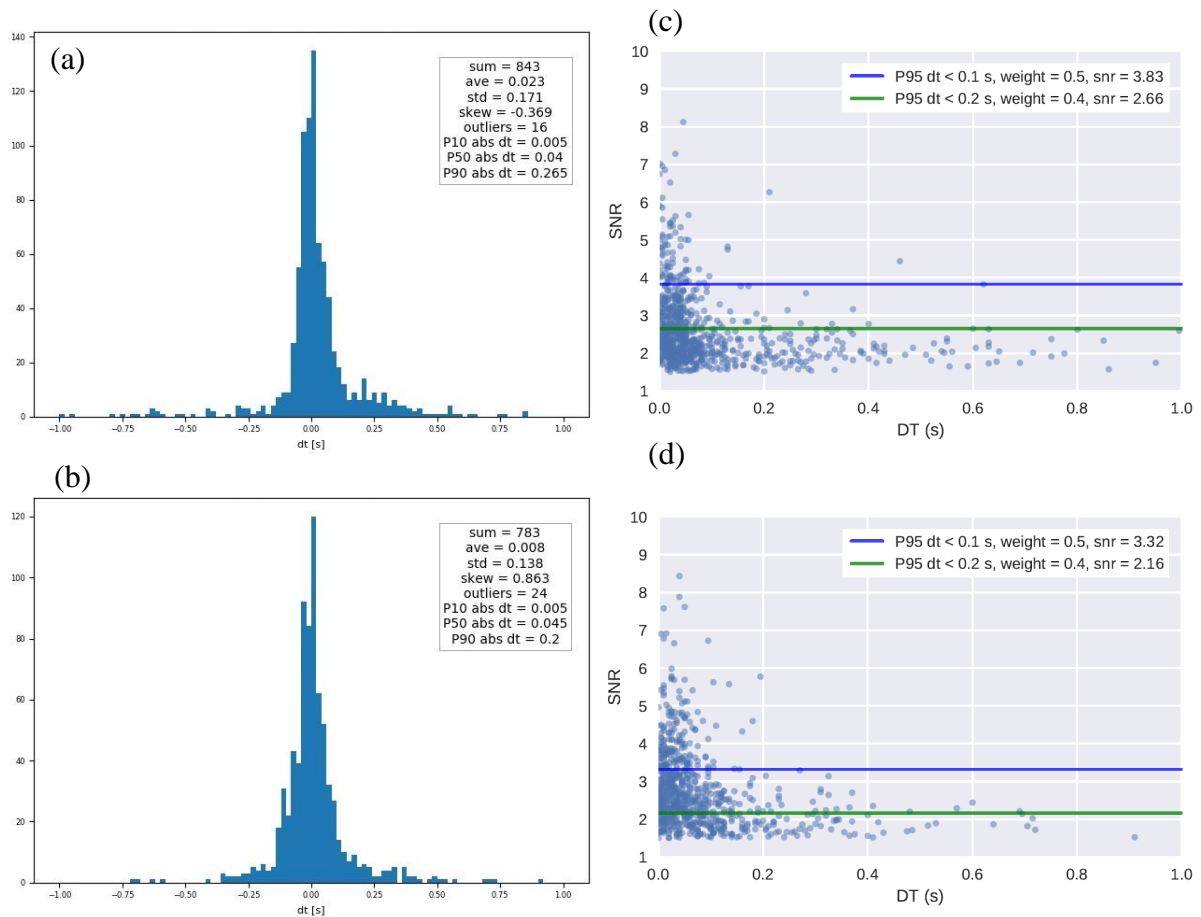


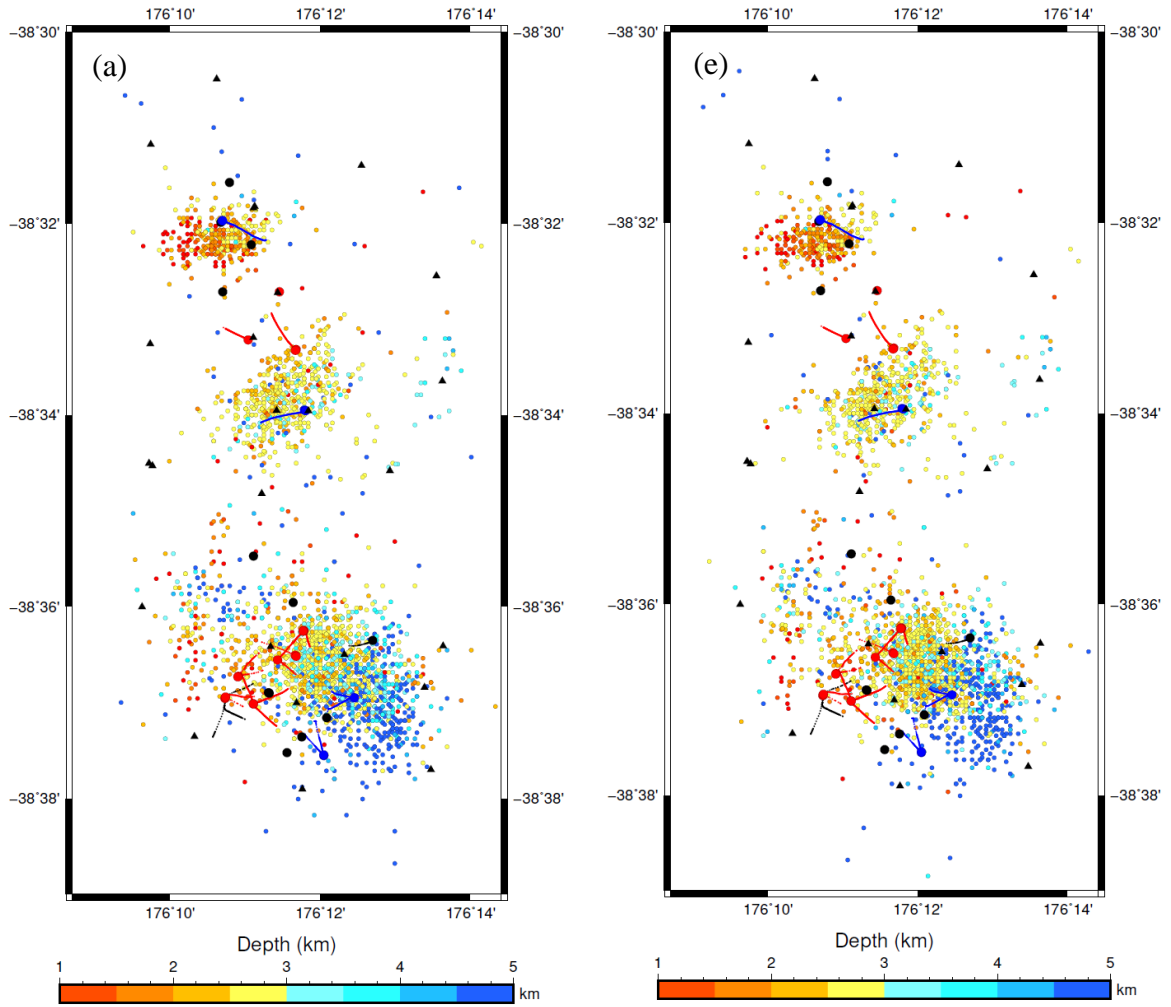
Figure A2.10. Histograms of the difference between the automatic pick and the manual pick (auto - manual) for (a) the MinMax picker and (b) the Spectrogram picker for a total of 1090 manual S picks. Outliers were defined as $> \pm 1$ s and were excluded from the statistics shown. The signal to noise of the picker characteristic function versus the absolute difference between the auto and manual pick for each of the pickers is shown in (c) and (d). The coloured lines show the SNR level above which 95% of the auto picks are within 0.1s (blue line) and 0.2s (green line) of the manual picks. These SNR levels were used to weight the S picks and assign uncertainties in the rest of the processing. Parameters used for the pickers were - MinMax sampling window = 0.15s, averaging windows = [0.2, 1, 3]. Spectro window = 0.25s, averaging windows = [0.5, 1].

The signal-to-noise of the characteristic functions of the two pickers was again used to weight picks in a weighting scheme similar to that of the P picks. Again, if two picks were made for the same arrival the final pick was the highest weighted of the two, or the average of the two if the weight was the same. The S picks were given approximately half the weight of the P picks and only S picks with weight greater than 0.4 were used (corresponding to SNR's above 2.66 and 2.16 for the minmax picker and spectro picker respectively).

For the analysis of the 2012-2017 dataset, automatic S picks were determined only for stations with a P wave pick and of the 45,740 P picks determined for the 3301 events, 13,332 S arrivals were picked (29% S to P pick ratio) which is similar to that of the manual picking. Of the 13,332 S picks, 3,786 (25%) were given a weight of 0.5, 10,787 (75%) were given a weight of 0.4. After review of the effect on location and the distribution of S residuals, S picks with weight of 0.1 (corresponding to the lowest CF-SNR picks) were excluded from the analysis.

Event locations (P & S picks)

Event locations were recalculated with NonLinLoc using both the P and S picks. Only events with at least one S pick were considered (3125 of the 3301 events from the P pick only locations). The initial NonLinLoc run with both P and S waves produced event locations largely similar to those with just P picks with some slight variation in locations (Figure A2.11a). Adding the S picks however shifted the event RMS residuals and also caused shifts in the P pick residuals (Figure A2.11). Subsequent filtering of high residual S picks (greater than ± 0.5 s) and events with particularly high RMS residuals (greater than 0.23s) resulted in event RMS residuals, P pick residuals and S pick residuals with approximately gaussian distributions without effecting event locations (Figure A2.11).



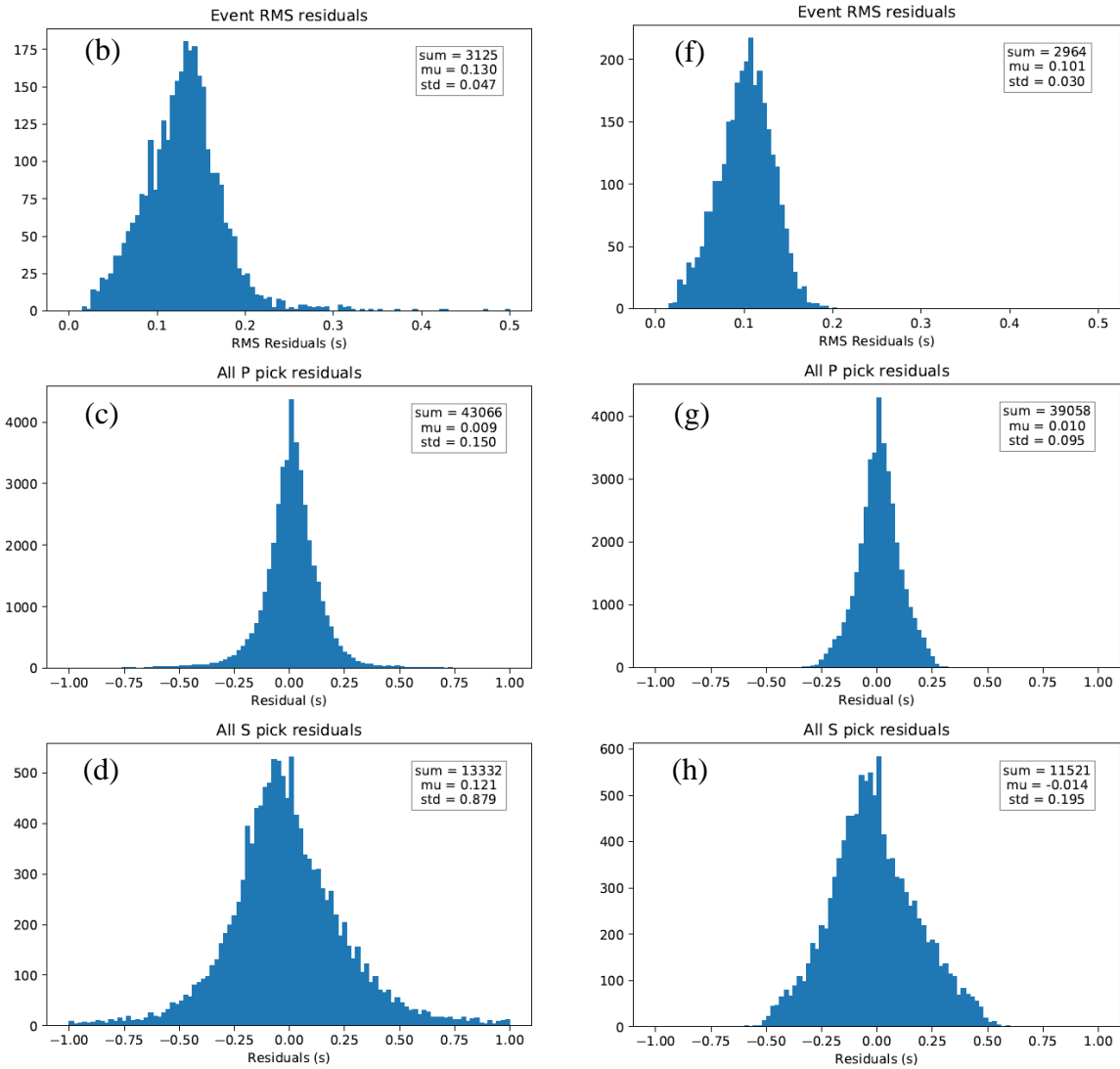


Figure A2.11. Event locations – (a) and (d), event RMS residuals – (b) and (f) and P and S pick residuals - (c) and (e) before (a, b, c) and after (d, f, e) filtering events and picks.

Table A2.3. Event and pick filters applied to the initial NLLoc run. The filters were applied in succession in order from top to bottom of the table. The percentage of events/picks removed by each filter relative to the input catalog is also shown.

Filter	Events/Picks removed	%age removed
Event RMS < 0.23s	65	2%
P pick residual < 0.25s	2592	6%
S pick residual < 0.5s	1414	10%
Events with < 8 P picks	96	3%

The final catalog of P and S picks consisted of 2964 events, with 39,058 P picks and 11,521 S picks (S to P ~ 30%). The distributions of P and S picks per event is shown in Figure A2.12.

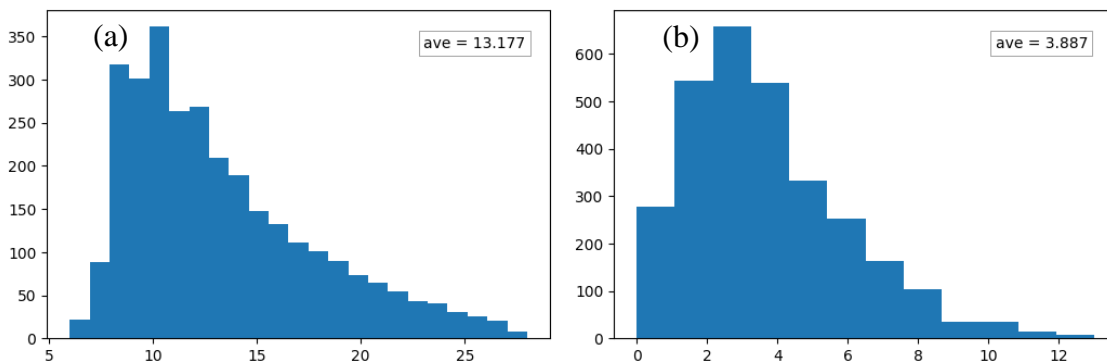


Figure A2.12. Number of P (a) and S (b) picks per event for the final catalog of 2964 events.

Double-difference relocation

Absolute arrival time accuracy for both P waves, and particularly S waves (since they are superposed on P-wave coda), can vary for both manual and automatic picking techniques. Accuracy can depend on the signal-to-noise and the nature of arrivals (for example whether arrivals are emergent), instrument response and GPS timing errors (e.g. Diehl and Kissling, 2009). Partly to address these issues, Waldhauser and Ellsworth, (2000) developed an algorithm (hypoDD) which takes advantage of the differential arrival times between events, which can be determined with higher precision and accuracy. The observed differential arrival times can be calculated using both the difference between catalog arrival times (either automatically or manually picked arrivals) for each pair of events and/or by using waveform cross-correlation (WCC) techniques which provides high accuracy relative times. The WCC approach is based on the assumption that waves generated by two similar sources (those with similar source mechanisms), that have propagated along similar paths, will generate similar waveforms. Waldhauser and Ellsworth, (2000) state that this is a reasonable assumption for events separated by less than $\frac{1}{4}$ wavelength of the highest frequency of importance in the seismogram, which is related to the first Fresnel zone. Using an average P wave velocity of 3-4 km/s and average S velocity of 1.7-2.3 km/s for the Rotokawa and Ngatamariki region and using high frequencies of importance of 10-15 Hz for P waves and 5-10 Hz for S waves results in estimates for the $\frac{1}{4}$ wavelength of 50-100 m for P waves and 42.5-57.5 m for S waves. These provide ball-park estimates for the distance over which very highly similar waveforms would be expected for the same source mechanism. For event separations greater than this, differences

in the amount of scattering experienced along the ray-paths due to velocity heterogeneities can lead to dissimilar waveforms.

The program ph2dt was used to select event pairs for the catalog differential times and also for selecting which event pairs would be cross-correlated to derive cross-correlation differential times. Parameters within ph2dt were set to ensure that all event pairs within the three main clusters of activity (Rotokawa, Southern Ngatamariki and Northern Ngatamariki) were initially considered in the differential times (by setting the maximum event separation to be 2 km) (Table A2.4). Due to the scattered events between the two fields, using a maximum separation of 2 km also provided linked events between the three clusters of seismicity. Catalog picks were weighted by averaging the weights of the two picks that were determined via the SNR determined during the automatic picking.

Table A2.4. Settings used in ph2dt to obtain catalog differential times.

Parameter	Description	Setting
MAXDIST	Maximum distance (in km) between event pair and station	50
MAXSEP	Maximum hypocentral separation between event pairs in kms	2
MAXNGH	Maximum number of neighbours per event	3000
MINLNK	Minimum number of links required to define a neighbour	8
MINOBS	Minimum number of links per pair	8
MAXOBS	Max number of links per pair	80

A parallelised version of python package hypoDDpy was used to perform cross-correlations for event-station pairs for each year of data. This package makes use of the obspy cross-correlation module xcorr_pick_correction that finds the time correction required to obtain the maximum correlation value between two waveforms over small time windows around the P and S picks (Figure A2.13) based on the method of Deichmann and Garcia-Fernandez (1992).

A range of time window and filtering parameters were trialled for a subset of closely spaced events for Southern Ngatamariki and Rotokawa. The cross-correlations were visually inspected and histograms of cross-correlation values and time shifts produced to determine the optimal settings. In general, the time-shifts calculated via cross-correlation were found to be largely invariant to the changes in filtering and windowing. The values of the cross-correlation were however influenced by the filtering applied. Specifically, bandpass filtering between 1-10 Hz produced higher correlations with more correlation values above 0.8 (Figure A2.14). Considering this result, and that the dominant signal of both P and S waves for these earthquakes is between 1-10 Hz, bandpass filtering of 1-10 Hz was used for the cross-correlation. P pick correlations were performed on the Z component data whilst S pick correlations were performed on both the east and north channels with equal weight being given to both channels for determining the S correlation value and time shift. A time window of 0.2 s about each pick was used. Of the 5,127,424 P wave and 923,307 S wave event-station pairs that were cross-correlated, 18,414 P wave and 2,874 S wave cross-correlation measurements had correlation values exceeding the threshold of 0.75. The square of the cross-correlation value was used to weight the cross-correlation data in hypoDD.

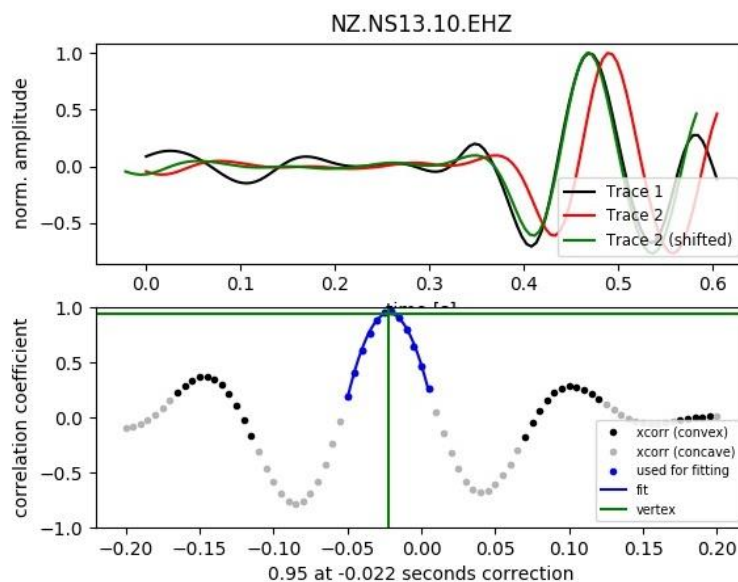


Figure A2.13. Example of the waveform cross-correlation method used. The upper window shows the two original waveforms (Trace 1 and Trace 2) from two different events. The lower window shows the correlation values calculated for relative time shifts of the two traces for up to ± 0.2 s. The maximum correlation value and time shift is found by fitting a parabola to the

concave part of the time shift versus correlation function thereby providing a sub-sample estimate of the relative time-shift between the traces required to achieve the maximum correlation. The green line in the upper window shows the position of trace 2 shifted by the time shift required to obtain the maximum correlation.

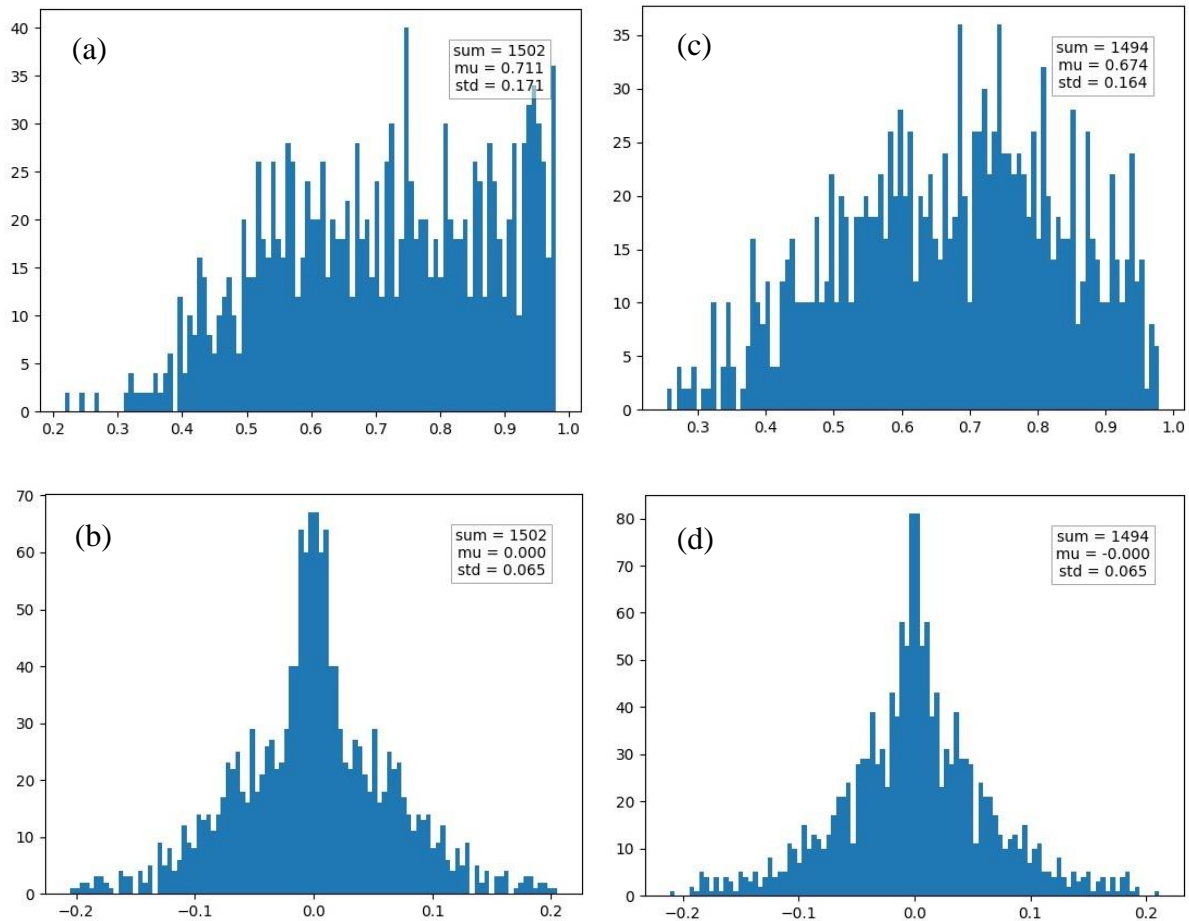


Figure A2.14. Cross-correlation values (a) and (b) and time shifts (c) and (d) for different band-pass filters of 1-10 Hz (a) and (c) and 1-20 Hz (b) and (d) for all station-event pairs for a set of 11 events separated by less than 500m occurring on the same day in southern Ngatamariki. Only a small difference in time shifts is observed for the two different filters however the 1-10 Hz filtering results in higher correlation values, particularly values over 0.8. N.B. the slight differences in the extent of the x and y axes.

HypoDD v2.1b was used to perform relative relocation of the events. The average 1D velocity model from the Monte Carlo VELEST work of Sewell et al. (2017) was again used in the locations. Many inversion schemes and settings were trialed for the relocation whilst monitoring the change in the hypocentre distribution, catalog and cross-correlation residuals and inversion statistics to determine the final settings and inversion scheme used. The final

inversion scheme is shown in Table A2.5. The first two iterations place 100 times more weight on catalog data with distance cut-offs at 2 km and a catalog residual cut-off of 6 standard deviations in the second set of iterations. The last three iterations place 100 times more weight on cross-correlation data with a distance cut-off starting at 1 km decreasing to 0.5 km on the last set of iterations. A cross-correlation residual cut-off of 6 standard deviations was applied on the last two sets of iterations. OBSCT (the minimum number of common stations per event pair for catalog data) was set to 10 which resulted in the formation of one cluster that contained all events across the two fields except for 164 isolated events with less than 10 common stations per event pair that were not included in the relocation. The maximum azimuth gap separation for event pairs was set to 180.

Table A2.5. HypoDD inversion scheme. NITER – number of iterations for each set of parameters, WTCCP/WTCCS – weighting for cross-correlation P wave/S wave measurements, WTCTP/WTCTS - weighting for catalog P wave/S wave measurements, WRCC/WRCT – residual cut-off value (in multiples of the standard deviation of all residuals) for cross-correlation/catalog measurements, WDCC/WDCT – distance cut-off (kms) for cross-correlation/catalog measurements, DAMP – damping parameter.

NITER	WTCCP	WTCCS	WRCC	WDCC	WTCTP	WTCTS	WRCT	WDCT	DAMP
5	0.01	0.01	-999	2	1	1	-999	2	500
5	0.01	0.01	-999	2	1	1	6	2	500
5	1	1	-999	1	0.01	0.01	6	2	500
5	1	1	6	1	0.01	0.01	6	2	500
5	1	1	6	0.5	0.01	0.01	6	2	500

Statistics on the residuals and other quality measures with each iteration are presented in Figure A2.15. Catalog residuals were reduced by a factor of approximately 1.6 whilst cross-correlation residuals were reduced by a factor of approximately 10. As can be seen in Figure A2.15d, the first 2-3 iterations of the first set of iterations with high weighting on the catalog data produced the majority of the shift in hypocentres. Subsequent iterations placing more weight on the cross-correlation data produced relatively small shifts in the hypocentres as expected. Figure A2.16 compares the hypocentres after the first set of iterations (after the fifth iteration) versus those after the final set of iterations (after the 25th iteration). Figure A2.17a-e and Figure A2.17f-h

show the distribution of the number of data, residuals and mean cross-correlation value versus the inter-event distance after the first and last set of iterations respectively. These show a general increase with increasing inter-event distance, as expected given the distance weighting criteria. The final cross-correlation RMS residuals are similar for both the P wave and S wave cross-correlation data, suggesting both data agree well. For inter-event distances of less than ~100 m (approximately the $\frac{1}{4}$ wavelength distance) cross-correlation values are generally >0.85 and the cross-correlation data was fit to an RMS residual of <5 ms for both P and S waves which is close to the level of accuracy of the cross-correlation data.

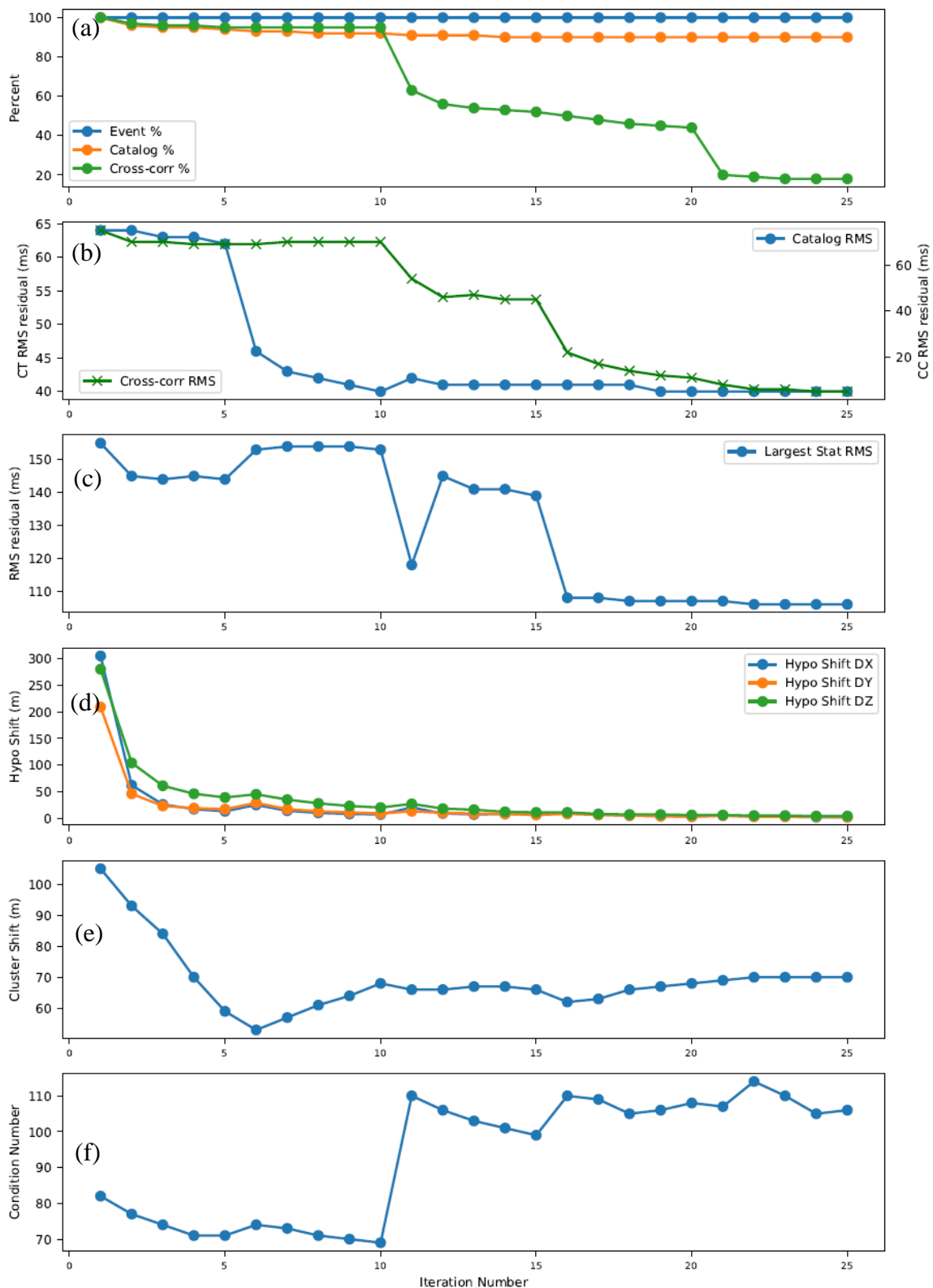


Figure A2.15. Inversion statistics for each iteration of the final hypoDD run. (a) the percentage of each data typ, (b) the RMS residual for cross-correlation (cc) and catalog data (ct), (c) the largest station residual, (d) the average hypocentre shift (m) in x, y and z (depth), (e) the shift (m) in the cluster centroid, (f) the condition number.

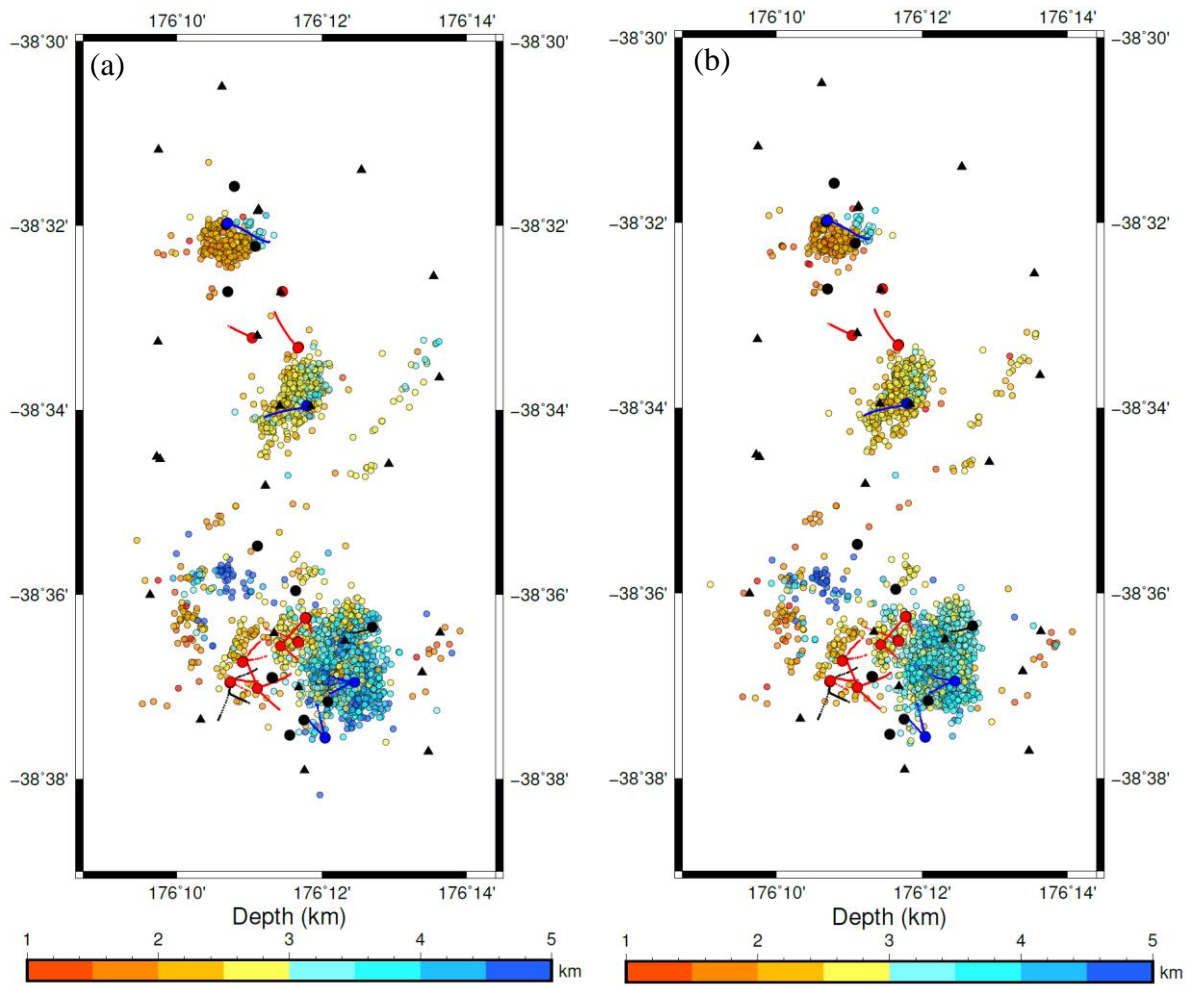


Figure A2.16. Hypocentres after the first set of iterations (a) and after the final set of iterations (b).

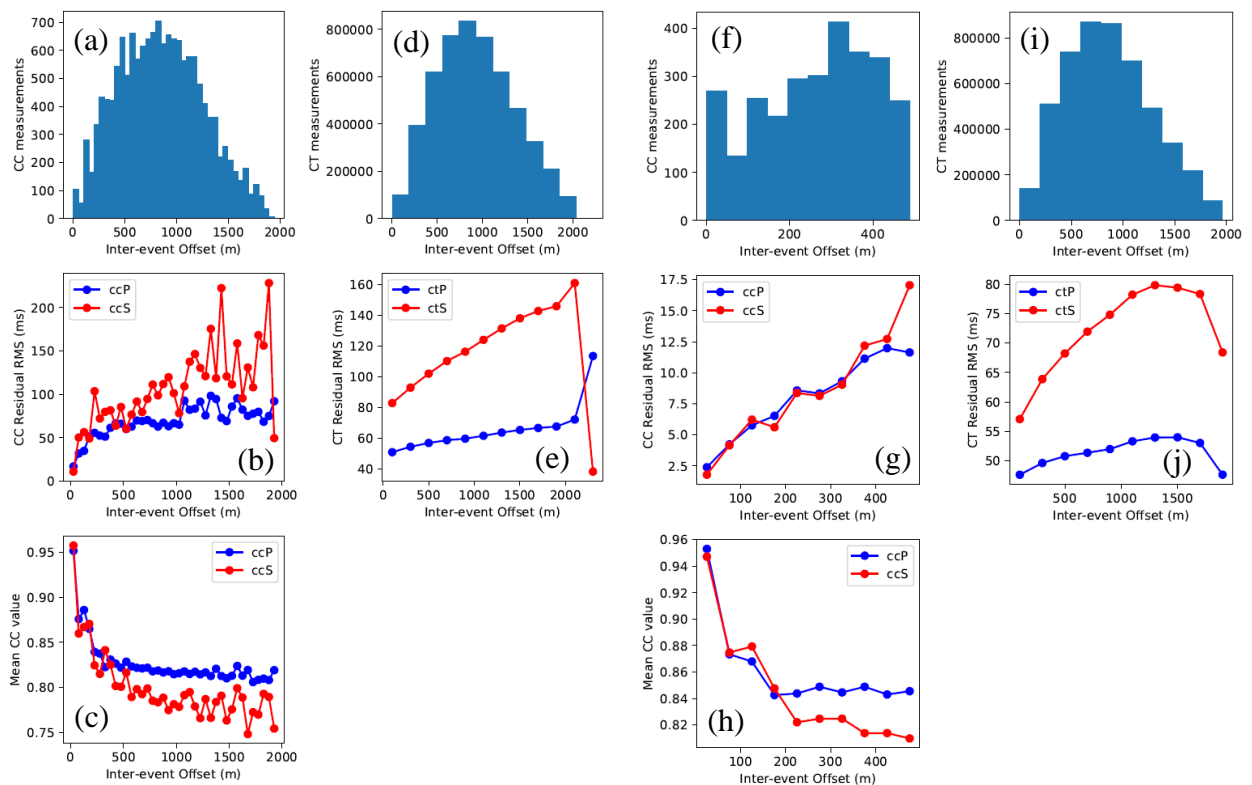


Figure A2.17. Number of cross-correlation data (a & f), catalog data (d & i), cross-correlation residuals (b & g), catalog residuals (e & j) and mean cross-correlation values (c & h) after the first set of iterations (a-e) and after the last set of iterations (f-j) versus the inter-event distance. Values for residuals and cc values versus inter-event distances are averages over inter-event distance bins of 50 m for cross-correlation data and 200 m for catalog data. N.B. differences in scales when comparing between the first and final set of iterations.

Figure A2.18 shows a comparison between the automatically derived hypocentres for 2012-2017 versus those determined by GNS Science using manual picks. Although these hypocentres are from different time periods and there are a number of differences between how these hypocentres were located besides the picking method (for example changes in the network layout, manual picks were performed separately for Rotokawa and Ngatamariki – i.e. events at Rotokawa were picked only on stations at Rotokawa and vice versa), they provide a useful check on the accuracy of the automated methodology presented here. For the most part, the horizontal differences between the three main clusters of seismic activity across the geothermal fields are relatively minor (generally less than 100-200m). There are notable differences though, particularly for the Rotokawa cluster which appears to extend further to the northeast and southeast in the automatic 2012-2017 locations versus the 2010-2012 manually picked locations by approximately 500m. Although these may be real migrations of seismic

activity over time, there are a number of other possible causes for this including changes in the Rotokawa network geometry, possible shifts due to lateral velocity variation caused by using both Rotokawa and Ngatamariki stations for the automated locations and differences in the methodology between the manual and automated processing (e.g. settings used in hypoDD, settings and method used for cross-correlation, etc). These should be investigated further before any confidence could be placed on these apparent migrations of activity. A number of new areas of apparent seismicity appear to have been identified over the 2012-2017 period that are also worthy of further investigation. A lineation of ~30 events that occurred as swarms on two days (24/11/2015 and 18/1/2016) appears to delineate a possible NE-SW fault to the south-east of Ngatamariki (Area 1 in Figure A2.18a). Seismic activity north of the Waikato River at Rotokawa appears to be more active over the 2012-17 period, with ~100 events occurring within Area 2 in Figure A2.18a. A further apparent NE-SW lineation of ~50 events appears to occur in northwest Rotokawa not far from production wells in that area, that might be associated with the Production Field Fault (McNamara et al., 2016). In addition to these, there appears to be increased, relatively shallow activity in the production area at Rotokawa over the 2012-17 period compared to the 2010-12 period.

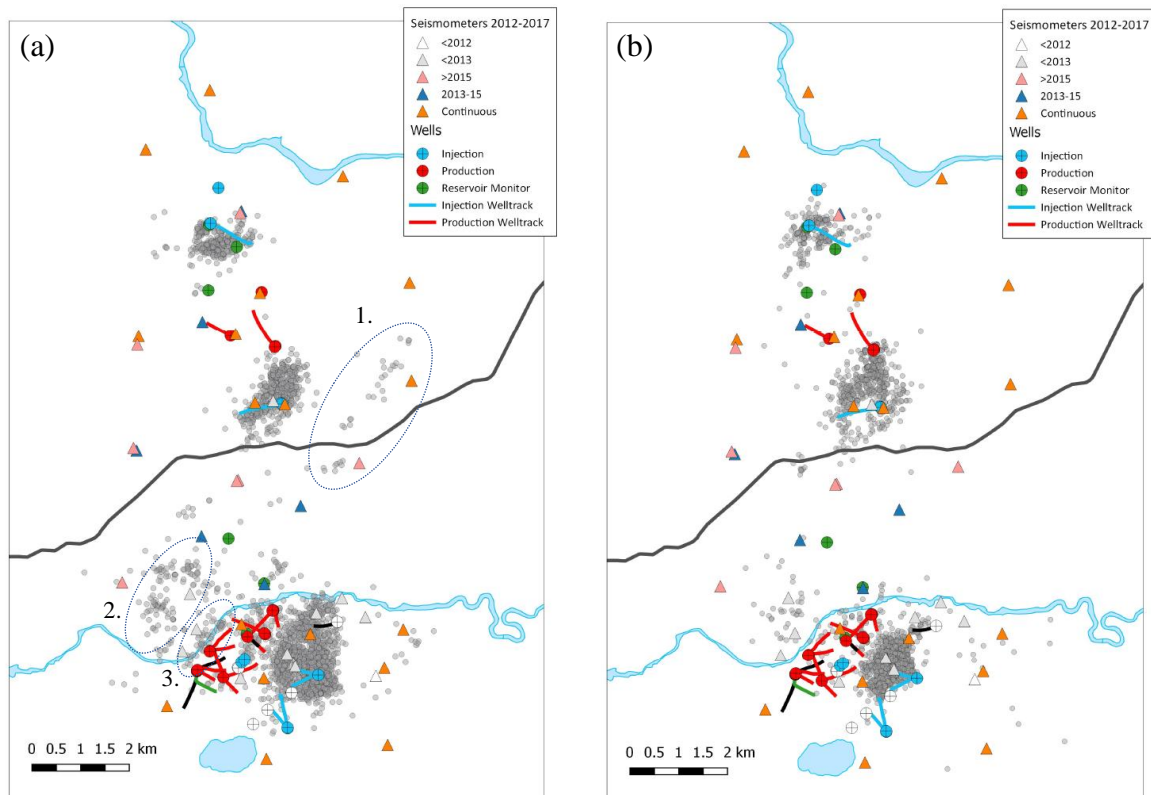


Figure A2.18. Comparison between hypocentres determined via the automated process presented here (a) and those determined via manual picking by GNS Science (b). Although the time periods are

different (auto locations shown are mid-2012 to mid-2017 whilst the manual locations shown Rotokawa are from 2010 to mid-2012 and for Ngatamariki are from mid-2012 to mid-2014) the hypocentre locations are broadly similar. Possible new areas of seismic activity identified during 2012-17 are outlined by the blue dotted ellipses – 1. South-east Ngatamariki, 2. Rotokawa North, 3. Rotokawa Northwest Production area.

Figure A2.19 shows event depths over time in relation to injection well feedzones and hypocentres determined by GNS Science via manual picking. Event depths for Ngatamariki determined here are broadly similar to those determined by GNS Science via manual picking and are approximately at the same depth as the injection well feedzones. Event depths for Rotokawa however are approximately 1 km deeper relative to the GNS Science locations and the injection well feedzones. This is likely due to the 1D velocity model used for these locations being unrepresentative of the Rotokawa area. Event depths over time show some small apparent variations over time – there is a slight decrease in event depths for Rotokawa on the order of 100 m, a possible decrease for southern Ngatamariki between 2013-2015 whilst events in norther Ngatamariki have remained relatively constant except for 2017 where a set of deeper events appears to have occurred. These trends are worthy of further investigation once a more representative velocity model is established for the region and with additional events obtained via matched filter processing.

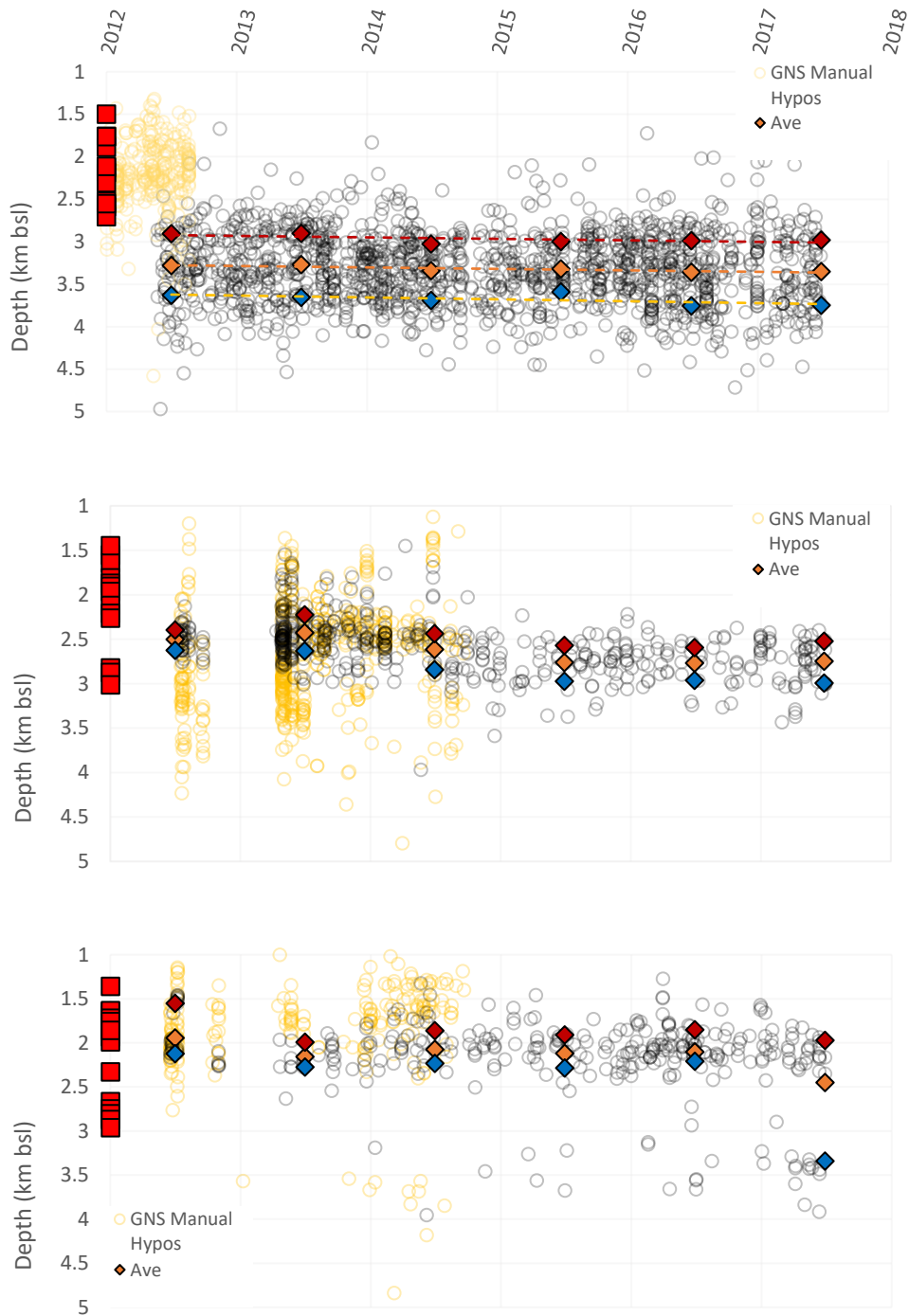
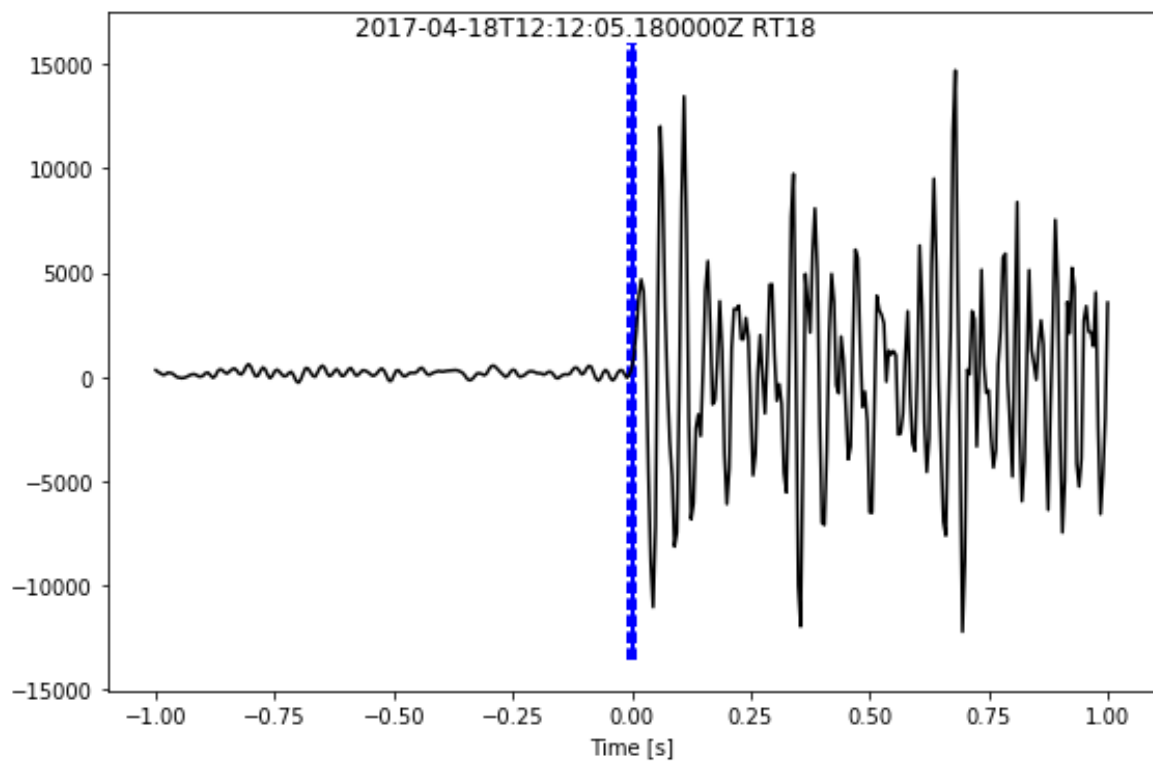
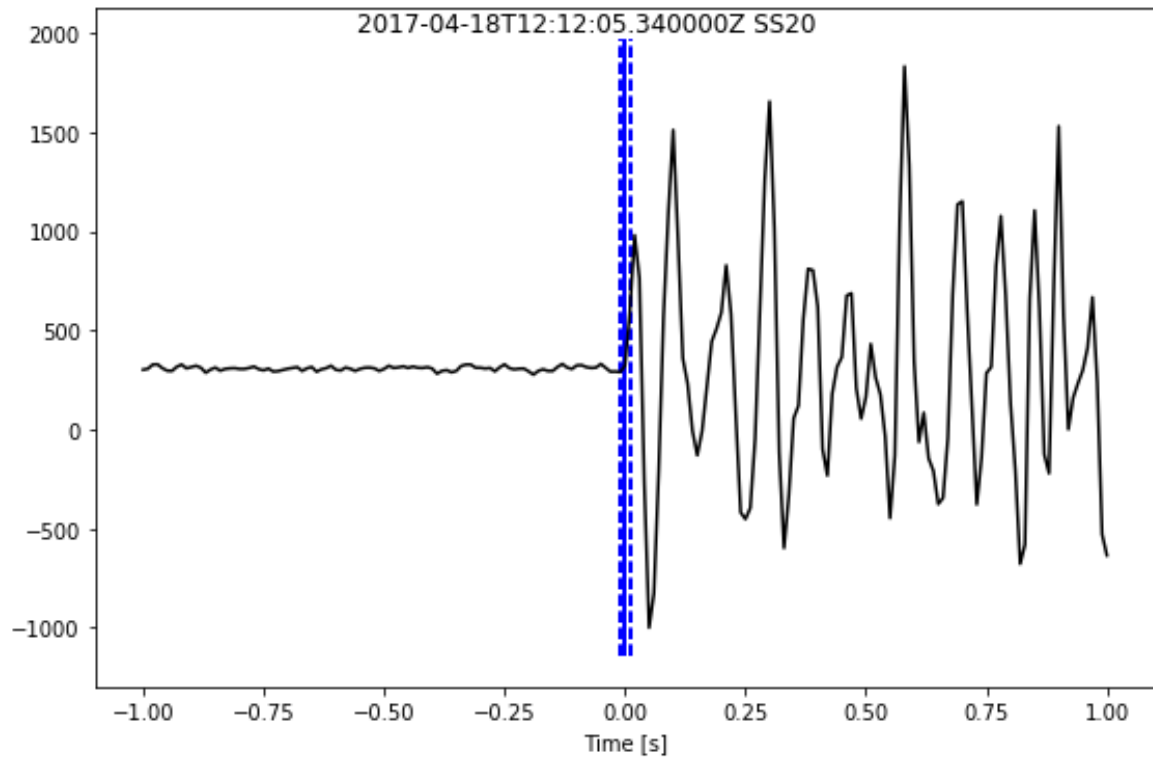


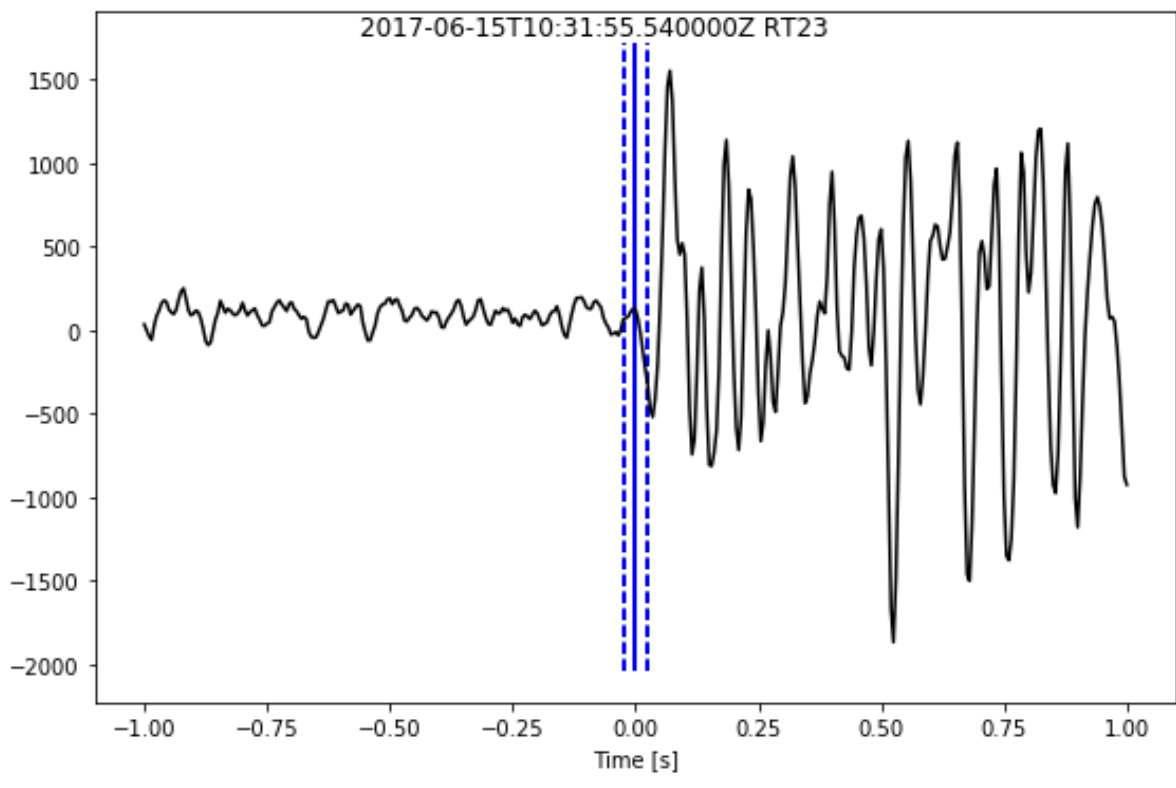
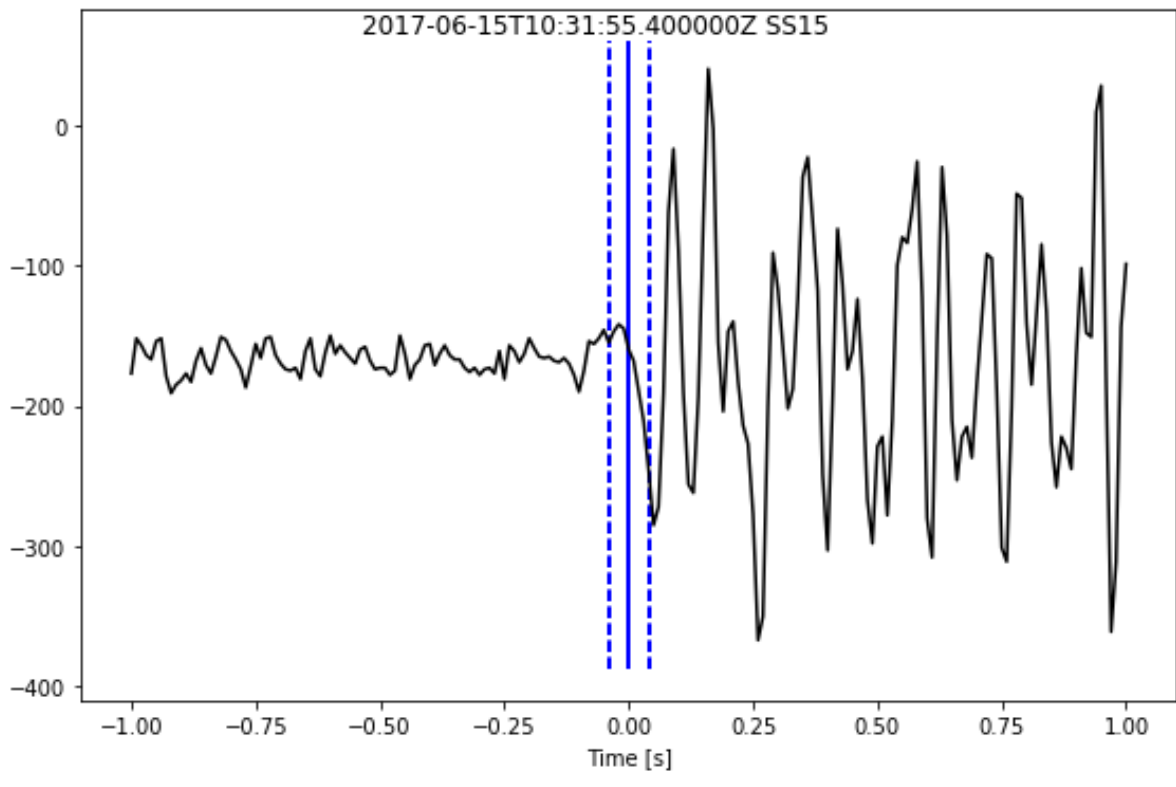
Figure A2.19. Event depths over time for the 2012-2017 period for Rotokawa, southern Ngatamariki and northern Ngatamariki. Automatic locations from the analysis presented here are shown as grey circles, whilst manually picked locations of GNS Science are shown as yellow circles. The average, 20th percentile and 90th percentile depths for each year are shown as the orange, red and blue diamonds. Feedzones of injection wells being utilised during these time periods are shown as red squares.

A.3. Example manual and automatic picks from the tomography dataset

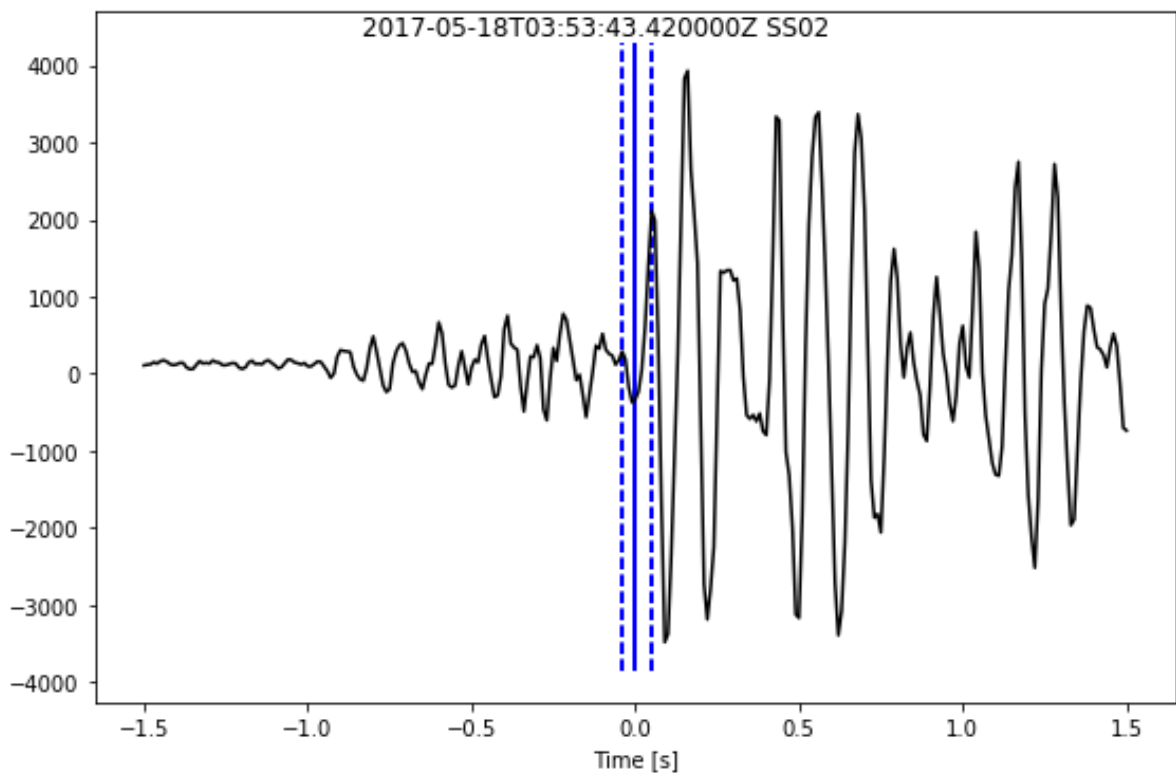
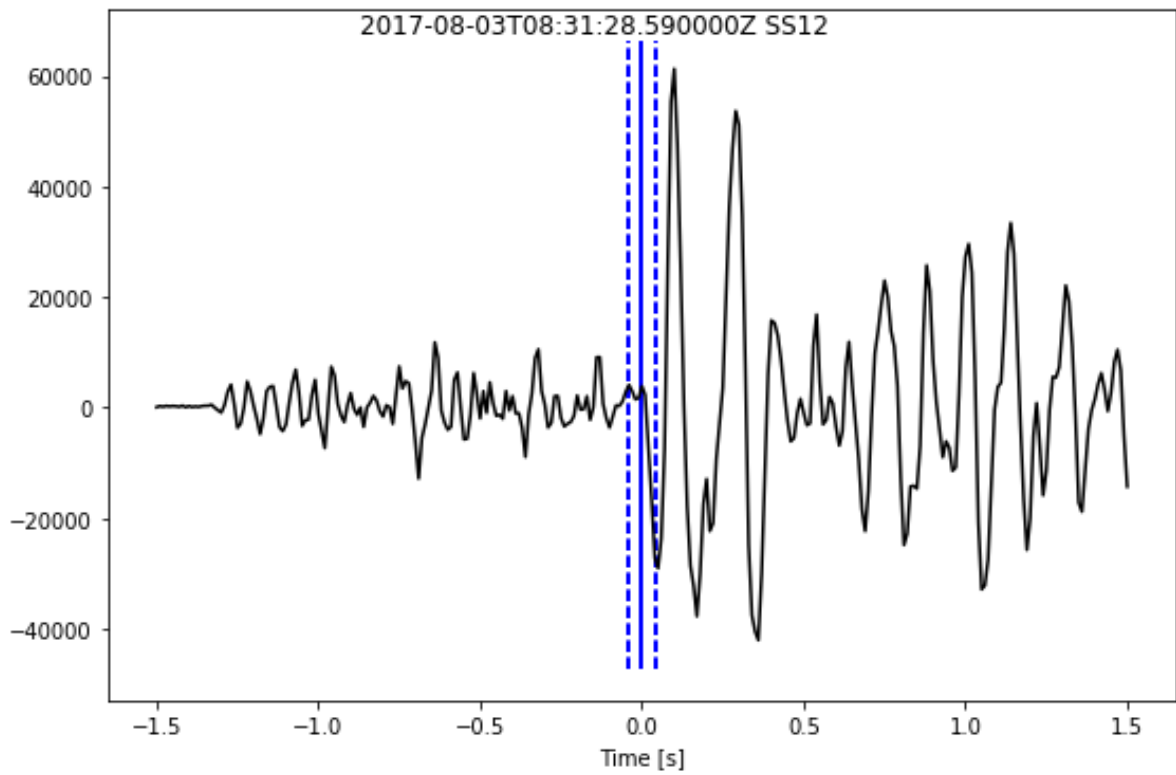
Manual P, Weight = 1.0. (Solid line = pick, dashed lines = uncertainties)



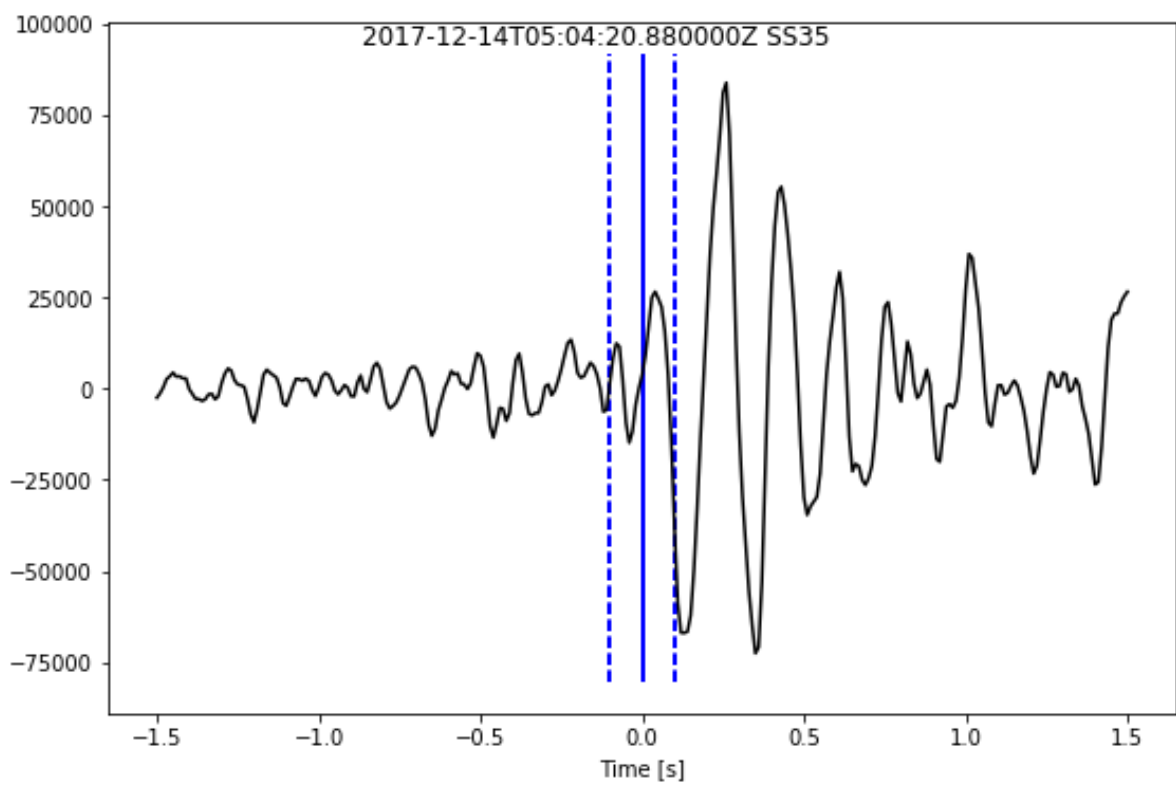
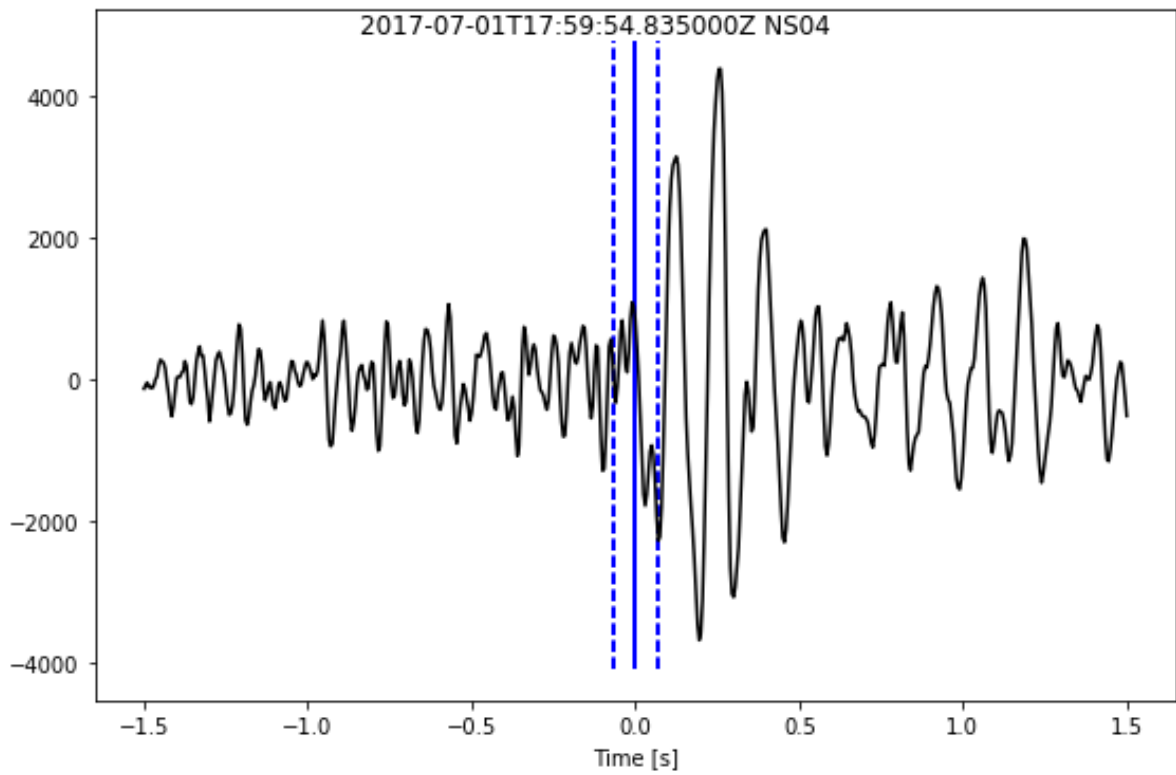
Manual P, Weight = 0.8



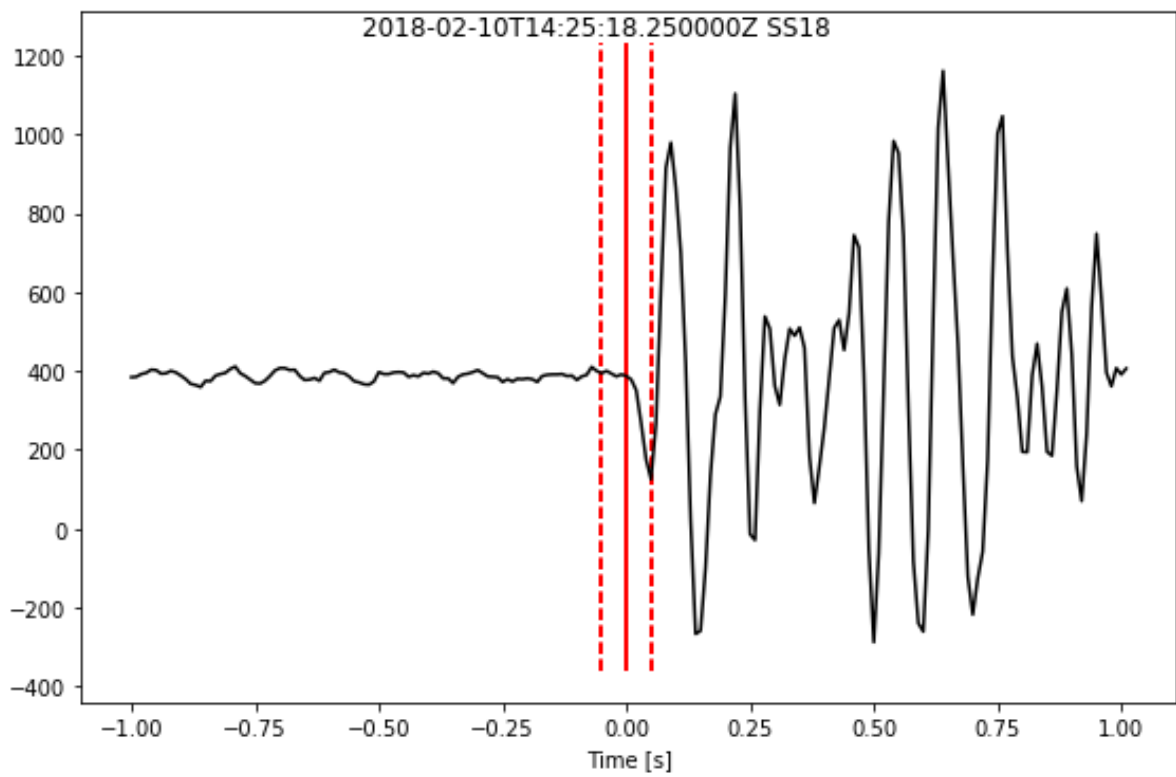
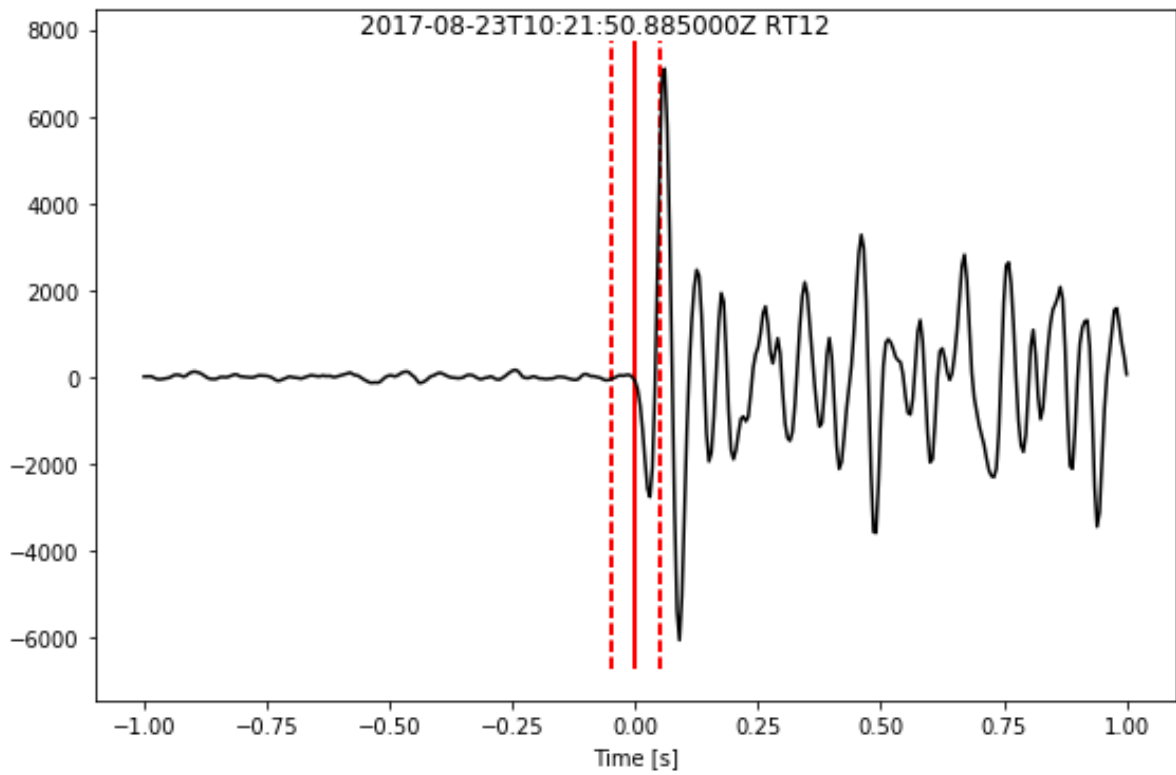
Manual S, Weight = 1.0



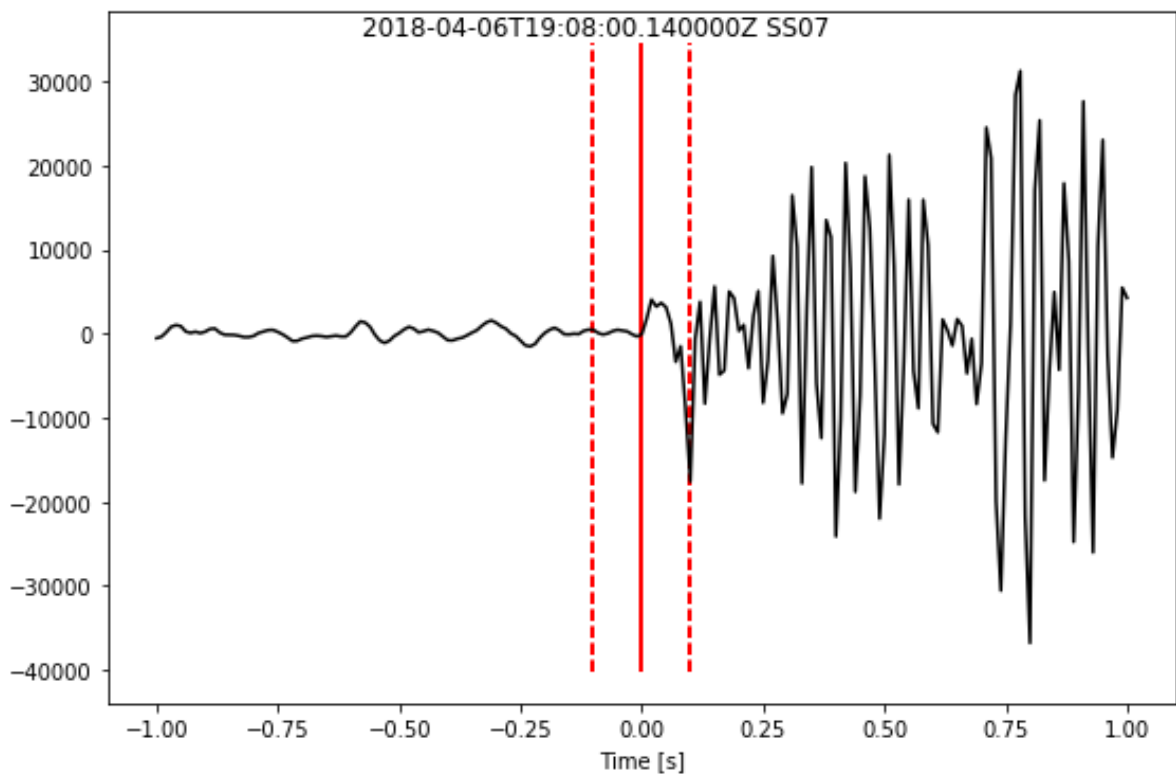
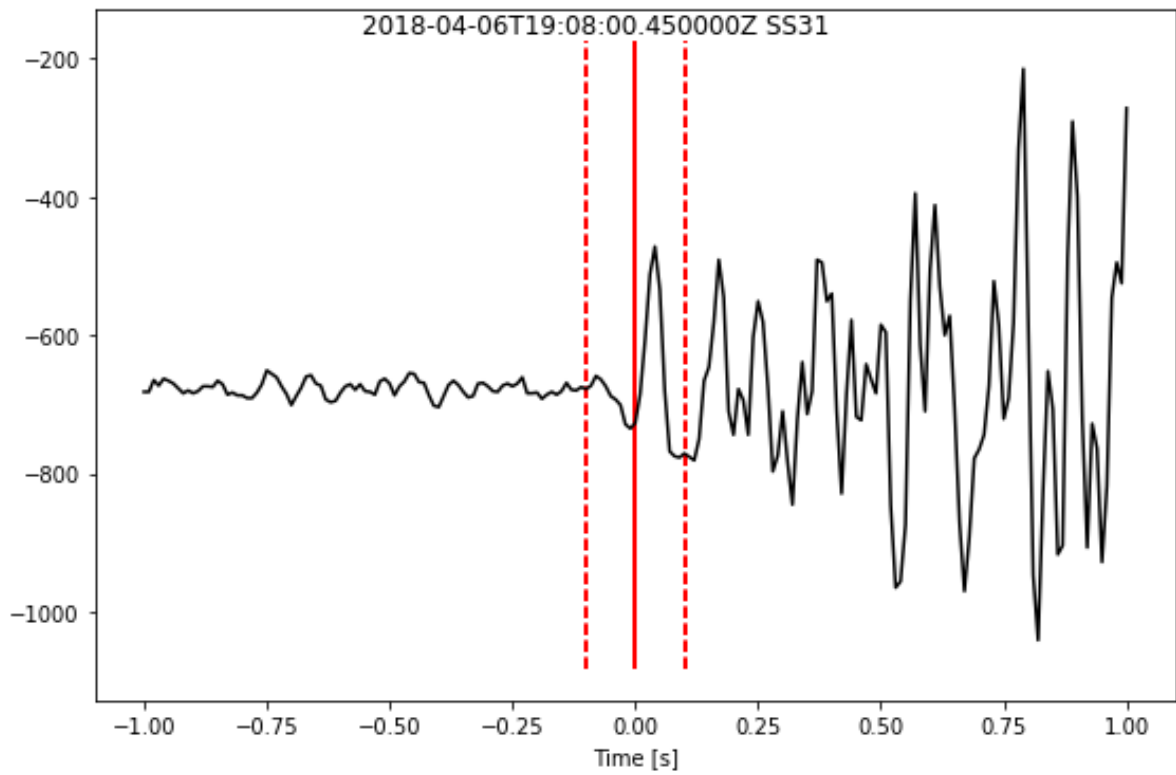
Manual S, Weight = 0.8



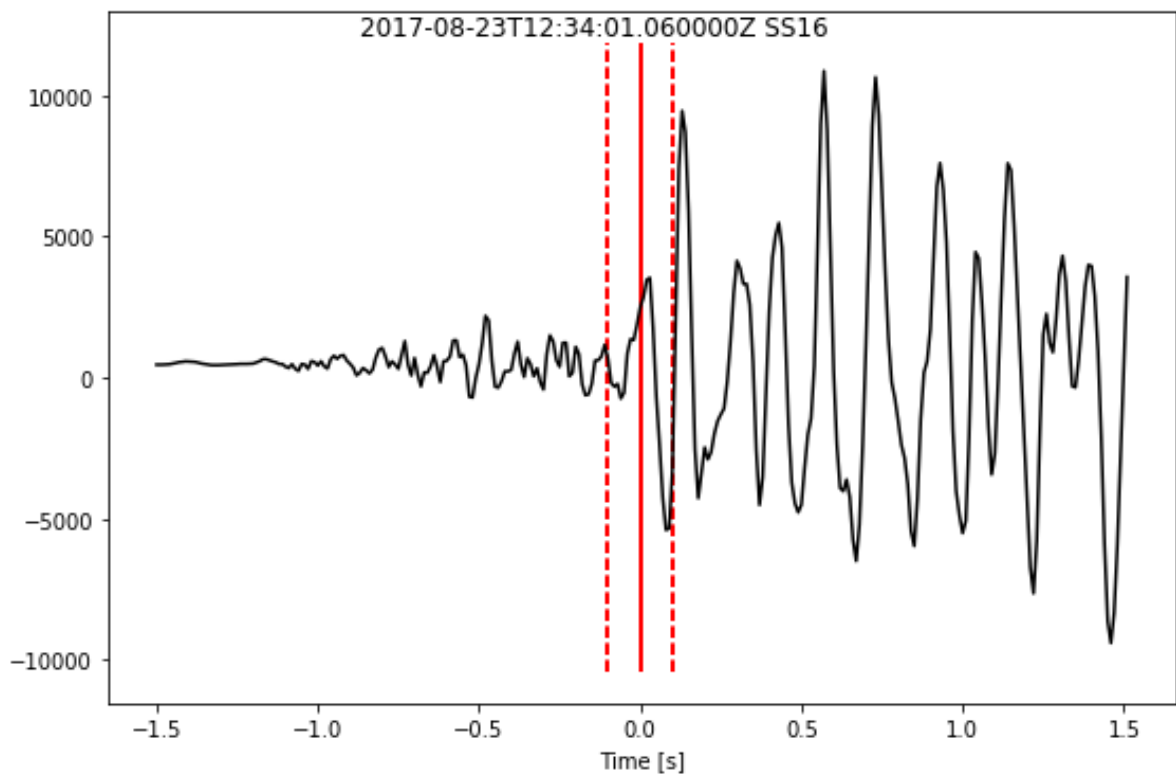
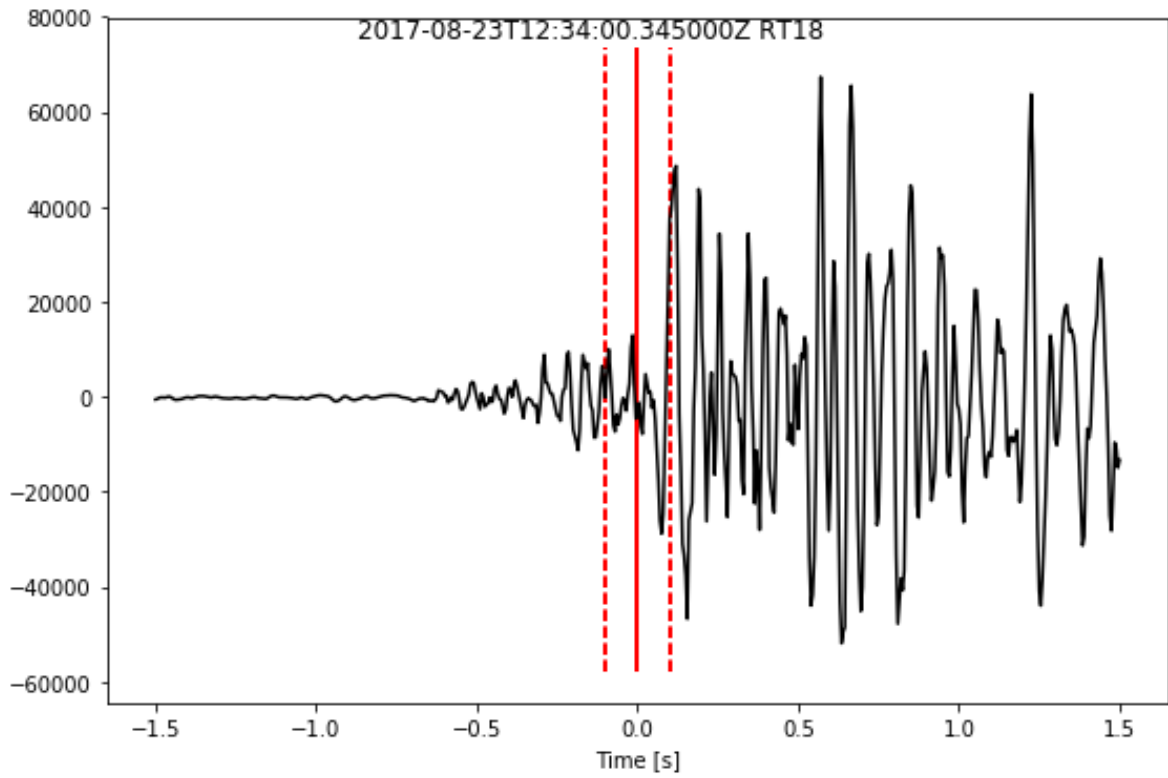
Auto P, Weight = 1.0



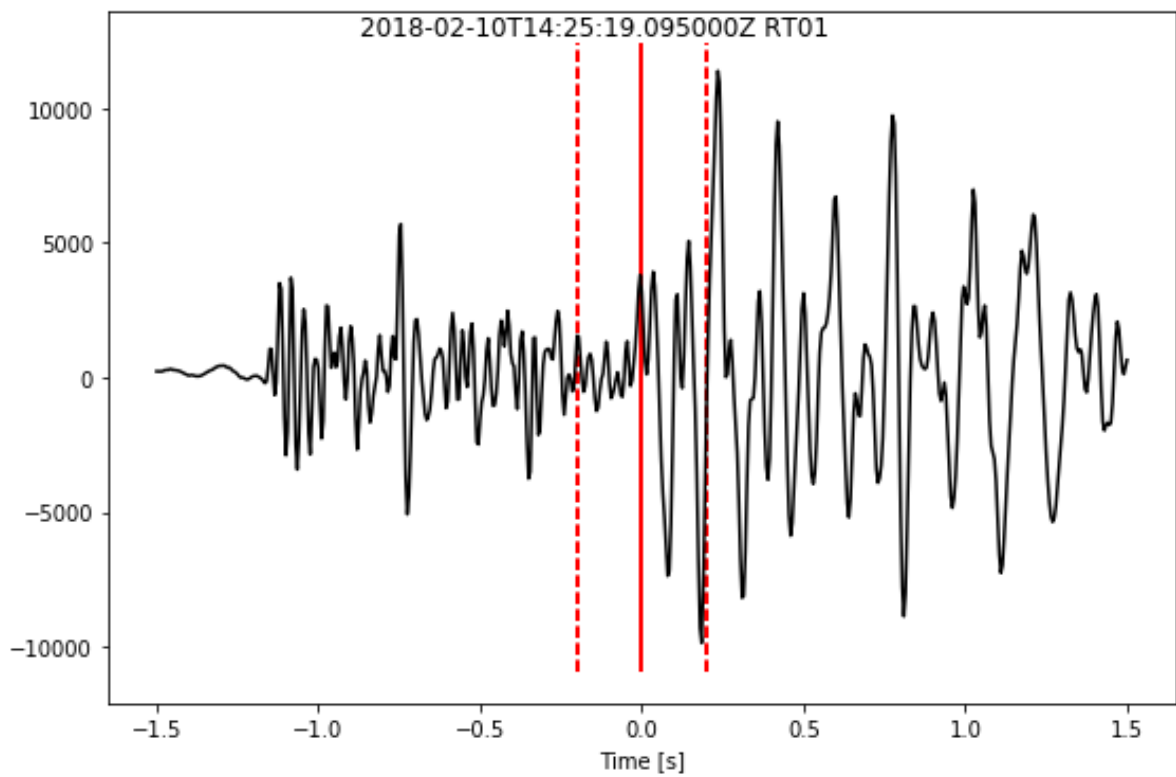
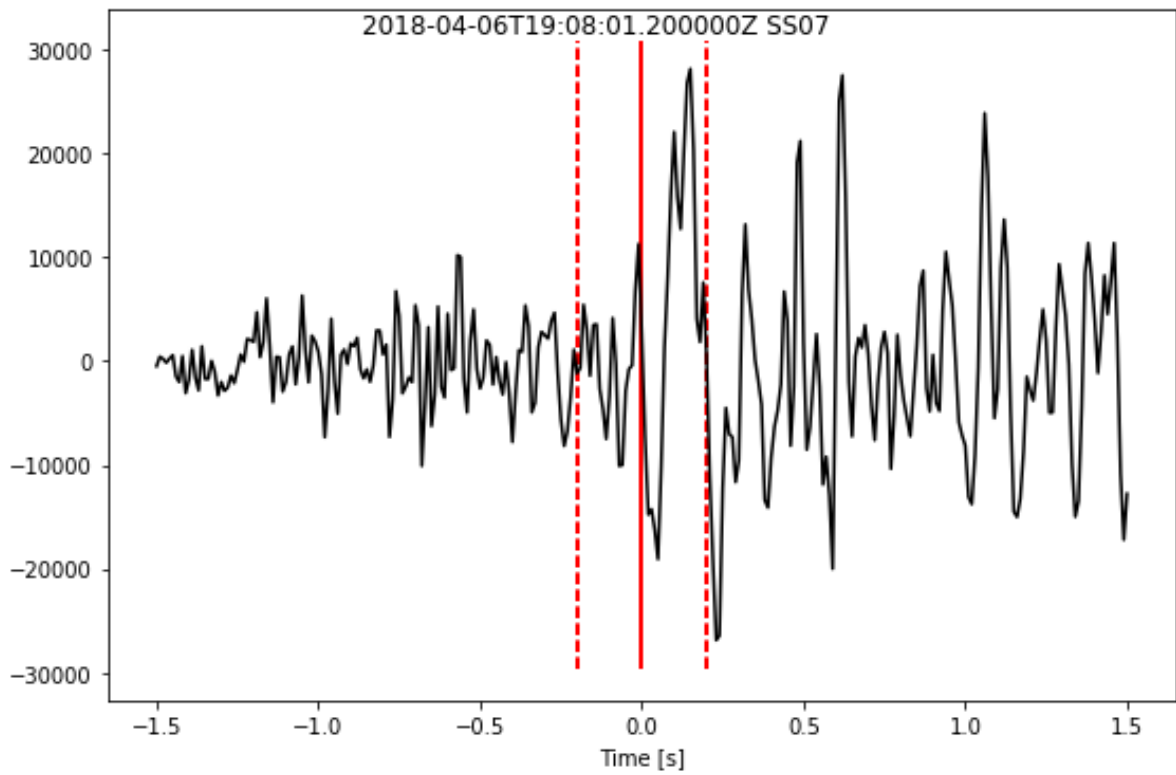
Auto P, Weight = 0.8



Auto S, Weight = 1.0



Auto S, Weight = 0.8



A.4. Original Stratigraphy of Logged Intervals

Summary of the original description of the stratigraphy of the intervals in this study from wellsite geology and post-drilling geological analysis (Modified from NM8 - Lewis et al. 2012a, NM9 - Lewis et al. 2013, NM10 - Lewis et al. 2012b Rare (<5%); minor (5–20%) common (20–50%); abundant (>50%))

Well	Depth From (mRF)	Depth To (mRF)	Formation	Lithology	Description
NM9	1930	2495	Tahorakuri Fm	Crystal-poor tuff	Crystal-poor (quartz-bearing) tuff. Alteration: Intense to quartz and pyrite, with minor calcite, clay, chlorite and epidote; common wairakite; pyrophyllite, kaolinite, and dickite at 2360 mRF; magnetite below 2450 mRF.
NM9	2495	2580	Tahorakuri Fm	Volcaniclastic rock	Quartz-, ferromagnesian-, and lithic-bearing volcaniclastic rock. Alteration: Intense to quartz, pyrite and chlorite; rare to minor epidote, wairakite, and magnetite; pyrophyllite at 2500 and 2550 mRF.
NM9	2580	2950	Tahorakuri Fm	Crystal-poor tuff	Crystal-poor (quartz-bearing) tuff, possible dyke at 2890 mRF. Alteration: Intense to quartz-clay-(magnetite) with minor sporadic pyrite-chlorite-calcite-epidote; andalusite at 2660 mRF; biotite below 2760 mRF; actinolite below 2830 mRF.

NM9	2950	3145	NM Intrusion	Quartz-bearing Diorite	Coarse-grained intermediate to felsic intrusion rock with framework of equigranular feldspars (mostly plagioclase) and quartz, enclosing pyroxene, amphibole, and magnetite. Alteration: Moderate-strong to chlorite, epidote, and pyrite with rare biotite and actinolite. Plagioclase replaced by calcite and clay.
NM9	3145	3551	NM Intrusion	Tonalite	Porphyritic felsic intrusion. Abundant euhedral plagioclase and common rounded and embayed quartz crystals. Alteration: Strong. Plagioclase partially replaced by calcite and clay. Selective replacement of ferromagnesian minerals by chlorite, pyrite and magnetite below 3280 mRF. Minor to common epidote below 3350 mRF.

A.5. Station Correction Terms

Vp Station Corrections

Stat	Ave	Std	P50 ave	P50 std	P10 Ave	P10 std
HRRZ	-0.51	0.29	-0.64	0.28	-0.73	0.12
SS01	-0.27	0.14	-0.36	0.10	-0.41	0.05
SS31	-0.04	0.08	-0.09	0.07	-0.11	0.04
PRRZ	-1.09	0.37	-1.30	0.28	-1.41	0.11
SS32	-0.33	0.15	-0.43	0.11	-0.47	0.05
NS01	-0.17	0.09	-0.23	0.06	-0.25	0.03
SS03	-0.06	0.06	-0.09	0.06	-0.10	0.04
WPRZ	-0.27	0.11	-0.34	0.08	-0.37	0.04
SS04	-0.06	0.06	-0.10	0.05	-0.11	0.03
NS03	-0.02	0.04	-0.04	0.04	-0.05	0.03
SS02	-0.31	0.12	-0.39	0.08	-0.43	0.04
SS05	0.01	0.04	0.00	0.04	-0.01	0.03
SS06	-0.17	0.07	-0.22	0.05	-0.24	0.02
SS07	0.01	0.03	-0.01	0.04	-0.01	0.03
NS18	-0.10	0.05	-0.13	0.04	-0.14	0.02
SS08	0.01	0.02	0.01	0.02	0.01	0.02
SS09	-0.23	0.09	-0.29	0.05	-0.32	0.02
SS10	0.02	0.02	0.02	0.02	0.03	0.02
SS11	-0.17	0.06	-0.21	0.04	-0.23	0.02
NS04	-0.06	0.03	-0.08	0.02	-0.08	0.02

NS12	0.02	0.14	0.02	0.16	0.04	0.15
SS12	0.03	0.02	0.04	0.02	0.06	0.01
NS13	-0.06	0.07	-0.07	0.07	-0.06	0.07
SS35	-0.33	0.13	-0.42	0.08	-0.48	0.04
NS17	-0.15	0.06	-0.19	0.03	-0.21	0.02
NS07	-0.02	0.02	-0.03	0.02	-0.03	0.02
ALRZ	-0.89	0.26	-1.07	0.16	-1.12	0.07
SS14	-0.01	0.01	-0.01	0.01	0.00	0.01
NS11	-0.02	0.01	-0.02	0.01	-0.02	0.01
NS14	0.01	0.07	0.01	0.08	0.03	0.07
NS16	-0.12	0.05	-0.16	0.03	-0.18	0.02
NS15	-0.02	0.01	-0.02	0.01	-0.02	0.00
SS36	-0.34	0.13	-0.43	0.08	-0.47	0.04
RT24	0.00	0.00	0.00	0.00	0.00	0.00
SS15	-0.03	0.01	-0.04	0.01	-0.04	0.01
SS16	-0.01	0.00	-0.01	0.00	-0.01	0.00
SS17	-0.12	0.04	-0.15	0.02	-0.17	0.01
SS19	-0.01	0.01	-0.02	0.01	-0.03	0.01
SS18	-0.14	0.04	-0.17	0.02	-0.18	0.02
SS20	-0.04	0.01	-0.05	0.01	-0.05	0.01
SS21	-0.09	0.03	-0.11	0.02	-0.12	0.02
SS22	-0.07	0.03	-0.09	0.02	-0.10	0.02
SS23	-0.17	0.05	-0.21	0.02	-0.23	0.01

RT23	-0.16	0.06	-0.20	0.04	-0.23	0.02
SS25	-0.03	0.02	-0.04	0.02	-0.05	0.02
SS24	-0.04	0.02	-0.05	0.02	-0.06	0.02
RT17	-0.04	0.03	-0.06	0.02	-0.07	0.02
RT18	-0.04	0.03	-0.05	0.03	-0.07	0.02
RT19	-0.02	0.03	-0.03	0.03	-0.04	0.02
SS26	-0.14	0.06	-0.17	0.04	-0.20	0.03
SS37	-0.46	0.15	-0.57	0.08	-0.61	0.04
RT12	-0.01	0.03	-0.02	0.03	-0.04	0.02
SS27	-0.05	0.03	-0.07	0.03	-0.09	0.02
RT14	-0.02	0.03	-0.03	0.03	-0.05	0.02
SS28	-0.06	0.05	-0.08	0.04	-0.11	0.02
RT01	-0.05	0.05	-0.08	0.04	-0.11	0.02
SS29	-0.04	0.05	-0.07	0.04	-0.09	0.03
ARAZ	-0.29	0.13	-0.38	0.09	-0.42	0.04
RT21	0.02	0.05	0.00	0.05	-0.02	0.05
SS30	-0.04	0.06	-0.07	0.05	-0.10	0.03
RT05	-0.04	0.06	-0.07	0.05	-0.10	0.03
SS38	-0.15	0.09	-0.21	0.07	-0.25	0.04
THQ2	-0.09	0.10	-0.15	0.08	-0.20	0.05

Vs station corrections

Stat	Ave	Std	P50 Ave	P50 Std	P10 Ave	P10 Std
------	-----	-----	------------	---------	------------	---------

HRRZ	-0.82	0.51	-1.06	0.50	-1.21	0.27
SS01	-0.45	0.29	-0.60	0.26	-0.69	0.17
SS31	-0.05	0.20	-0.12	0.23	-0.17	0.16
PRRZ	-1.78	0.62	-2.15	0.48	-2.34	0.24
SS32	-0.55	0.31	-0.72	0.27	-0.81	0.18
NS01	-0.33	0.22	-0.44	0.21	-0.50	0.15
SS03	0.17	0.16	0.14	0.19	0.10	0.14
WPRZ	-0.55	0.27	-0.69	0.25	-0.76	0.18
SS04	0.02	0.16	-0.03	0.18	-0.07	0.14
NS03	0.22	0.14	0.22	0.17	0.20	0.13
SS02	-0.54	0.27	-0.69	0.24	-0.77	0.17
SS05	0.18	0.14	0.17	0.17	0.15	0.13
SS06	-0.21	0.18	-0.29	0.19	-0.33	0.14
SS07	0.53	0.14	0.58	0.15	0.57	0.13
NS18	-0.24	0.17	-0.31	0.17	-0.36	0.13
SS08	0.07	0.12	0.07	0.15	0.05	0.13
SS09	-0.26	0.20	-0.35	0.20	-0.41	0.15
SS10	0.35	0.13	0.38	0.15	0.38	0.13
SS11	-0.26	0.17	-0.33	0.17	-0.37	0.13
NS04	0.35	0.14	0.38	0.15	0.36	0.13
NS12	-0.14	0.16	-0.18	0.18	-0.20	0.16
SS12	0.45	0.14	0.52	0.14	0.53	0.12
NS13	-0.20	0.12	-0.24	0.12	-0.27	0.11

SS35	0.09	0.17	0.05	0.20	0.02	0.15
NS17	0.00	0.14	-0.04	0.16	-0.08	0.13
NS07	0.73	0.17	0.82	0.14	0.82	0.13
ALRZ	-1.52	0.48	-1.84	0.35	-1.95	0.20
SS14	0.37	0.13	0.42	0.13	0.41	0.12
NS11	0.00	0.00	0.00	0.00	0.00	0.00
NS14	0.00	0.00	0.00	0.00	0.00	0.00
NS16	0.06	0.16	0.03	0.18	-0.01	0.15
NS15	0.13	0.12	0.15	0.14	0.14	0.13
SS36	-0.27	0.24	-0.39	0.24	-0.47	0.17
RT24	0.09	0.12	0.09	0.15	0.07	0.13
SS15	0.10	0.12	0.11	0.14	0.09	0.13
SS16	0.14	0.13	0.16	0.15	0.14	0.13
SS17	-0.14	0.15	-0.18	0.17	-0.22	0.15
SS19	0.09	0.13	0.09	0.15	0.06	0.14
SS18	-0.28	0.16	-0.34	0.17	-0.38	0.15
SS20	-0.14	0.12	-0.16	0.14	-0.19	0.13
SS21	-0.01	0.13	-0.02	0.15	-0.06	0.13
SS22	-0.17	0.13	-0.21	0.14	-0.24	0.13
SS23	-0.41	0.17	-0.49	0.16	-0.55	0.14
RT23	-0.05	0.17	-0.09	0.19	-0.15	0.15
SS25	-0.10	0.12	-0.13	0.13	-0.16	0.12
SS24	-0.13	0.12	-0.16	0.14	-0.19	0.12

RT17	0.00	0.00	0.00	0.00	0.00	0.00
RT18	-0.24	0.14	-0.30	0.14	-0.35	0.13
RT19	-0.04	0.12	-0.06	0.14	-0.09	0.12
SS26	-0.13	0.15	-0.18	0.16	-0.24	0.13
SS37	-0.49	0.25	-0.63	0.22	-0.70	0.16
RT12	0.16	0.14	0.16	0.17	0.13	0.15
SS27	-0.22	0.16	-0.27	0.17	-0.32	0.14
RT14	-0.22	0.16	-0.28	0.17	-0.34	0.14
SS28	-0.24	0.17	-0.31	0.18	-0.38	0.14
RT01	0.01	0.16	-0.04	0.18	-0.11	0.15
SS29	-0.26	0.18	-0.33	0.18	-0.40	0.15
ARAZ	0.00	0.23	-0.09	0.24	-0.18	0.17
RT21	0.72	0.16	0.78	0.15	0.75	0.14
SS30	-0.01	0.17	-0.07	0.18	-0.14	0.15
RT05	-0.17	0.19	-0.24	0.19	-0.32	0.15
SS38	0.55	0.17	0.56	0.20	0.51	0.16
THQ2	-0.23	0.25	-0.36	0.24	-0.46	0.17

Electronic Appendices

Expanded array dataset consisting of time slices for all events located and used, seismometer station information in xml format and a QML format earthquake catalog.

Files used for earthquake location via NonLinLoc & hypoDD.

Tomography catalog in QML format and time slices for events in tomography. Input and output files used for tomoDD including input and output velocity models.

TIMA mineralogy scans as high-resolution .png image files.

The data for the pXRF, XRD and TIMA has not been included in the electronic appendix due to confidentiality. The data can be requested from Mercury Energy (contact Farrell Siega - Farrell.Siega@mercury.co.nz or Aimee Calibugan - Aimee.Calibugan@mercury.co.nz)